

THE APPLICATION OF ARYLAMINES AS REDOX
AUXILIARIES, POLAR CRYSTALS, AND
ORGANIC SEMICONDUCTORS

by

LESTER TRUMMER GRAY III

SILAS C. BLACKSTOCK, COMMITTEE CHAIR
PATRICK R. LECLAIR
DAVID E. NIKLES
KEVIN H. SHAUGHNESSY
TIMOTHY S. SNOWDEN

A DISSERTATION

Submitted in partial fulfillment of the requirements
for the degree of Doctor of Philosophy
in the Department of Chemistry
in the Graduate School of
The University of Alabama

TUSCALOOSA, ALABAMA

2012

Copyright Lester Trummer Gray III 2012
ALL RIGHTS RESERVED

ABSTRACT

Arylamines and derivatives thereof have been developed for use in several applications. Among these include: the development of an arylamine moiety to act as a trigger and redox catalyst for an organic reaction, the use of a specific arylamine moiety as a synthon in the preparation of a series of polar organic crystalline materials, and a preliminary investigation of an arylamine salt as a potential organic semiconductor.

The synthesis of novel norbornadiene (N) derivatives with appended redox-auxiliary (RA) units for use as switchable photoelectrochromic materials is reported. The photochemical and electrochemical properties are investigated by UV-vis spectroscopy, chemical actinometry, and cyclic voltammetry. The pendant RA functions as a stable redox unit capable of catalyzing the conversion of the N form to the quadricyclane (Q) form, releasing stored ring-strain energy as heat. Aside from demonstrating the principle of RA catalysis, the new N derivatives demonstrate possible utility as recyclable solar fuels or as photo-electrical switchable systems for informational or mechanical applications at the molecular level.

A second project involving the preparation of a series of *m*-phenylenediamine derivatives which assemble (crystallize) preferentially with polar order is described. The crystal structures of these analogs have been elucidated by X-ray crystallography, and their crystalline properties explored by differential scanning calorimetry. Insight gained through this study has led to a greater understanding of the requirements for polar ordering of these molecules, allowing for the rational design of certain polar organic crystals derived from such structures.

Finally, a preliminary study of the structure and properties of radical cation and dication salts of tetra(*p*-anisyl)-*p*-phenylenediamine (TAPD), which show promise for use as organic one-electron oxidants and as organic semiconductors, is presented. The preparation and characterization of TAPD salts is described. Their electrochemical properties have been explored by powder pellet I-V electrochemical measurements.

LIST OF ABBREVIATIONS AND SYMBOLS

A	Amperes
AA	aryl amino
anhyd	anhydrous
br	broad (spectral)
°C	degree Celsius
calc	calculated
CAN	ceric ammonium nitrate
C ₆ D ₆	deuterated benzene
CDCl ₃	deuterated chloroform
CD ₂ Cl ₂	deuterated methylene chloride
CD ₃ CN	deuterated acetonitrile
cm	centimeter(s)
conc	concentrated
CV	cyclic voltammetry
Δ	heat
δ	chemical shift
d	doublet (spectral)
DSC	differential scanning calorimetry
dd	doublet of doublets (spectral)

DMSO- <i>d</i> 6	deuterated dimethylsulfoxide
dppf	1,1'-bis(diphenylphosphino)ferrocene
E°'	formal oxidation potential
g	gram(s)
h	hour(s)
HOMO	highest occupied molecular orbital
HRMS	high resolution mass spectroscopy
Hz	Hertz
I	electrical current
<i>J</i>	coupling constant (NMR)
LUMO	lowest unoccupied molecular orbital
m	multiplet (spectral)
mg	milligram(s)
MHz	megahertz
min	minute(s)
mL	milliliter(s)
mmol	millimole(s)
mp	melting point
mV	millivolt(s)
μA	microamperes
N	norbornadiene
NaOt-Bu	sodium <i>tert</i> -butoxide
Ns	nosyl

nm	nanometer(s)
NMR	nuclear magnetic resonance
ORTEP	Oak Ridge Thermal Ellipsoid Plot
PD	<i>p</i> -phenylenediamino
Pd(dba) ₂	bis-(dibenzylideneacetone)palladium
pet	petroleum
Ph	phenyl
ppm	part(s) per million
P(<i>t</i> -Bu) ₃	tri- <i>tert</i> -butylphosphine
Q	quadricyclane
rt	room temperature
s	second(s); singlet (spectral)
SCE	saturated calomel electrode
TBABF ₄	<i>n</i> -tetrabutylammonium tetrafluoroborate
TLC	thin-layer chromatography
TMS	tetramethylsilane
Ts	tosyl
V	volt(s)

ACKNOWLEDGMENTS

Foremost, I would like to thank my research advisor, Professor Silas C. Blackstock, for his willingness to invest such a great amount of time and energy into my training as a scientist. He believed in me even through times when I myself did not and, with great patience, pushed me to persevere. He possesses a passion for research and a teaching acumen which I have found unmatched throughout my academic career. I am forever in his debt, and will be honored to carry his name as my doctor-father.

I also extend my great appreciation to my committee members, Professors Patrick LeClair, David Nikles, Kevin Shaughnessy, and Timothy Snowden. Their insight and suggestions have been invaluable to my research, and their questions inspirational to my development of a broader and deeper understanding of chemistry.

I would be remiss not to acknowledge my fellow graduate students and group members, past and present, who have provided encouragement, offered much fruitful discourse, and contributed to a pleasant work environment.

I offer up my heartfelt gratitude to my parents, whose steadfast love and unwavering support I have leaned on, not only during my graduate studies, but throughout my entire life.

Finally, I thank my wife and best friend, Martha, for her love, her patience, and her understanding, through times good and bad, through trials and through triumphs. A true Proverbs thirty-one woman, she is loved and cherished more than she knows.

CONTENTS

ABSTRACT	ii
LIST OF ABBREVIATIONS AND SYMBOLS	iv
ACKNOWLEDGMENTS	vii
LIST OF TABLES	xi
LIST OF FIGURES	xii
LIST OF SCHEMES	xvi
COMPOUND STRUCTURE LEGEND.....	xviii

CHAPTER 1

REDOX-AUXILIARY CATALYSIS FOR PHOTOELECTROCHROMIC SWITCHING

1.1 Introduction.....	1
1.2 Synthesis of AA-N-Ts and PD-N-Ts.....	8
1.3 Optical and Electrochemical Properties of Norbornadienes	12
1.4 AA-N-Ts/AA-Q-Ts Photochemistry	15
1.5 AA-N-Ts/AA-Q-Ts Redox Chemistry	28
1.6 PD-N-Ts/PD-Q-Ts Photochemistry	37
1.7 PD-N-Ts Crystal Structure	43
1.8 The Necessity of the RA Unit: 4-BrPh-N-Ts and Ph-N-Ac	44
1.9 Other RA-N Systems: Preliminary Studies of AA-N-Ns and AA-bis(N-Ts).....	49

1.10	Conclusions	55
1.11	Experimental	55

CHAPTER 2

CRYSTAL ENGINEERING OF POLAR *m*-PHENYLENEDIAMINE DERIVATIVES

2.1	Introduction	86
2.2	Introduction to Single Crystal X-ray Diffractometry	87
2.3	Introduction to Differential Scanning Calorimetry	88
2.4	Introduction to Polar Crystals	89
2.5	Polar Order Observed in <i>m</i>-Phenylenediamine Derivatives	90
2.6	Synthesis	92
2.7	Dipole Calculations	94
2.8	X-ray Diffractometry	96
2.9	Differential Scanning Calorimetry	105
2.10	Non-polar <i>m</i>-Phenylenediamine Derivatives	110
2.11	Synthesis	110
2.12	Dipole Calculations	111
2.13	X-ray Diffractometry	112
2.14	Polar Order by Rational Design: H-<i>m</i>PD-OMac	116
2.15	Synthesis	116
2.16	X-ray Diffractometry	117
2.17	Conclusions	118

2.19 Experimental	119
--------------------------------	-----

CHAPTER 3

SEMICONDUCTIVE TETRA-P-ANISYL-P-PHENYLENEDIAMINE RADICAL CATION AND DICATION SALTS

3.1 Introduction	126
3.2 Synthesis of TAPD and TAPD Salts	127
3.3 Cyclic Voltammetry.....	128
3.4 Redox Titrations of TAPD	129
3.5 Solvent Stability Testing of TAPD Salts	133
3.6 Conductance Measurements	137
3.7 Conclusions.....	144
3.8 Experimental	145
REFERENCES	148
APPENDIX A – NMR Spectra.....	155
APPENDIX B – Crystallographic Data	185

LIST OF TABLES

2.7.1	AM1 benchmark dipole calculations	94
2.8.1	Comparative crystal parameters for polar <i>m</i> PDs.....	96
2.9.1	DSC data for polar <i>m</i> PDs.....	105
2.13.1	Comparative crystal parameters for non-polar <i>m</i> PDs	112

LIST OF FIGURES

1.1.1. A cartoon representation of the proposed RA effect	3
1.1.2. Arylamino (AA) and <i>p</i> -phenylenediamino (PD) RA units	4
1.1.3. The target RA-substituted N derivatives	8
1.3.1. Optical spectra of N , AA-N-Ts , and PD-N-Ts at 5.0×10^{-5} M in acetonitrile	13
1.3.2. Cyclic voltammogram of AA-N-Ts - 1.0 mM in dichloromethane (0.1 M TBABF ₄) at 20 mV/s scan rate.....	14
1.3.3. Cyclic voltammogram of PD-N-Ts - 1.0 mM in dichloromethane (0.1 M TBABF ₄) at 20 mV/s scan rate.....	15
1.4.1. Arc lamp photoreaction of AA-N-Ts with irradiation >385 nm in deaerated benzene at 5.0×10^{-5} M	17
1.4.2. ¹ H-NMR (360 MHz) of AA-N-Ts in <i>d</i> 6-benzene before exposure to indirect sunlight	18
1.4.3. ¹ H-NMR (360 MHz) of AA-N-Ts in <i>d</i> 6-benzene after 55 min exposure to indirect sunlight (complete conversion to AA-Q-Ts).....	19
1.4.4. Solar photoconversion of AA-N-Ts to AA-Q-Ts through a glass window in deaerated benzene at 5.0×10^{-5} M	20
1.4.5. An example setup for actinometry and the chemical equations describing ferrioxalate photochemistry.....	21
1.4.6. An example dataset for an AA-N-Ts actinometry experiment depicting changes in absorbance of the AA-N-Ts solutions and ferrioxalate/phenanthroline complexes	22
1.4.7. Arc lamp photoconversion of AA-N-Ts to AA-Q-Ts with irradiation >400 nm in deaerated toluene at 5.0×10^{-5} M.....	24
1.4.8. Arc lamp photoconversion of AA-N-Ts to AA-Q-Ts with irradiation >400 nm in deaerated tetrahydrofuran at 5.0×10^{-5} M	25

1.4.9. Arc lamp photoconversion of AA-N-Ts to AA-Q-Ts with irradiation >400 nm in deaerated acetone at 5.0×10^{-5} M	26
1.4.10. Arc lamp photoconversion of AA-N-Ts to AA-Q-Ts with irradiation >400 nm in deaerated acetonitrile at 5.0×10^{-5} M.....	27
1.5.1. AA-Q-Ts (1.0 mM in benzene) to AA-N-Ts by RA catalysis with Orange CRET (0.1 mol%) – Aliquots removed and diluted to 5.0×10^{-5} M for UV-vis.....	31
1.5.2. Thermal conversion of AA-Q-Ts to AA-N-Ts (13 mM in benzene) at rt monitored by $^1\text{H-NMR}$	33
1.5.3. AA-Q-Ts to AA-N-Ts (5.0×10^{-5} M in benzene) RA catalysis with Orange CRET (5.0 mol%)	35
1.5.4. Optical spectrum of AA-Q-Ts prepared for CV (diluted x100 in benzene).....	36
1.5.5. Optical spectrum of the AA-Q-Ts CV sample after four scans (diluted x100 in benzene) demonstrating complete conversion to AA-N-Ts	37
1.6.1. Solar/arc lamp photoconversion of PD-N-Ts to PD-Q-Ts (5.0×10^{-5} M in benzene)	38
1.6.2. An example dataset for an PD-N-Ts actinometry experiment depicting changes in absorbance of the PD-N-Ts solutions and ferrioxalate/phenanthroline complexes	39
1.6.3. Thermal conversion of PD-Q-Ts to PD-N-Ts (13 mM in benzene) at rt monitored by $^1\text{H-NMR}$	40
1.6.4. PD-Q-Ts (5.0×10^{-5} M in benzene) to PD-N-Ts RA catalysis with Orange CRET (0.1 mol%)	42
1.7.1. Molecular conformation of PD-N-Ts as derived from the X-ray crystal structure	44
1.8.1. Cyclic voltammogram of 4-BrPh-N-Ts - 1.0 mM in dichloromethane (0.1 M TBABF ₄) at 20 mV/s scan rate.....	45
1.8.2. 4-BrPh-Q-Ts (1.2×10^{-4} M in benzene) oxidation with Orange CRET (5.0 mol%)	46
1.8.3. Cyclic voltammogram of Ph-N-Ac - 1.0 mM in dichloromethane (0.1 M TBABF ₄) at 20 mV/s scan rate.....	48
1.8.4 Ph-Q-Ac (1.3×10^{-4} M in benzene) oxidation with Orange CRET (5.0 mol%).....	49
1.9.1 Optical spectra of AA-N-Ns and AA-N-Ts (5.0×10^{-5} M in benzene)	52

1.9.2 Arc lamp photoconversion of AA-N-Ns with irradiation >455 nm in deaerated benzene at 5.0 x 10 ⁻⁵ M	53
2.4.1. Molecular dipole orientation in non-polar (red) and polar (blue) crystalline solids	90
2.7.1. AM1-calculated dipole moments for polar <i>mPD</i> analogs.....	95
2.8.1. Two-dimensional plane of the Cl-<i>mPD</i> lattice depicting close contacts	99
2.8.2. Two-dimensional layer and nested layers of Cl-<i>mPD</i>	100
2.8.3. Color-contrasted representation of layer stacking in Cl-<i>mPD</i>	101
2.8.4. Interlayer molecular dipole interactions and relative distances	102
2.8.5. F-<i>mPD</i> crystal packing diagram	103
2.8.6. Cl-<i>mPD</i> crystal packing diagram.....	103
2.8.7. Br-<i>mPD</i> crystal packing diagram	104
2.8.8. Cl-<i>mPD-SMe</i> crystal packing diagram.....	104
2.9.1. DSC trace of F-<i>mPD</i>	106
2.9.2. DSC trace of Cl-<i>mPD</i>	107
2.9.3. DSC trace of Br-<i>mPD</i>	107
2.9.4. DSC trace of Cl-<i>mPD-SMe</i>	108
2.9.5. Post-DSC ¹ H-NMR of Cl-<i>mPD-SMe</i>	109
2.12.1. AM1-calculated dipole moments for non-polar <i>mPD</i> analogs.....	111
2.13.1. H-<i>mPD</i> crystal packing diagram.....	115
2.13.2. Cl-<i>mPD-OiPr</i> crystal packing diagram	115
2.14.1. Rationale for putative polar ordering of H-<i>mPD-OMac</i>	116
2.16.1. H-<i>mPD-OMac</i> crystal packing diagram	118
3.3.1. Cyclic voltammogram of TAPD - 1.0 mM in dichloromethane (0.1 M TBABF ₄) at 20 mV/s scan rate.....	129

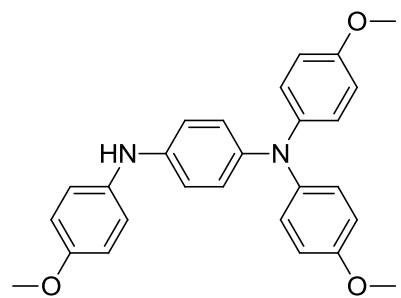
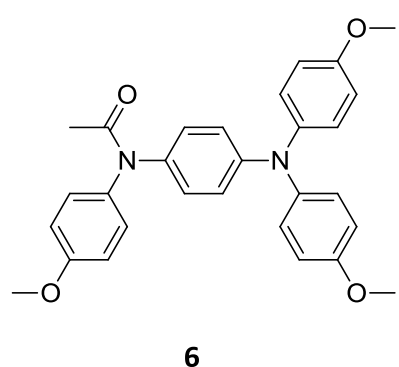
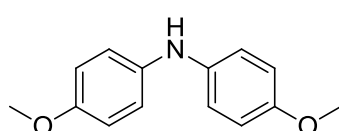
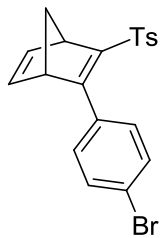
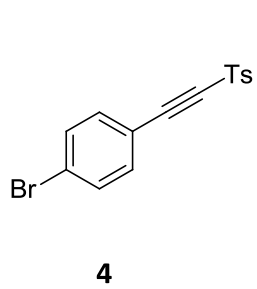
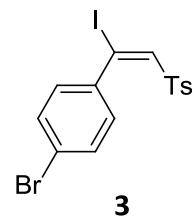
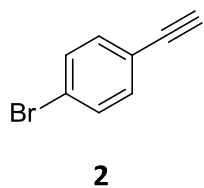
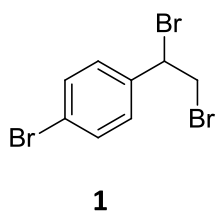
3.4.1. Redox titration of TAPD (8.56×10^{-6} M in acetonitrile) with Orange CRET to 1.0 equivalent	130
3.4.2. Redox titration of TAPD (8.56×10^{-6} M in acetonitrile) with Orange CRET from 1.0 to 2.25 equivalents	131
3.4.3. Redox titration of TAPD (1.03×10^{-5} M in acetonitrile) with CAN to 1.0 equivalent	132
3.4.4. Redox titration of TAPD (1.03×10^{-5} M in acetonitrile) with CAN from 1.0 to 2.25 equivalents	133
3.5.1. Stability of TAPD⁺(PF₆) (1.29×10^{-5} M in HPLC-grade acetonitrile) monitored by UV-vis	134
3.5.2. Stability of TAPD^{++(PF₆)₂} (1.07×10^{-5} M in HPLC-grade acetonitrile) monitored by UV-vis	135
3.5.3. Stability of TAPD^{++(PF₆)₂} (1.07×10^{-5} M in HPLC-grade acetonitrile) with 2.5 v/v% TFAA monitored by UV-vis.....	136
3.6.1. Powder pellet I-V curve of TAPD⁺(PF₆) – 12.0 mg, 20 mV/s	137
3.6.2. Powder pellet step-potential of TAPD⁺(PF₆) – 12.0 mg, -1.0 V, 360 s	138
3.6.3. Powder pellet step-potential of TAPD⁺(PF₆) – 12.0 mg, +1.0 V, 360 s	139
3.6.4. Powder pellet I-V curve of TAPD^{++(PF₆)₂} – 17.3 mg, 20 mV/s	140
3.6.5. Powder pellet step-potential of TAPD^{++(PF₆)₂} – 17.3 mg, -1.0 V, 360 s	141
3.6.6. Powder pellet step-potential of TAPD^{++(PF₆)₂} – 17.3 mg, +1.0 V, 360 s	142
3.6.7. Powder pellet I-V curve of TAPD^{++(PF₆)₂} – 17.3 mg, 200 mV/s, 128 scans	143
3.6.8. Powder pellet I-V curve of TAPD^{++(PF₆)₂} – 17.3 mg, 200 mV/s, 256 scans	144

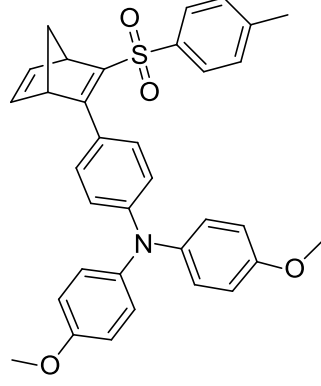
LIST OF SCHEMES

1.1.1. A literature example of redox catalysis involving Diels-Alder cycloadditions	1
1.1.2. The N-Q photo-switchable system	4
1.1.3. A conceptualized N-Q catalytic cycle	5
1.1.4. The N-Q system and the postulated RA-substituted photoelectrochromic system.....	6
1.1.5. The mechanistic pathway of triplet-sensitized N-to-Q conversion.....	7
1.2.1. Synthesis of 4-BrPh-N-Ts	10
1.2.2. Synthesis of AA and PD RA units	11
1.2.3. Synthesis of AA-N-Ts and PD-N-Ts	12
1.5.1. A proposed redox cycle for the AA-Q-Ts to AA-N-Ts conversion	28
1.5.2. The electronic influence of the RA	29
1.5.3. AA-Q-Ts to AA-N-Ts RA catalysis with Orange CRET	30
1.8.1 Synthesis of Ph-N-Ac	47
1.9.1 Synthesis of AA-N-Ns	51
1.9.2. Synthesis of AA-bis(N-Ts)	54
2.5.1. AM1-calculated conformational analysis of Cl-mPD	91
2.6.1. Synthesis of X- <i>m</i> PD compounds.....	93
2.6.2. Synthesis of Cl-mPD-SMe	94
2.11.1. Synthesis of non-polar <i>m</i> PD derivatives.....	111
2.15.1. Synthesis of H-mPD-OMac	117

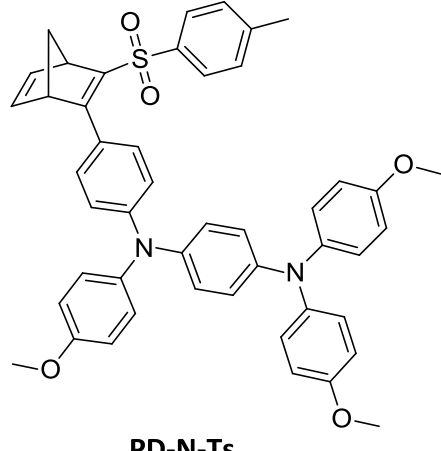
3.2.1. Synthesis of TAPD	127
3.2.2. Synthesis of TAPD⁺(PF₆) and TAPD^{++(PF₆)₂}	128

COMPOUND STRUCTURE LEGEND

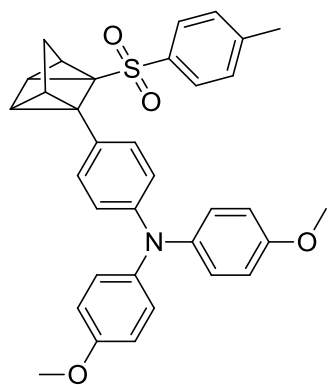




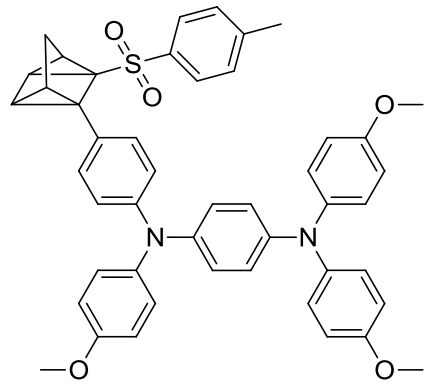
AA-N-Ts



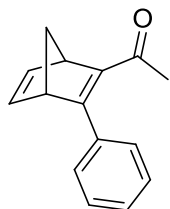
PD-N-Ts



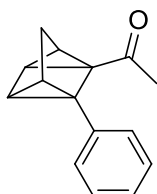
AA-Q-Ts



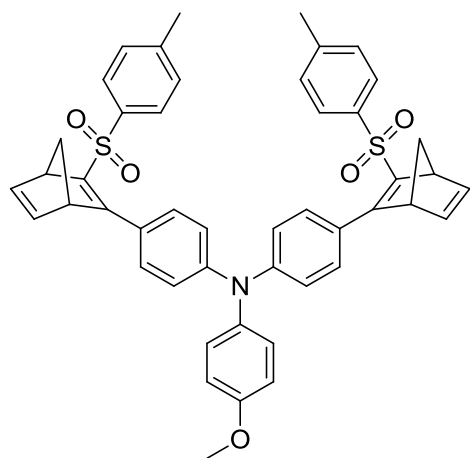
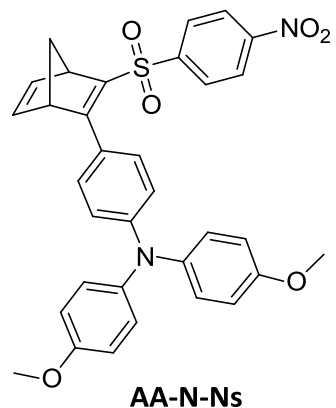
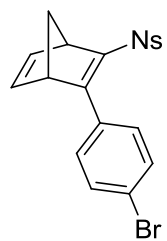
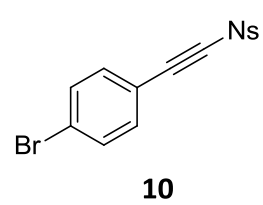
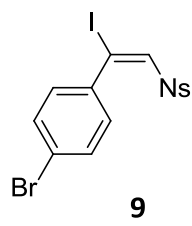
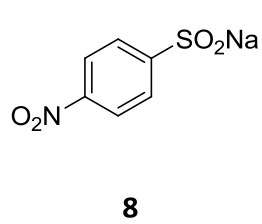
PD-Q-Ts



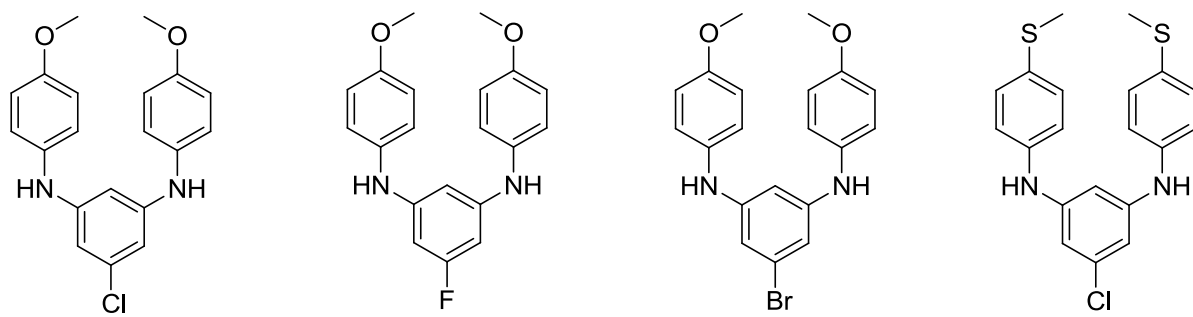
Ph-N-Ac



Ph-Q-Ac



AA-bis(N-Ts)

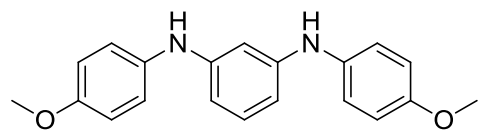


Cl-*m*PD

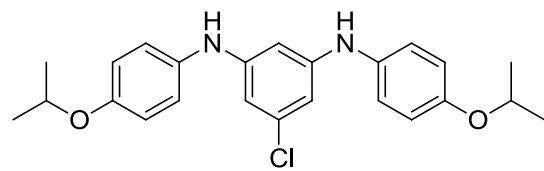
F-*m*PD

Br-*m*PD

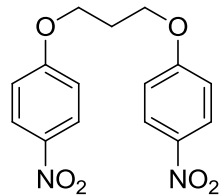
Cl-*m*PD-SMe



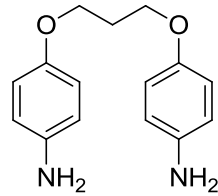
H-*m*PD



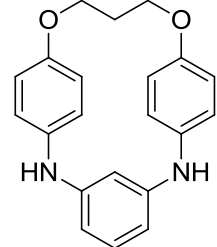
Cl-*m*PD-O*i*Pr



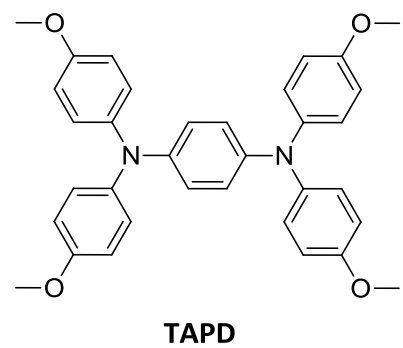
11



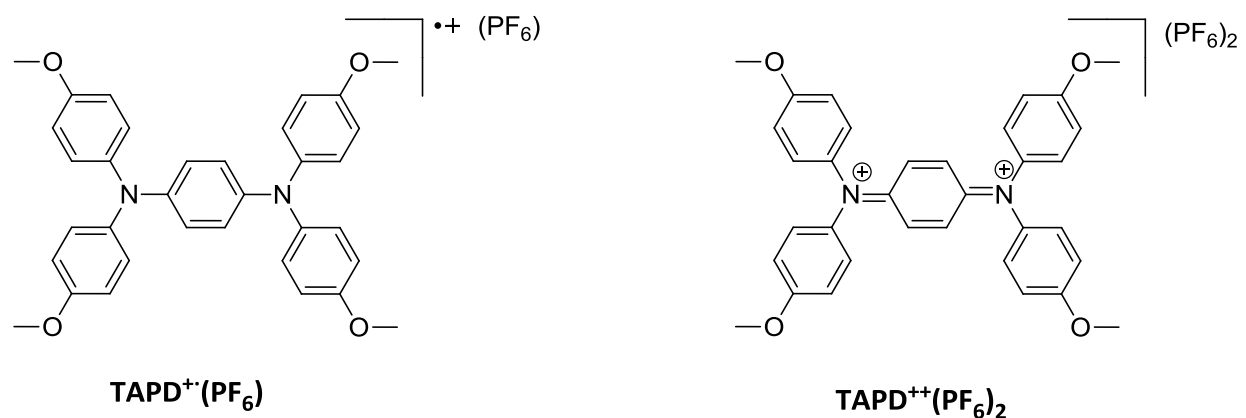
12



H-*m*PD-OMac



TAPD

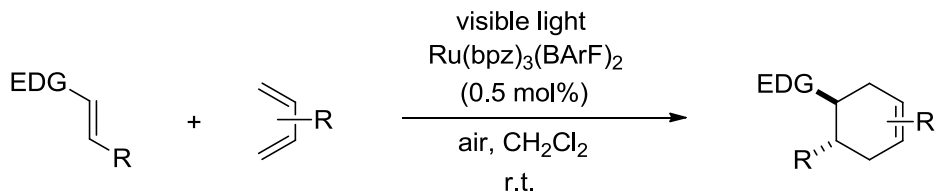


Chapter 1

Redox-Auxiliary Catalysis for Photoelectrochromic Switching

1.1 Introduction

Redox catalysis is a rare but potentially valuable tool in organic synthesis and materials science¹⁻⁴ which involves utilizing changes in oxidation state to catalyze a chemical transformation. The active catalytic species may be the reactive function itself, or it could be a “redox messenger”: a molecule which serves to transfer its charge state to the reactive function. A recent example involving the redox catalysis of radical Diels-Alder cycloaddition reactions⁵ is shown below (Scheme 1.1.1).



Scheme 1.1.1. A literature example of redox catalysis involving Diels-Alder cycloadditions

Though promising, the emerging field of electrochemical reaction chemistry is underdeveloped. This is especially true as it pertains to organic electrosynthetic applications, an area which is very much in its nascency. And while redox catalysis can demonstrate synthetic utility in specific cases, it is limited in scope and general applicability. This is due in no small

part to the necessity that the product of a propagation step be a stronger oxidant than the oxidized starting material if a catalytic redox chain is to be established. This is a demanding requirement that is not easily met.

In an effort to generalize redox catalysis, we have developed a novel concept which we have termed “redox-auxiliary” (RA) catalysis. This new approach differs distinctly from the traditional redox catalytic systems. In RA catalysis, the active catalyst is neither the oxidized form of the reactive function, nor is it a discrete redox carrier. The catalyst is, in fact, the oxidized species of an appended auxiliary incorporated onto the reactive function by a covalent bond.

This prompts us to introduce and clearly define what we refer to as the RA effect. The concept could best be framed as a postulate which asks if an attached redox group (auxiliary) can be used to promote and catalyze a reaction. Figure 1.1.1 depicts this RA effect. The RA is appended to a reactive function. Upon oxidation to the radical cation species, an electronic perturbation is transferred from the RA to the reactive function. This perturbation lowers the activation barrier at the reactive function, thereby enhancing the reaction rate and effecting the desired chemical transformation.

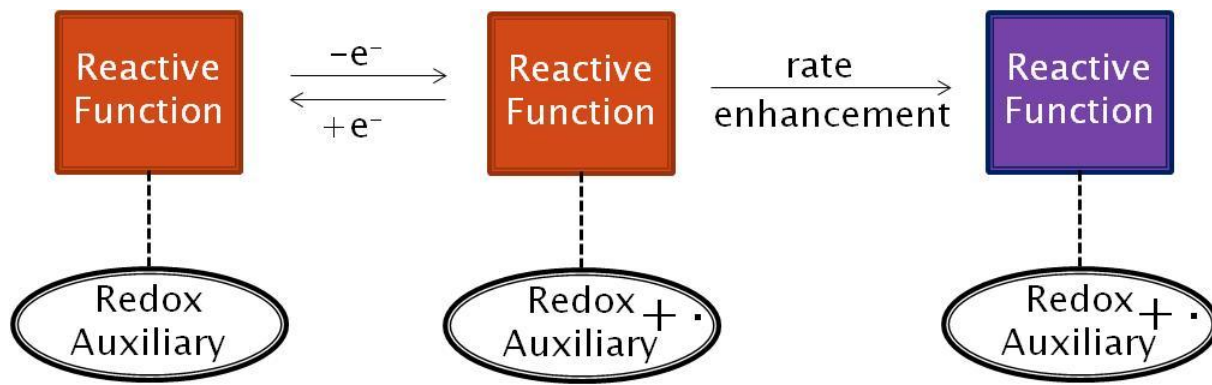


Figure 1.1.1. A cartoon representation of the proposed RA effect

Note that the oxidation of the RA is reversible. This reversibility, as will later be seen, is an essential feature for the system to establish the redox cycle and undergo catalytic turnover based on electron exchange between the redox states of the RA unit. This feature of the RA catalysis approach is expected to allow a more general applicability of redox catalysis to a wide range of reactions.

The RA unit must be a stable radical carrier and, as previously mentioned, will be covalently bound to the reactive function. As our stable radical carrier, we opted to employ arylamines (Figure 1.1.2) due to their high degree of thermal stability, general lack of sensitivity to atmosphere, as well as ease of oxidation.

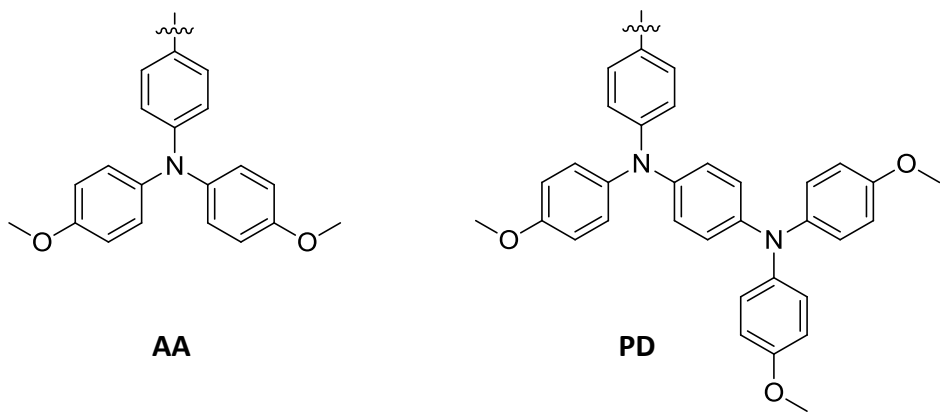
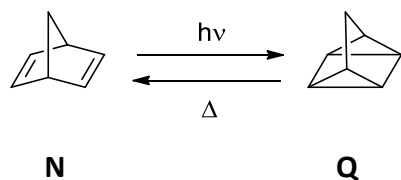


Figure 1.1.2. Arylamino (AA) and *p*-phenylenediamino (PD) RA units

As for the reactive function, the well known norbornadiene-quadracyclane (N-Q) photo-switchable system^{6,7} was chosen as a favorable model system. The N-Q system (Scheme 1.1.2) is optimal for demonstrating the proposed RA effect for a number of reasons. Berson reports that the Q isomer is 24 ± 0.9 Kcal mol⁻¹ higher in energy than N.⁸ This high degree of ring strain present in the Q isomer lends itself toward facile opening to the N form. Also, the conversion takes place via a radical mechanism which we hypothesized would be readily susceptible to the electronic perturbation imparted by the oxidized form of the appended RA. Furthermore, there is a practical application for an N-Q system in which Q-to-N isomerization may be triggered by redox catalysis. The N-Q system has been extensively studied for use as a solar fuel.⁹ As Dubosonov and Chernoivanov report in their review, various approaches have been taken in efforts to develop a feasible N-Q system for this purpose.



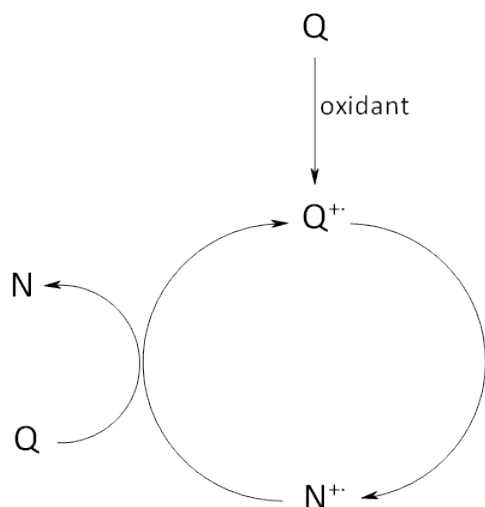
Scheme 1.1.2. The N-Q photo-switchable system

The electrochemical properties of the parent N-Q system have been explored by Gassman and Yamaguchi.¹⁰ They reported the chemically irreversible oxidation of N at $E_{1/2}^{\text{ox}} = 1.56$ V and Q at $E_{1/2}^{\text{ox}} = 0.91$ V vs SCE. Thus, it was recognized that electron-transfer (ET) catalysis of the Q to N conversion should be possible because N^{+} is capable of oxidizing Q, as shown in Scheme 1.1.3. However, the chemical instability of N and Q radical cations render this cycle (as written in Scheme 1.1.3) untenable.

Gassman and Hershberger¹¹ attempted the conversion of Q to N by direct oxidation at a platinum anode and observed rapid fouling of the electrode surface. It was found however, that by including tri-*p*-tolylamine (3.4 mol%), electrochemical conversion of Q to N could be effected. The relatively low oxidation potential of tri-*p*-tolylamine ($E^{\circ'} = 0.66$ V vs SCE) allowed it to act as a sort of redox carrier in the system, negating the need for the high applied potentials that led to anode fouling.

While Gassman's result was promising, it suffered some serious drawbacks which limited its feasibility as a recyclable system. It was found that when the applied potential was halted, the conversion of Q to N likewise immediately ceased. There was also a side reaction produced during the conversion, leading to a build-up of contaminants.

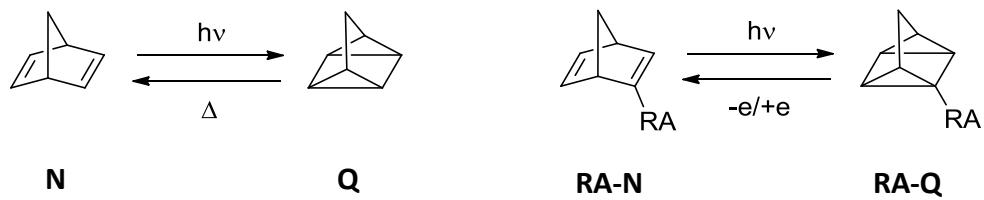
Nevertheless, there is a valuable lesson in Gassman's results. The oxidant used involved an endothermic ET reaction with Q. Under these conditions, the radical cation state resides almost entirely on the stable oxidant, with the Q or N radical cation lifetimes apparently quite



Scheme 1.1.3. A conceptualized N-Q catalytic cycle

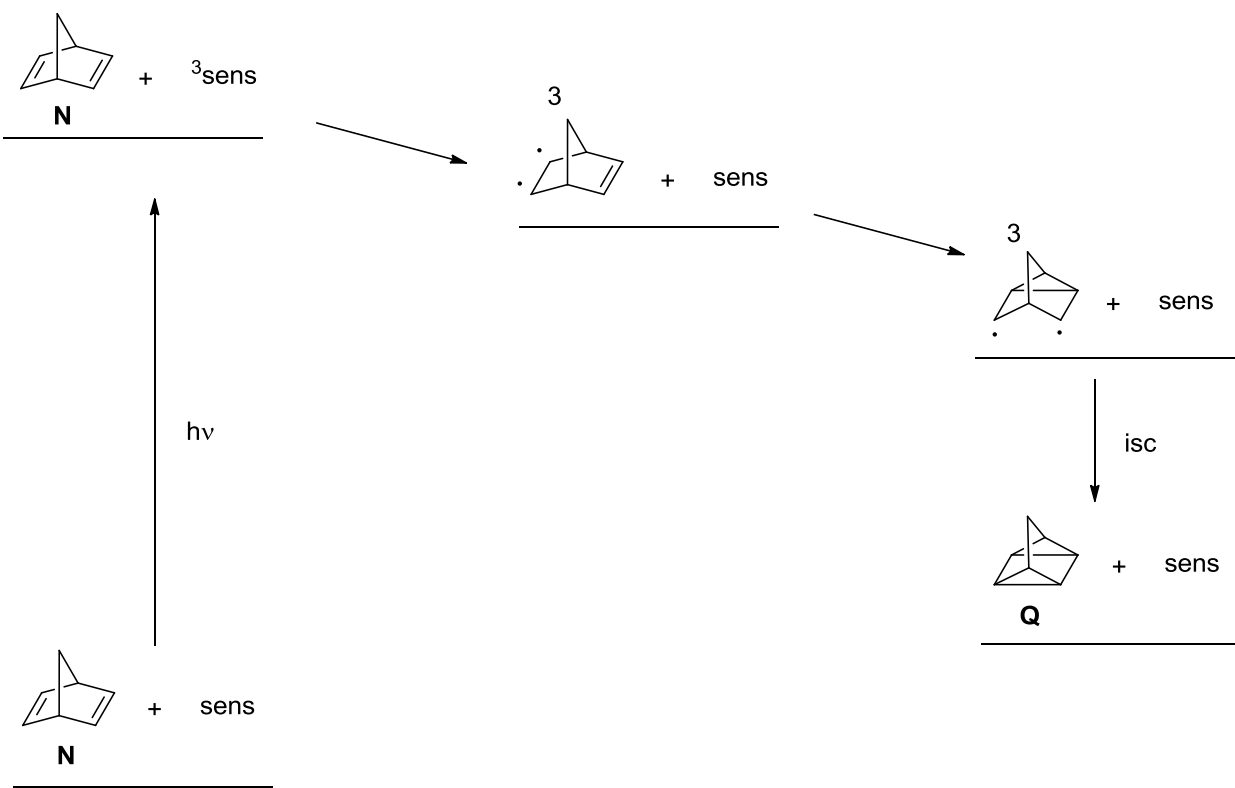
short, though long enough for this facile and exothermic reaction to occur. Learning from this, we sought to investigate the possibility that an RA system could maintain sufficiently long radical cation lifetimes, while avoid the shortcomings of Gassman's system through the prospect of RA catalysis in this case.

Our approach has been to attach a redox-active group (the RA), to an N structure to provide electrochemical triggering of the Q-to-N conversion upon redox change of the RA, hence yielding a material that is isomerized in one direction (N to Q) with light, and in the other direction (Q to N) by electron loss (Scheme 1.1.4). The result would be a new photoelectrochromic material that is switchable between forms by two different types of stimuli.



Scheme 1.1.4. The N-Q system and the postulated RA-substituted photoelectrochromic system

In practice, the parent N-Q system is not a practical photochrome because its photoisomerization must be triplet sensitized.¹² The sensitizer is excited to the triplet state by the appropriate wavelength of UV irradiation. A mechanistic pathway for this transformation proposed by Gould,¹³ with insight from previous studies by Hammond^{14,15} and Gorman,¹⁶ is depicted in Scheme 1.1.5. The triplet character of the excited sensitizer is transferred to N to form the diradical triplet species. This diradical rearranges, accompanied by the homolysis of a double bond and the simultaneous formation of a cyclopropane ring. This triplet species then undergoes intersystem crossing to the singlet Q.



Scheme 1.1.5. The mechanistic pathway of triplet-sensitized N-to-Q conversion

The difficulties associated with utilizing the N-Q system as a solar fuel are twofold. Foremost, N exhibits a λ_{max} of 205 nm¹⁷ and an absorption edge of 250 nm.¹⁸ Therefore, wavelengths necessary to effect the photoconversion of N to Q lie entirely outside of the range of the solar spectrum at the lithosphere, which is shielded by radiation of less than 290 nm by atmospheric ozone.¹⁹ These factors render direct N-to-Q solar photoconversion impossible. The aforementioned triplet sensitizers, which absorb at higher wavelengths, may be used to photoconvert N to Q with visible light; however, these are not photostable at long irradiation times. This will result in both the degradation of the sensitizer, as well as the accumulation of contaminants. Thus, triplet sensitization will not produce a viable recyclable system.

Substituted N's containing groups that extend the pi system allow, in some cases, the direct N-to-Q photoconversion, and such structures can be effective photochromic materials.²⁰⁻²⁴

In our case, the target structure is an arylamino-substituted N structure, AA-N, in which the AA group is the RA connected to the reactive N function via the *p*-position of one of the aryl rings of the triarylamine. For synthetic purposes, it became necessary to also include an electron withdrawing tosyl group on the N alkene, thus yielding an **AA-N-Ts** product (Figure 1.1.3). The tosyl moiety can be removed by reduction with sodium amalgam if desired,²⁵ but we have thus far investigated the photo-electro features of **AA-N-Ts** with the tosyl group included. A related structure containing a *p*-phenylenediamino (PD) redox auxiliary, **PD-N-Ts**, has also been prepared. The photo and electro properties of both **AA-N-Ts** and **PD-N-Ts** have been explored.

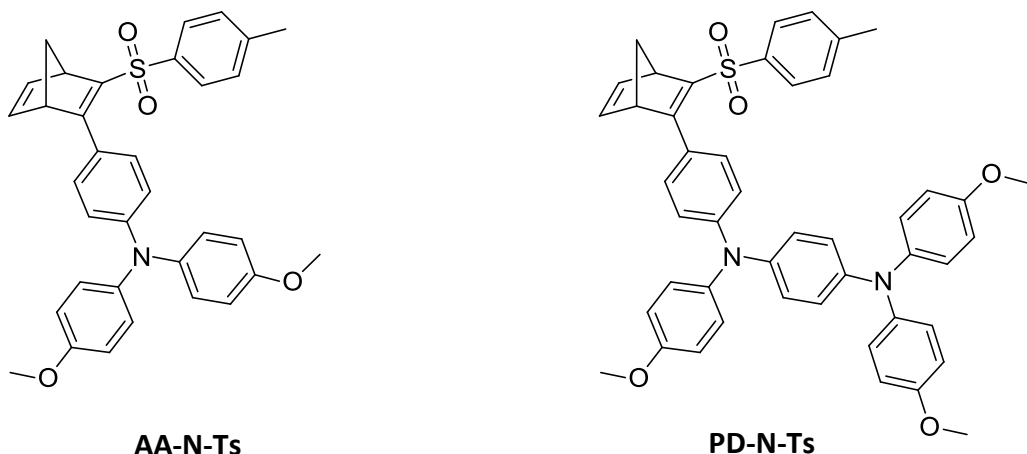
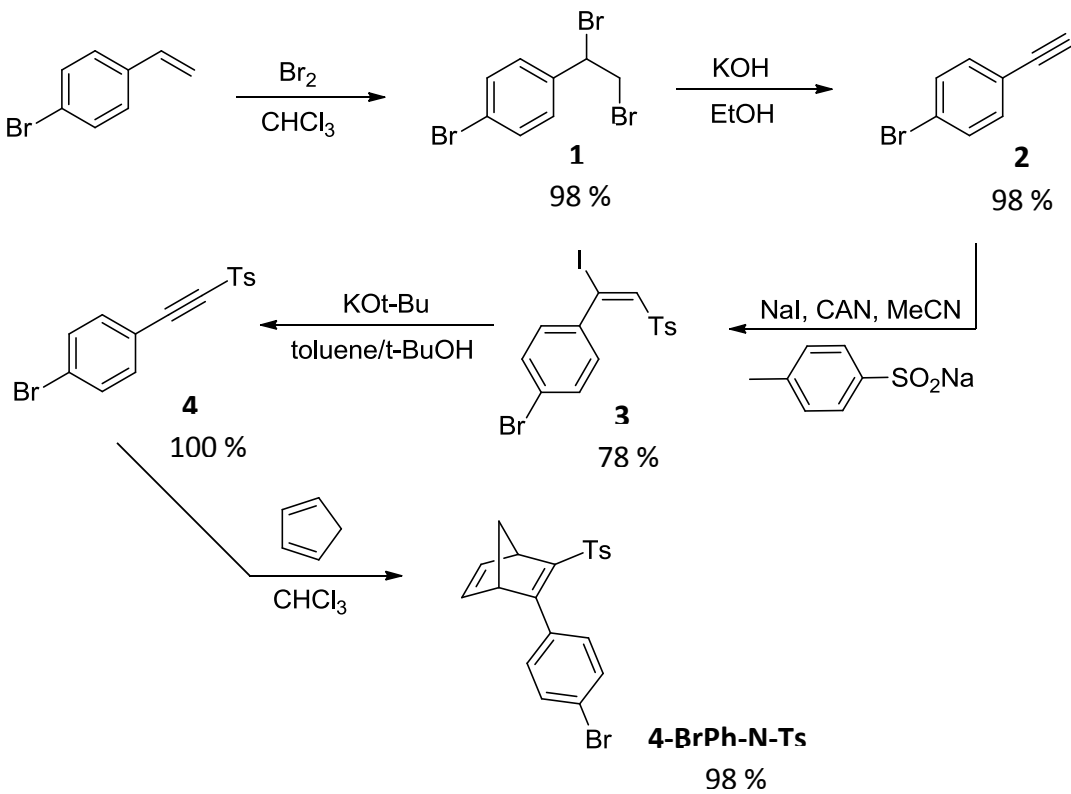


Figure 1.1.3. The target RA-substituted N derivatives

1.2 Synthesis of AA-N-Ts and PD-N-Ts

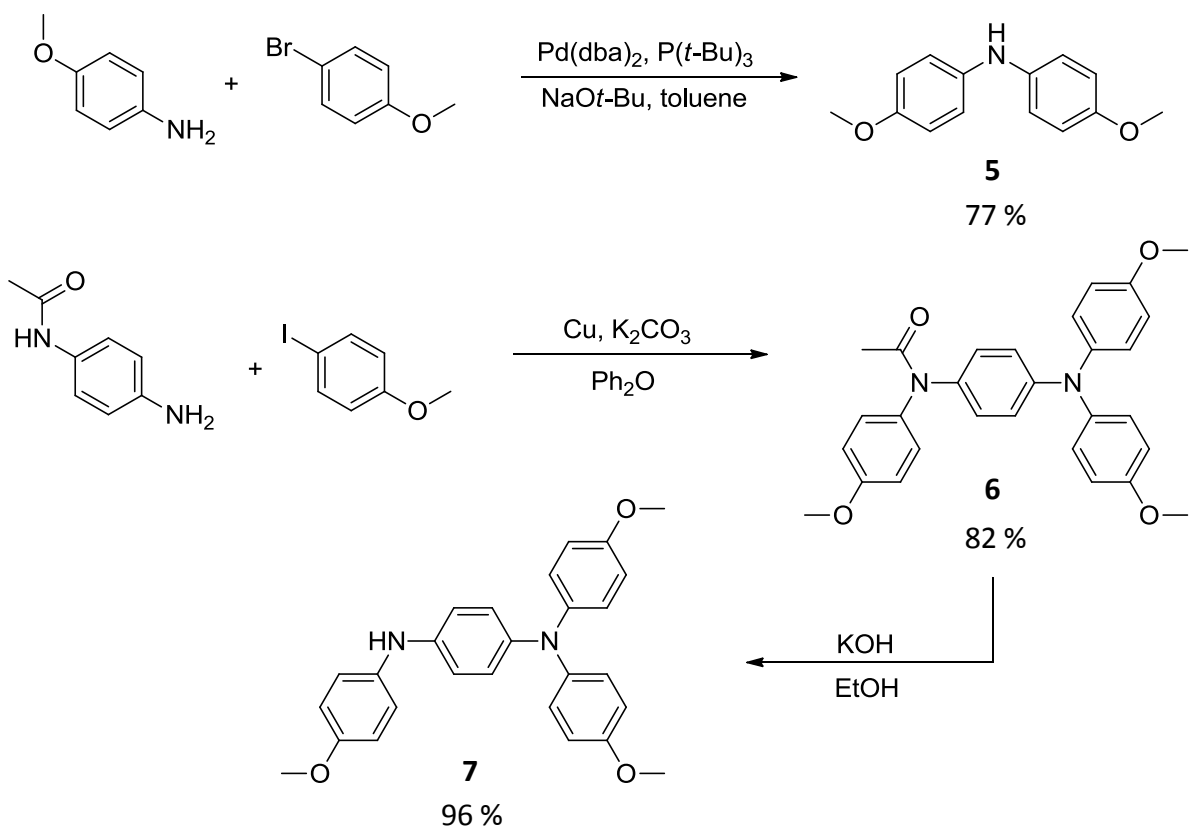
AA-N-Ts and **PD-N-Ts** are synthesized from the intermediate, **4-BrPh-N-Ts**. The synthetic route is depicted in Scheme 1.2.1. Commercially available 4-bromostyrene was brominated according to our own procedure. Reported methods for the synthesis of tribromide **1** involve relatively expensive reagents, such as diacetoxyl iodobenzene²⁶ or

(bromodimethyl)sulfonium bromide,²⁷ which we found to be unnecessary. Double elimination of HBr in the presence of potassium hydroxide²⁸ afforded the phenylacetylene **2**. This compound is unreactive as a dieneophile, thus it is necessary to install a strong electron-withdrawing group. The tosyl moiety was chosen as a good candidate for this role. However, the direct sulfonylation of acetylenes is not described in the literature and our attempts were unsuccessful. Efforts to directly sulfonylate 4-(N,N-dianisylamino)phenylacetylene involved treating the alkyne with *n*-butyl lithium at -78 °C in anhydrous tetrahydrofuran under inert atmosphere, followed by addition of a solution of tosyl chloride. Quenching with aqueous ammonium chloride, then extracting with diethyl ether yielded no detectable amount of the desired product. An analogous reaction using mesyl chloride was likewise met with failure. We therefore found it necessary to first couple **2** to sodium *p*-toluenesulfinate in the presence of sodium iodide and ceric ammonium nitrate²⁹ to arrive at the sulfonylated vinyl iodide **3**. *cis*-Elimination of HI under the influence of potassium *tert*-butoxide in *tert*-butanol gave the acetylenic sulfone **4**. This alkyne underwent a Diels-Alder reaction³⁰ with cyclopentadiene in chloroform to afford **4-BrPh-N-Ts** (Scheme 1.2.1).

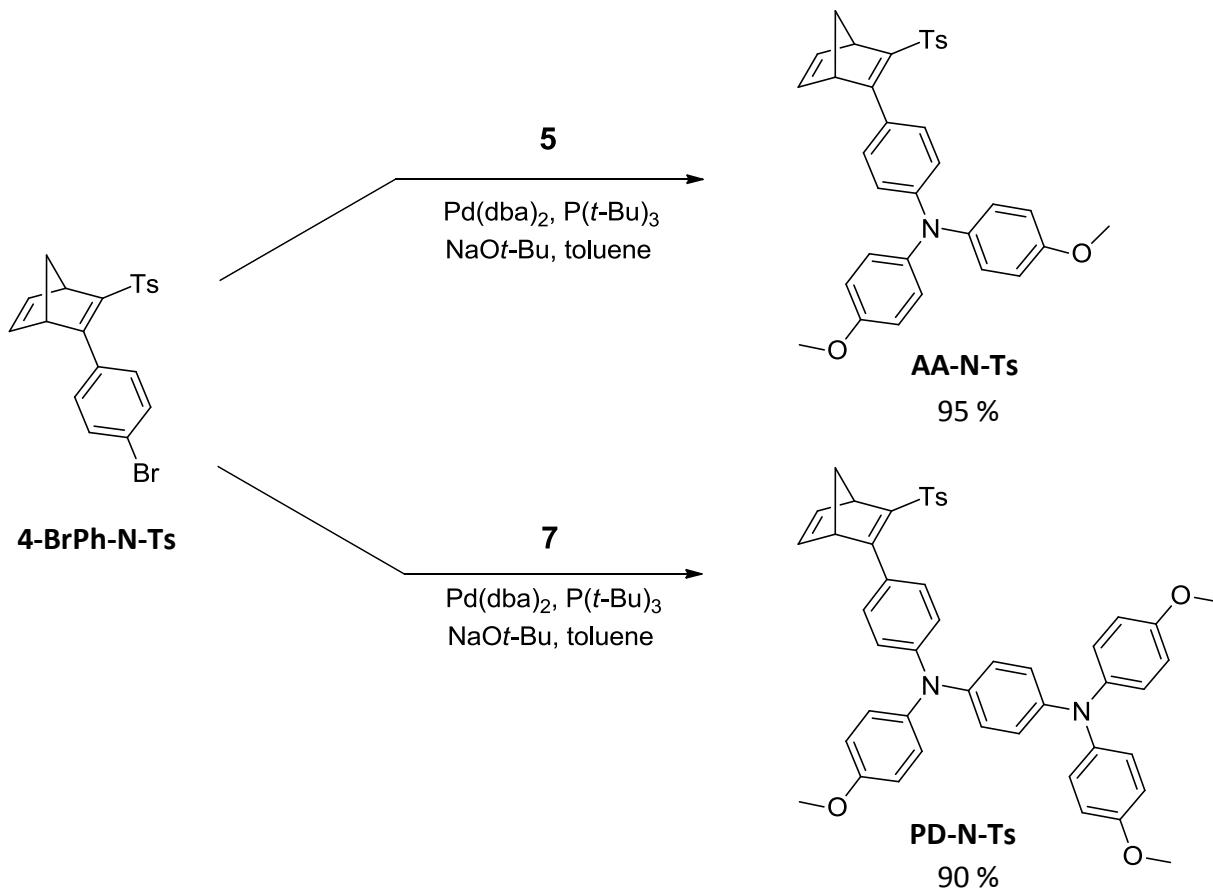


Scheme 1.2.1. Synthesis of **4-BrPh-N-Ts**

The synthesis of the RA units is shown in Scheme 1.2.2. Compound **5** is prepared by N-arylation of *p*-anisidine with *p*-bromoanisole using the protocol of Hartwig et al.³¹ The N-acetylated arylamine **6** was synthesized via Ullmann coupling as previously described by former group member Trent Selby.³² De-acetylation with potassium hydroxide in ethanol yielded trianisyl-*p*-phenylenediamine **7**. **AA-N-Ts** and **PD-N-Ts** are synthesized using the aforementioned N-arylation protocol of Hartwig et al (Scheme 1.2.3).



Scheme 1.2.2. Synthesis of AA and PD RA units



Scheme 1.2.3. Synthesis of **AA-N-Ts** and **PD-N-Ts**

1.3 Optical and Electrochemical Properties of Norbornadienes

Ultraviolet-visible (UV-vis) spectroscopy was utilized to characterize **AA-N-Ts** and **PD-N-Ts**. It also proved to be an invaluable tool for monitoring the progress of N/Q isomerization reactions to determine the relative and absolute concentrations of the isomeric species.

Figure 1.3.1 depicts an overlay of **AA-N-Ts**, **PD-N-Ts**, and the parent N compound, all at equal concentrations (5.0×10^{-5} M) in acetonitrile. The parent N structure exhibits a relatively weak π -to- π^* absorption, and only in the deep UV. With additional substituents in **AA-N-Ts** and **PD-N-Ts**, a dramatic bathochromic shift is observed, exhibiting absorption edges well into the visible spectrum. Both **AA-N-Ts** and **PD-N-Ts** are bright yellow solids.

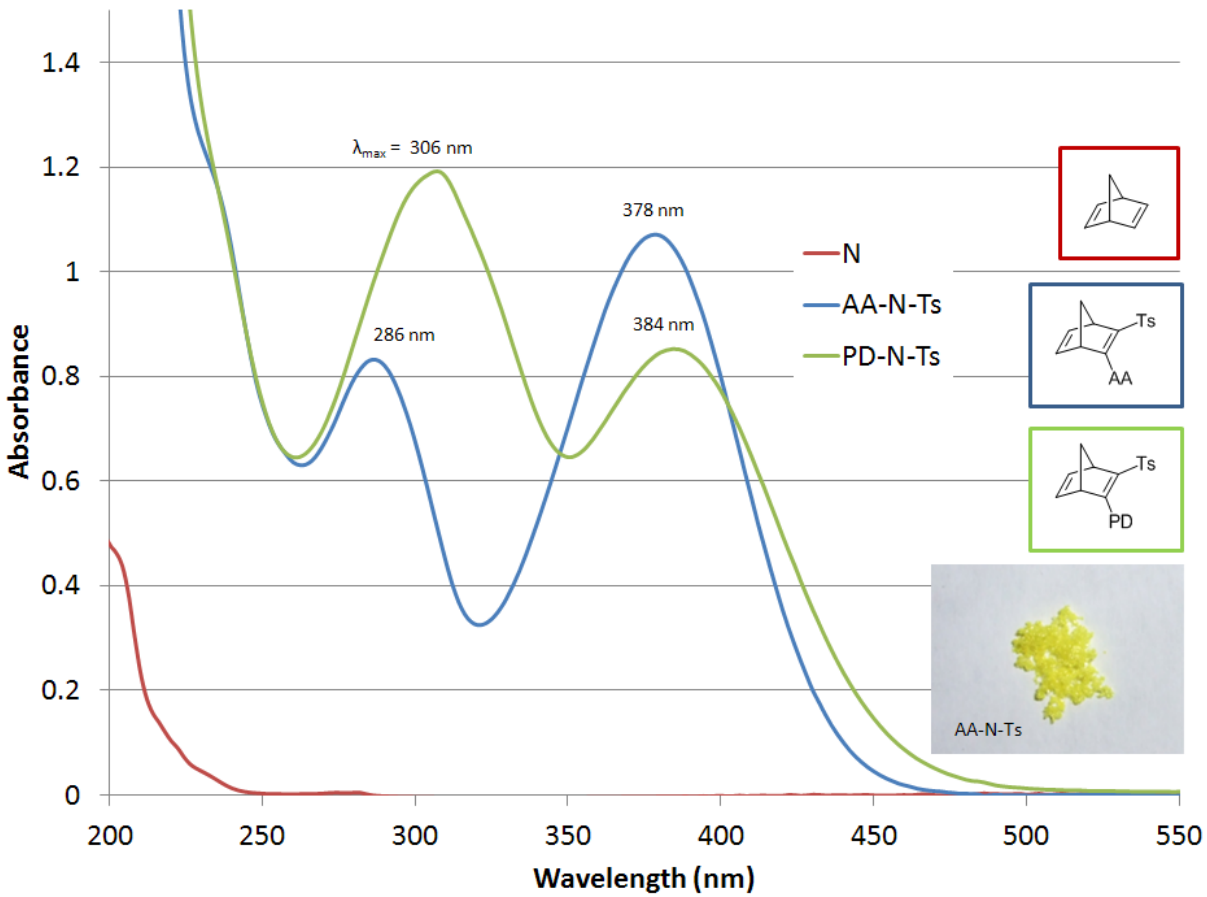


Figure 1.3.1. Optical spectra of **N**, **AA-N-Ts**, and **PD-N-Ts** at 5.0×10^{-5} M in acetonitrile

The oxidation potentials of **AA-N-Ts** and **PD-N-Ts** were measured by cyclic voltammetry (CV) (Figures 1.3.2 and 1.3.3). A reversible oxidation curve is observed with $E^{\circ'} = 859$ mV (vs. SCE) for **AA-N-Ts** and 551 mV (vs. SCE) for **PD-N-Ts**.

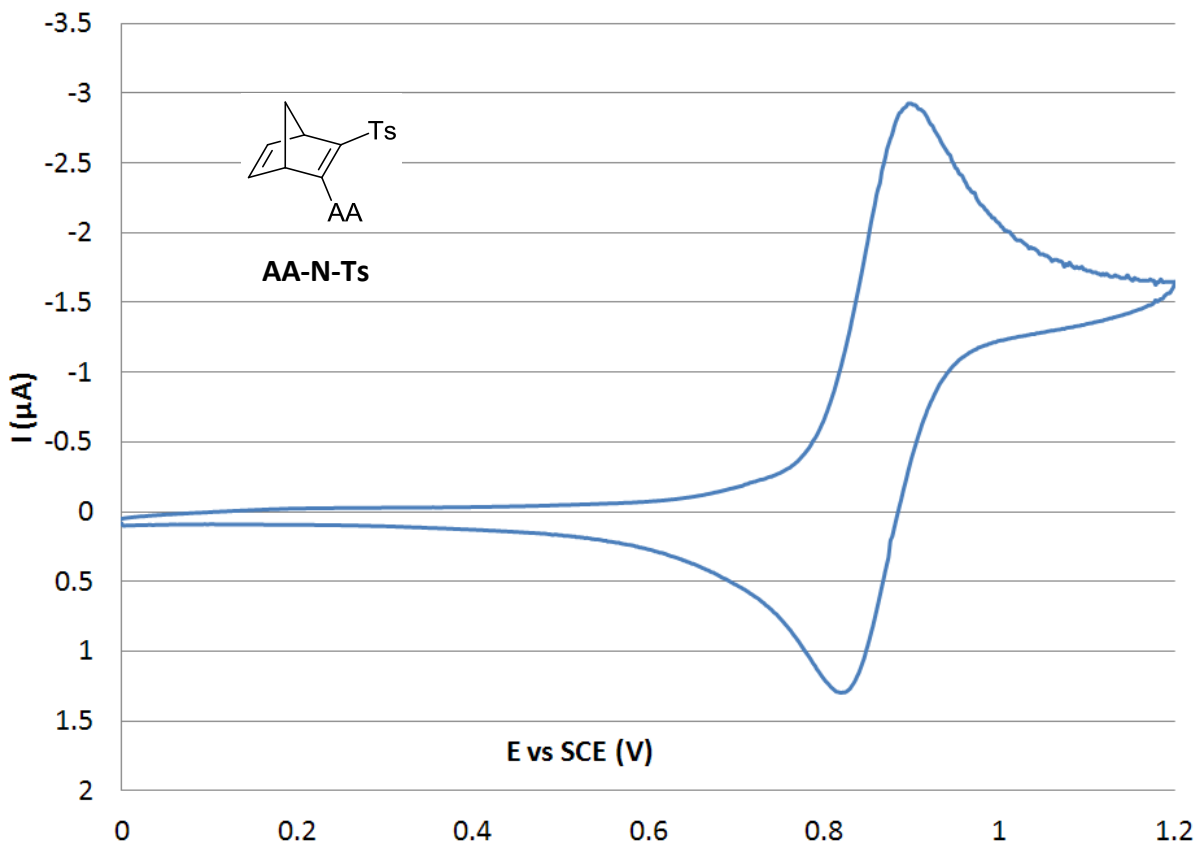


Figure 1.3.2. Cyclic voltammogram of AA-N-Ts - 1.0 mM in dichloromethane (0.1 M TBABF₄) at 20 mV/s scan rate

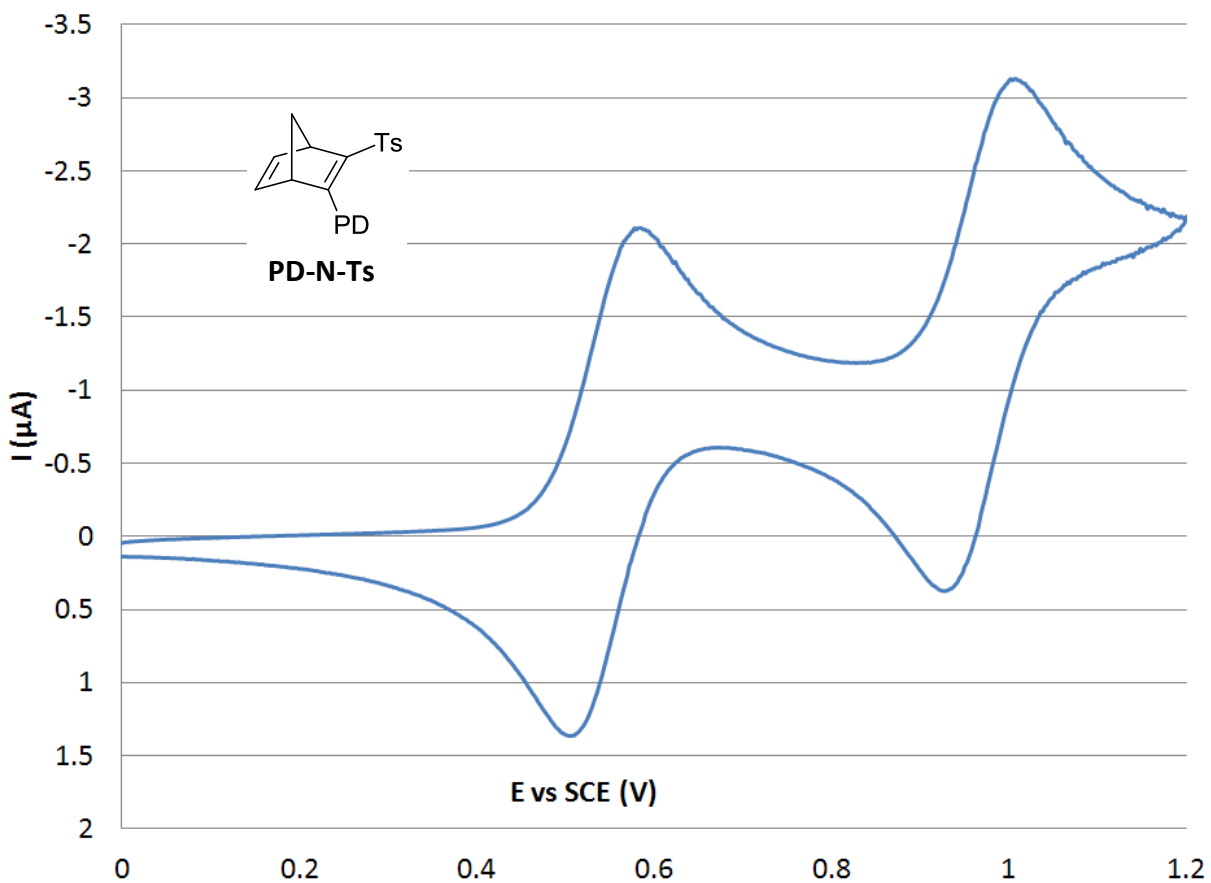


Figure 1.3.3. Cyclic voltammogram of **PD-N-Ts** - 1.0 mM in dichloromethane (0.1 M TBABF₄) at 20 mV/s scan rate

1.4 AA-N-Ts/AA-Q-Ts Photochemistry

Our earliest attempts at photoconversion of **AA-N-Ts** to **AA-Q-Ts** involved the use of a Rayonet reactor equipped with 350 nm bulbs. This was moderately effective; however, we found that a 500 W Hg-Xe arc lamp offered more precise control over the reaction conditions. The arc lamp possessed several advantages as follows: We were able to control the temperature easily by filtering out the infrared (IR) component of the beam with a simple water-filled quartz tube. Also, the beam can be focused to a very tight point (less than 1 cm²), which allowed us to direct all incident light into the sample. Lastly, a variety of chromatic filters can be used in the beam

path to fine tune the wavelength of the incident light to more precisely excite the active absorbance band.

Photoreaction of **AA-N-Ts** was found to proceed cleanly and rapidly upon irradiation with visible light (Figure 1.4.1). As is evidenced by the UV-vis spectra, the long wavelength absorbance of **AA-N-Ts** disappears as the presence of a new absorption band (presumed **AA-Q-Ts**) appears at shorter wavelength. In fact, this photochromic behavior allows for a qualitative assessment as to the extent of photoreaction, simply by observing the bleaching of color from the initially bright yellow **AA-N-Ts** solution. Also of note is the concomitant increase in the short wavelength absorbance as the Q isomer is formed.

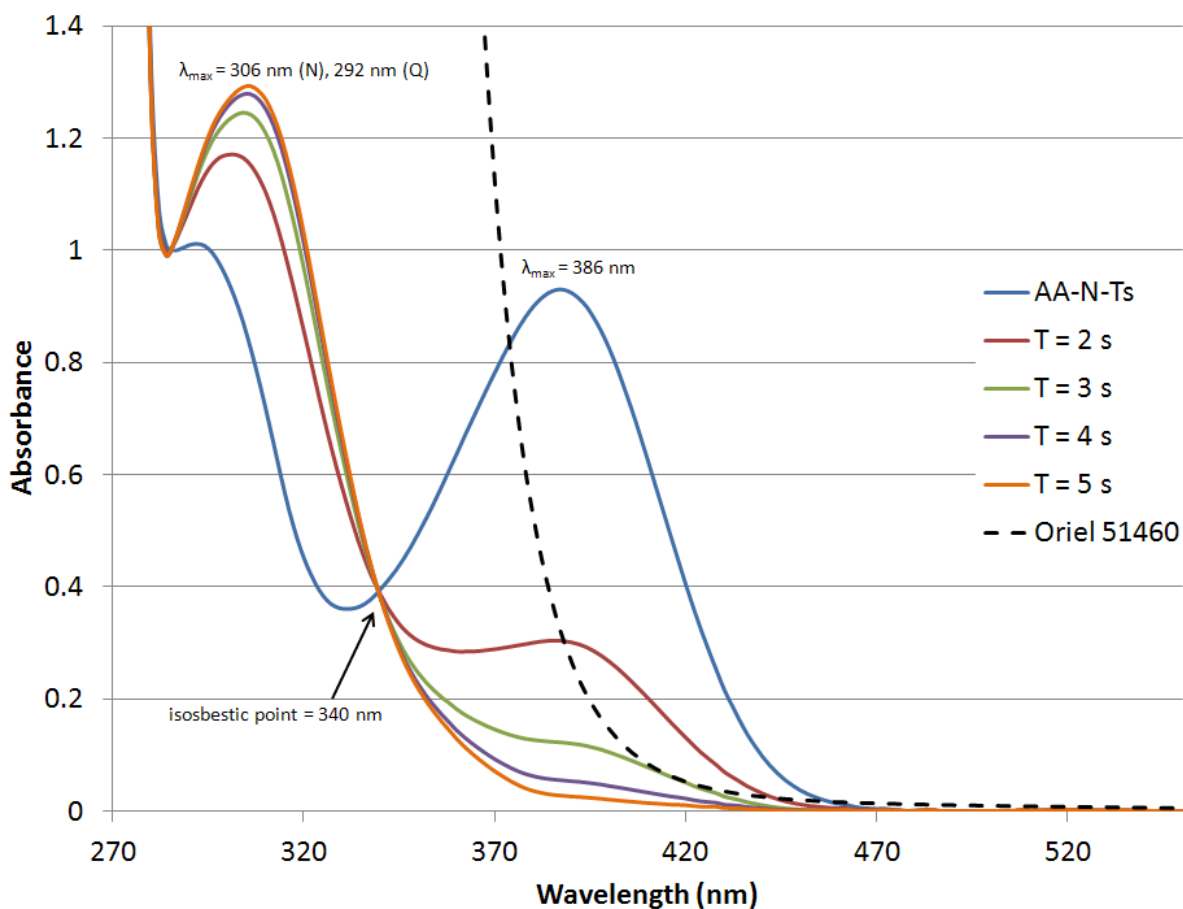
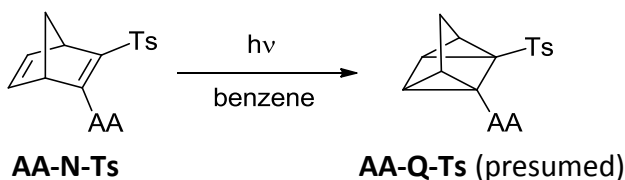


Figure 1.4.1. Arc lamp photoreaction of AA-N-Ts with irradiation >385 nm in deaerated benzene at 5.0×10^{-5} M

A clear isosbestic point (340 nm) can be seen, indicating clean conversion from one species to another. At this point, we are supposing that the **AA-Q-Ts** isomer is the species being formed during irradiation. $^1\text{H-NMR}$ was utilized to determine the identity of the **AA-N-Ts** photoreaction product.

AA-N-Ts was dissolved in C₆D₆ and placed in an NMR tube. A measurement was taken prior to irradiation (Figure 1.4.2). The sample was then exposed to indirect sunlight in a windowsill until bleaching of the solution was observed (55 min). A second ¹H-NMR measurement was taken, and the photoconversion product was confirmed to be **AA-Q-Ts** (Figure 1.4.3).

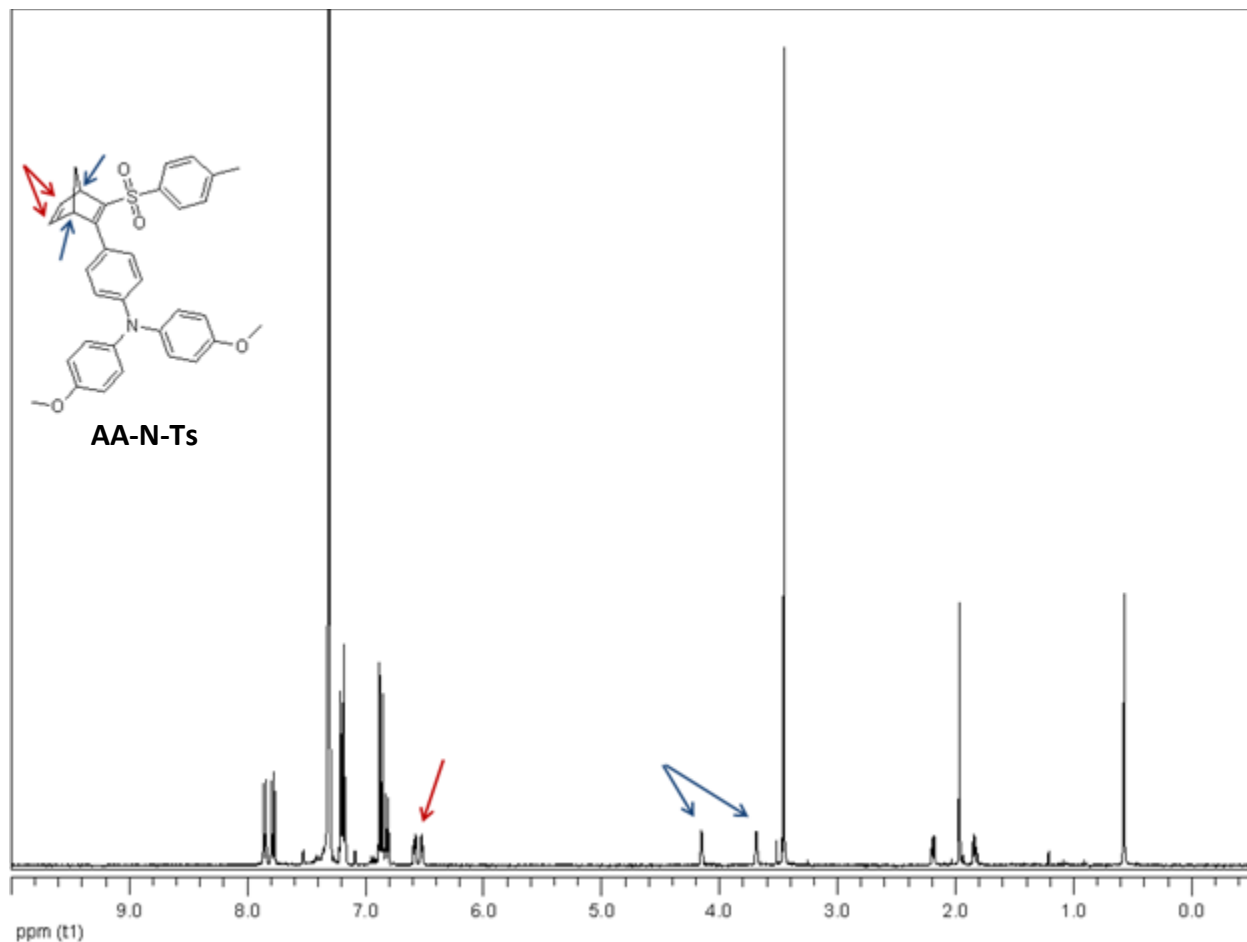


Figure 1.4.2. ¹H-NMR (360 MHz) of **AA-N-Ts** in *d*6-benzene before exposure to indirect sunlight

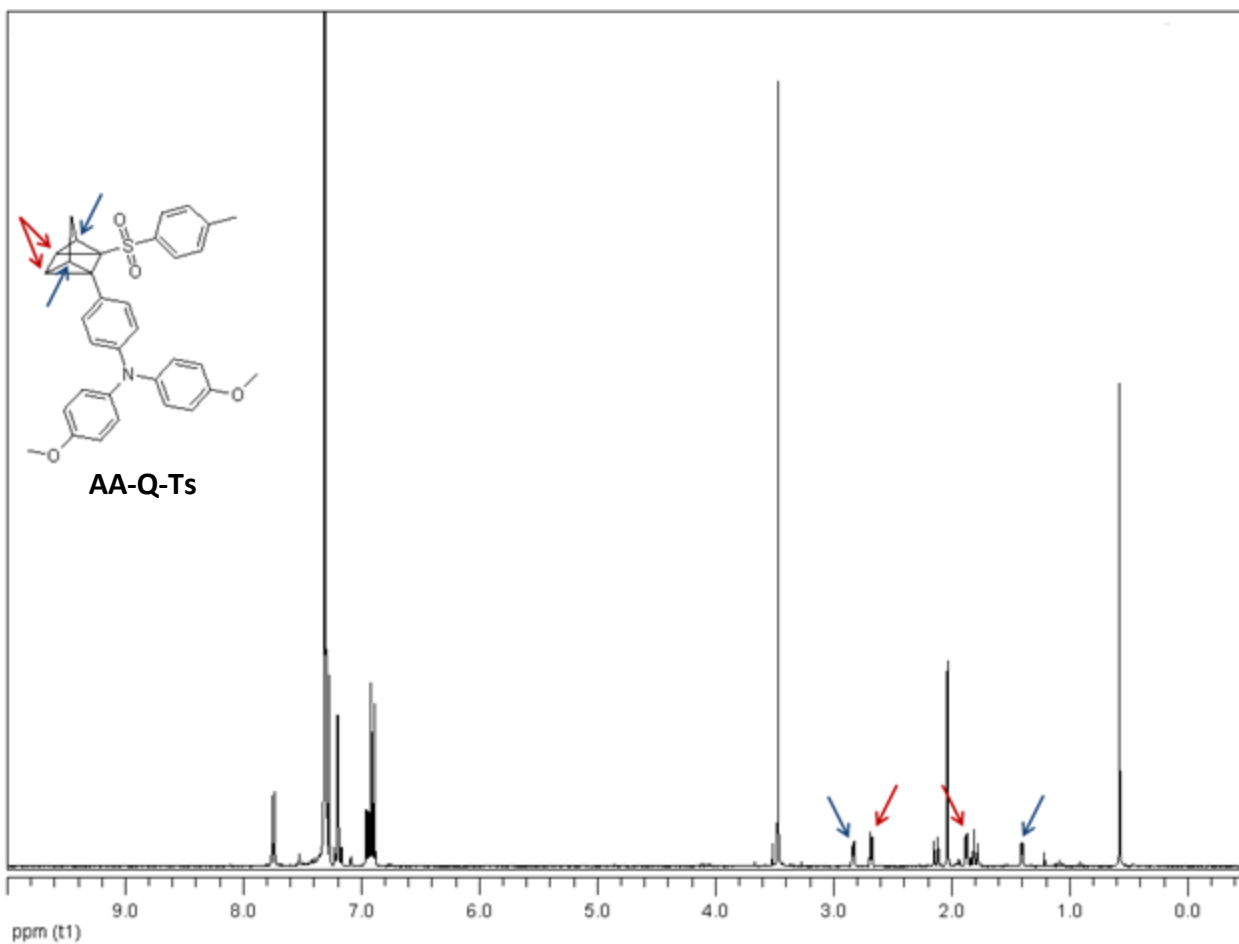


Figure 1.4.3. ^1H -NMR (360 MHz) of AA-N-Ts in *d*6-benzene after 55 min exposure to indirect sunlight (complete conversion to AA-Q-Ts)

Peak assignments were confirmed by one-dimensional, selective nuclear Overhauser effect spectroscopy (1D-NOESY). It can be seen by the disappearance of the two signals at 6.58 and 6.52 ppm, indicative of the olefinic protons (denoted by the red arrow in Figure 1.4.2), accompanied by the appearance of two new upfield signals (red arrows, Figure 1.4.3) that the expected product, AA-Q-Ts has formed. The protons on the bridgehead carbons of AA-N-Ts (blue arrows, Figure 1.4.2) also exhibit a significant upfield shift when converted to the Q isomer.

Having established that the photoisomerization proceeds by irradiation with visible light from an arc lamp, we then sought to evaluate conversion of AA-N-Ts to AA-Q-Ts by solar

irradiation. In this experiment, a dilute sample of **AA-N-Ts** in benzene was placed in a quartz cuvette and exposed to indirect sunlight in a windowsill (Figure 1.4.4).

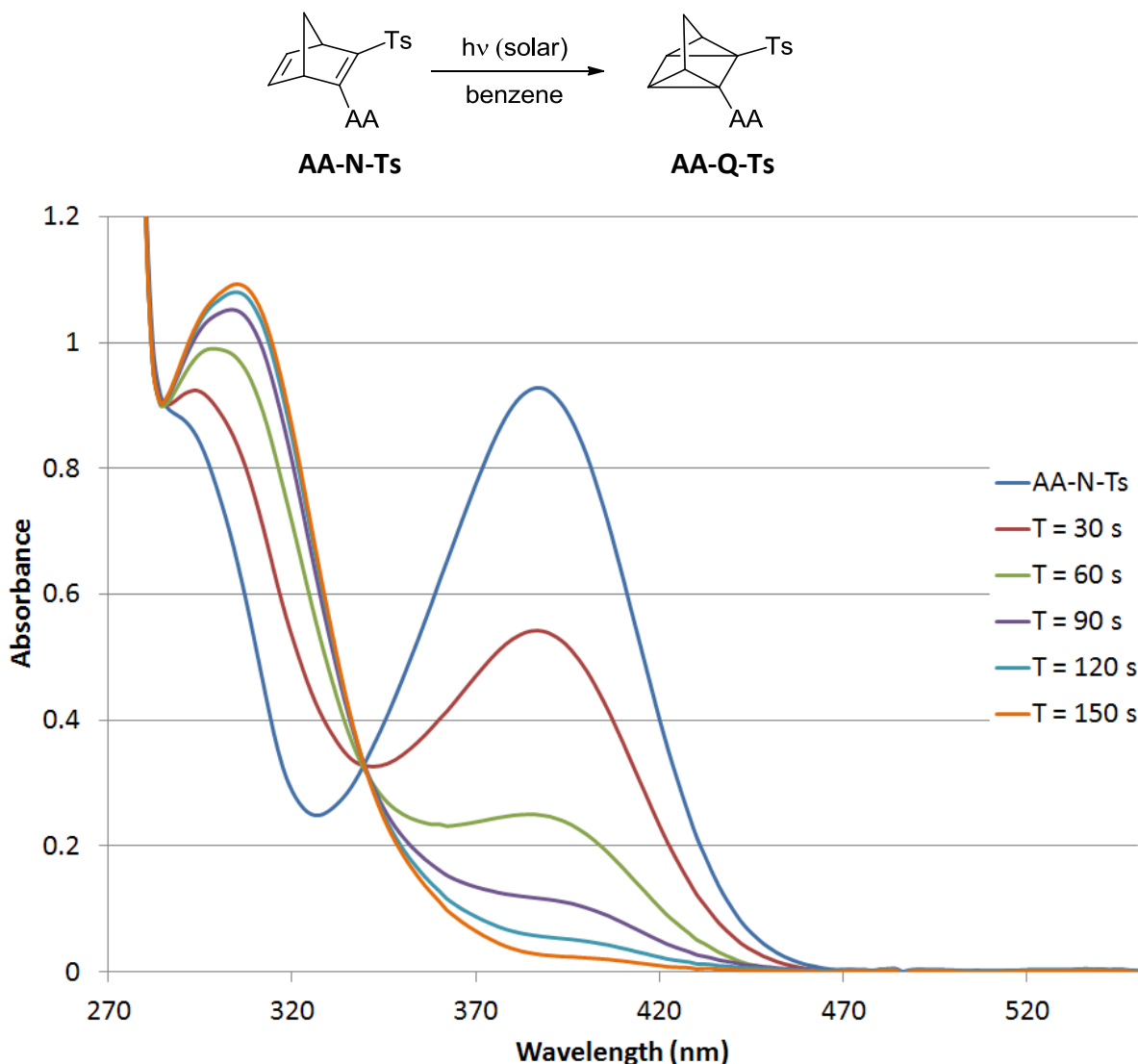


Figure 1.4.4. Solar photoconversion of **AA-N-Ts** to **AA-Q-Ts** through a glass window in deaerated benzene at 5.0×10^{-5} M

It is readily apparent that the **AA-N-Ts** photoconversion is effected by solar irradiation, though the reaction time is significantly longer than when using the arc lamp. Nevertheless, complete conversion by indirect sunlight was observed in only 150 seconds, suggesting that the **AA-N-Ts** system is quite photosensitive.

We have measured the efficiency (quantum yield) of the photoconversion by ferrioxalate actinometry³³⁻³⁶ using a 405 nm GaN laser drawing 50 mA and emitting approximately 20 mW (Figure 1.4.5).

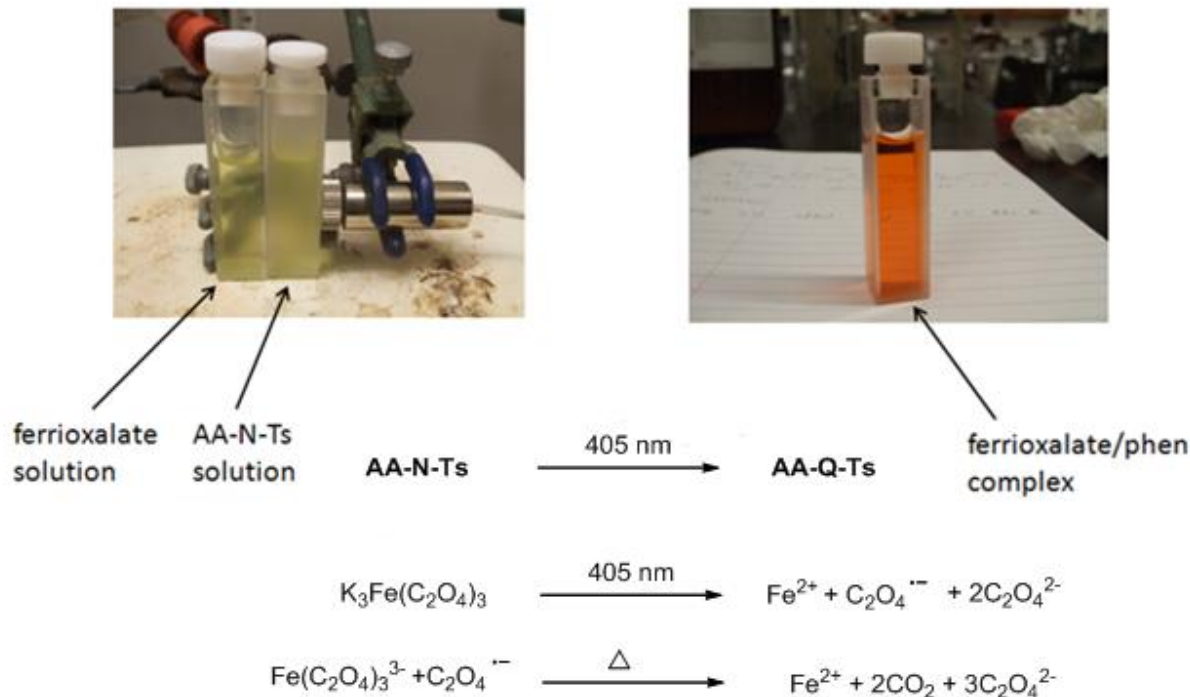


Figure 1.4.5. An example setup for actinometry and the chemical equations describing ferrioxalate photochemistry

The experiment involves first establishing a blank measurement to determine the number of photons emitted by the source laser. This is done by placing two UV-vis cuvettes together in direct contact with the laser. The first cuvette contains the photoreaction solvent and the second cuvette contains an aqueous solution of potassium ferrioxalate. After irradiating for a given period of time, the iron(II) cations formed are complexed with a buffered 1,10-phenanthroline solution. This complex is bright orange and has a known molar absorptivity. From this data can be derived the number of photons per second absorbed by the ferrioxalate solution behind the benzene blank. The procedure is repeated using a known concentration of the **AA-N-Ts** sample.

The difference in the amount of iron(II) formed during the blank run, and the amount formed during the sample run indicate the number of photons absorbed by **AA-N-Ts**. A typical dataset collected during an actinometry experiment is shown in Figure 1.4.6.

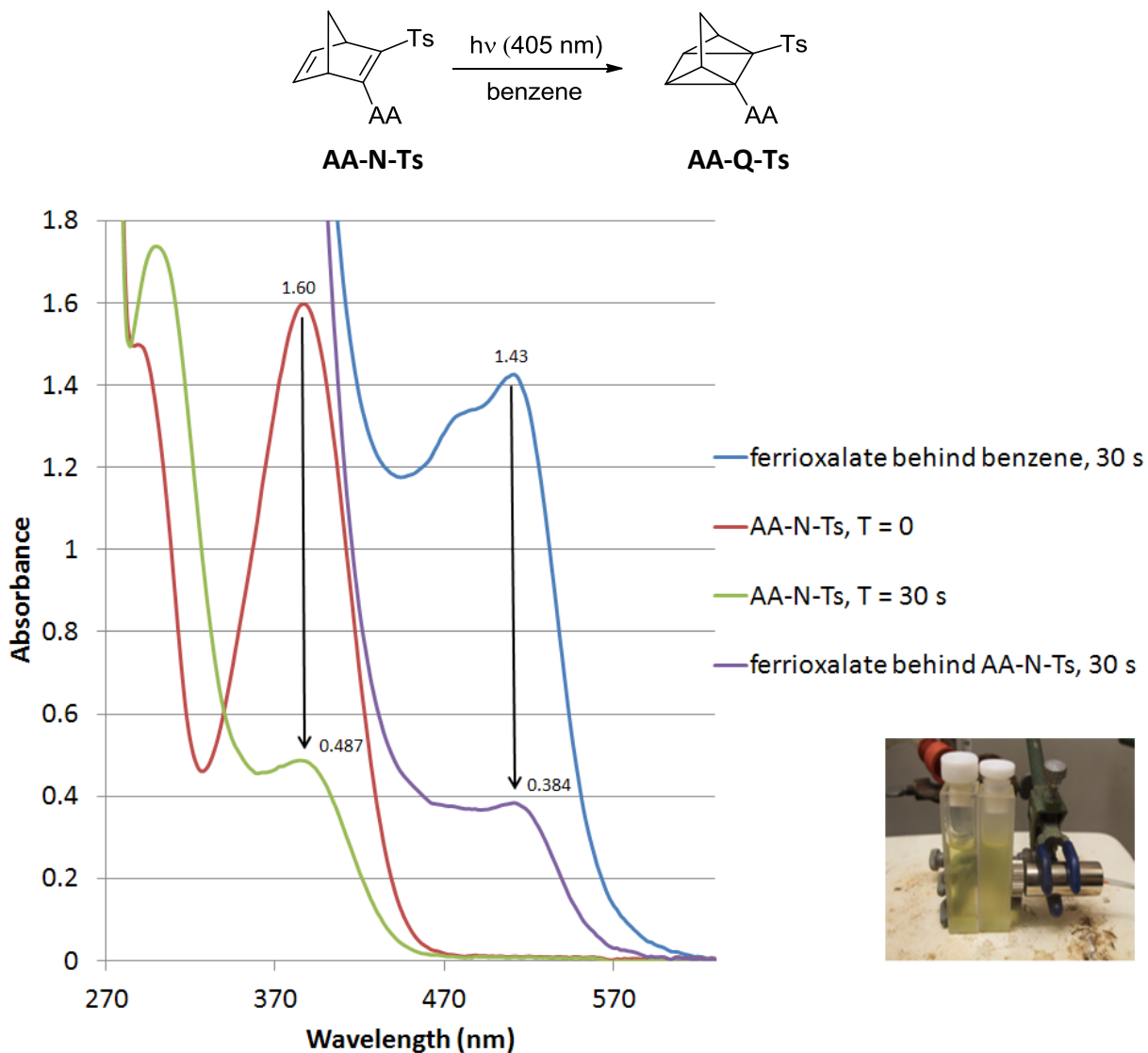


Figure 1.4.6. An example dataset for an **AA-N-Ts** actinometry experiment depicting changes in absorbance of the **AA-N-Ts** solutions and ferrioxalate/phenanthroline complexes

The quantum yield (Φ) for **AA-N-Ts** conversion to **AA-Q-Ts** (i. e. the number of product molecules produced per photon absorbed) was determined four times yielding $\Phi = 0.63, 0.60, 0.59$, and 0.59 for an average of 0.60 ± 0.02 . This photochemical efficiency is high (60 % of the

photons absorbed yield product), and compares favorably to other 2,3-disubstituted N derivatives optimized for photochemical efficiency.³⁷⁻³⁹

All **AA-N-Ts-to-AA-Q-Ts** photoconversion experiments shown to this point were run in benzene. It was found early in our studies of the RA compounds that this is an optimal solvent for effecting rapid, clean conversion to the Q isomer. We did, however, explore other solvents to determine their efficacy in photoconverting **AA-N-Ts**.

As shown previously (Figure 1.4.1), benzene is an exceptional solvent for use with the **AA-N-Ts/AA-Q-Ts** system, as full photoconversion is achieved in only five seconds at 5.0×10^{-5} M concentration. Toluene also was found to give good results, being nearly equivalent to benzene (Figure 1.4.7).

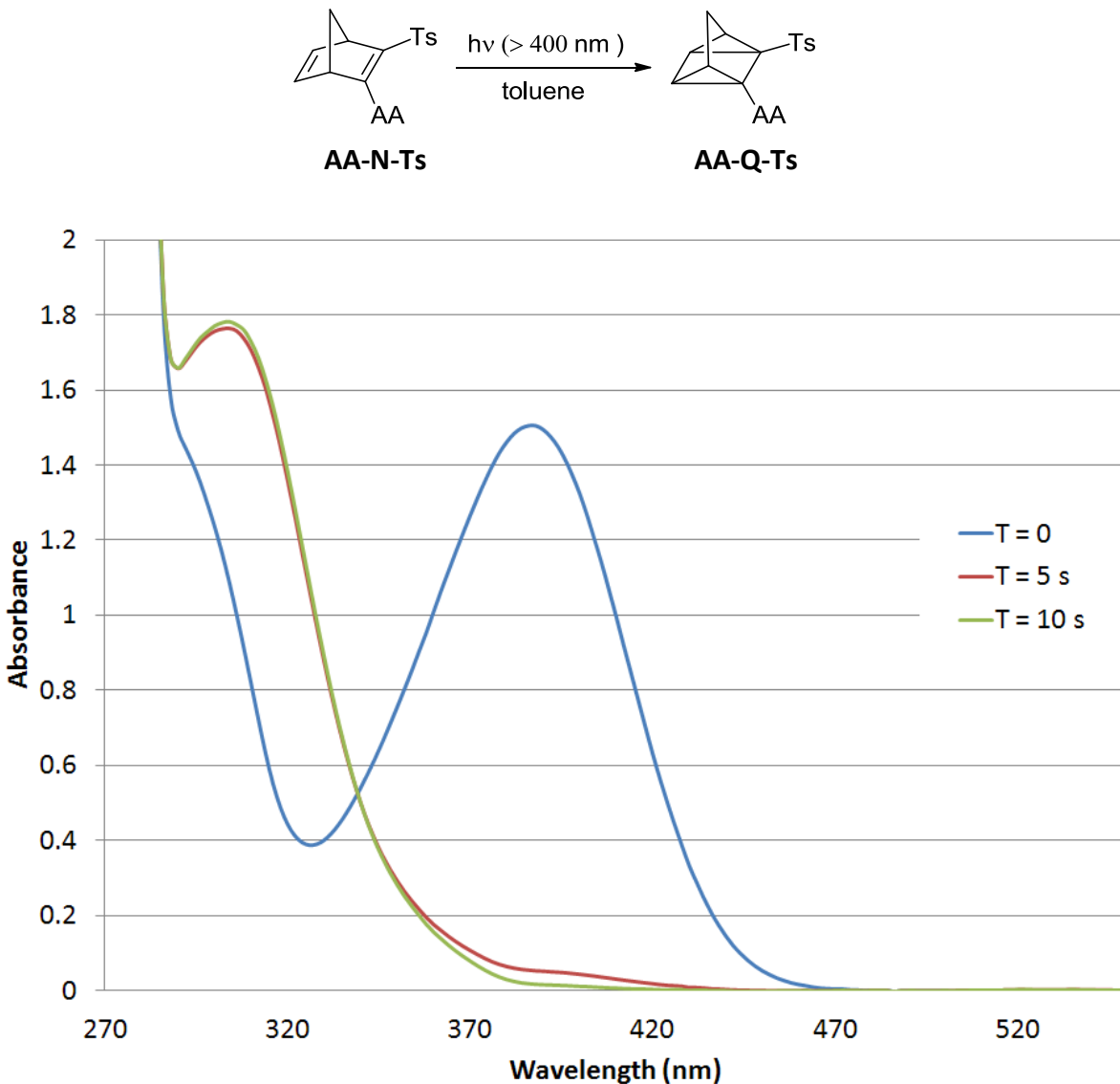


Figure 1.4.7. Arc lamp photoconversion of **AA-N-Ts** to **AA-Q-Ts** with irradiation >400 nm in deaerated toluene at 5.0×10^{-5} M

In tetrahydrofuran (Figure 1.4.8), the photoconversion proceeds more slowly. Also, the conversion is not complete; there is some detectable amount of **AA-N-Ts** present after 30 seconds which does not diminish after 60 seconds.

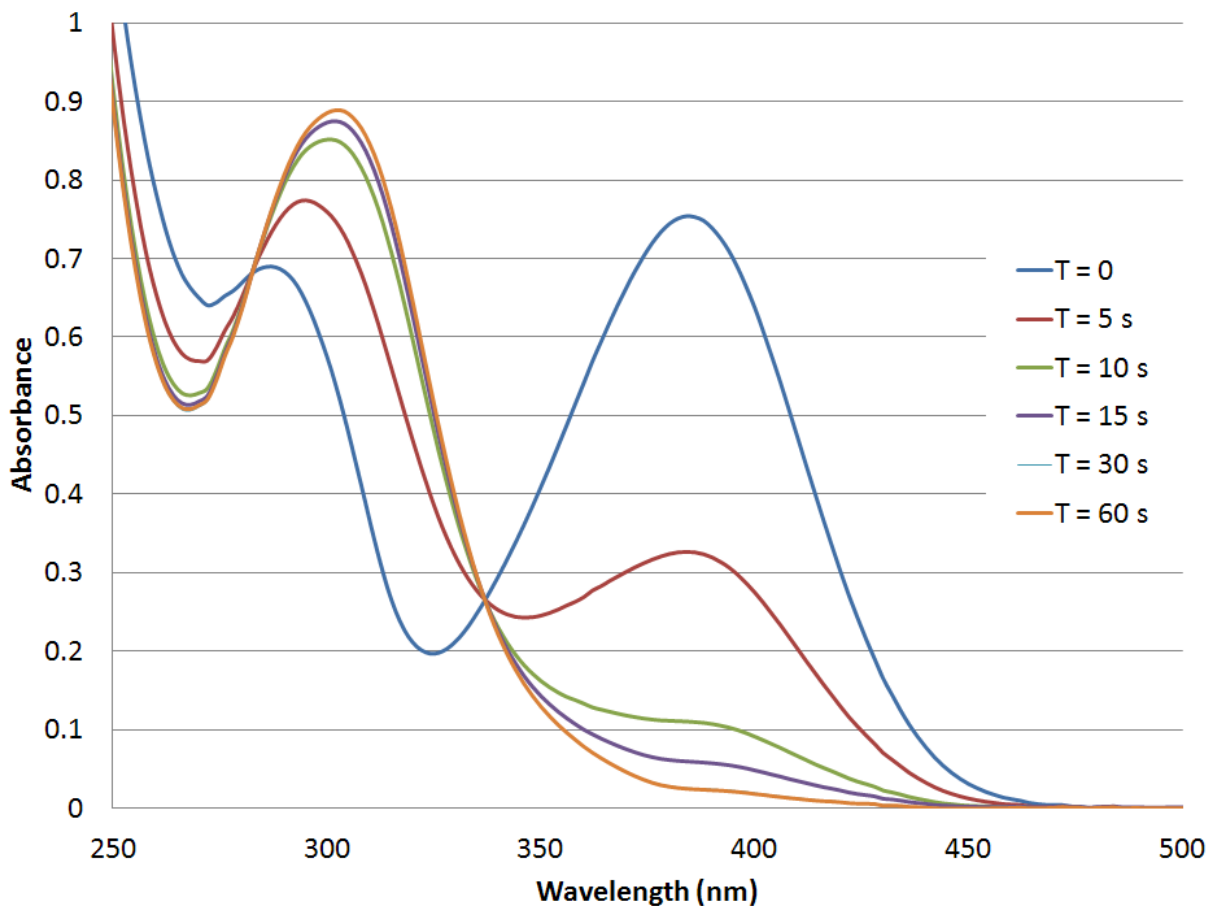
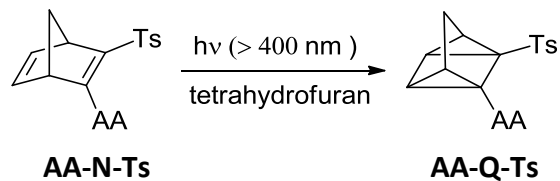


Figure 1.4.8. Arc lamp photoconversion of **AA-N-Ts** to **AA-Q-Ts** with irradiation >400 nm in deaerated tetrahydrofuran at 5.0×10^{-5} M

This effect is more pronounced when using acetone as the solvent (Figure 1.4.9). The timescale necessary for conversion increases, as well as the amount of residual unconverted **AA-N-Ts**.

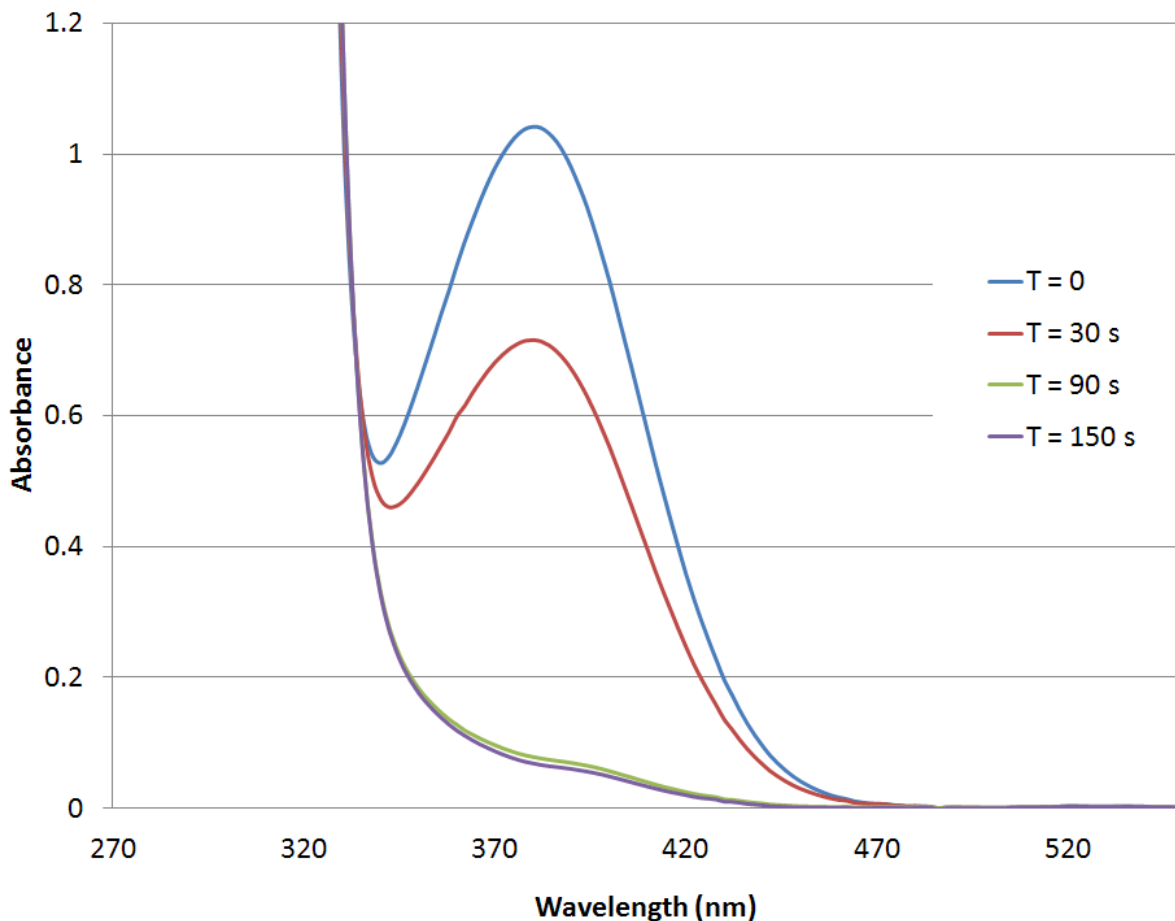
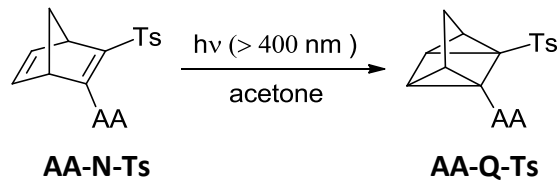


Figure 1.4.9. Arc lamp photoconversion of **AA-N-Ts** to **AA-Q-Ts** with irradiation >400 nm in deaerated acetone at 5.0×10^{-5} M

Acetonitrile was also tested, and an unusual behavior was observed. **AA-N-Ts** was partially converted (~50 %), reaching a photostationary state, then upon further irradiation, began increasing in concentration of **AA-N-Ts** (Figure 1.4.10).

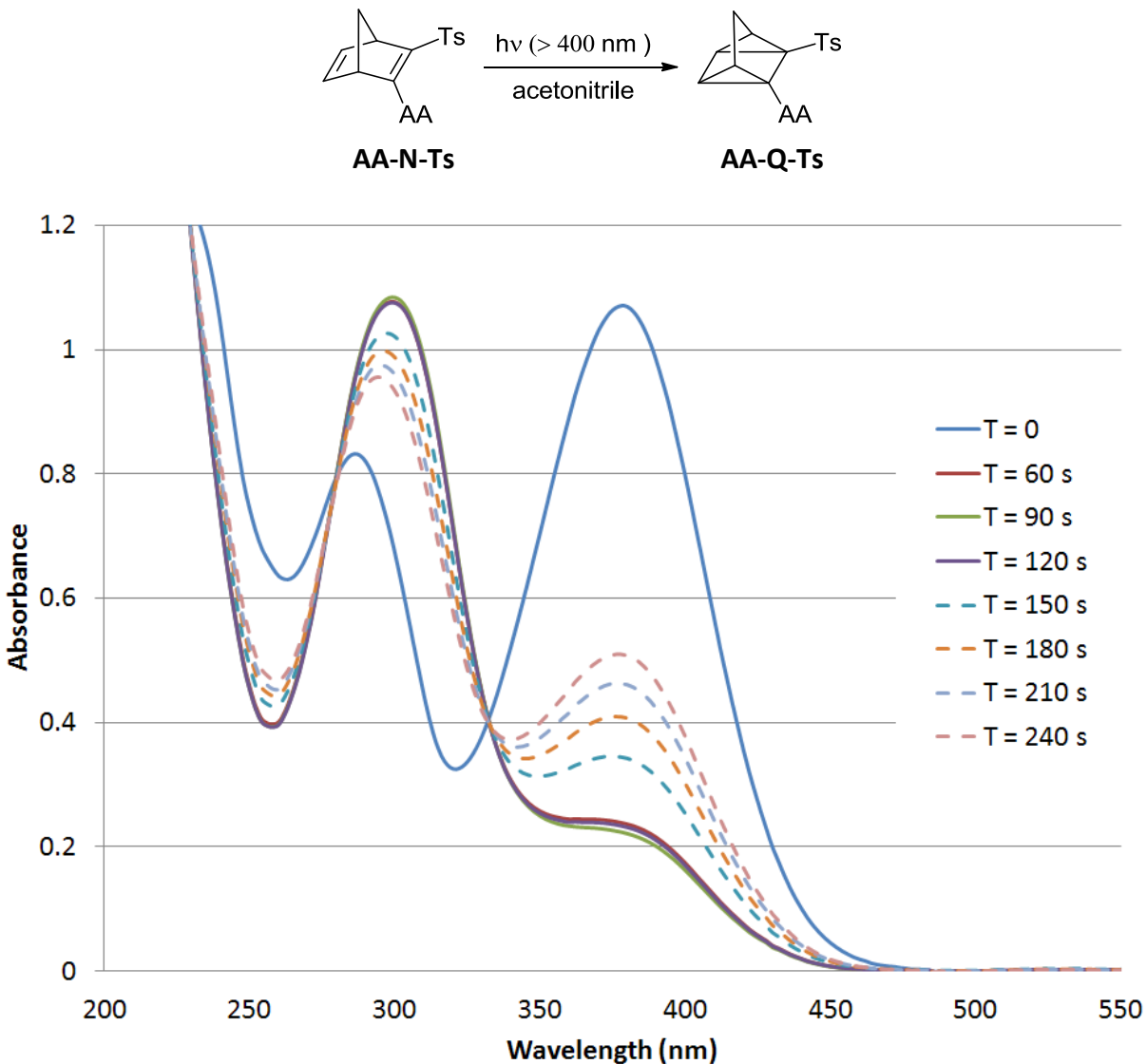
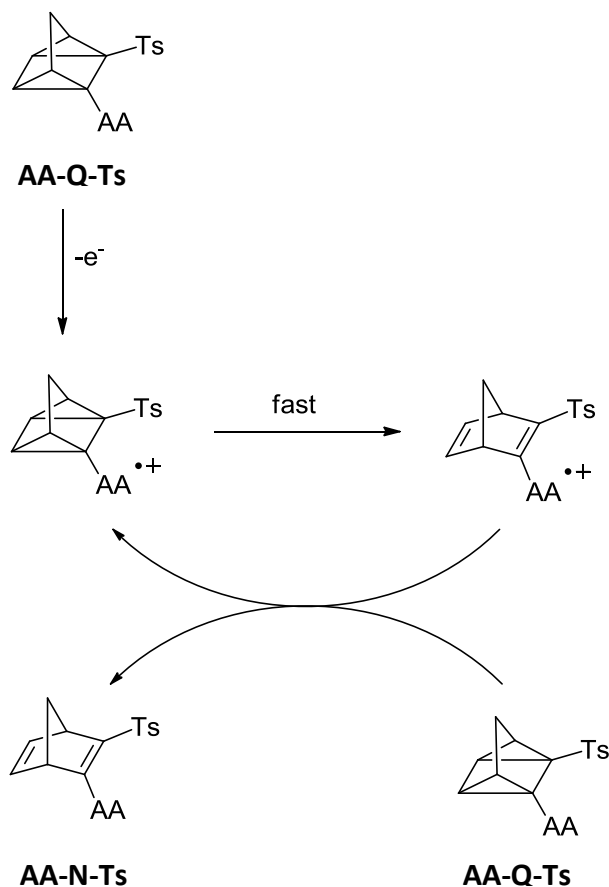


Figure 1.4.10. Arc lamp photoconversion of AA-N-Ts to AA-Q-Ts with irradiation $>400 \text{ nm}$ in deaerated acetonitrile at $5.0 \times 10^{-5} \text{ M}$

There seems to be a clear pattern from the data revealing slower photoconversion reaction times with increasing solvent polarity. This could possibly be due to the solvent's ability to assist in single-electron transfer, affecting the efficacy of the redox catalysis.

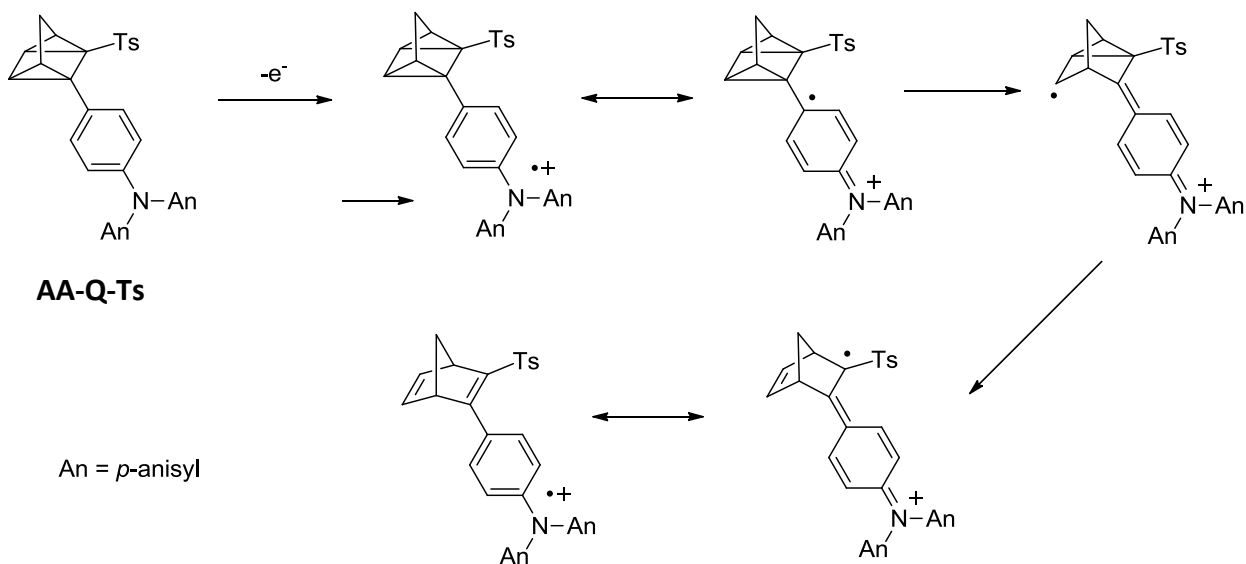
1.5 AA-N-Ts/AA-Q-Ts Redox Chemistry

With **AA-Q-Ts** in hand, we sought to investigate its redox chemistry. It was expected that upon oxidation of **AA-Q-Ts** to its radical cation, a rapid, catalytic isomerization to **AA-N-Ts** would occur. A proposed redox cycle for this conversion is shown in Scheme 1.5.1. When **AA-Q-Ts** is oxidized, it rapidly opens to form **AA-N-Ts**. The **AA-N-Ts** radical cation then becomes the active catalyst, oxidizing **AA-Q-Ts** and leaving the cycle as neutral **AA-N-Ts**.



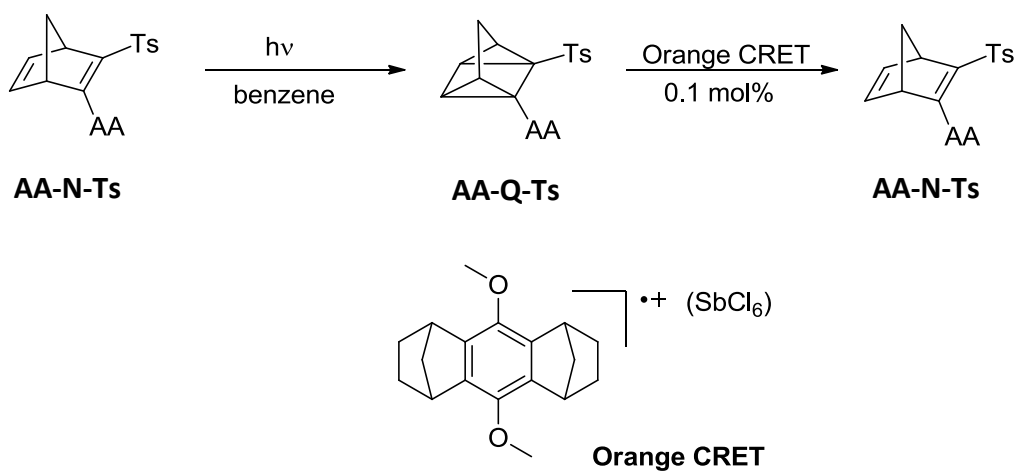
Scheme 1.5.1. A proposed redox cycle for the **AA-Q-Ts** to **AA-N-Ts** conversion

It is important to keep in mind that the reactive function is not directly oxidized. Instead, the RA is oxidized and exerts an electronic perturbation via resonance which effects the transformation to **AA-N-Ts**. This electronic influence is shown in Scheme 1.5.2.



Scheme 1.5.2. The electronic influence of the RA

The redox catalysis of **AA-Q-Ts** to **AA-N-Ts** was initially tested using a substoichiometric chemical oxidant (Scheme 1.5.3). Orange CRET,⁴⁰ a one-electron oxidant was chosen due to its stability and ease of handling. A sample of **AA-N-Ts** in benzene was prepared and photoconverted by arc lamp to **AA-Q-Ts**. A solution of Orange CRET in dichloromethane was added, and an aliquot of the sample was analyzed by UV-Vis (Figure 1.5.1)



Scheme 1.5.3. AA-Q-Ts to AA-N-Ts RA catalysis with Orange RET

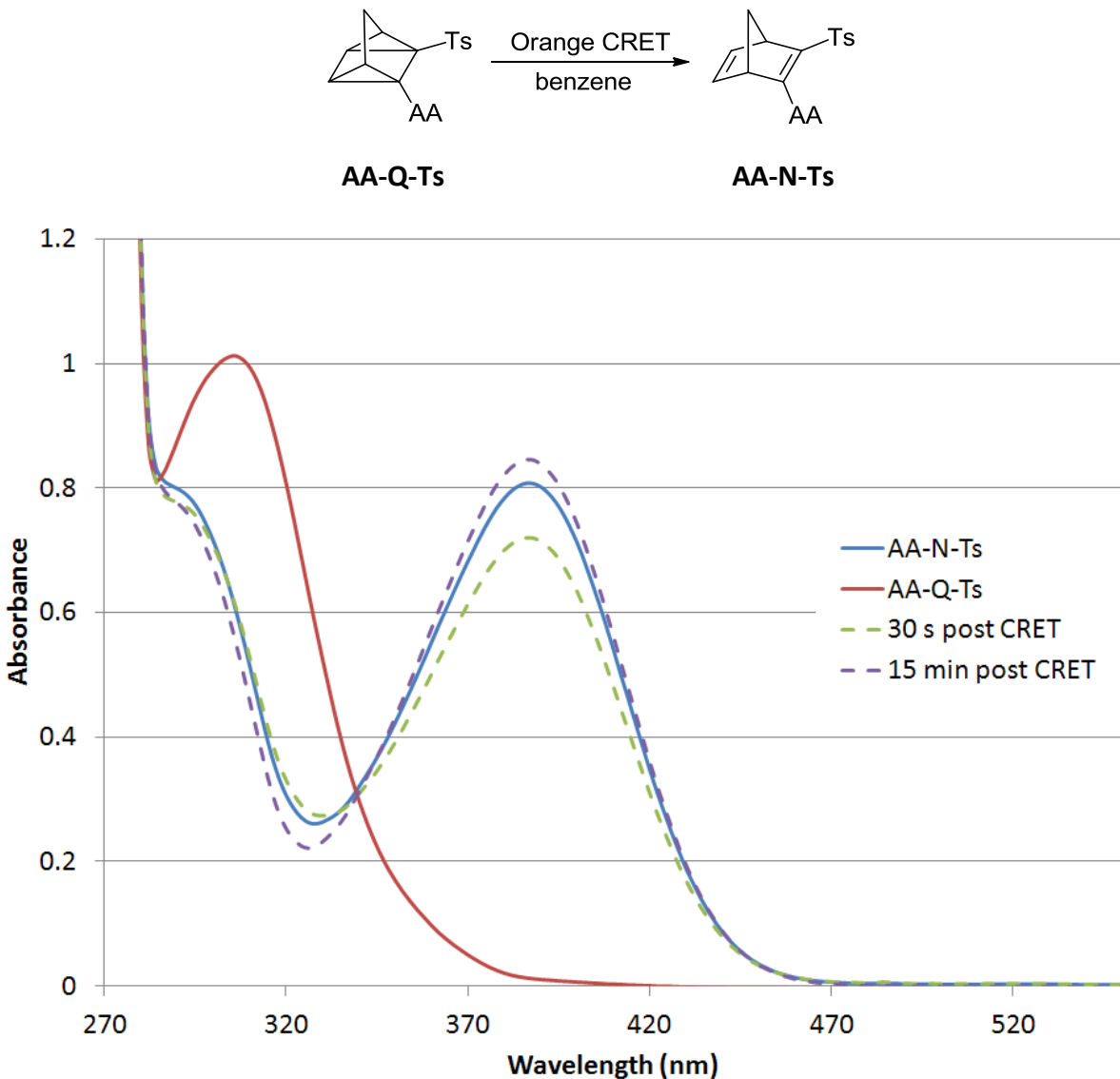


Figure 1.5.1. **AA-Q-Ts** (1.0 mM in benzene) to **AA-N-Ts** by RA catalysis with Orange CRET (0.1 mol%) – Aliquots removed and diluted to 5.0×10^{-5} M for UV-vis

After 30 seconds, the conversion is nearly complete. At 15 minutes, the concentration of **AA-N-Ts** is actually slightly higher than the sample, as prepared, before irradiation. This phenomenon is commonly observed due to **AA-N-Ts** possessing an extremely high sensitivity to light. Even ambient light from fluorescent bulbs in the laboratory is sufficient to cause partial photoconversion to **AA-Q-Ts** within a matter of minutes. To negate this effect, samples are

handled in the dark as much as possible. Optimally, all work should be done in a darkroom with red lighting.

In order to determine the extent of rate acceleration for the conversion of **AA-Q-Ts** to **AA-N-Ts** by RA catalysis, it was necessary to measure the rate of thermal conversion as a basis for comparison. This was performed by dissolving **AA-N-Ts** in C₆D₆ in an NMR tube, degassing by three freeze-pump-thaw (FTP) cycles followed by flame sealing. The sample was photoconverted and an initial ¹H-NMR spectrum was recorded. The sample tube was kept in a dark cabinet at room temperature (20 °C) and further ¹H-NMR measurements were made at various time intervals (Figure 1.5.2)

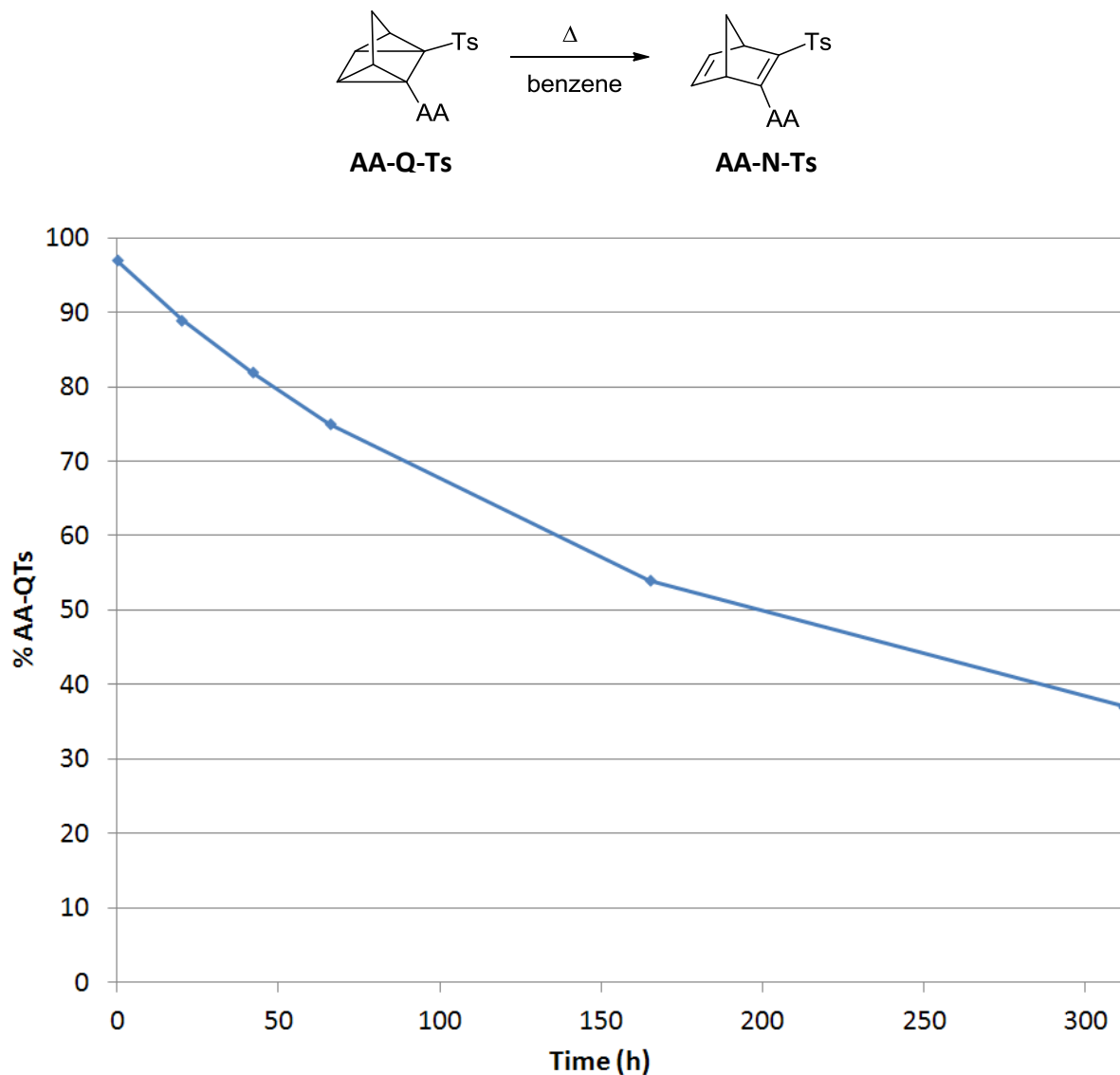


Figure 1.5.2. Thermal conversion of **AA-Q-Ts** to **AA-N-Ts** (13 mM in benzene) at rt monitored by ^1H -NMR

From this data we obtain a half-life ($t_{1/2}$) of 237 hours for **AA-Q-Ts** at 20 °C. Figure 1.5.1 showed that a 0.1 mol% catalyst loading resulted in 11 % of **AA-Q-Ts** remaining after 30 seconds. This gives a $t_{1/2} = 9.4$ seconds. Contrasting this value with the value obtained by the thermal conversion experiment (237 h = 853200 s), we arrive at a rate acceleration equal to 9.1×10^4 .

Higher catalyst loading naturally resulted in greater rate acceleration. An RA-catalysis experiment using 5.0 mol% Orange CRET is shown in Figure 1.5.3. With a 5.0 mol% catalyst load, the reaction is faster than can be observed by UV-Vis. At the first measurement ($T = 10$ s), the reaction has gone to completion, as subsequent measurements show no further progress. Though we were unable to observe an intermediate point which would allow for an accurate half-life calculation, it is possible to assign a *maximum* figure. If we consider that it requires seven half-lives for essentially all (>99 %) of the **AA-Q-Ts** to decay, then it can be calculated that $t_{1/2} \leq 1.4$ s. This gives a minimum rate acceleration of 6.0×10^5 .

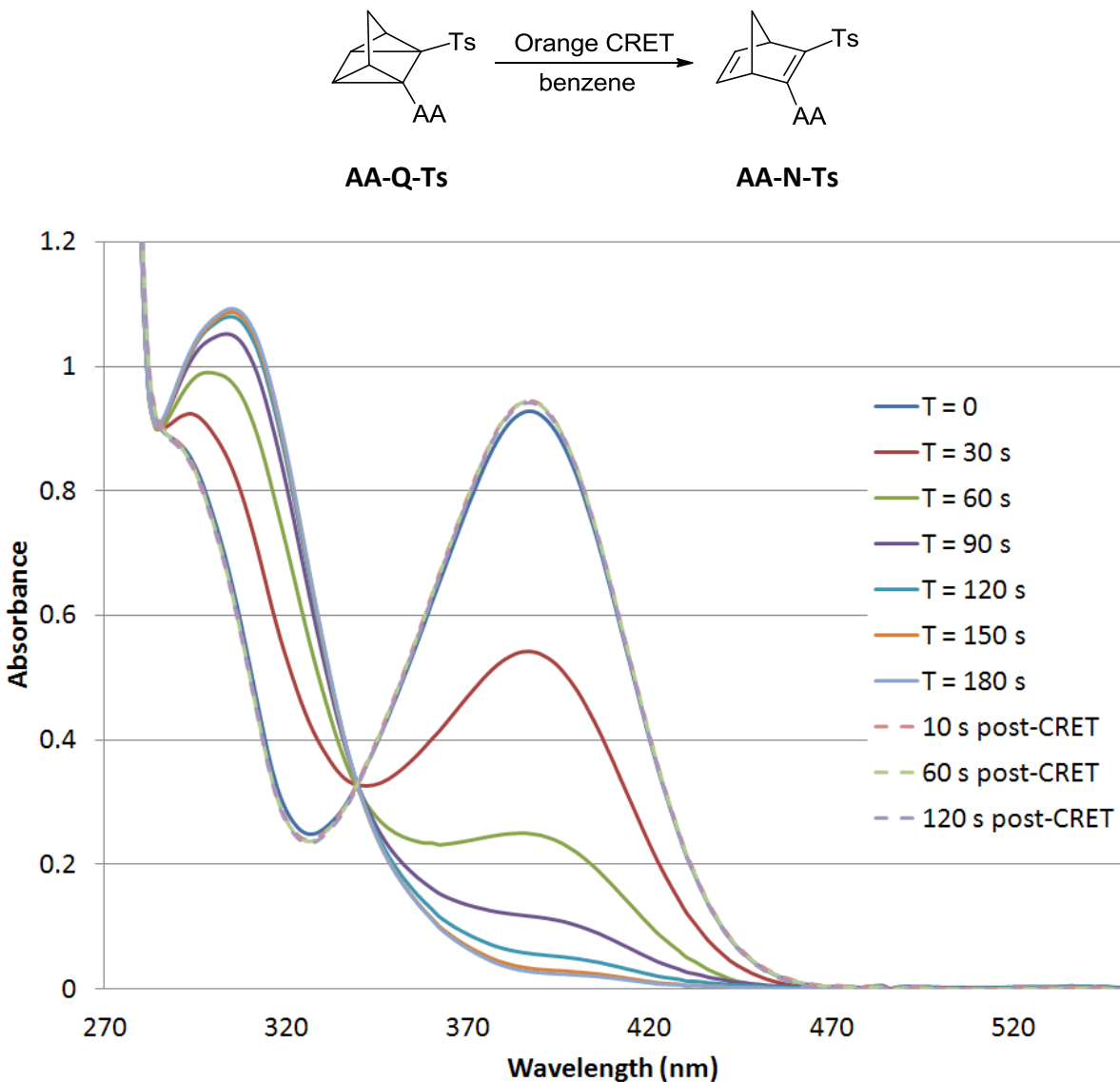


Figure 1.5.3. AA-Q-Ts to AA-N-Ts ($5.0 \times 10^{-5} \text{ M}$ in benzene) RA catalysis with Orange CRET (5.0 mol%)

It was also found that **AA-Q-Ts** could be oxidized to **AA-N-Ts** at a platinum electrode. This was discovered while performing CV experiments on **AA-Q-Ts**. CV measurements had already been made on **AA-N-Ts**, and the CV traces for **AA-Q-Ts** appeared identical. It was not expected that much change in the redox potential would be observed between the two isomers, but it was somewhat surprising to see no change. This led us to the idea that **AA-Q-Ts** was being

oxidized to **AA-N-Ts** at the electrode surface and the latter was the species being observed in the CV trace.

An experiment was setup to test to what extent, if any, **AA-Q-Ts** was being converted to **AA-N-Ts** during the CV experiment. A sample of **AA-Q-Ts** was prepared for CV, and an aliquot was removed and diluted by a factor of 100 and analyzed by UV-Vis (Figure 1.5.4).

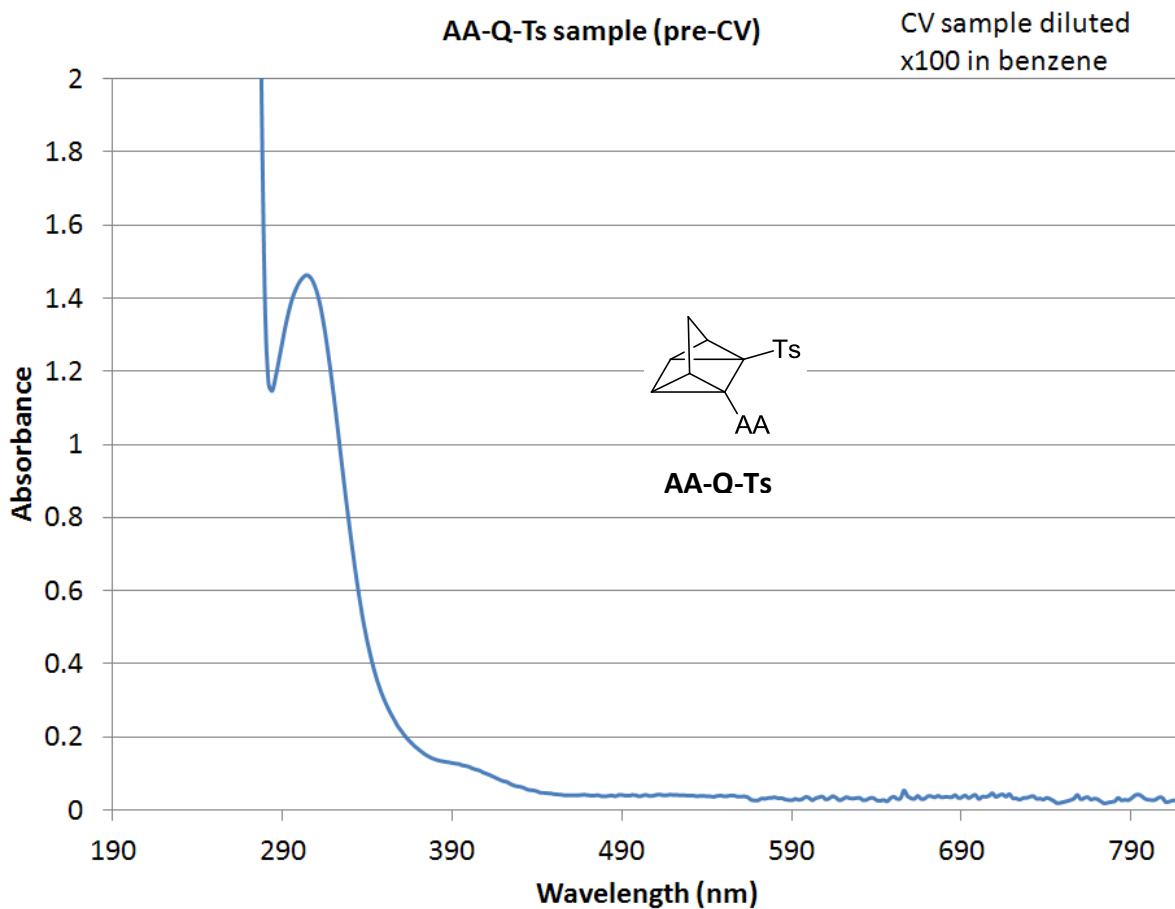


Figure 1.5.4. Optical spectrum of **AA-Q-Ts** prepared for CV (diluted x100 in benzene)

Four CV scans from 0.0 to 1.2 V vs. SCE at various rates were performed, and then another aliquot of the sample was removed and analyzed as before (Figure 1.5.5).

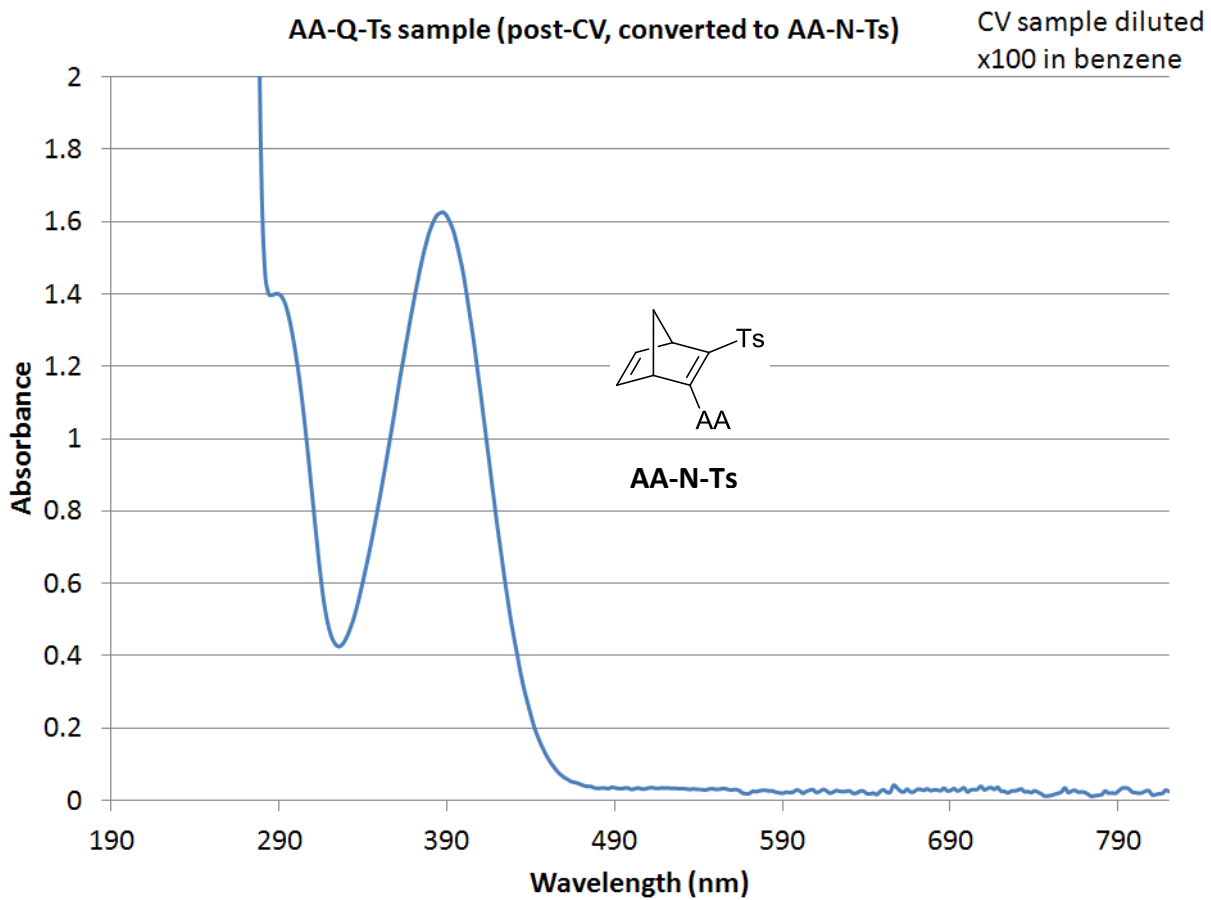


Figure 1.5.5. Optical spectrum of the **AA-Q-Ts** CV sample after four scans (diluted x100 in benzene) demonstrating complete conversion to **AA-N-Ts**

As can be seen from the data in Figure 1.5.5, the **AA-Q-Ts** has undergone complete conversion to **AA-N-Ts** after the CV experiment. Oxidation at a platinum electrode is effective in converting **AA-Q-Ts** to **AA-N-Ts**.

1.6 PD-N-Ts/PD-Q-Ts Photochemistry

Photoconversion of **PD-N-Ts** to **PD-Q-Ts** is effected by visible light, though it was found that solar irradiation was sufficient only to result in partial conversion (Figure 1.6.1). Solar photoconversion was slow, and eventually appeared to reach a photostationary state. At that point, the sample was irradiated with an arc lamp, which effected full conversion to **PD-Q-Ts**. It

was found that a 400 nm cutoff filter was required, as experiments showed that when a 380 nm filter was used as with the irradiation of **AA-N-Ts**, the system established a photostationary state. This phenomenon tends to suggest that excitation of the low-wavelength band activates the back conversion of **PD-Q-Ts** to **PD-N-Ts**.

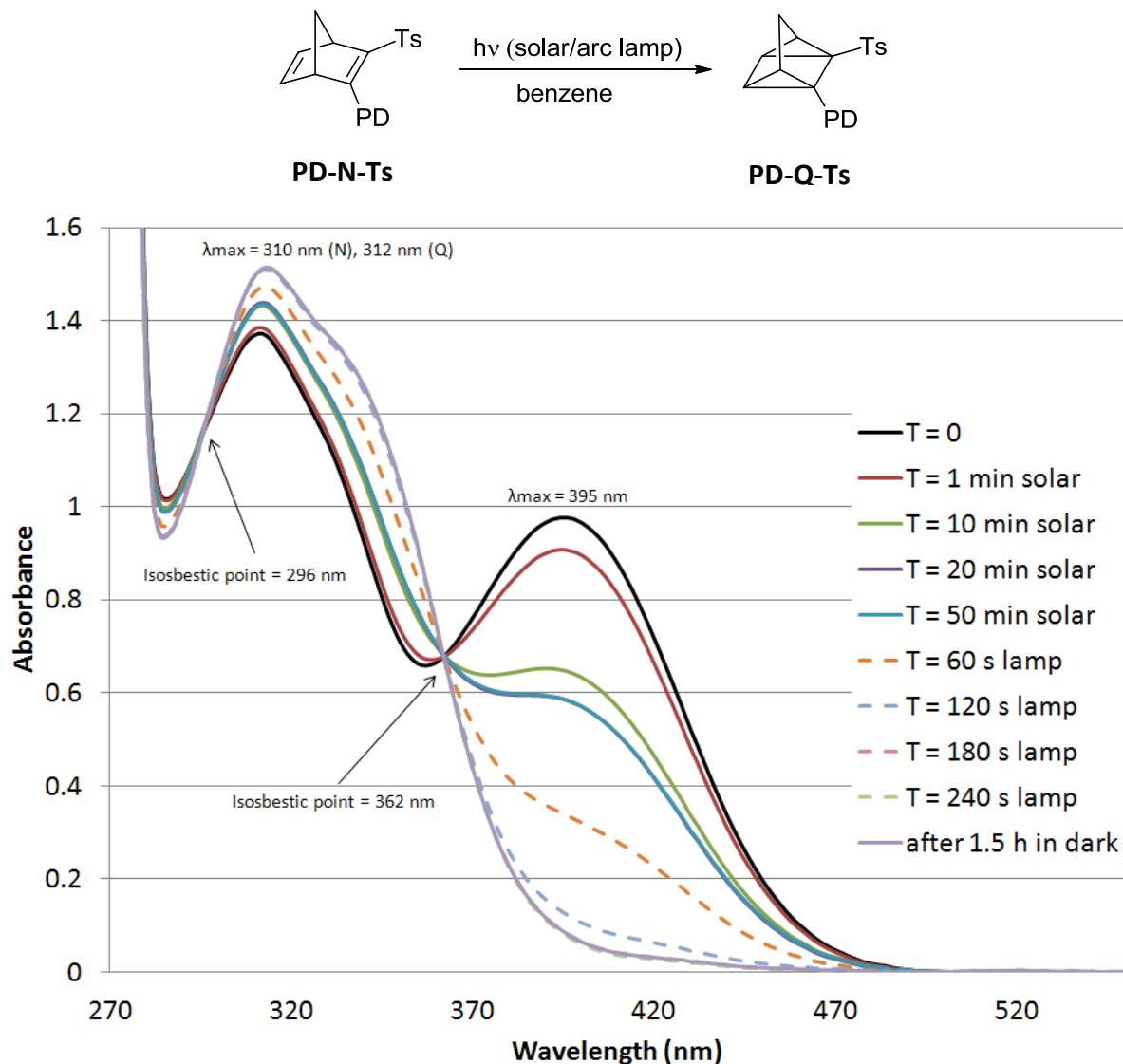


Figure 1.6.1. Solar/arc lamp photoconversion of **PD-N-Ts** to **PD-Q-Ts** ($5.0 \times 10^{-5} \text{ M}$ in benzene)

Qualitatively, it was readily apparent that **PD-N-Ts** was not sensitive towards photoconversion as **AA-N-Ts**. Ferrioxalate actinometry was used to quantify this property. The

procedure was analogous to the one used for the quantum yield determination of **AA-N-Ts**-to-**AA-Q-Ts** photoconversion. An example dataset is depicted in Figure 1.6.2. The experiment was run a total of four times, giving $\Phi = 0.033, 0.032, 0.033$, and 0.033 for a mean of 0.03275 (± 0.00043). This is a dramatic reduction in efficiency of the photoconversion compared with **AA-N-Ts**.

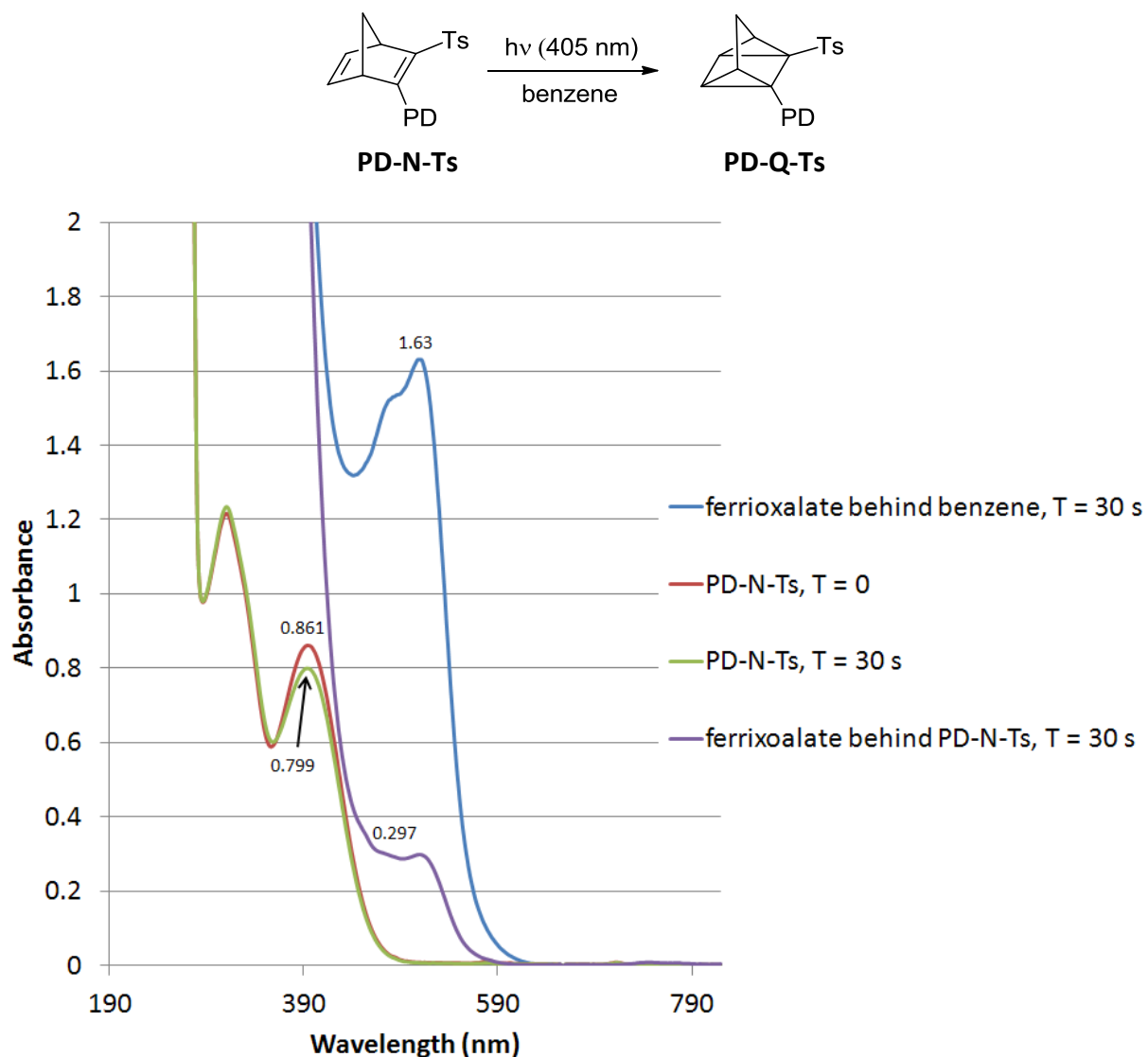


Figure 1.6.2. An example dataset for an **PD-N-Ts** actinometry experiment depicting changes in absorbance of the **PD-N-Ts** solutions and ferrioxalate/phenanthroline complexes

The thermal stability of **PD-Q-Ts** was tested in analogous fashion to **AA-Q-Ts**. A sample of **PD-N-Ts** was dissolved in C₆D₆ in an NMR tube, degassed with three FTP cycles, then flame sealed. The sample was photoconverted to **PD-Q-Ts** and the thermal decay at 20 °C was monitored by ¹H-NMR (Figure 1.6.3). The half-life of **PD-Q-Ts** was found to be significantly greater than that of **AA-Q-Ts** (292 vs. 237 h).

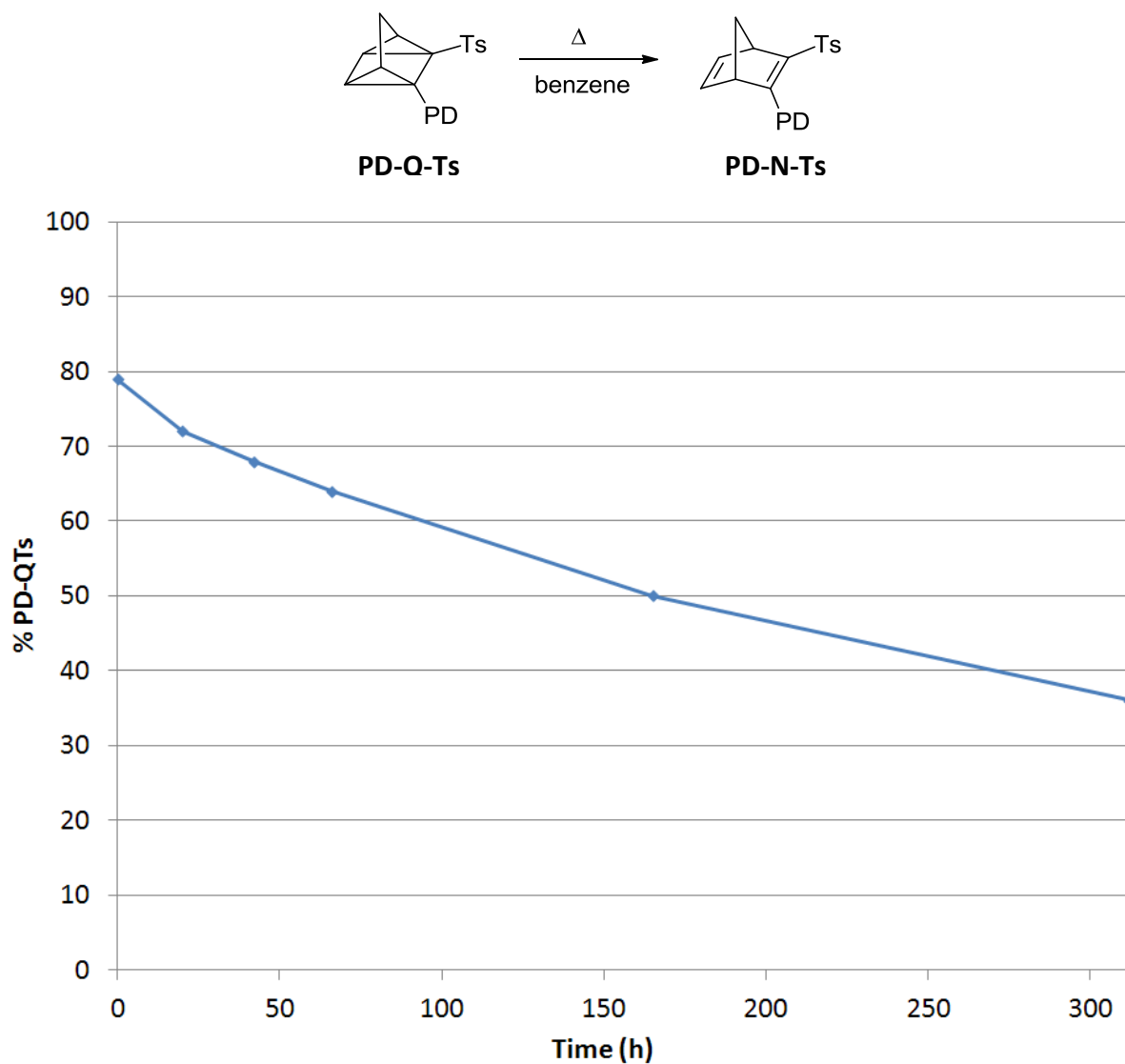


Figure 1.6.3. Thermal conversion of **PD-Q-Ts** to **PD-N-Ts** (13 mM in benzene) at rt monitored by ¹H-NMR

To determine the extent of rate acceleration imparted by RA catalysis, a sample of **PD-N-Ts** was irradiated and then oxidized with Orange CRET (Figure 1.6.4). Notice a distinct advantage the PD system has here over the AA system. At dilute (5.0×10^{-5} M) concentration, the *TON* for **PD-Q-Ts** to **PD-N-Ts** is 50 times greater than that of the AA RA catalysis. This marked improvement may be attributed to the greater stability, and hence lifetime of the PD radical cation. Not only is the oxidation potential lower, but the PD unit is also able to delocalize its radical character across the two nitrogen atoms. Another factor which possibly contributes to PD's greater lifetime is its somewhat higher degree of steric encapsulation, which could act as a barrier to any reductant or passivating agent, such as triplet oxygen.

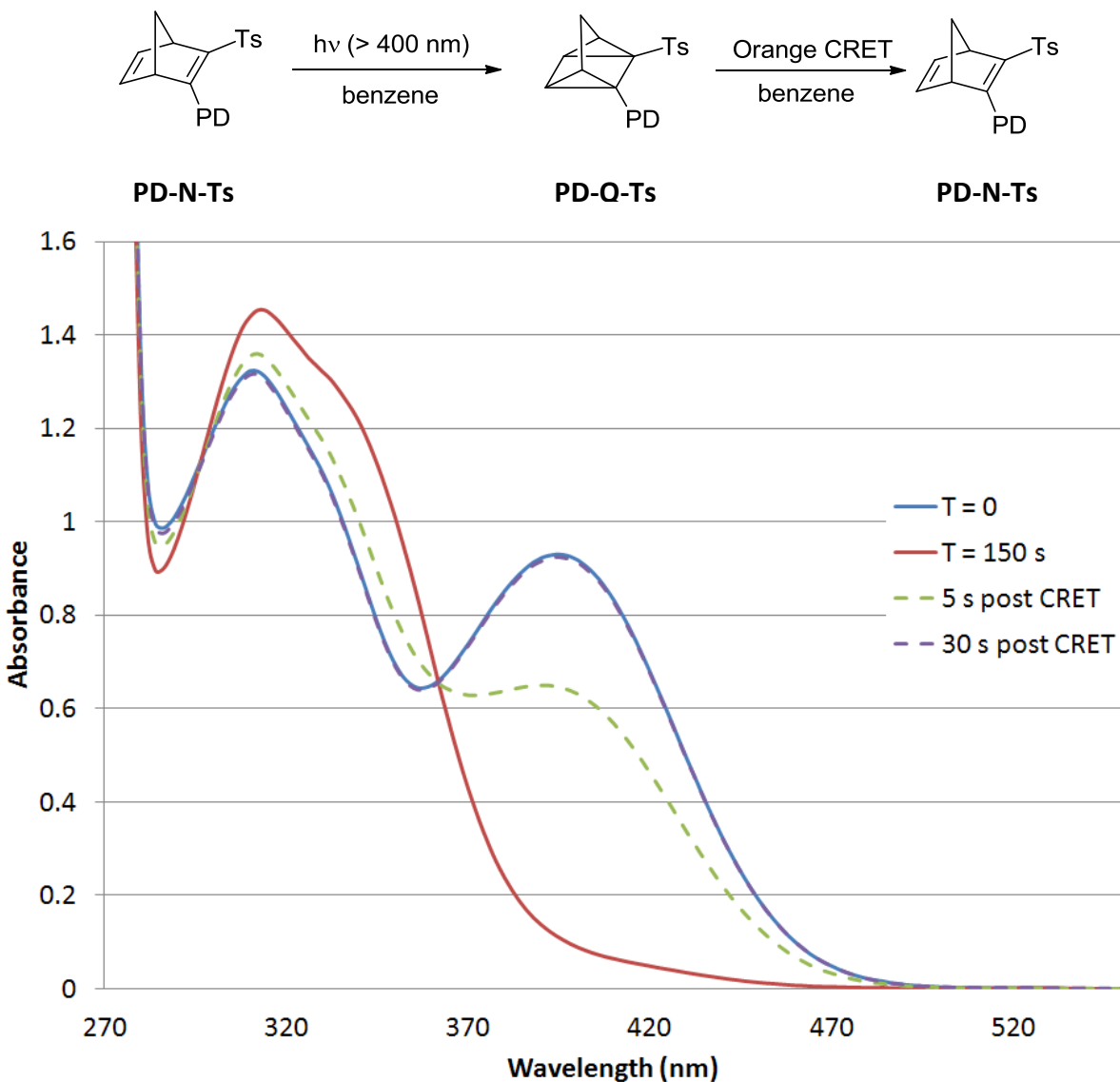


Figure 1.6.4. **PD-Q-Ts** ($5.0 \times 10^{-5} \text{ M}$ in benzene) to **PD-N-Ts** RA catalysis with Orange CRET (0.1 mol%)

A consequence of the **PD** system's reduced photosensitivity can be seen in the above figure. Recall that in the case of the **AA** system, oxidation of **AA-Q-Ts** would result in a higher final concentration of **AA-N-Ts** than was present in the sample as prepared. Here we see that the oxidation product returns to a concentration equal to that of the starting sample and no greater. Therefore, it is not critical to handle samples of **PD-N-Ts** in darkness.

1.7 PD-N-Ts Crystal Structure

An interesting distinguishing factor between the AA and PD systems is that of the propensity for **PD-N-Ts** to crystallize. Though many methods were employed, we were entirely unsuccessful in growing crystals of **AA-N-Ts**. It is an amorphous solid. A possible explanation for this could be that we are dealing with a (presumed) racemic mixture of enantiomers in both **AA-N-Ts** and **PD-N-Ts**, with the chiral centers being the bridgehead carbons of the norbornadiene skeleton. It may well be, and this could be proven if we were able to resolve the enantiomers, that an enantiopure sample will indeed crystallize. I hypothesize that the disorder imposed by racemic mixture of molecules interferes with the crystal packing of **AA-N-Ts** to the extent that no crystal lattice can be established. There is another factor to consider with **PD-N-Ts**, however. The bulky PD unit is the dominant feature of the molecule, as is evident from the molecular conformation taken from the X-ray crystal structure (Figure 1.7.1). The pi stacking and C-H pi interactions affecting the crystal packing of **PD-N-Ts** may be enough so as to overcome the disorder of the norbornadiene unit's racemic character. The crystal system is triclinic and the space group is P-1.

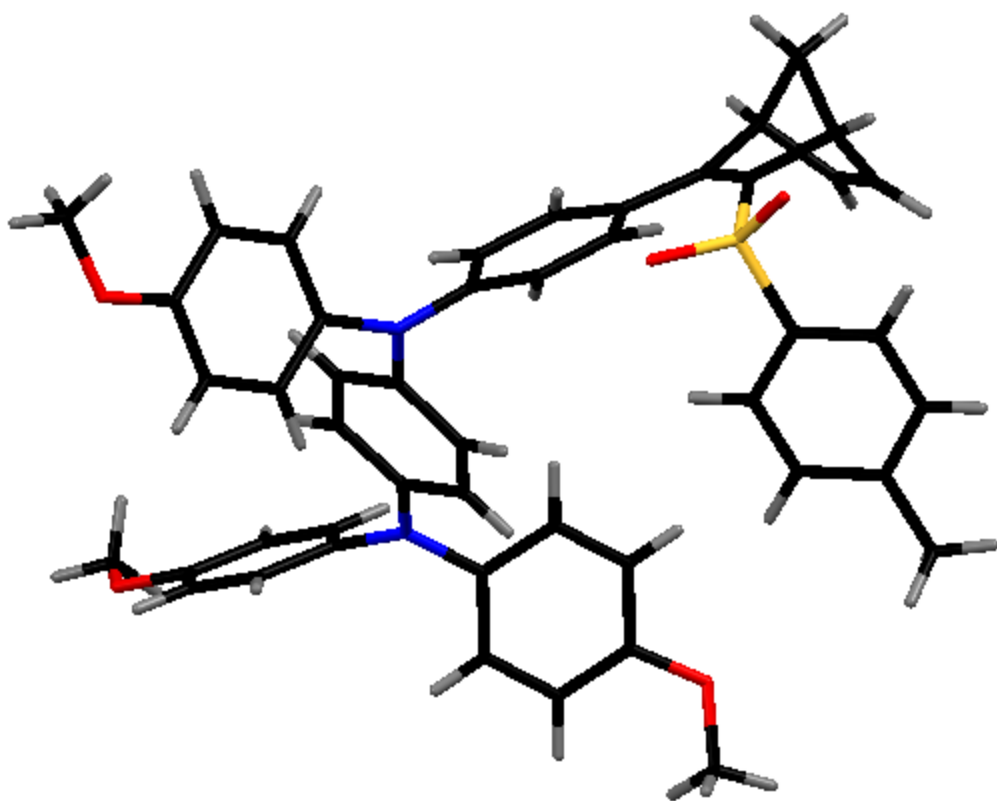


Figure 1.7.1. Molecular conformation of **PD-N-Ts** as derived from the X-ray crystal structure

1.8 The Necessity of the RA Unit: **4-BrPh-N-Ts** and **Ph-N-Ac**

Thus far we have described the optical and redox properties of RA-N-Ts systems in depth, but now the questions arise: What is the RA's contribution to the N-Q system? Is it really a necessary feature for photoelectrochromic switching? We shall address these questions by examining two N-Q systems which lack an RA unit: **4-BrPh-N-Ts** and **Ph-N-Ac**.

Both systems were investigated to determine photochemical and redox properties. Experiments analogous to those performed with the **AA-N-Ts** and **PD-N-Ts** systems show marked differences here with no RA present.

CV was employed to establish oxidation potentials and to determine the presence of redox couples. **4-BrPh-N-Ts** was subjected to applied potential out to 1.8 V vs. SCE which is the maximum voltage in dichloromethane (Figure 1.8.1). It can be seen from the CV trace of **4-BrPh-N-Ts** that the compound shows only the beginning of an irreversible oxidation at about 1.6 V vs. SCE.

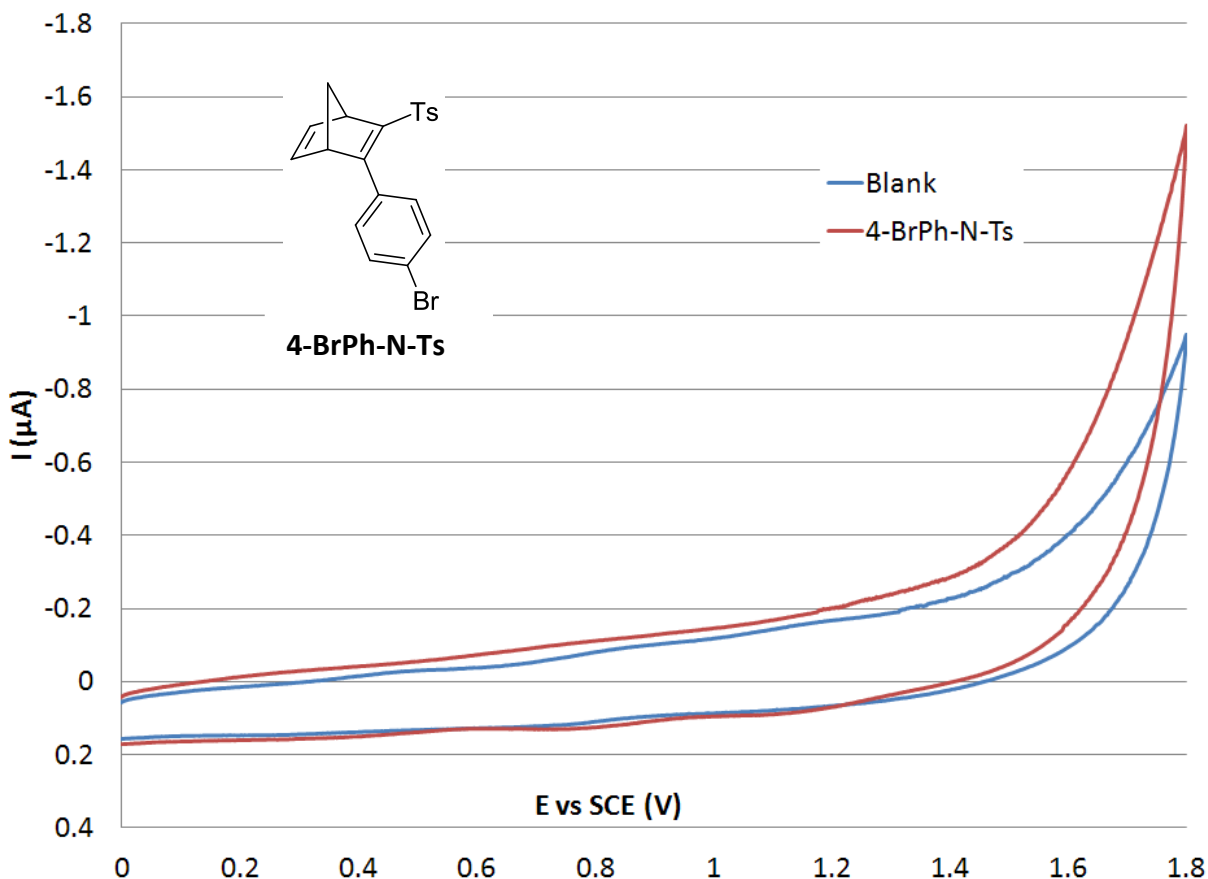


Figure 1.8.1. Cyclic voltammogram of **4-BrPh-N-Ts** - 1.0 mM in dichloromethane (0.1 M TBABF₄) at 20 mV/s scan rate

The **4-BrPh-N-Ts** system was examined to determine the efficacy of redox catalysis in converting **4-BrPh-Q-Ts** to **4-BrPh-N-Ts** (Figure 1.8.2). In contrast to systems bearing RA units, **4-BrPh-Q-Ts** does not show redox catalysis to the N isomer under these conditions. This

is to be expected, as the system's irreversible oxidation should not allow for the propagation of a catalytic cycle by the proposed mechanism.

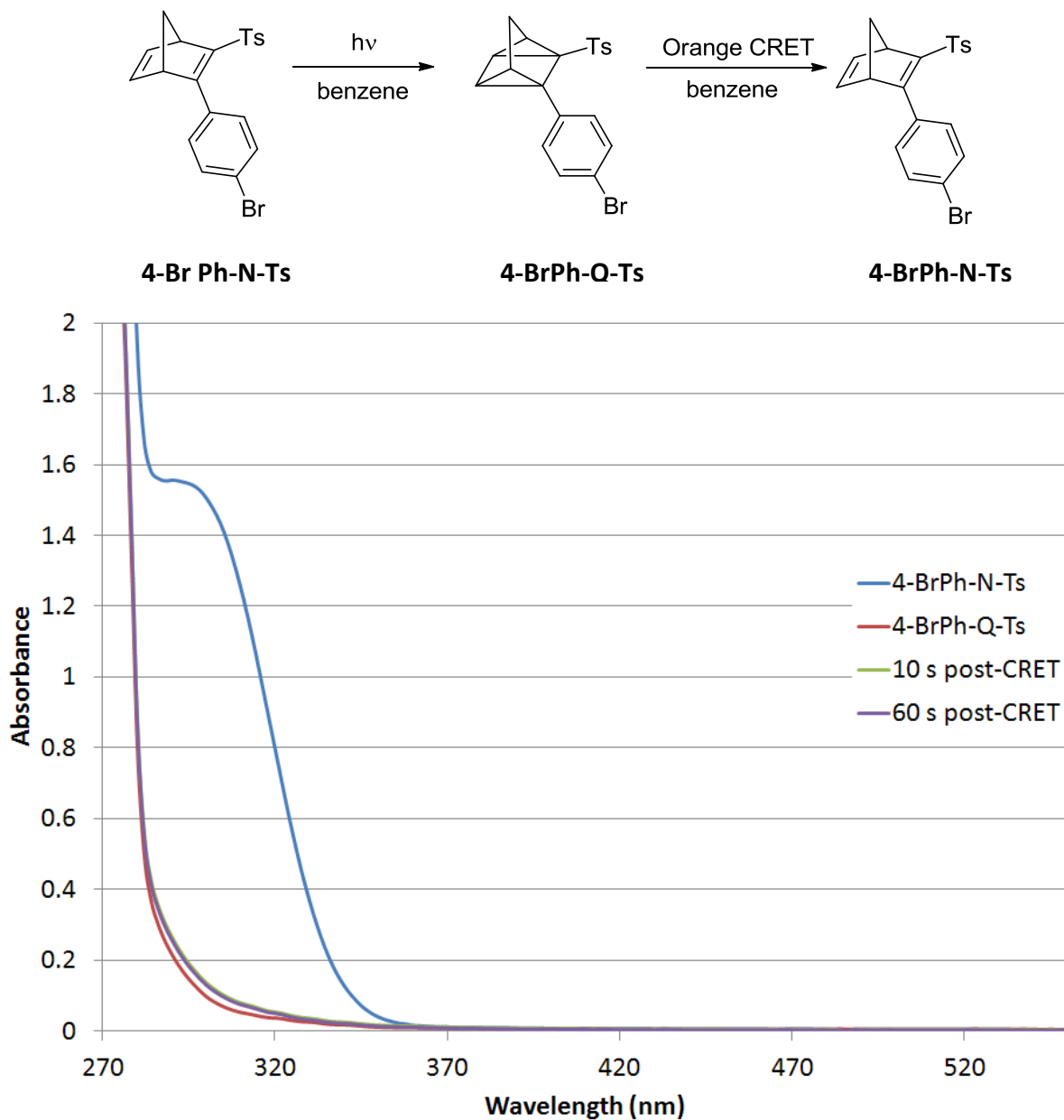
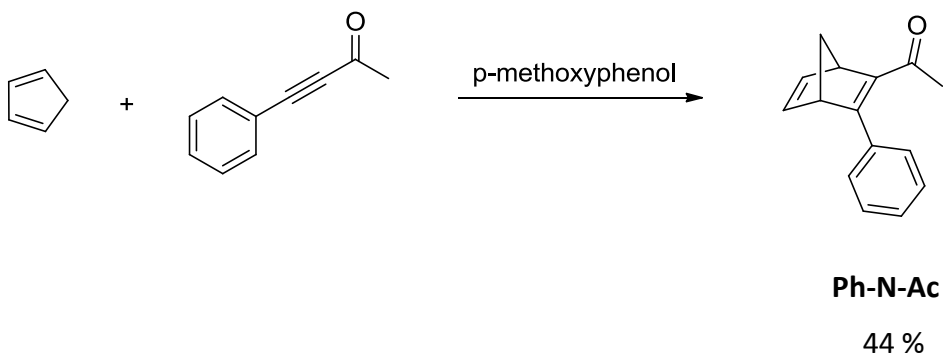


Figure 1.8.2. 4-BrPh-Q-Ts (1.2×10^{-4} M in benzene) oxidation with Orange CRET (5.0 mol%)

We prepared **Ph-N-Ac** (Scheme 1.8.1), which was described in the aforementioned report by Gassman and Hershberger. Freshly-distilled cyclopentadiene was reacted with 4-phenyl-3-

butyn-2-one (neat) in the presence of a small amount of *p*-methoxyphenol to inhibit polymer formation.



Scheme 1.8.1 Synthesis of **Ph-N-Ac**

The product was analyzed by CV (Figure 1.8.3). As was the case with **4-BrPh-N-Ts**, **Ph-N-Ac** shows an irreversible oxidation, though with a slightly lower onset (about 1.5 V vs. SCE).

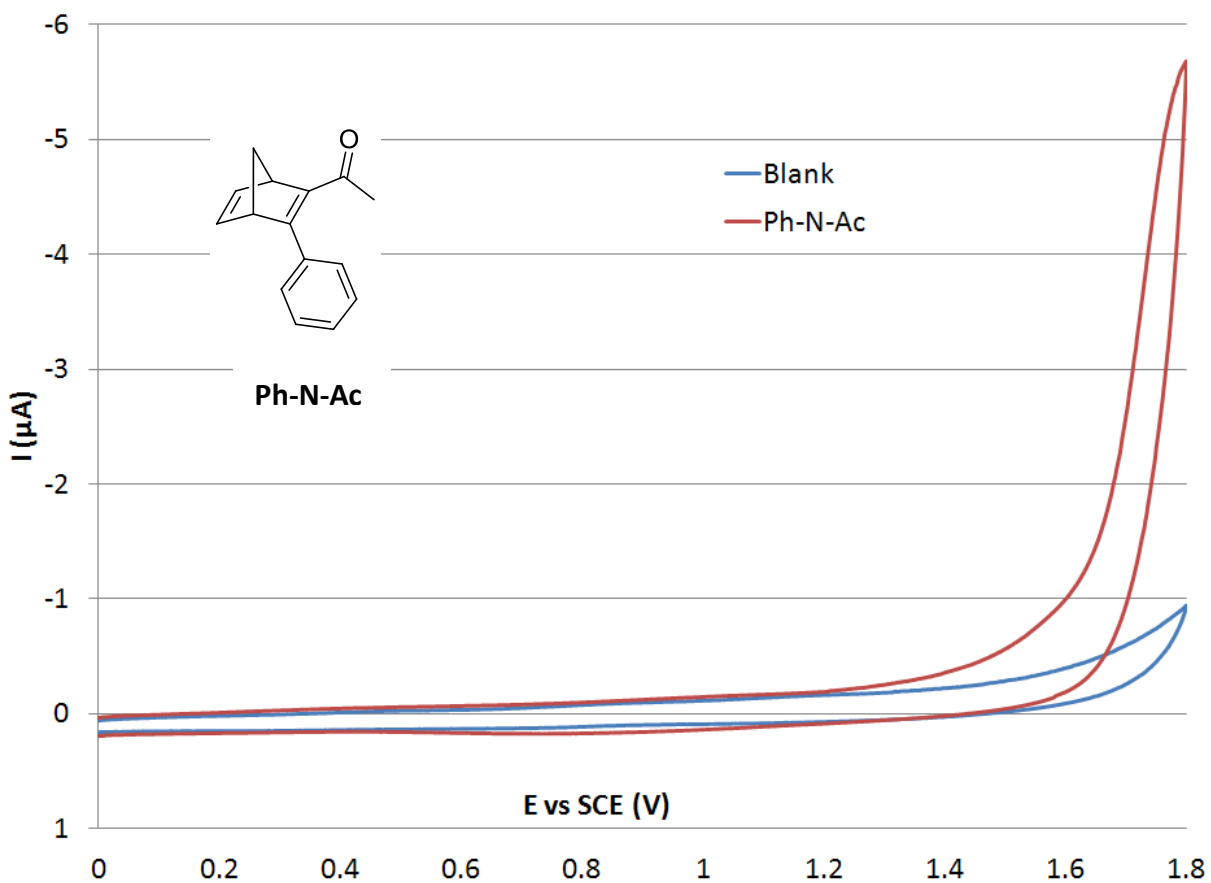


Figure 1.8.3. Cyclic voltammogram of **Ph-N-Ac** - 1.0 mM in dichloromethane (0.1 M TBABF₄) at 20 mV/s scan rate

The **Ph-N-Ac** system was examined to determine the efficacy of redox catalysis in converting **Ph-Q-Ac** to **Ph-N-Ac** (Figure 1.8.4). The result was quite interesting, as there is some degree of redox catalysis occurring. Though full conversion from **Ph-Q-Ac** to **Ph-N-Ac** was not attained, the amount converted was significantly greater than stoichiometric to Orange CRET (as was observed in the case of **4-BrPh-Q-Ts**).

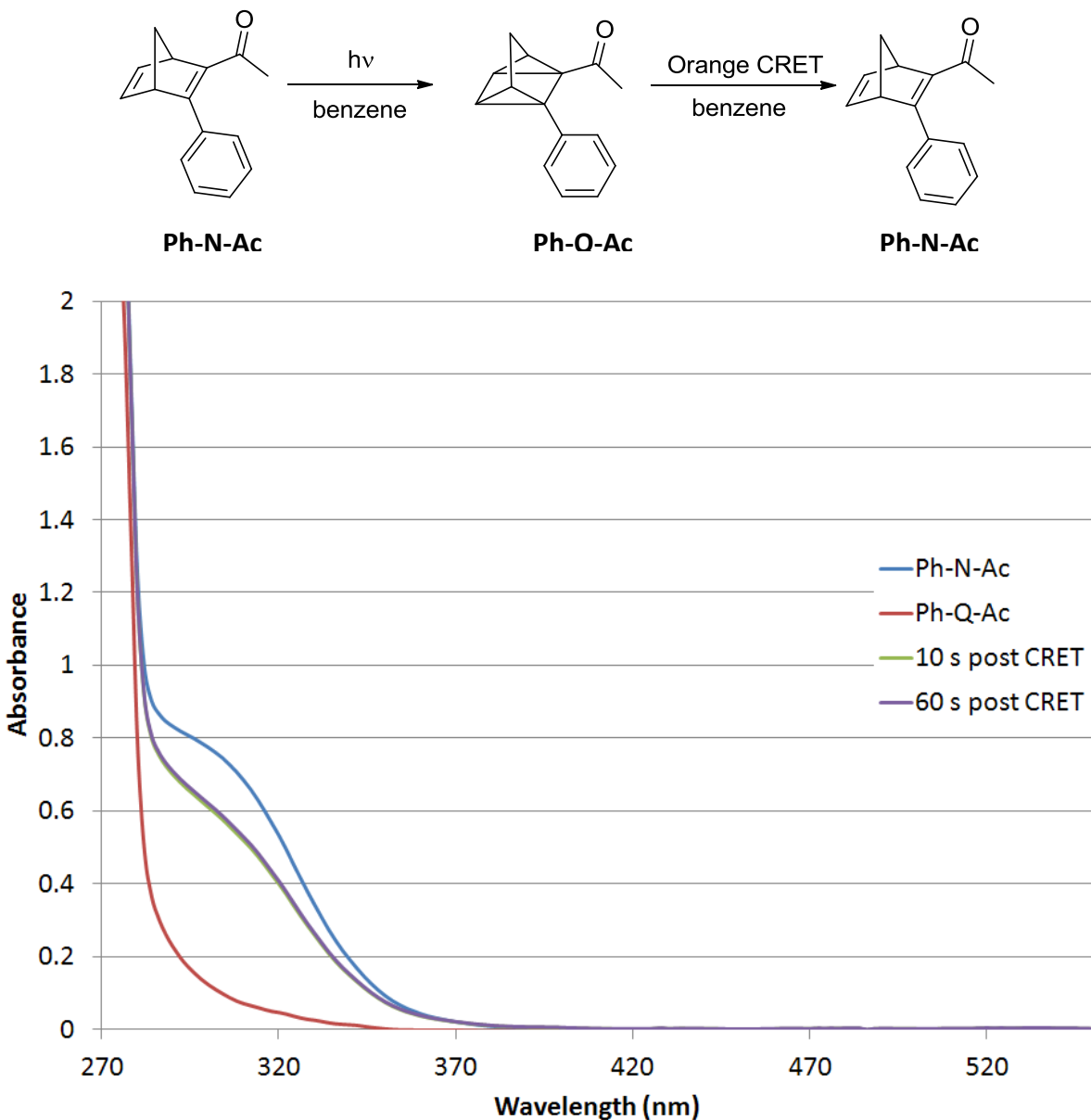
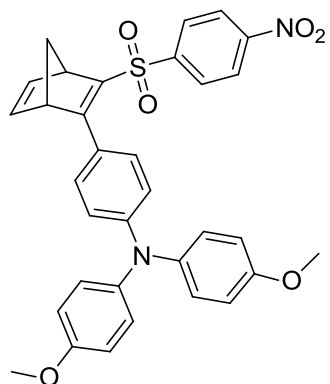


Figure 1.8.4 **Ph-Q-Ac** (1.3×10^{-4} M in benzene) oxidation with Orange CRET (5.0 mol%)

1.9 Other RA-N systems: Preliminary Studies of AA-N-Ns and AA-bis(N-Ts)

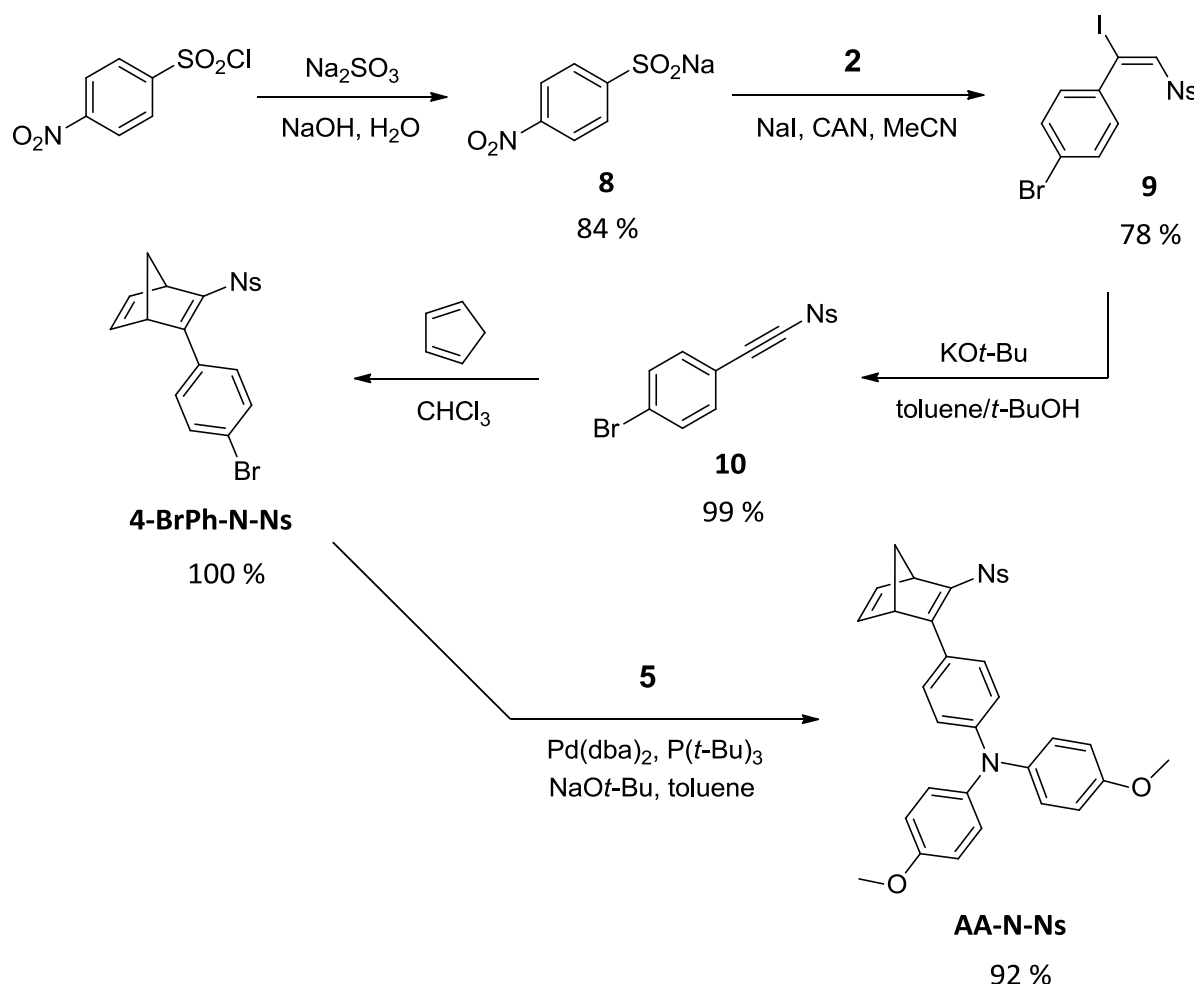
During the course of our investigation into RA-N systems, two were synthesized which have not been adequately explored. The synthesis of **AA-N-Ns** and **AA-bis(N-Ts)**, as well as what limited data on hand pertaining to these compounds is described herein.

AA-N-Ns was synthesized with the rationale that the substitution of a nosyl moiety in place of the tosyl moiety of **AA-N-Ts** would lead to a more pronounced bathochromic shift, placing a greater portion of the compound's optical absorbance band into the visible portion of the electromagnetic spectrum. It was hypothesized that stronger electron-withdrawing effect of the nosyl moiety would lead to a greater push-pull effect across the alkene of the N skeleton.



AA-N-Ns

The synthetic route to **AA-N-Ns** (Scheme 1.9.1) was analogous to that of **AA-N-Ts**, the only exception being the requirement to synthesize the sulfinate salt. This reaction was not a trivial one, however. In the aqueous media required to dissolve the sulfite reagent, a competition between the desired reaction and hydrolysis of the sulfonyl chloride took place. This initially led to the formation of large amounts of the hydrolysis product. Reaction optimization revealed that conditions favoring the sulfinate product require a large excess of sodium sulfite, as well as cooling to ice-bath temperature.



Scheme 1.9.1 Synthesis of **AA-N-Ns**

The UV-vis spectrum of **AA-N-Ns** is shown overlaid with that of **AA-N-Ts** (Figure 1.9.1). The expected bathochromic shift did occur upon installation of the nosyl moiety. However, the high-wavelength absorbance exists as a shoulder on a more intense absorbance band demonstrating a λ_{max} of 366 nm in benzene. Note also that the peak absorbance of **AA-N-Ns** is only around half that of **AA-N-Ts**. The absorption edge of **AA-N-Ns** is greatly shifted to higher wavelength, trailing off past 540 nm.

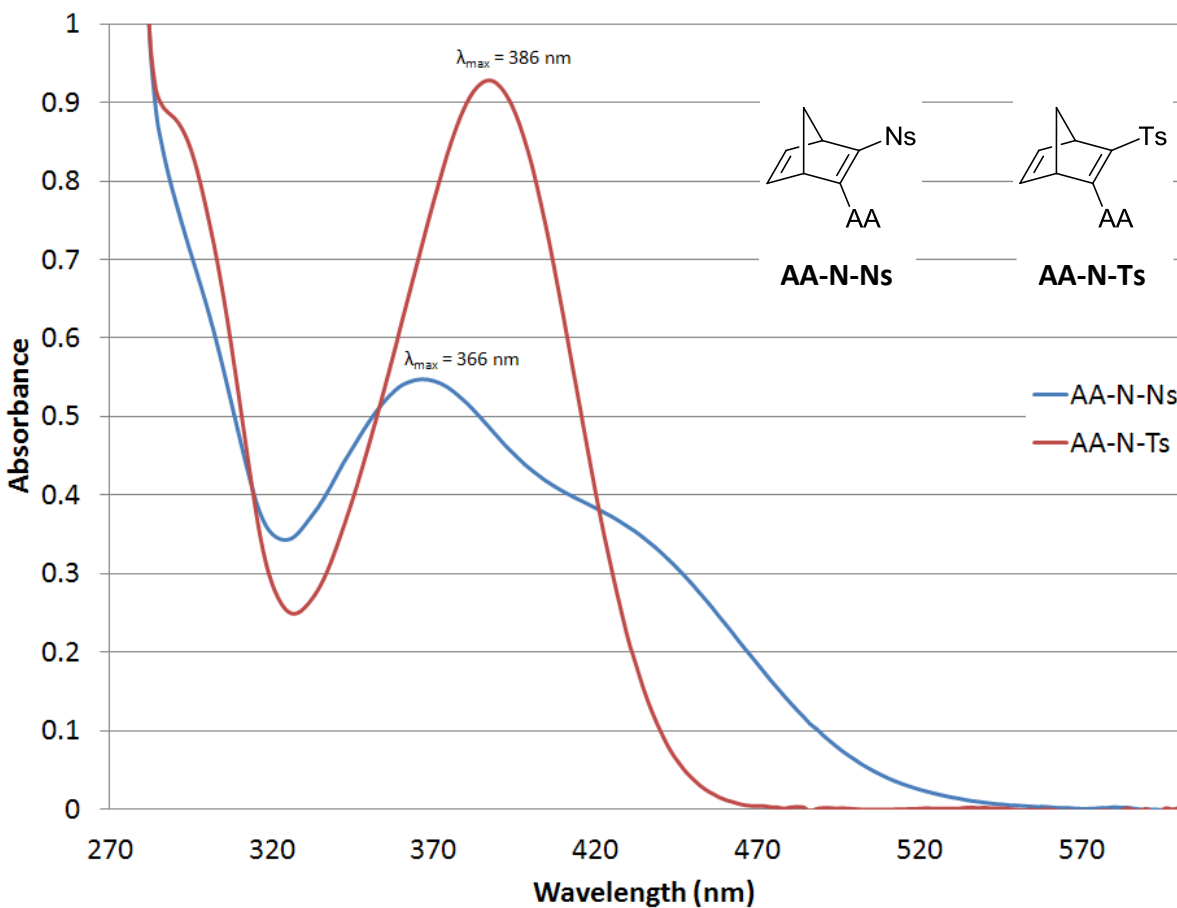


Figure 1.9.1 Optical spectra of **AA-N-Ns** and **AA-N-Ts** ($5.0 \times 10^{-5} \text{ M}$ in benzene)

The photochemical behavior of **AA-N-Ns** was investigated, at least in a preliminary manner. A sample of $5.0 \times 10^{-5} \text{ M}$ sample of **AA-N-Ns** in benzene was irradiated with an arc lamp behind an IR filter and a 455 nm cutoff filter (Figure 1.9.2). After 5 min irradiation, no detectable change was observed. It may be the case that the long-wavelength absorbance band is not the active band in this compound. Further investigation of the photochemical behavior of **AA-N-Ns** is warranted.

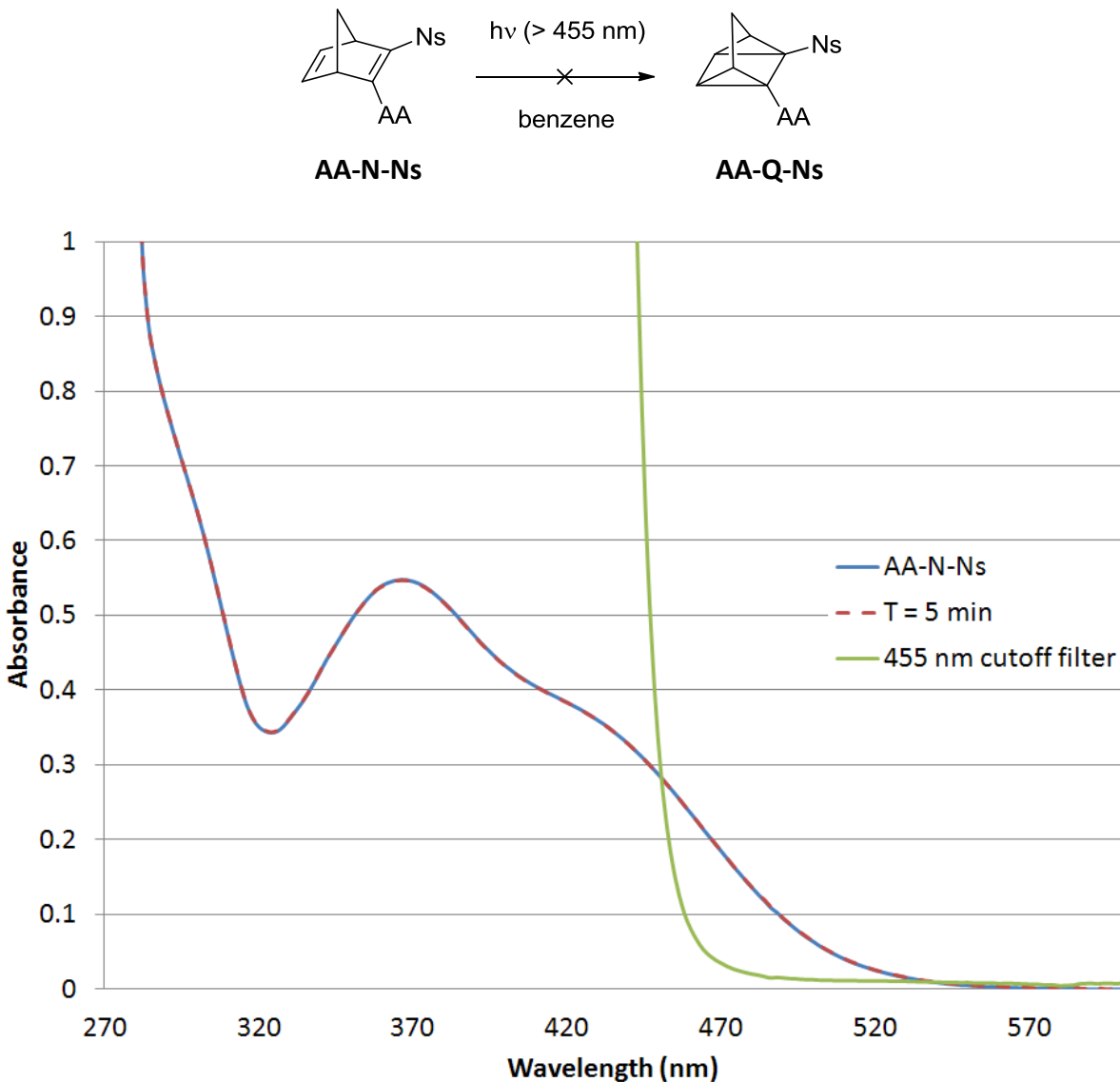
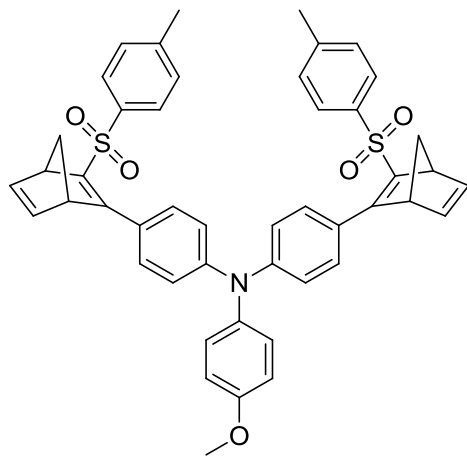


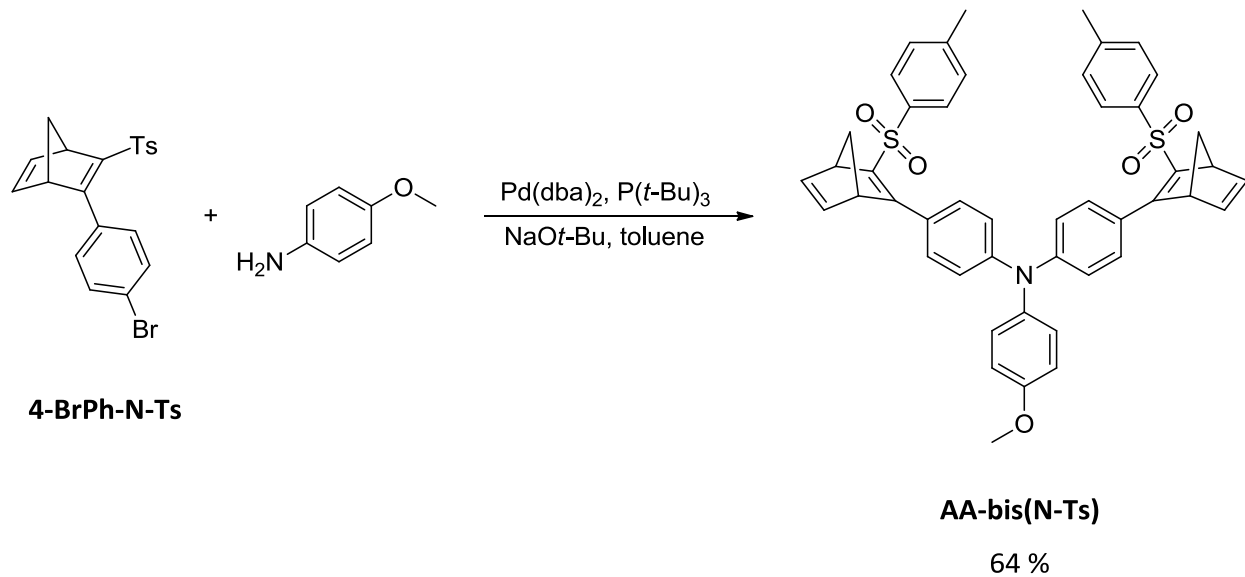
Figure 1.9.2 Arc lamp photoconversion of AA-N-Ns with irradiation >455 nm in deaerated benzene at 5.0×10^{-5} M

Another RA-N derivative, **AA-bis(N-Ts)** was synthesized with the rationale that more energy could be derived per AMU by substituting two N reactive functions on a single AA unit.



AA-bis(N-Ts)

The preparation of **AA-bis(N-Ts)** is accomplished by reacting two equivalents **4-BrPh-N-Ts** with one equivalent *p*-anisidine under the N-arylation conditions of Hartwig et al.



Scheme 1.9.2. Synthesis of **AA-bis(N-Ts)**

1.10 Conclusions

We have synthesized two novel photoelectrochromic N derivatives, **AA-N-Ts** and **PD-N-Ts**, which support our hypothesis for RA catalysis. Both derivatives are converted from their N to Q forms by visible light, with **AA-N-Ts** exhibiting conversion upon exposure to indirect solar irradiation. The quantum yield at 405 nm for the **AA-N-Ts** system is high ($\Phi = 60\%$), while the **PD-N-Ts** sensitivity is much lower ($\Phi = 3.3\%$). The reason for this discrepancy remains unclear. The presence of the RA unit creates an N-based system exhibiting a redox couple with sufficient lifetime to propagate a redox-catalysis chain with high turnover. The strained Q isomers of these derivatives possess half-lives in solution on the order of days. Upon oxidation, electronic perturbation imparted by the RA unit effect the Q-to-N conversion with a rate enhancement greater than five orders of magnitude. Preliminary studies of two other RA-N derivatives, **AA-N-Ns** and **AA-bis(N-Ts)** have been conducted.

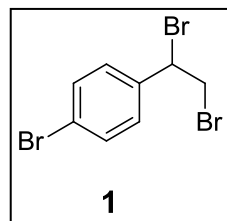
1.11 Experimental

General Methods and Materials

Norbornadiene was purchased from *Alfa Aesar* and distilled immediately prior to use to remove BHT. Sodium p-toluenesulfinate and 4-phenyl-3-butyn-2-one were purchased from *TCI America*. 4-bromostyrene was purchased from *Amfinecom Inc.* Copper iodide was purchased from *Lancaster Chemical Co.* All other reagents were purchased from *Aldrich Chemical Co.* and were used without further purification unless otherwise noted. Column chromatography was performed on silica gel (Silicycle, 40-63 μm). Melting points were recorded on a *Mel Temp* apparatus by Laboratory Devices and are uncorrected. Nuclear magnetic resonance spectra were recorded on Bruker AM360 and AM500 spectrometers. Chemical shifts (δ) are reported relative

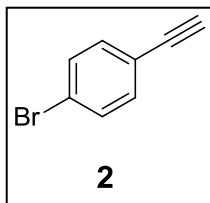
to positions of the residual hydrogen signals of the deuterated solvent. UV-visible spectra were collected on a Hewlett Packard 8452A diode array spectrophotometer. CV was performed on a PAR 273 electrochemical potentiostat (EG&G Instruments). *n*-Tetrabutylammonium tetrafluoroborate (TBABF₄), a supporting electrolyte, was purchased from *TCI America* and was purified according to standard literature procedures,⁴¹ or recrystallized from 30 % ethanol three times, then dried in a vacuum oven (100 °C, 0.1 Torr) for 30 h. Methylene chloride, a CV solvent (Fisher) was pre-dried by stirring over conc sulfuric acid, washed with H₂O, neutralized with 5 % aqueous potassium hydroxide, and finally distilled from calcium hydride under nitrogen atmosphere according to standard literature procedures.⁴¹

Synthesis

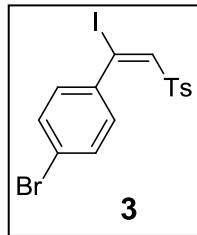


Commercially available 4-bromostyrene (40.00 g, 218.5 mmol) was dissolved in chloroform (350 mL) in a 1 L round-bottom flask. The solution was magnetically stirred, and bromine (36.67 g, 229.4 mmol) in chloroform (50 mL) was added dropwise over a 10 minute period. The reaction mixture was stirred for a further 10 minutes to give a reddish solution. A 5 % aqueous sodium bisulfite solution (400 mL) was added and stirred vigorously for 15 minutes (until the organic phase decolorized). The organic phase was separated, dried over anhyd magnesium sulfate, and evaporated *in vacuo*. The resultant clear, colorless oil was subjected to high vacuum, at which point **1** rapidly solidified to a crystalline mass (73.07 g, 98 %): mp = 58-59 °C, lit⁴² = 56-58 °C.

¹H-NMR (360 MHz, CDCl₃) δ 7.52 (d, *J* = 8.5 Hz, 2H), 7.28 (d, *J* = 8.5 Hz, 2H), 5.09 (dd, *J*₁ = 5.1 Hz, *J*₂ = 11.0 Hz, 1H), 4.07 (dd, *J*₁ = 5.1 Hz, *J*₂ = 10.3 Hz, 1H), 3.97 (m, 1H).

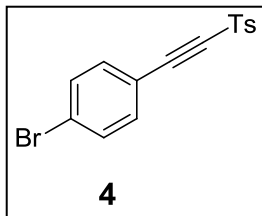


Tribromide **1** (73.07 g, 213.1 mmol) was stirred in ethanol (320 mL) in a 1 L round-bottom flask. The flask was fitted with a Liebig condenser, and the mixture heated to reflux. Once all solid material had dissolved, potassium hydroxide pellets (85 %, 56.27 g, 852.5 mmol) were added through the top of the condenser. The reaction mixture was stirred at reflux under N₂ atmosphere for 2.5 h. The reaction flask was transferred directly to a rotary evaporator and concentrated *in vacuo* to a sticky solid. This material was partitioned between 5 % aqueous ammonium chloride (400 mL) and methylene chloride (400 mL). The organic phase was washed with H₂O (2 x 200 mL), dried over Na₂SO₄, and evaporated *in vacuo* to yield **2** (which decomposes relatively rapidly, and should be used immediately, or stored at -20 °C for only a short time.) as pale yellow crystals (37.83 g, 98 %): mp = 63-64 °C, lit⁴³ = 64 °C. ¹H-NMR (360 MHz, CDCl₃) δ 7.46 (d, *J* = 8.4 Hz, 2H), 7.35 (d, *J* = 8.4 Hz, 2H), 3.128 (s, 1H).

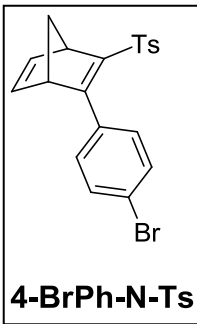


Terminal alkyne **2** (5.43 g, 30.0 mmol), sodium *p*-toluenesulfinate (6.41 g, 36.0 mmol), and sodium iodide (5.40 g, 36.0 mmol) were placed in a flame-dried, 1 L round-bottom flask with magnetic stir bar. Acetonitrile (270 mL) was added and the mixture was stirred. Ceric ammonium nitrate (41.12 g, 75.00 mmol) was dissolved in acetonitrile (180 mL), and added to the stirring mixture at once. The reaction mixture was stirred under N₂ atmosphere for 1.5 h. The reaction flask was transferred directly to a rotary evaporator and stripped of solvent *in vacuo*. The resultant yellow solid was partitioned between H₂O (450 mL) and methylene chloride (450 mL) in the reaction flask. The biphasic mixture was stirred, and solid sodium sulfite was added in small portions by scoopula until the brown color of excess iodine disappeared. The organic phase was pale yellow at this point. The

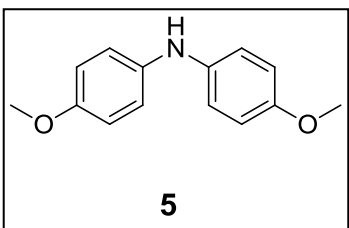
mixture was transferred to a 2 L separatory funnel. The layers were separated and the aqueous phase was extracted with methylene chloride (450 mL). Pooled organics were washed with H₂O (100 mL), dried over anhyd sodium sulfate and evaporated *in vacuo* to give a pale, yellow solid. This solid was dissolved in a minimal amount of hot methanol, allowed to cool to rt, and then placed in a freezer. Vacuum filtration yielded **3** as colorless needles (5.50 g, 78 %): mp = 157-159 °C. ¹H-NMR (360 MHz, CDCl₃) δ 7.50 (d, *J* = 8.3 Hz, 2H), 7.42 (d, *J* = 8.6 Hz, 2H), 7.34 (s, 1H), 7.23 (d, *J* = 8.0 Hz, 2H), 7.11 (d, *J* = 8.6 Hz, 2H), 2.43 (s, 3H); ¹³C-NMR (125 MHz, acetone-*d*6) δ 145.55, 142.50, 140.39, 138.49, 131.77, 130.61, 130.08, 128.56, 123.89, 112.04, 22.22. HRMS m/z: calc. for M⁺ C₁₅H₁₂O₂BrIS = 461.8795, found = 461.8786.



Vinyl iodide **3** (32.38 g, 69.76 mmol) was placed in a 2 L round-bottom flask with magnetic stir bar. Toluene (800 mL) was added, and the mixture was stirred, ensuring that all solid was dissolved. Potassium *tert*-butoxide (0.375 M in *tert*-butanol) was titrated into the stirring solution over a 2 h period until TLC (silica gel, methylene chloride/hexanes 1:1) indicated complete consumption of **3**. The solvent was then evaporated *in vacuo*. The resultant residue was partitioned between methylene chloride (500 mL) and H₂O (500 mL). The layers were separated and the aqueous phase was extracted with methylene chloride (500 mL). Pooled organics were washed with H₂O (100 mL), dried over anhyd sodium sulfate and evaporated *in vacuo* to yield **4** as pale, yellow crystals (23.71 g, quant): mp = 135-137 °C. ¹H-NMR (360 MHz, CDCl₃) δ 7.95 (d, *J* = 8.4 Hz, 2H), 7.52 (d, *J* = 8.6 Hz, 2H), 7.40 (d, *J* = 8.2 Hz, 2H), 7.37 (d, *J* = 8.6 Hz, 2H), 2.49 (s, 3H); ¹³C-NMR (125 MHz, acetone-*d*6) δ 146.92, 140.15, 135.34, 133.40, 131.38, 128.41, 127.22, 118.06, 92.35, 88.01, 22.69. HRMS m/z: calc. for M⁺ C₁₅H₁₁O₂BrS = 333.9663, found = 333.9663.

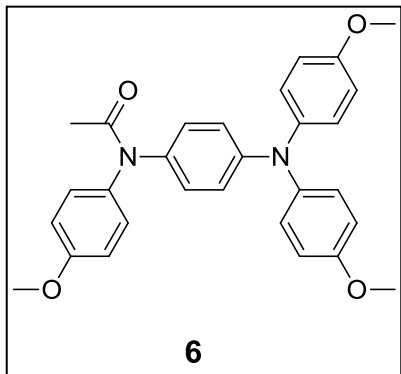


Acetylenic sulfone **4** (4.22 g, 12.6 mmol), cyclopentadiene (1.23 mL, 15.1 mmol) and chloroform (20 mL) were combined in 50 mL round-bottom flask with magnetic stir bar. The flask was sealed with a plastic stopper secured with several wraps of black electrical tape. The reaction flask was placed on a 60 °C oil bath and stirred for 15 h. The solvent was evaporated *in vacuo* to give a pale, yellow oil which crystallized upon standing. Recrystallization from ethanol yielded **4-BrPh-N-Ts** as colorless prisms (4.97 g, 98 %): mp = 138-139 °C. ¹H-NMR (360 MHz, CDCl₃) δ 7.49 (d, *J* = 8.4, 2H), 7.46 (d, *J* = 8.1, 2H), 7.31 (d, *J* = 8.4, 2H), 7.20 (d, *J* = 8.0, 2H), 6.74 (dd, *J*₁ = 3.3 Hz, *J*₂ = 4.3 Hz, 1 H), 6.54 (dd, *J*₁ = 3.3 Hz, *J*₂ = 4.3 Hz, 1H), 3.91 (br s, 1H), 3.81 (br s, 1 H), 2.38 (s, 3H), 2.30 (d, *J* = 6.8 Hz, 1H), 2.00 (d, *J* = 6.8 Hz, 1H); ¹³C-NMR (125 MHz, acetone-*d*6) δ 163.16, 148.88, 145.22, 143.54, 140.68, 138.28, 134.21, 131.90, 131.10, 130.75, 128.70, 123.85, 71.66, 61.07, 55.84, 22.53. HRMS m/z: calc. for M⁺ C₂₀H₁₇O₂BrS = 400.0139, found = 400.0133.



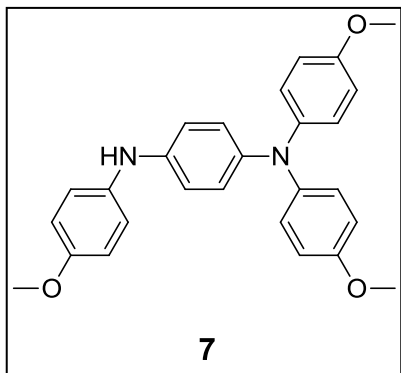
Sublimed *p*-anisidine (12.32 g, 0.1000 mol) and 4-bromoanisole (12.51 mL, 0.1000 mol) were placed in a flame-dried 500 mL round-bottom flask with magnetic stir bar inside a dry box. The mixture was stirred in toluene (200 mL) until dissolved. Pd(db_a)₂ (0.115 g, 0.200 mmol), P(*t*-Bu)₃ (0.040 g, 0.20 mmol), and NaOt-Bu (14.42 g, 0.1500 mol) were added and the flask was fitted with an oil bubbler then transferred to a 60 °C oil bath. The reaction mixture was stirred under N₂ for 1 h then diluted with ~200 mL tetrahydrofuran and vacuum filtered through a 60 x 20 mm plug of basic alumina (activity III). The filtrate was concentrated *in vacuo* to give a sticky purple solid. Recrystallization from ethanol afforded very

pale purple crystals (17.71 g, 77 %): mp = 99-101 °C, lit⁴⁴ = 101-103 °C. ¹H-NMR (360 MHz, CDCl₃) δ 6.93 (d, *J* = 8.5 Hz, 2H), 6.83 (d, *J* = 8.5 Hz, 2H), 3.78 (s, 6H).



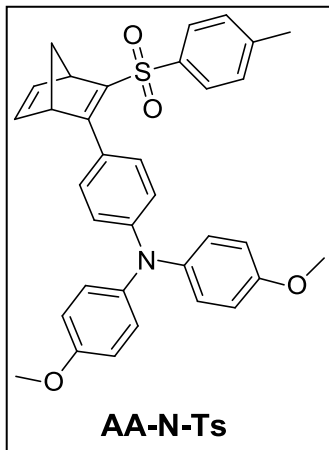
Commercially available 4-Aminoacetanilide (5.00 g, 33.3 mmol), 4-iodoanisole (38.97 g, 165.5 mmol), copper powder (6.35 g, 100 mmol), anhyd potassium carbonate (13.83 g, 100 mmol), and diphenyl ether (15.0 mL) were combined in a 250 mL round-bottom flask. The reaction mixture was heated to 190 °C in a silicone oil bath and mechanically stirred for 48 h.

During the course of the reaction, a large amount of water was evolved and driven off as steam. This was particularly noticeable during the first several hours. The reaction mixture was removed from heat and allowed to cool, then diluted in ~150 mL benzene and vacuum filtered through celite. The filtrate was concentrated *in vacuo*. Dry column vacuum chromatography (silica gel, ethyl acetate/hexanes 5 % gradient) afforded **6** as a pale yellow solid (12.82 g, 82 %): mp = 110-112 °C, lit⁴⁵ = 111 °C. ¹H-NMR (360 MHz, CDCl₃) δ 7.19 (d, *J* = 8.9 Hz, 2H), 7.10-6.97 (m, 6H), 6.94-6.75 (m, 8H), 3.79 (s, 9H), 2.06 (s, 3H).

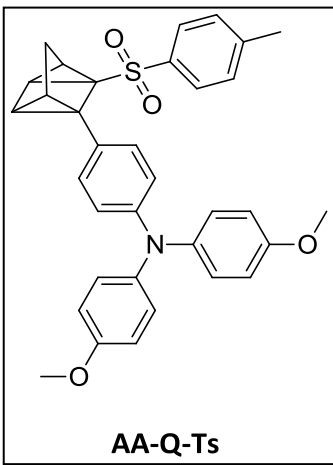


Arylamine **6** (12.34 g, 26.34 mmol), potassium hydroxide (3.55 g, 63.31 mmol), and ethanol (40 mL) were combined in a 250 mL round-bottom flask with magnetic stir bar. The reaction mixture was refluxed under N₂ for 24 h, allowed to cool, and then poured into 600 mL H₂O. This was extracted with diethyl ether (450 mL x 3) and the pooled organics were dried over

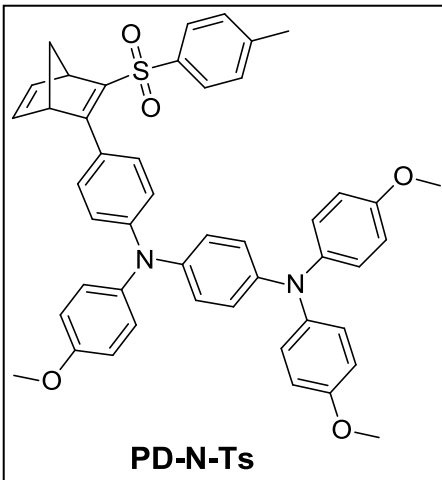
anhyd potassium carbonate. The solution was filtered and concentrated in vacuo to a volume of ~50 mL then passed through a short column of basic alumina (activity III). Concentration to dryness gave **7** (which oxidizes rapidly and must be stored under inert atmosphere at -20 °C) as a tan solid (10.80 g, 96 %): mp = 85-87 °C, lit⁴⁵ = 87-88 °C. ¹H-NMR (500 MHz, CD₃CN) δ 6.97 (d, *J* = 8.9 Hz, 2H), 6.89 (d, *J* = 9.0 Hz, 4H), 6.85-6.80 (m, 6H), 6.79 (d, *J* = 9.0 Hz, 4H) 6.23 (br s, 1H), 3.72 (s, 9H).



Aryl bromide **4-BrPh-N-Ts** (0.807 g, 2.00 mmol), **5** (0.459 g, 2.00 mmol), Pd(dba)₂ (0.058 g, 0.10 mmol), P(*t*-Bu)₃ (0.020 g, 0.10 mmol), and NaOt-Bu (0.288 g, 3.00 mmol) was dissolved in 4.0 mL anhyd tetrahydrofuran in a dry box. The reaction mixture was stirred under N₂ for 48 h, then taken up in ethyl acetate and filtered through a 12.5x25 mm plug of basic alumina (activity III). The filtrate was concentrated *in vacuo*, and the resultant brown oil placed under high vacuum to give an orange foam-like solid. Flash column chromatography (basic alumina, ether/pet ether 1:1) yielded **AA-N-Ts** as a bright-yellow, amorphous solid (1.05 g, 95 %). T_g = 71-83 °C. ¹H-NMR (360 MHz, DMSO-*d*6) δ 7.53 (d, *J* = 8.2 Hz, 2H), 7.35 (d, *J* = 8.8 Hz, 2H), 7.34 (d, *J* = 8.2 Hz, 2H), 7.07 (d, *J* = 8.9 Hz, 4H), 6.95 (d, *J* = 9.0 Hz, 4H), 6.80 (dd, *J*₁ = 3.2 Hz, *J*₂ = 4.5 Hz, 1H), 6.64 (m, 3H), 3.93 (br s, 1H), 3.86 (br s, 1H), 3.75 (s, 6H), 2.37 (s, 3H), 2.08 (d, *J* = 6.8 Hz, 1H), 1.87 (d, *J* = 6.8 Hz, 1H); ¹³C-NMR (125 MHz, acetone-*d*6) δ 164.20, 157.81, 150.91, 144.61, 143.94, 143.46, 140.89, 139.30, 130.84, 130.50, 128.58, 128.46, 125.68, 118.47, 116.13, 70.48, 60.63, 56.58, 55.76, 22.54. Anal. calc. for C₃₄H₃₁NO₄S: C, 74.29; H, 5.68; N, 2.55%. Found: C, 74.14; H, 5.69; N, 2.48%.

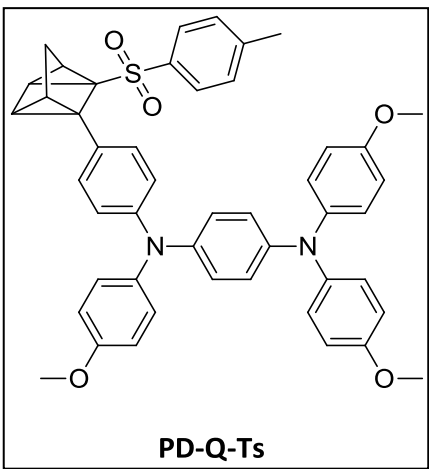


AA-N-Ts (0.100 g, 0.182 mmol), anhyd potassium carbonate (0.503 g, 3.64 mmol), and benzene (5.0 mL) were combined in a vial with a magnetic stir bar and fitted with a rubber septum. The mixture was purged with N₂ for 5 min while stirring. The septum was replaced with a plastic screw-on cap (while under a cone of N₂) and then wrapped with paraffin film. The vial was placed inside a Rayonet reactor with 350 nm bulbs and irradiated for 7 h while stirring. The reaction mixture was filtered through a 0.5 cm plug of basic alumina (activity III), held in place by a small plug of glass wool, all contained within a disposable pipet. The reaction mixture was pushed through the pipet filter by N₂ pressure. *USE CAUTION - disposable pipets can easily burst under pressure. The filtrate was concentrated *in vacuo* to obtain a puffy, pale yellow solid (0.077 g, 77%). T_g = 64-74 °C. ¹H-NMR (360 MHz, C₆D₆) δ 7.75 (d, *J* = 8.2 Hz, 2H), 7.28 (d, *J* = 9.0 Hz, 4H), 7.23-7.16 (m, 4H), 6.95 (d, *J* = 8.0 Hz, 2H), 6.90 (d, *J* = 9.0 Hz, 4H), 3.47 (s, 6H), 2.83 (dd, *J*₁ = 1.4 Hz, *J*₂ = 5.2 Hz, 1H), 2.68 (dd, *J*₁ = 2.6 Hz, *J*₂ = 5.2 Hz, 1H), 2.13 (d, *J* = 11.8 Hz, 1H), 2.03 (s, 3H), 1.87 (dd, *J*₁ = 2.6 Hz, *J*₂ = 4.8 Hz, 1H), 1.79 (d, *J* = 11.8 Hz, 1H), 1.40 (dd, *J*₁ = 1.4 Hz, *J*₂ = 4.8 Hz, 1H).

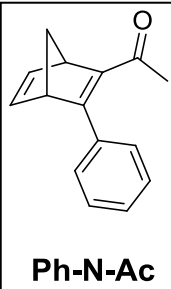


Aryl bromide **4-BrPh-N-Ts** (0.807 g, 2.00 mmol), **7** (0.853 g, 2.00 mmol), Pd(dba)₂ (0.115 g, 0.200 mmol), P(*t*-Bu)₃ (0.040 g, 0.20 mmol), and NaOt-*t*-Bu (0.288 g, 3.00 mmol) was dissolved in 4.0 mL anhyd toluene in a dry box. The reaction mixture was stirred under N₂ for 23 h on a 50 °C oil bath, then taken up in tetrahydrofuran and filtered through a 12.5x25 mm plug of basic alumina (activity III). The filtrate

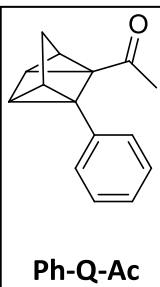
was concentrated *in vacuo*, and the resultant brown oil was absorbed onto silica gel and loaded onto a silica gel column. Elution with ethyl acetate/hexanes 1:3 yielded **PD-N-Ts** as a bright-yellow solid (1.35 g, 90 %): mp = 207-208 °C. ¹H-NMR (360 MHz, CDCl₃) δ 7.54 (d, *J* = 8.3 Hz, 2H), 7.38 (d, *J* = 8.9 Hz, 2H), 7.19 (d, *J* = 8.0 Hz, 2H), 7.10 (d, *J* = 8.9 Hz, 2H), 7.06 (d, *J* = 9.0 Hz, 4H), 6.93 (d, *J* = 9.0 Hz, 2H), 6.86 (d, *J* = 9.0 Hz, 4H), 6.86 (d, *J* = 8.9 Hz, 2H), 6.83 (d, *J* = 9.0 Hz, 4H), 6.69 (dd, *J*₁ = 3.0 Hz, *J*₂ = 5.0 Hz, 1H), 6.54 (dd, *J*₁ = 2.9 Hz, *J*₂ = 4.5 Hz, 1H), 3.91 (br s, 1H), 3.88 (br s, 1H), 3.82 (s, 3H), 3.80 (s, 6H), 2.39 (s, 3H), 2.25 (d, *J* = 6.8 Hz, 1H), 1.96 (d, *J* = 6.8 Hz, 1H). HRMS m/z: calc. for M⁺ C₄₇H₄₂N₂O₅S = 746.2824, found = 746.2814. Crystals for XRD analysis were grown by vapor diffusion of pet ether into a saturated solution of **PD-N-Ts** in ethyl acetate at rt.



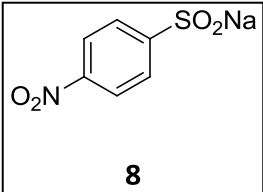
PD-N-Ts (7.5 mg, 1.0×10^{-5} mol) was dissolved in 0.75 mL C_6D_6 in an NMR tube. The tube was connected to a high vacuum manifold using a Cajon coupling. The sample was frozen with liquid nitrogen, and then vacuum was applied. When the pump reached ultimate vacuum (~ 0.05 Torr), the vacuum valve was closed at the manifold. The liquid nitrogen was then removed and the sample allowed to thaw. This thawing was accompanied by a noticeable amount of gas evolution. This completed one freeze-pump-thaw cycle, a process which was repeated twice more. By the end of the third and final cycle, no gas evolution could be observed, and the sample was determined to be thoroughly degassed. At this point, the sample was frozen once more, and vacuum was reapplied. The vacuum was not turned off at the manifold this time; the pump was allowed to pull an active vacuum on the frozen solution during the flame-sealing process. The sample was sealed by slowly and evenly heating the wall of the tube around its circumference using a propane torch until the sides eventually collapsed fully inward, being pulled by the applied vacuum. The tube was then heated at the sealed juncture and gently pulled until the molten glass separated. The sample was irradiated for 30 min with a 500 W Hg-Xe arc lamp behind an Oriel 51472 (400 nm) cut-off filter, and a water-filled quartz cylinder (to absorb IR). The product was not isolated, though the reaction yield (based on NMR) was 79 %.



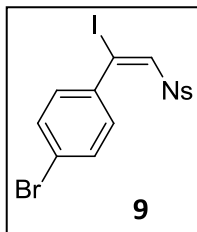
Freshly distilled cyclopentadiene (1.280 mL, 15.50 mmol), 4-phenyl-3-butyn-2-one (1.580 mL, 11.07 mmol), and 15 mg *p*-methoxyphenol (to inhibit polymer formation) were combined in a 65 mL pressure vessel with magnetic stir bar inside a dry box. The vessel was sealed, removed from the dry box, and placed on a 160 °C oil bath. *CAUTION – the sealed vessel is under very high pressure during the reaction. The reaction mixture was stirred for 18 h, at which point the vessel was removed from heat and immediately submerged in an ice bath. Rapid cooling is imperative in order to avoid dimerization of excess cyclopentadiene (the dimer, dicyclopentadiene, is difficult to remove from the product). The reaction mixture was diluted in ~20 mL dichloromethane, and then transferred to a 50 mL round-bottom flask. The solvent was removed *in vacuo*, and the crude material was purified by Kugelrohr distillation to give **Ph-N-Ac** as a yellow oil (1.02 g, 44 %):
¹H-NMR (360 MHz, CDCl₃) δ 7.40-7.26 (m, 5H), 6.99 (dd, *J*₁ = 3.0 Hz, *J*₂ = 5.0 Hz, 1H), 6.89 (dd, *J*₁ = 3.2 Hz, *J*₂ = 4.6 Hz, 1H), 4.09 (br s, 1H), 3.79 (br s, 1H), 2.24 (dt, *J*₁ = 1.6 Hz, *J*₂ = 6.6 Hz, 1H), 2.05 (dt, *J*₁ = 1.5 Hz, *J*₂ = 6.6 Hz, 1H), 2.00 (s, 3H).



Ph-N-Ac (8.3 mg, 4.0 × 10⁻⁵ mol) was dissolved in 500 μL CD₂Cl₂ in an NMR tube. The sample was purged with N₂ for 1 min. The sample was irradiated for 1 h with a 500 W Hg-Xe arc lamp behind a water-filled quartz cylinder (to absorb IR) while magnetically stirring. The product was not isolated, though the reaction yield (based on NMR) was > 99 %.

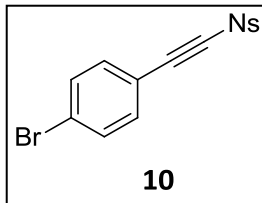


Sodium sulfite (6.30 g, 50.00 mmol) was dissolved in H₂O (25 mL) and cooled to 0 °C on an ice bath. Commercially available 4-nitrobenzenesulfonyl chloride (1.11 g, 5.00 mmol) was added in small portions over a 10 min period. The reaction mixture was stirred a 0 °C for 20 min, then removed from the ice bath and stirred for an additional 2.5 h. The mixture was made strongly basic (pH ~14) by the careful addition of 1 N sodium hydroxide. 1,4-dioxane (200 mL) was added, and a colorless crystalline mass rapidly formed. Vacuum filtration afforded a filtrate which was evaporated in vacuo. The resultant orange-yellow solid was dissolved in a minimal amount of hot toluene/ethanol (1:1) and the solution was allowed to cool to room temperature. Upon standing, yellow crystals began to form, and the solvent was allowed to evaporate until the mother liquor became nearly colorless. Vacuum filtration yielded **8** (0.88 g, 84 %) as bright yellow needles: ¹H-NMR (360 MHz, DMSO-*d*6) δ 8.17 (d, *J* = 8.6 Hz, 2H), 7.68 (d, *J* = 8.6 Hz, 2H).

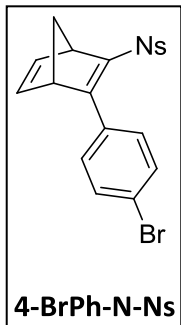


Sulfinate salt **8** (0.75 g, 3.6 mmol), 4-bromophenylacetylene (0.65 g, 3.6 mmol), and sodium iodide (0.64 g, 4.3 mmol) were placed in a 250 mL round-bottom flask with stir bar. Acetonitrile (30 mL) was added and the mixture stirred under N₂. A solution of ceric ammonium nitrate (4.93 g, 9.0 mmol) in acetonitrile (25 mL) was added at once and the brown reaction mixture was stirred for 1 h 45 min. The reaction flask was transferred directly to a rotary evaporator, and the solvent was evaporated in vacuo. The resultant residue was partitioned between methylene chloride (50 mL) and H₂O (50 mL). The organic phase was separated and washed with H₂O (50 mL) then 5 % sodium bisulfate (50 mL). Pooled aqueous phases were back-extracted with methylene chloride

(50 mL). Pooled organics were washed with brine (10 mL), dried over magnesium sulfate, and evaporated in *vacuo* to afford a pale yellow solid. Recrystallization from hot ethanol yielded **9** (1.39 g, 78 %) as colorless crystals: $^1\text{H-NMR}$ (360 MHz, CDCl_3) δ 8.27 (d, $J = 8.9$ Hz, 2H), 7.78 (d, $J = 8.9$ Hz, 2H), 7.46 (d, $J = 8.6$ Hz, 2H), 7.38 (s, 1H) 7.10 (d, $J = 8.6$ Hz, 2H).

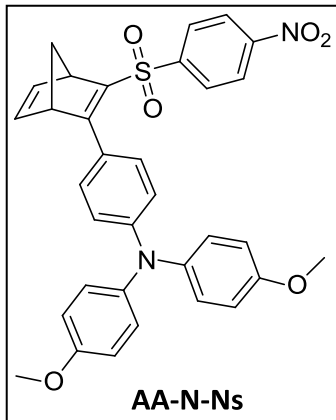


Vinyl iodide **9** (0.174, 0.352 mmol) was dissolved in 5.0 mL toluene/*tert*-butanol (1:1) and stirred under N_2 on a 50 °C oil bath until dissolved. 0.30 M potassium *tert*-butoxide solution in toluene (1.20 mL) was added and the reaction mixture was stirred for 40 min. The reaction flask was removed from heat and transferred directly to a rotary evaporator. Evaporation of solvent *in vacuo* gave a yellow residue which was partitioned between diethyl ether (10 mL) and H_2O (10 mL). The aqueous phase was extracted twice more with diethyl ether (2 x 10 mL). Pooled organics were washed with brine (10 mL), dried over magnesium sulfate, and evaporated *in vacuo* to yield **10** (0.128 g, 99 %) as a yellow solid: $^1\text{H-NMR}$ (360 MHz, CDCl_3) δ 8.45 (d, $J = 8.7$ Hz, 2H), 8.27 (d, $J = 8.7$ Hz, 2H), 7.56 (d, $J = 8.4$ Hz, 2H), 7.41 (d, $J = 8.4$ Hz, 2H).



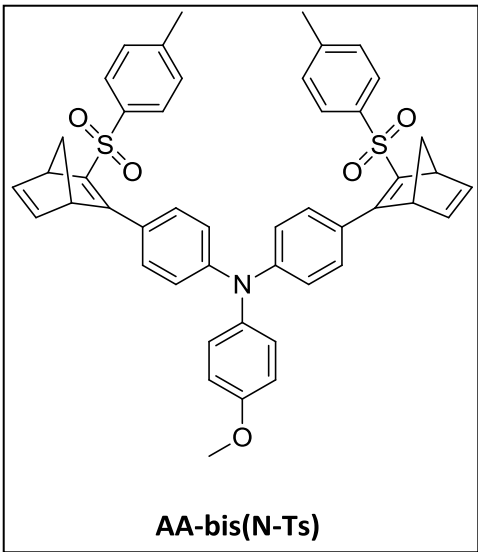
Acetylenic sulfone **10** (0.640 g, 1.74 mmol), cyclopentadiene (171 uL, 2.09 mmol) and chloroform (30 mL) were placed in a 65 mL pressure vessel with stir bar. The vessel was sealed and stirred on a 60 °C oil bath for 64 h. The solvent was evaporated in *vacuo* to yield **4-BrPh-N-Ns** (0.758 g, 100 %) as a pale yellow solid: $^1\text{H-NMR}$ (360 MHz, $\text{DMSO}-d_6$) δ 8.34 (d, $J = 8.9$ Hz, 2H), 7.89 (d, $J = 8.9$ Hz, 2H), 7.41 (d, $J = 8.4$ Hz, 2H), 7.34 (s, 1H).

Hz, 2H), 7.62 (d, J = 8.5 Hz, 2H), 7.38 (d, J = 8.7 Hz, 2H), 6.92 (dd, J_1 = 3.2 Hz, J_2 = 4.6 Hz, 1H), 6.69 (dd, J_1 = 3.0 Hz, J_2 = 4.7 Hz 1H), 3.95 (br s, 1H), 3.91 (br s, 1H), 2.25 (d, J = 7.0 Hz, 1H), 1.97 (d, J = 7.0 Hz, 1H).



Aryl bromide **4-BrPh-N-Ns** (0.216 g, 0.500 mmol), **5** (0.115 g, 0.500 mmol), Pd(dba)2 (0.029 g, 5.0x10⁻⁵ mol), P(t-Bu)3 (0.010 g, 5.0 x 10⁻⁵ mol), NaOt-Bu (0.072 g, 0.75 mmol), and toluene (1.0 mL) were placed in a 5 mL Schlenk tube inside a dry box. The tube was sealed and stirred on a 60 °C oil bath for 3 h. The reaction mixture was allowed to cool to room temperature, then diluted in tetrahydrofuran

and filtered through a plug of basic alumina (activity III). The filtrate was adsorbed onto Celite and loaded onto a column of silica gel. Elution with ethyl acetate/hexanes (1:3) yielded **AA-N-Ns** (0.268 g, 92 %) as a red solid: ¹H-NMR (500 MHz, DMSO-*d*6) δ 8.33 (d, J = 8.8 Hz, 2H), 7.89 (d, J = 8.8 Hz, 2H), 7.34 (d, J = 8.8 Hz, 2H), 7.07 (d, J = 8.9 Hz, 4H), 6.95 (d, J = 8.9 Hz, 4H), 6.83 (dd, J_1 = 3.0 Hz, J_2 = 4.7 Hz 1H), 6.74 (dd, J_1 = 3.0 Hz, J_2 = 4.4 Hz 1H), 6.63 (d, J = 8.8 Hz, 2H), 3.98 (br s, 1H), 3.96 (br s, 1H), 3.76 (s, 6H), 2.14 (d, J = 6.7 Hz, 1H), 1.92 (d, J = 6.7 Hz, 1H).



Aryl bromide **4-BrPh-N-Ts** (0.403 g, 1.00 mmol), *p*-anisidine (0.062 g, 0.50 mmol), Pd(dba)₂ (0.058 g, 0.10 mmol), P(*t*-Bu)₃ (0.020 g, 0.10 mmol), NaOt-Bu (0.144 g, 1.50 mmol), and anhyd toluene (2.0 mL) were placed in a 5 mL Schlenck tube inside a dry box. The tube was sealed and stirred on a 60 °C oil bath for 6.5 h. The reaction vessel was then removed from heat and allowed to cool to rt. The reaction mixture was diluted with ~5 mL ethyl acetate, and then filtered through a 40 x 20 mm plug of basic alumina (activity III). The filtrate was concentrated *in vacuo* to give a reddish-brown oil. The oil was placed under high vacuum to obtain a dark, fluffy solid. The solid was adsorbed onto Celite and loaded onto a short (5 cm) column of basic alumina (activity I). Elution with diethyl ether gave **AA-bis(N-Ts)** (0.490 g, 64 %) as a yellow solid.

Photochemical Experiments

[Figure 1.3.1. Optical spectra of N, AA-N-Ts, and PD-N-Ts at 5.0 x 10⁻⁵ M in acetonitrile]

Solutions (5.0 x 10⁻⁵ M in acetonitrile) of **N**, **AA-N-Ts**, and **PD-N-Ts** were prepared by successive dilution. **N** (5.1 μL, 5.0 x 10⁻⁵ mol) was dissolved in acetonitrile to 10.0 mL in a volumetric flask to give a 5.0 x 10⁻³ M solution. A 500 μL gas-tight syringe was used to transfer 100 μL of the **N** solution to an empty 10.0 mL volumetric flask. This flask was filled to the mark with acetonitrile to give a 5.0 x 10⁻⁵ M solution. The solution (3.0 mL) was placed in a quartz cuvette and the optical spectrum was measured. **AA-N-Ts** (2.7 mg, 5.0 x 10⁻⁶ mol) was dissolved in acetonitrile to 10.0 mL in a volumetric flask to give a 5.0 x 10⁻⁴ M solution. A 500 μL gas-

tight syringe was used to transfer 1.0 mL of the **AA-N-Ts** solution to an empty 10.0 mL volumetric flask. This flask was filled to the mark with acetonitrile to give a 5.0×10^{-5} M solution. The solution (3.0 mL) was placed in a quartz cuvette and the optical spectrum was measured. **PD-N-Ts** (3.7 mg, 5.0×10^{-6} mol) was dissolved in acetonitrile to 10.0 mL in a volumetric flask to give a 5.0×10^{-4} M solution. A 500 μ L gas-tight syringe was used to transfer 1.0 mL of the **PD-N-Ts** solution to an empty 10.0 mL volumetric flask. This flask was filled to the mark with acetonitrile to give a 5.0×10^{-5} M solution. The solution (3.0 mL) was placed in a quartz cuvette and the optical spectrum was measured.

[Figure 1.4.1. Arc lamp photoreaction of AA-N-Ts with irradiation >385 nm in deaerated benzene at 5.0×10^{-5} M]

AA-N-Ts (2.7 mg, 5.0×10^{-6} mol) was dissolved in benzene to 10.0 mL in a volumetric flask to give a 5.0×10^{-4} M solution. A 500 μ L gas-tight syringe was used to transfer 1.0 mL of the **AA-N-Ts** solution to an empty 10.0 mL volumetric flask. This flask was filled to the mark with benzene to give a 5.0×10^{-5} M solution. The solution (3.0 mL) was placed in a quartz cuvette and the optical spectrum was measured. The sample was then irradiated with the 500 W Hg-Xe arc lamp behind an Oriel cut-off filter 51460 (385 nm) and a water-filled quartz cylinder (to absorb IR). Subsequent optical spectra were measured after 2, 3, 4, and 5 s total irradiation time.

[Figures 1.4.2. and 1.4.3. ^1H -NMR spectra (360 MHz) of AA-N-Ts in *d*6-benzene before and after exposure to indirect sunlight]

AA-N-Ts (2.7 mg, 5.0×10^{-6} mol) was dissolved in C_6D_6 (0.75 mL) and placed in an NMR tube. The sample was purged with N_2 for 1 min then capped and sealed with paraffin film. The ^1H -

NMR was measured. The tube was placed in an Erlenmeyer flask, and then set in a windowsill, exposing the sample to indirect sunlight for 55 min. The $^1\text{H-NMR}$ was measured.

[Figure 1.4.4. Solar photoconversion of AA-N-Ts to AA-Q-Ts through a glass window in deaerated benzene at 5.0×10^{-5} M]

AA-N-Ts (2.7 mg , $5.0 \times 10^{-6} \text{ mol}$) was dissolved in benzene to 10.0 mL in a volumetric flask to give a $5.0 \times 10^{-4} \text{ M}$ solution. A $500 \mu\text{L}$ gas-tight syringe was used to transfer 1.0 mL of the **AA-N-Ts** solution to an empty 10.0 mL volumetric flask. This flask was filled to the mark with benzene to give a $5.0 \times 10^{-5} \text{ M}$ solution. The solution (3.0 mL) was placed in a quartz cuvette and the optical spectrum was measured. The cuvette was set in a windowsill, exposing the sample to indirect sunlight. Subsequent optical spectra were measured after $30, 60, 90, 120$, and 150 s total irradiation time.

[Figure 1.4.6. An example dataset for an AA-N-Ts actinometry experiment depicting changes in absorbance of the AA-N-Ts solutions and ferrioxalate/phenanthroline complexes]

Potassium oxalate monohydrate (8.29 g , 45.0 mmol) was dissolved in DI H_2O to 30.0 mL to give a 1.50 M solution. Anhyd iron(III) chloride (2.43 g , 15.0 mmol) was dissolved in DI H_2O to 10.0 mL to give a 1.50 M solution. The two solutions were combined in a 125 mL Erlenmeyer flask and stirred for 5 min . The flask was sealed with paraffin film and placed in an ice bath in the dark for 30 min to obtain bright green crystals which were recrystallized twice from warm ($\sim 50^\circ\text{C}$) H_2O . To dry the resulting potassium ferrioxalate trihydrate crystals, the material was placed in a foil-covered Erlenmeyer flask and heated on an oil bath to 50°C . A stream of dry air was blown over the crystals overnight ($\sim 16 \text{ h}$). A stock solution of ferrioxalate was prepared by dissolving potassium ferrioxalate trihydrate (0.590 g , 1.20 mmol) to 100 mL with 0.05 M

aqueous sulfuric acid. This gave a stabilized 0.012 M ferrioxalate solution. A stock solution of phenanthroline (the developing reagent) was prepared by dissolving 1,10-phenanthroline (0.100 g, 0.554 mmol) and sodium acetate trihydrate (22.50 g, 165.3 mmol) to 100 mL with aqueous 0.5 M sulfuric acid. Both stock solutions were stored in amber bottles in a dark cabinet.

The actinometry experiment was carried out as follows: first a blank consisting of 3.0 mL benzene in a quartz cuvette was placed in direct contact with a second cuvette containing 3.0 mL ferrioxalate stock solution. The lens of a 405 nm GaN laser drawing 50 mA was placed in direct contact with the benzene blank. The blank was irradiated for 30 s while stirring, and then the ferrioxalate solution was treated with 0.50 mL phenanthroline solution and allowed to stand for ~5 min. The orange Fe^{2+} /phenanthroline complex was observed by UV-vis and its absorbance at 510 nm was recorded (1.43). **AA-N-Ts** (1.14 mg, 2.07×10^{-6} mol) was placed in a 25.0 mL volumetric flask and filled to the mark with benzene to give an 8.30×10^{-5} M solution. The **AA-N-Ts** solution (3.0 mL) in a quartz cuvette was observed by UV-vis and its absorbance at 386 nm was recorded (1.60). This cuvette was then placed in direct contact with a second cuvette containing 3.0 mL ferrioxalate stock solution. The lens of a 405 nm GaN laser drawing 50 mA was placed in direct contact with the cuvette containing **AA-N-Ts**. The sample was irradiated for 30 s while stirring, and then the ferrioxalate solution was treated with 0.50 mL phenanthroline solution and allowed to stand for ~5 min. The **AA-N-Ts** sample was observed by UV-vis and its absorbance at 386 nm was recorded (0.451). The Fe^{2+} /phenanthroline complex was observed by UV-vis and its absorbance at 510 nm was recorded (0.415).

The number of photons absorbed by **AA-N-Ts** was determined by calculating the difference in moles of Fe^{2+} generated in the ferrioxalate solutions from the blank run and the **AA-N-Ts** run according to the following equation:³³

$$\text{moles Fe}^{2+} = \frac{V_1 \times V_3 \times \Delta A(510 \text{ nm})}{10^3 \times V_2 \times l \times \varepsilon(510 \text{ nm})}$$

where V_1 is the irradiated volume, V_2 is the aliquot of the irradiated solution taken for the determination of the Fe^{2+} ions (which is equal to V_1 , since no aliquot was removed), V_3 is the final volume after complexation with phenanthroline (all in mL), l is the optical pathlength (in cm) of the cuvette, $\Delta A(510 \text{ nm})$ the optical difference in absorbance between the irradiated **AA-N-Ts** solution and that of the blank, $\varepsilon(510 \text{ nm})$ is the molar absorptivity of the $\text{Fe}^{2+}/\text{phenanthroline}$ complex ($11100 \text{ L mol}^{-1} \text{ cm}^{-1}$ at $\lambda_{\max} 510 \text{ nm}$). Substituting the experimental values for **AA-N-Ts** gave 3.22×10^{-7} moles Fe^{2+} :

$$3.22 \times 10^{-7} \text{ mole Fe}^{2+} = \frac{3.0 \text{ mL} \times 3.5 \text{ mL} \times (1.43 - 0.415)}{10^3 \times 3.0 \text{ mL} \times 1.0 \text{ cm} \times 11100}$$

The moles of photons absorbed by the irradiated solution per unit time are given by the following equation:

$$N\hbar\nu / t = \frac{\text{moles of Fe}^{2+}}{\Phi_\lambda \times t \times F}$$

where Φ_λ is the quantum yield of Fe^{2+} ion production at the irradiation wavelength (1.14 at 405 nm) (note that the quantum yield is greater than one. This is due to the fact that two Fe^{2+} ions are generated for every reactive photon), t is the irradiation time, and F is the mean fraction of light absorbed by the ferrioxalate solution (this may be assumed to be equal to unity, provided that no light may be detected exiting the ferrioxalate solution. This can be determined by placing a white

sheet of paper behind the cuvette to check for unabsorbed light). Substituting the experimental values for **AA-N-Ts** gave 9.42×10^{-9} moles h/s.

$$9.42 \times 10^{-9} \text{ moles h/s} = \frac{3.22 \times 10^{-7} \text{ moles of Fe}^{2+}}{1.14 \times 30 \text{ s} \times 1}$$

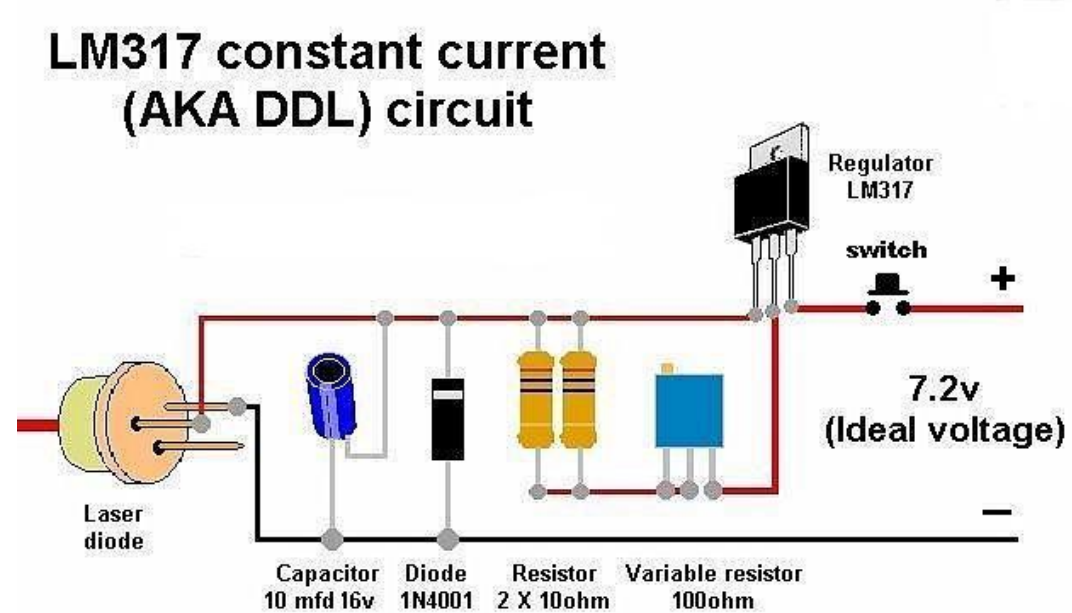
The moles of **AA-N-Ts** reacted may be determined by applying Beer's Law: $A = \epsilon \times l \times c$ where the absorbance at 386 nm prior to irradiation was 1.60, the pathlength was 1.0 cm, and the concentration was 8.30×10^{-5} M gave an $\epsilon = 19277$. Likewise, the concentration of **AA-N-Ts** after irradiation may be determined by Beer's Law, where the absorbance at 386 nm was 0.451, ϵ was 19277 and the pathlength was 1.0 cm gave a concentration of **AA-N-Ts** equal to 2.34×10^{-5} M. Calculating the difference in pre- and post-irradiation concentrations of **AA-N-Ts** (8.30×10^{-5} M - 2.34×10^{-5} M) gave a decrease of 5.96×10^{-5} M. Converting this to moles of **AA-N-Ts** reacted was calculated by multiplying the change in concentration by the volume (in L). Thus, 5.96×10^{-5} M x 0.0030 L gave 1.79×10^{-7} moles **AA-N-Ts** reacted. Dividing by the irradiation time (30 s) gave 5.97×10^{-9} moles reacted per s. Quantum yield was then calculated by dividing the moles of **AA-N-Ts** reacted per s by the moles of photons absorbed by **AA-N-Ts** per s:

$$\Phi = \frac{5.97 \times 10^{-9} \text{ moles AA-N-Ts reacted per s}}{9.42 \times 10^{-9} \text{ moles photons absorbed per s}} = 0.63$$

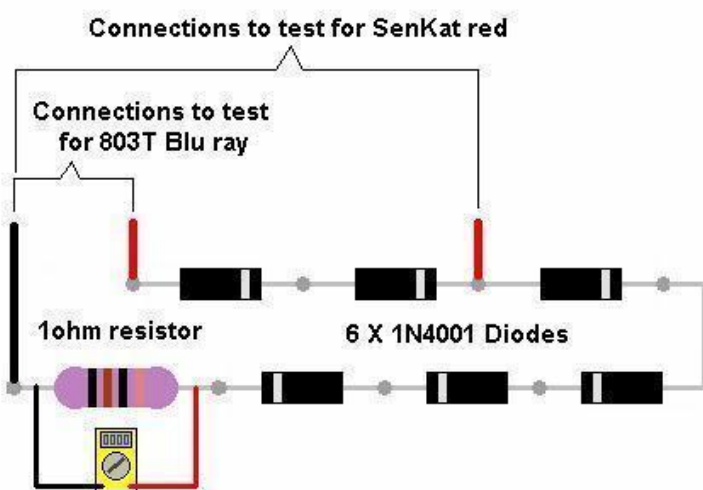
This procedure was repeated three times, giving $\Phi = 0.60 \pm 0.02$.

*CAUTION – the reader attempts the following at their own risk. The device described is capable of burning unprotected skin, and direct eye exposure will result in instantaneous and

permanent blindness. Appropriate eye protection is an absolute requirement. The light source for the actinometry experiments (a 405 nm GaN diode laser) was assembled on Veroboard according to the following schematic:



A dummy load must also be constructed to test the current output of the driver. The 1N4001 diodes are heat sensitive, and if soldering them in place on Veroboard, it is imperative to protect them with a heat sink (large alligator clips work well). The easiest way is to assemble the device on a breadboard. The construction of the dummy load is based on the following schematic:



Drive circuit test load for Red and Blu ray laser diodes

Connect to driver circuit where the laser diode will go.
Measure mv across resistor which gives you drive current in ma

The diode used was a PHR-803T (from a Blu-ray player) press-fitted into an AixiZ module with a focusable, collimating acrylic lens. Power at the driver was adjusted to an output of 50 mA, which is estimated to result in a net output of 20 mW.

[Figures 1.4.7.-1.4.10. Arc lamp photoconversions of AA-N-Ts to AA-Q-Ts with irradiation >400 nm in various deaerated solvents at 5.0×10^{-5} M]

In each case, **AA-N-Ts** (2.7 mg, 5.0×10^{-6} mol) was dissolved in the corresponding solvent to 10.0 mL in a volumetric flask to give a 5.0×10^{-4} M solution. A 500 μL gas-tight syringe was used to transfer 1.0 mL of the **AA-N-Ts** solution to an empty 10.0 mL volumetric flask. This flask was filled to the mark with solvent to give a 5.0×10^{-5} M solution. The solution (3.0 mL) was placed in a quartz cuvette and the optical spectrum was measured. The sample was then irradiated with the 500 W Hg-Xe arc lamp behind an Oriel cut-off filter 59480 (400 nm) and a water-filled quartz cylinder (to absorb IR). Subsequent optical spectra were measured at time intervals which varied between the solvents tested

[Figure 1.6.1. Solar/arc lamp photoconversion of PD-N-Ts to PD-Q-Ts (5.0×10^{-5} M in benzene)]

PD-N-Ts (3.7 mg, 5.0×10^{-6} mol) was dissolved in benzene to 10.0 mL in a volumetric flask to give a 5.0×10^{-4} M solution. A 500 μ L gas-tight syringe was used to transfer 1.0 mL of the **PD-N-Ts** solution to an empty 10.0 mL volumetric flask. This flask was filled to the mark with benzene to give a 5.0×10^{-5} M solution. The solution (3.0 mL) was placed in a quartz cuvette and the optical spectrum was measured. The cuvette was set in a windowsill, exposing the sample to indirect sunlight. Subsequent optical spectra were measured after 30, 60, 90, 120, and 150 s total irradiation time. At this point, the reaction appeared to have reached a photostationary state, so the sample was irradiated with the 500 W Hg-Xe arc lamp behind an Oriel 59480 cut-off filter (400 nm) and water-filled quartz cylinder (to absorb IR). Subsequent optical spectra were measured after 60, 120, 180, and 240 s total arc lamp irradiation time. The sample was placed in a dark cabinet, and a final optical spectrum was measured after 1.5 h.

[Figure 1.9.1. Optical spectra of AA-N-Ns and AA-N-Ts (5.0×10^{-5} M in benzene)]

AA-N-Ns (2.9 mg, 5.0×10^{-6} mol) was dissolved in benzene to 10.0 mL in a volumetric flask to give a 5.0×10^{-4} M solution. A 500 μ L gas-tight syringe was used to transfer 1.0 mL of the **AA-N-Ns** solution to an empty 10.0 mL volumetric flask. This flask was filled to the mark with benzene to give a 5.0×10^{-5} M solution. The solution (3.0 mL) was placed in a quartz cuvette and the optical spectrum was measured and overlaid with a previously measured spectrum of **AA-N-Ts** at the same concentration.

[Figure 1.9.2. Arc lamp photoconversion of AA-N-Ns with irradiation >455 nm in deaerated benzene at 5.0×10^{-5} M]

AA-N-Ns (2.9 mg, 5.0×10^{-6} mol) was dissolved in benzene to 10.0 mL in a volumetric flask to give a 5.0×10^{-4} M solution. A 500 μ L gas-tight syringe was used to transfer 1.0 mL of the AA-N-Ns solution to an empty 10.0 mL volumetric flask. This flask was filled to the mark with benzene to give a 5.0×10^{-5} M solution. The solution (3.0 mL) was placed in a quartz cuvette and the optical spectrum was measured. The sample was irradiated with the 500 W Hg-Xe arc lamp behind an Oriel 51484 cut-off filter (455 nm) and water-filled quartz cylinder (to absorb IR). A subsequent optical spectrum was measured after 5 min irradiation time.

Electrochemical and Redox Experiments

[Figures 1.3.2. and 1.3.3. Cyclic voltammograms of AA-N-Ts and PD-N-Ts - 1.0 mM in dichloromethane (0.1 M TBABF₄) at 20 mV/s scan rate]

In each case, TBABF₄ (0.823 g, 2.50 mmol) was dissolved in freshly distilled methylene chloride to 25.0 mL in a volumetric flask to give a 0.100 M solution. An amount (8.0 mL) of this solution was placed in a four-neck electrochemical cell with a magnetic stir bar. A blank CV scan (0.0 to 1.2 V vs SCE, 20 mV/s) was measured to ensure that no trace impurities existed in the solution as prepared. An amount of AA-N-Ts (4.4 mg, 8.0×10^{-6} mol) or PD-N-Ts (6.0 mg, 8.0×10^{-6} mol) which would give a 1.0 mM solution was added to and thoroughly dissolved in the electrolyte solution. The potential was scanned from 0.0 to 1.2 V vs SCE at a rate of 20 mV/s.

[Figure 1.5.1. AA-Q-Ts (1.0 mM in benzene) to AA-N-Ts by RA catalysis with Orange CRET (0.1 mol%) – Aliquots removed and diluted to 5.0×10^{-5} M for UV-vis]

AA-N-Ts (2.7 mg, 5.0×10^{-6} mol) was dissolved in benzene (5.0 mL) to give a 1.0 mM solution. The solution was placed in a vial and purged with N₂ for 5 min. A 150 µL aliquot was removed and diluted to 3.0 mL to give a 5.0×10^{-5} M solution. The optical spectrum was measured. The 1.0 mM solution was irradiated with a 500 W Hg-Xe arc lamp with an Oriel 59480 cut-off filter (400 nm) and water-filled quartz cylinder (to absorb IR) for 4 min (until the yellow color bleached). A 150 µL aliquot was removed, diluted to 3.0 mL and measured by UV-vis. At this point, full conversion to **AA-Q-Ts** had been attained. Orange CRET (0.30 mg, 5.0×10^{-7} mol) was dissolved to 1.0 mL in methylene chloride to give a 5.0×10^{-4} M solution. A 10 µL portion of this (0.10 mol%) was added to the 1.0 mM **AA-N-Ts** solution and the vial was shaken for several seconds to ensure thorough mixing. A 150 µL aliquot was removed, diluted to 3.0 mL, and measured by UV-vis 30 s after addition of the Orange CRET solution. Partial conversion to **AA-N-Ts** was observed. A 150 µL aliquot was removed, diluted to 3.0 mL and measured by UV-vis 15 min after addition of the Orange CRET solution. At this point, full conversion to **AA-N-Ts** was observed.

[Figure 1.5.3. AA-Q-Ts to AA-N-Ts (5.0×10^{-5} M in benzene) RA catalysis with Orange CRET (5.0 mol%)]

AA-N-Ts (2.7 mg, 5.0×10^{-6} mol) was dissolved in benzene to 10.0 mL in a volumetric flask to give a 5.0×10^{-4} M solution. A 500 µL gas-tight syringe was used to transfer 1.0 mL of the **AA-N-Ts** solution to an empty 10.0 mL volumetric flask. This flask was filled to the mark with benzene to give a 5.0×10^{-5} M solution. The solution (3.0 mL) was placed in a quartz cuvette and the optical spectrum was measured. The cuvette was set in a windowsill, exposing the sample to indirect sunlight. Subsequent optical spectra were measured after 30, 60, 90, 120, 150, and 180 s

total irradiation time. By this point, full conversion to **AA-Q-Ts** had been attained. Orange CRET (1.51 mg, 2.50×10^{-6} mol) was dissolved to 1.0 mL in methylene chloride to give a 1.65 mM solution. A 3.0 μ L portion of this (5.0 mol%) was added to the **AA-Q-Ts** solution and the cuvette was shaken for several seconds to ensure thorough mixing. Subsequent optical spectra were measured at 10, 60, and 120 s after addition of the Orange CRET solution. Full conversion to **AA-N-Ts** had been achieved by time 10 s, and no further change was observed at longer times.

[**Figures 1.5.4. and 1.5.5. Optical spectra of the AA-Q-Ts CV sample before and after four scans (diluted x100 in benzene) demonstrating complete conversion to AA-N-Ts]**

TBABF₄ (0.823 g, 2.50 mmol) was dissolved in freshly distilled methylene chloride to 25.0 mL in a volumetric flask to give a 0.100 M solution. An amount (8.0 mL) of this solution was placed in a four-neck electrochemical cell with a magnetic stir bar. A blank CV scan (0.0 to 1.2 V vs SCE, 20 mV/s) was measured to ensure that no trace impurities existed in the solution as prepared. **AA-Q-Ts** (4.4 mg, 8.0×10^{-6} mol) was added to and thoroughly dissolved in the electrolyte solution. Before any potential was applied, a 30 μ L aliquot of the **AA-Q-Ts** sample was removed and diluted to 3.0 mL in benzene. The optical spectrum was measured, and confirmed the sample to be **AA-Q-Ts**. Four CV measurements were made; the potential was scanned from 0.0 to 1.2 V vs SCE at rates of 20 mV/s, 100 mV/s, 200 mV/s, and again at 20 mV/s. Over the course of the four scans, a total time of ~10 min elapsed. The CV sample was stirred between scans. A 30 μ L aliquot was removed immediately after the four CV measurements and diluted to 3.0 mL in benzene. The optical spectrum was again measured, and showed that the bulk CV sample had fully converted to **AA-N-Ts**.

[Figure 1.6.4. PD-Q-Ts (5.0×10^{-5} M in benzene) to PD-N-Ts RA catalysis with Orange CRET (0.1 mol%)

PD-N-Ts (3.7 mg, 5.0×10^{-6} mol) was dissolved in benzene to 10.0 mL in a volumetric flask to give a 5.0×10^{-4} M solution. A 500 μ L gas-tight syringe was used to transfer 1.0 mL of the **PD-N-Ts** solution to an empty 10.0 mL volumetric flask. This flask was filled to the mark with benzene to give a 5.0×10^{-5} M solution. The solution (3.0 mL) was placed in a quartz cuvette and the optical spectrum was measured. The sample was irradiated with a 500 W Hg-Xe arc lamp behind an Oriel 59480 cut-off filter (400 nm) and water-filled quartz cylinder (to absorb IR). A subsequent optical spectrum was measured at after 150 s total irradiation time. Orange CRET (1.00 mg, 1.65×10^{-6} mol) was diluted to 10.0 mL in methylene chloride to give a 0.165 mM solution. A 0.90 μ L portion of this (0.1 mol%) was added to the **PD-Q-Ts** solution and the cuvette was shaken for several seconds to ensure thorough mixing. Subsequent optical spectra were measured at 5 and 30 s after addition of the Orange CRET solution.

[Figures 1.8.1. and 1.8.3. Cyclic voltammograms of 4-BrPh-N-Ts and Ph-N-Ac - 1.0 mM in dichloromethane (0.1 M TBABF₄) at 20 mV/s scan rate]

In each case, TBABF₄ (0.823 g, 2.50 mmol) was dissolved in freshly distilled methylene chloride to 25.0 mL in a volumetric flask to give a 0.100 M solution. An amount (8.0 mL) of this solution was placed in a four-neck electrochemical cell with a magnetic stir bar. A blank CV scan (0.0 to 1.8 V vs SCE, 20 mV/s) was measured to ensure that no trace impurities existed in the solution as prepared. An amount of **4-BrPh-N-Ts** (3.2 mg, 8.0×10^{-6} mol) or **Ph-N-Ac** (1.7 mg, 8.0×10^{-6}

mol) which would give a 1.0 mM solution was added to and thoroughly dissolved in the electrolyte solution. The potential was scanned from 0.0 to 1.8 V vs SCE at a rate of 20 mV/s.

[Figure 1.8.2. 4-BrPh-Q-Ts (1.2×10^{-4} M in benzene) oxidation with Orange CRET (5.0 mol%)]

An amount of **4-BrPh-N-Ts** (1.20 mg, 2.99×10^{-6} mol) was dissolved in benzene to 25.0 mL in a volumetric flask to give a 1.20×10^{-4} M solution. The solution (3.0 mL) was placed in a quartz cuvette and the optical spectrum was measured. The sample was irradiated with a 500 W Hg-Xe arc lamp behind a water-filled quartz cylinder (to absorb IR). A subsequent optical spectrum was measured after 5 min total irradiation time which indicated complete conversion to **4-BrPh-Q-Ts**. Orange CRET (1.00 mg, 1.65×10^{-6} mol) was diluted to 1.0 mL methylene chloride to give a 1.65 mM solution. A 10.8 μ L portion of this (5.0 mol%) was added to the **4-BrPh-Q-Ts** solution and the cuvette was shaken for several seconds to ensure thorough mixing. Subsequent optical spectra were measured at 10 and 60 s after addition of the Orange CRET solution.

[Figure 1.8.4. Ph-Q-Ac (1.3×10^{-4} M in benzene) oxidation with Orange CRET (5.0 mol%)]

Ph-N-Ac (1.38 mg, 6.56×10^{-6} mol) was dissolved in benzene to 10.0 mL in a volumetric flask to give a 6.56×10^{-4} M solution. A 500 μ L gas-tight syringe was used to transfer 2.0 mL of the **Ph-N-Ac** solution to an empty 10.0 mL volumetric flask. This flask was filled to the mark with benzene to give a 1.31×10^{-4} M solution. The solution (3.0 mL) was placed in a quartz cuvette and the optical spectrum was measured. The sample was irradiated with a 500 W Hg-Xe arc lamp behind a water-filled quartz cylinder (to absorb IR). A subsequent optical spectrum was measured after 7 min total irradiation time which indicated complete conversion to **Ph-Q-Ac**.

Orange CRET (1.00 mg, 1.65×10^{-6} mol) was diluted to 1.0 mL methylene chloride to give a 1.65 mM solution. An 11.9 μ L portion of this (5.0 mol%) was added to the **Ph-Q-Ac** solution and the cuvette was shaken for several seconds to ensure thorough mixing. Subsequent optical spectra were measured at 10 and 60 s after addition of the Orange CRET solution.

Thermal Conversion Experiments

[Figure 1.5.2. Thermal conversion of AA-Q-Ts to AA-N-Ts (13 mM in benzene) at rt monitored by $^1\text{H-NMR}$]

AA-N-Ts (5.5 mg, 1.0×10^{-5} mol) was dissolved in 0.75 mL C_6D_6 in an NMR tube and the $^1\text{H-NMR}$ was measured. The tube was connected to a high vacuum manifold using a Cajon coupling. The sample was frozen with liquid nitrogen, and then vacuum was applied. When the pump reached ultimate vacuum (~0.05 Torr), the vacuum valve was closed at the manifold. The liquid nitrogen was then removed and the sample allowed to thaw. This thawing was accompanied by a noticeable amount of gas evolution. This completed one freeze-pump-thaw cycle, a process which was repeated twice more. By the end of the third and final cycle, no gas evolution could be observed, and the sample was determined to be thoroughly degassed. At this point, the sample was frozen once more, and vacuum was reapplied. The vacuum was not turned off at the manifold this time; the pump was allowed to pull an active vacuum on the frozen solution during the flame-sealing process. The sample was sealed by slowly and evenly heating the wall of the tube around its circumference using a propane torch until the sides eventually collapsed fully inward, being pulled by the applied vacuum. The tube was then heated at the sealed juncture and gently pulled until the molten glass separated. The sample was irradiated for 3 min with a 500 W Hg-Xe arc lamp behind an Oriel 51472 (400 nm) cut-off filter and water-

filled quartz cylinder (to absorb IR). A $^1\text{H-NMR}$ measurement indicated 97 % conversion to **AA-Q-Ts**. The sample was stored in a dark cabinet at $\sim 20^\circ\text{C}$. Subsequent $^1\text{H-NMR}$ measurements at various time intervals over 312 h were made.

[Figure 1.6.3. Thermal conversion of PD-Q-Ts to PD-N-Ts (13 mM in benzene) at rt monitored by $^1\text{H-NMR}$]

PD-N-Ts (7.5 mg, 1.0×10^{-5} mol) was dissolved in 0.75 mL C_6D_6 in an NMR tube and the $^1\text{H-NMR}$ was measured. The tube was connected to a high vacuum manifold using a Cajon coupling. The sample was frozen with liquid nitrogen, and then vacuum was applied. When the pump reached ultimate vacuum (~ 0.05 Torr), the vacuum valve was closed at the manifold. The liquid nitrogen was then removed and the sample allowed to thaw. This thawing was accompanied by a noticeable amount of gas evolution. This completed one freeze-pump-thaw cycle, a process which was repeated twice more. By the end of the third and final cycle, no gas evolution could be observed, and the sample was determined to be thoroughly degassed. At this point, the sample was frozen once more, and vacuum was reapplied. The vacuum was not turned off at the manifold this time; the pump was allowed to pull an active vacuum on the frozen solution during the flame-sealing process. The sample was sealed by slowly and evenly heating the wall of the tube around its circumference using a propane torch until the sides eventually collapsed fully inward, being pulled by the applied vacuum. The tube was then heated at the sealed juncture and gently pulled until the molten glass separated. The sample was irradiated for 30 min with a 500 W Hg-Xe arc lamp behind an Oriel 51472 (400 nm) cut-off filter and water-filled quartz cylinder (to absorb IR). A $^1\text{H-NMR}$ measurement indicated 79 % conversion to **PD-**

Q-Ts. The sample was stored in a dark cabinet at ~20 °C. Subsequent $^1\text{H-NMR}$ measurements at various time intervals over 312 h were made.

Chapter 2

Crystal Engineering of Polar *m*-Phenylenediamine Derivatives

2.1 Introduction

Crystal engineering⁴⁶⁻⁵⁰ is a subdiscipline of supramolecular chemistry⁵¹⁻⁵⁴ which seeks to understand and apply the intramolecular forces which govern the assembly of molecules in the solid state. By observing crystal packing behavior related to molecular structure, an effort can be made to rationally design solids possessing specifically desired crystalline features. This ability to elucidate, discern, and control the molecular packing of the crystal lattice is of great importance to the areas of medicinal chemistry⁵⁵ and materials science.⁵⁶⁻⁵⁸

Designing crystals with polar order presents a great challenge to the crystal engineer.⁵⁹ In almost all cases, molecules in the solid state will orient themselves in such a way that their dipoles cancel. In the anomalous cases where polar order is observed, there must exist some overriding intermolecular force which supersedes this favorable cancellation of dipoles. It was our goal therefore, through observation of conformations and molecular geometries of organic materials in the solid state, to gain some insight into the requirements for polar order, and to apply the knowledge gained toward the rational design of such solids, which have demonstrated practical applications as NLO materials,^{60,61} piezoelectrics⁶² and ferroelectrics.⁶³

2.2 Introduction to Single Crystal X-ray Diffractometry

Single-crystal X-ray diffractometry (XRD) is perhaps the most valuable tool available to the crystal engineer. Its use is ubiquitous in the field of crystallography – Indeed without it, the crystal engineer would be rendered blind insofar as it pertains to elucidating complex crystal structures. The researcher’s observation would be limited to what may be seen with an optical microscope: namely, physical characteristics (i.e. crystal morphology). While these are important properties with a number of implications, they fall far short of providing the detailed structural information which XRD can establish.

The essential principle by which XRD operates hinges on the ability of electrons to diffract radiation emitted from an X-ray source. All materials absorb X-rays and scatter (diffract) the incident radiation.⁶⁴ As, Ladd and Palmer point out however, the interaction of X-rays with crystalline materials is complex, consisting of two parts. First is a geometrical component which is symmetry-dependent and related to the spatial arrangement of atoms within the unit cell. Secondly, a structural component exists that pertains to the types of atoms in the unit cell as well as their relative positions.

By combining these two components a specific equation for the crystal structure factor can be derived. The equation is deduced in a manner descriptive of the precise coordinates of atoms within the unit cell expressed in terms of Miller indices, which relate the three dimensions of the unit cell in terms of three numbers h , k , and l . A crystal can be categorized in groups relating to symmetry operations across these three faces.⁶⁵ This results in the definition of a point group. There are thirty-two unique point groups, which when combined with the fourteen Bravais lattices give a set of 230 unique space groups. Stout and Jensen note that space groups “describe the only ways in which identical objects can be arranged in an infinite lattice”.

In a practical sense,⁶⁶ the experimental method of performing an XRD analysis begins with growing high-quality crystals of suitable size (0.1-0.5 mm). Typically, this is done in solution, though some compounds crystallize well by sublimation. There are a variety of techniques commonly used to grow crystals from solution including: slow cooling of a saturated solution, slow evaporation, liquid diffusion, and vapor diffusion. When suitable crystals have been grown and a candidate for XRD selected, it should be evaluated using a polarizing stereomicroscope. In this procedure, an optically anisotropic crystal (all with the exception of cubic) is exposed to plane-polarized light and rotated about the microscope stage. A position will be reached where the crystal extinguishes (goes dark), then becomes light again upon further rotation. Optimally, the entire crystal will extinguish at once; if there are multiple crystal domains present, only a portion will extinguish at a given angle.

With a suitable crystal in hand, it is mounted to the goniometer head by means of adhering it to a thin glass fiber or nylon loop using grease or the specially-formulated inert oil “Paratone-N”. The goniometer head with the affixed crystal is then placed on its mount, and the crystal is centered in the X-ray beam. A cone of nitrogen gas may be kept passing over the crystal to cool it to a desired temperature. Data is collected as a series of frames that are recorded as the crystal is moved about four axes of rotation.

The raw data may then be reduced, solved, and refined utilizing a modern X-ray crystallography software package such as Bruker SHELXTL.⁶⁷

2.3 Introduction to Differential Scanning Calorimetry

Whereas XRD can be considered essential to the study of crystals and their properties, differential scanning calorimetry (DSC)⁶⁸ is better thought of as a complimentary technique.

When one desires to determine whether a bulk sample of crystalline material is comprised of a single crystal form or some mixture of polymorphs, DSC can provide the answer. When used in this manner, DSC essentially takes the place of bulk powder XRD, but gives the added benefit of providing valuable data including T_m , T_g , as well as specific heats of fusion.

DSC measures heat flow as a function of temperature. This is accomplished by simultaneously changing the temperature of two DSC “pans” contained within the calorimeter. The DSC pan is a metal (usually aluminum) container which is manufactured to very tight tolerances in order that the difference in mass between pans is negligible. One pan contains the sample material, crimped closed and weighed precisely on a microanalytical balance. The other pan is a reference which is likewise crimped closed, but left empty.

A common DSC experiment is “heat-cool-heat”, which involves equilibrating the sample at a predetermined cool temperature, heating, cooling, and then heating once more, at a constant or varied rate. By cycling the sample in such a way, one may determine the initial crystallinity of the sample, as any amorphous phase or polymorphic species will manifest as changes in heat flow upon reaching T_g or T_m . It may also be determined if the sample decomposes upon melting, recrystallizes as a polymorph from the melt, or re-orders into its original crystal form.

2.4 Introduction to Polar Organic Crystals

A polar crystal is one in which there exists a net alignment of molecular dipoles. Being a vector quantity, the dipoles may align either partially or completely. In the latter case, all dipoles are entirely aligned, creating a uniform anisotropy throughout the crystal lattice. Glaser refers to this as “perfect polar stacking”.⁶⁹ Figure 2.4.1 contrasts the arrangement of molecular dipoles in polar and non-polar crystals.

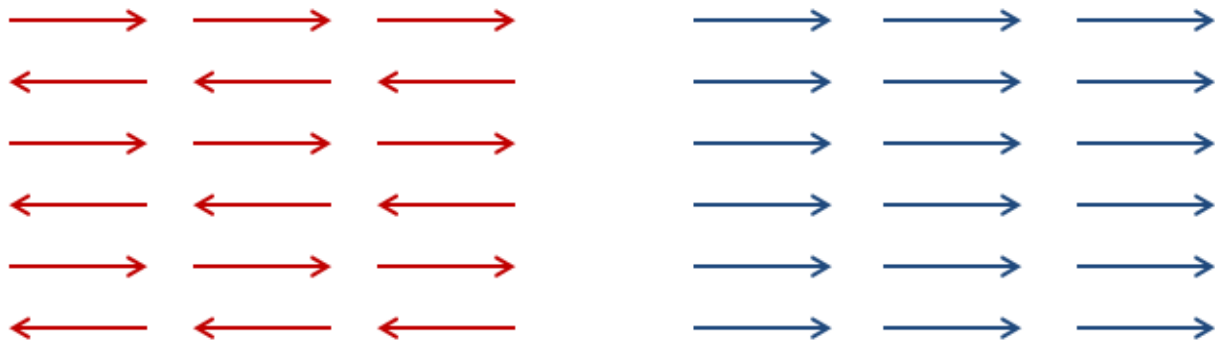
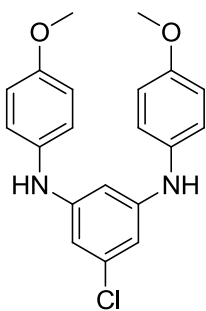


Figure 2.4.1. Molecular dipole orientation in non-polar (red) and polar (blue) crystalline solids

The above figure depicts a two-dimensional layer of molecules within a crystal lattice. It should be pointed out that the net dipole-cancelling configuration of molecular dipoles in a non-polar solid may be, and often is, more complex than that shown in Figure 2.4.1. For example, in some cases the two-dimensional layer may consist of aligned dipoles. However, these layers, when assembled into a three-dimensional structure, will alternate direction resulting in net dipole cancellation.

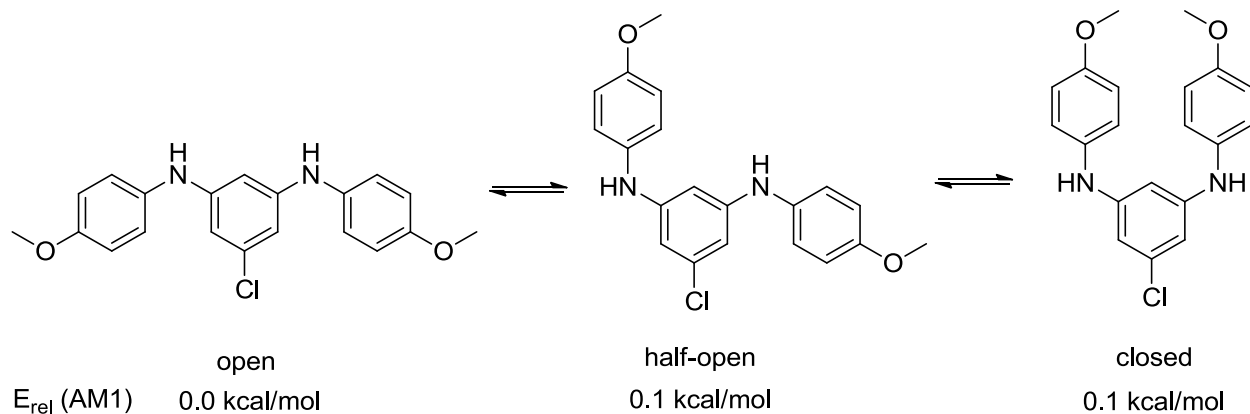
2.5 Polar Order Observed in *m*-Phenylenediamine Derivatives

The first polar *m*-phenylenediamine (*m*PD) derivative was discovered by former group member, J. Richard Duncan while synthesizing a redox-gradient polyarylamine.⁷⁰ He observed during the preparation of the synthetic intermediate **Cl-*m*PD**, that the product spontaneously crystallized and precipitated out of solution. This unusual behavior, not seen in the preparation of similar arylamines, prompted him to isolate single crystals of the material and determine the crystal structure by XRD. The results were quite intriguing; the space group was non-centrosymmetric (monoclinic, Cm) and non-enantiomorphous, indicating a polar crystal.



Cl-mPD

Some years after Duncan's initial result, we chose to revisit this system for an extensive study. AM1 was used to calculate the relative energies of various conformations of the molecule (Scheme 2.5.1). The AM1 calculations demonstrated only very small relative energy differences between conformations, with a slight preference for the "open" form. We would later find this to be of great significance to the molecular conformation assumed within the crystal lattice.

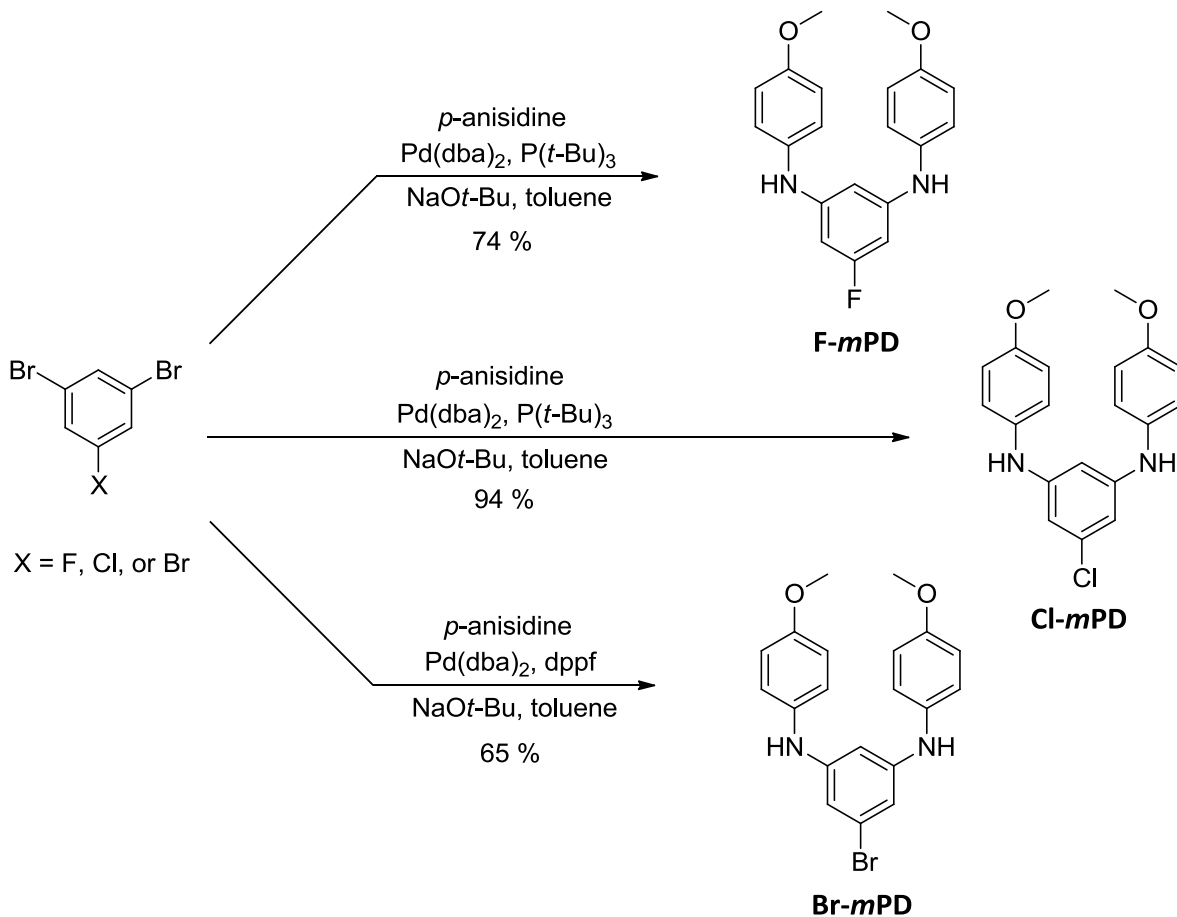


Scheme 2.5.1. AM1-calculated conformational analysis of **Cl-mPD**

We then synthesized a series of *m*PDs and determine their crystal structures. The objective of the synthesis of multiple analogs was to determine whether polar order in the crystal lattice was a feature specific to **Cl-mPD**, or if that order could be preserved when making substitutions on the *m*PD synthon. The most obvious analogs to test this were those derived by substituting other atoms from the halogen series in place of the chlorine at the 5-position. This, we believed would serve a two-fold purpose. First, was a matter of sterics, owing to the wide range in size of the halogen substituents, and second was the degree of electronic perturbation from variation in electronegativity. Also, we envisioned that replacing the oxygen atoms with sulfur would give similar effects, both steric and electronic. The size of the alkyl groups bound to these heavy atoms could be modified as well, providing varying degrees of steric hindrance.

2.6 Synthesis

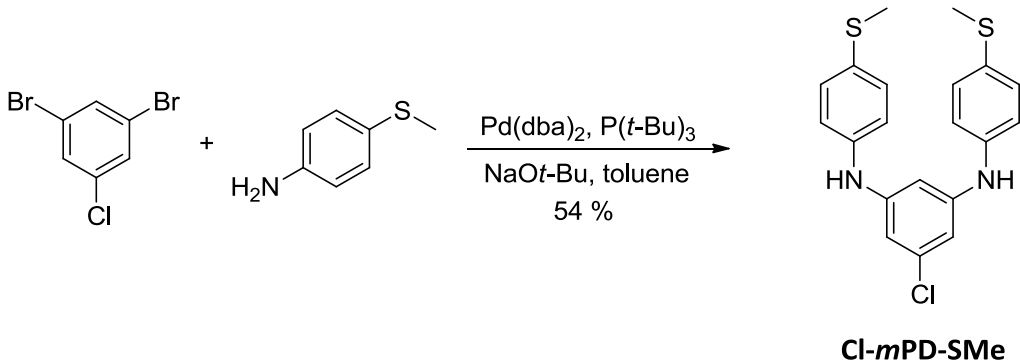
The synthesis of *m*PDs which were ultimately demonstrated by XRD to preferentially crystallize in polar space groups is detailed herein. The parent compound, **Cl-mPD** and its 5-fluoro substituted analog were constructed by reacting the appropriate 1,3,5-trihalobenzene with *p*-anisidine under the protocol of Hartwig et al (Scheme 2.6.1). Tri-*tert*-butylphosphine was the preferred ligand for most substrates due to its broad scope of effectiveness, as well as its ability to facilitate catalysis at room temperature. In the case of the the 5-bromo analog, however, this resulted in over-amination due to the loss of chemoselective control. A solution to this problem was found by employing the less active 1,1'-Bis(diphenylphosphino)ferrocene (dppf) ligand for use with this substrate. The resulting catalytic system offered a more easily controlled reaction which could be modulated to yield the desired *m*PD by carefully controlling the temperature.



Scheme 2.6.1. Synthesis of X-*m*PD compounds

Much effort was made to synthesize the 5-iodo analog, without success. Experimentation involving a multitude of catalyst and ligand systems, bases, solvents, and careful temperature control did not provide an effective method for maintaining chemoselective control. Despite our failure to arrive at the desired product, an improved method for the synthesis of the halide starting material, 1,3,5-triiodobenzene was developed during the course of our research (see appendix).

A sulfur analog, **Cl-*m*PD-Sme**, was synthesized by reacting 1,3-dibromo-5-chlorobenzene with 4-(methylthio)aniline under Hartwig conditions (Scheme 2.6.2).



Scheme 2.6.2. Synthesis of **Cl-*m*PD-SMe**

2.7 Dipole Calculations

Molecular dipole calculations for both the energy-minimized conformations and the crystal conformations were calculated by AM1. To test the accuracy of our calculations, we performed a series of benchmark measurements on a group of small molecules with well-known experimental dipoles (Table 2.7.1). We chose for our benchmark tests molecules which are subunits of the *m*PD analogs. This was done in order to obtain a more relevant set of benchmark numbers for comparison to the *m*PD structures.

Table 2.7.1. AM1 benchmark dipole calculations

Compound	AM1 (Debyes)	EXP. (Debyes)
Anisole	1.25	1.24
Aniline	1.54	1.54
p-Anisidine	1.90	1.82
Fluorobenzene	1.57	1.50
Chlorobenzene	1.31	1.57
Bromobenzene	1.45	1.54

Iodobenzene	1.43	1.43
m-Phenylenediamine	0.77	1.77

It is evident from the data presented in the above table that our AM1 calculations agree reasonably well with the experimental data for subunits of *mPD* analogs. Only in the *mPD* subunit was a marked departure from the experimental dipole moment observed.

Having established the general reliability of our AM1 dipole calculation methods, measurements were made on the polar *mPD* series. Dipole moments calculated for both energy-minimized (E_{\min}) conformations and crystal geometry (XRD) conformations are presented in Figure 2.7.1.

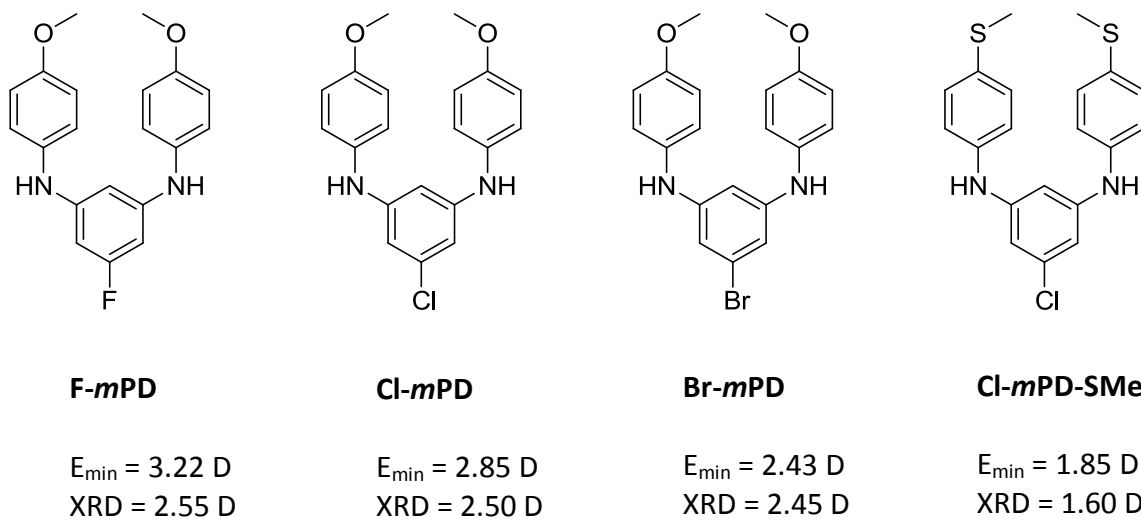


Figure 2.7.1. AM1-calculated dipole moments for polar *mPD* analogs

A discernable trend can be observed in the calculated dipole moments of polar *mPDs*. As expected, the dipole is greatest for **F-*mPD***, and decreases as the electronegativity of the 5-halo substituent decreases. For the sulfur analog, **Cl-*mPD-SMe***, the calculated dipole is significantly

lower than that of its oxy analog. This seems counter-intuitive, as one might expect that the lower electronegativity of sulfur compared to oxygen would lead to a greater net dipole.

There is an obvious discrepancy between the dipole moments calculated from the energy-minimized conformations and those calculated from the conformations observed in the crystal structure. This owes to the fact that the energy-minimized conformation is the “open” form (refer to Scheme 2.5.1), whilst in the crystal lattice, the molecule adopts the “closed” geometry. This will be seen in the following section detailing the crystal packing behavior of polar *m*PD derivatives.

2.8 X-ray Diffractometry

Single-crystal XRD was performed on the aforementioned *m*PD analogs. The pertinent data is summarized below.

Table 2.8.1. Comparative crystal parameters for polar *m*PDs

compound	F- <i>m</i> PD	Cl- <i>m</i> PD	Br- <i>m</i> PD	Cl- <i>m</i> PD-SMe
formula	C ₂₀ H ₁₉ N ₂ O ₂ F	C ₂₀ H ₁₉ N ₂ O ₂ Cl	C ₂₀ H ₁₉ N ₂ O ₂ Br	C ₂₀ H ₁₉ N ₂ S ₂ Cl
FW (g/mol)	338.39	354.84	399.28	386.97
crystallization conditions	slow evaporation from nitromethane	slow evaporation from acetonitrile	slow evaporation from acetonitrile	slow evaporation from ethyl acetate
crystal dimensions (mm)	0.64x0.26x0.16	0.60x0.60x0.42	0.20x0.11x0.10	0.34x0.28x0.10
crystal system	monoclinic	monoclinic	monoclinic	monoclinic
space group	Cm	Cm	Cm	Cc

<i>a</i> (Å)	7.5150(10)	7.4663(8)	7.4852(6)	18.5316(3)
<i>b</i> (Å)	17.187(2)	17.0964(18)	17.0964(18)	7.1762(11)
<i>c</i> (Å)	6.7768(9)	7.0281(7)	7.1322(6)	14.2150(2)
α (deg)	90	90	90	90
β (deg)	113.736(2)	112.206(2)	111.4910(10)	92.166(3)
γ (deg)	90	90	90	90
volume (Å ³)	801.27(19)	830.58(15)	847.69(12)	1889.1(5)
Z	2	2	2	4
D _{calc} (g/cm ³)	1.402	1.419	1.564	1.361
F _{0,0,0}	356	372	408	808
$\square(\text{MoK}\square)$ (mm ⁻¹)	0.099	0.247	2.441	0.428
diffractometer	Siemens	Siemens	Siemens	Siemens
	SMART	SMART	SMART	SMART
wavelength (Å)	0.71073	0.71073	0.71073	0.71073
temp (K)	173	173	173	173
θ range (deg)	3.19-28.18	3.13-28.31	2.39-28.33	2.20-28.35
limiting indices	-9≤h≤7 -22≤k≤22 -7≤l≤8	-9≤h≤8 -19≤k≤22 -8≤l≤9	-9≤h≤7 -22≤k≤22 -8≤l≤9	24≤h≤23 -9≤k≤9 -18≤l≤15
reflections total	2747	3316	2878	6167
reflections unique	976	1659	1394	3707
	(R _{int} =0.0130)	(R _{int} =0.0124)	(R _{int} =0.0184)	(R _{int} =0.0222)
decay correction	none	none	none	none

absorption correction	none	none	none	none
data/restraints/parameters	976/2/120	1659/2/119	1394/2/148	3707/2/229
secondary extinction coef	0.039(5)	0.010(2)	0.015(7)	0.0002(3)
GOF on F ²	1.086	1.072	1.071	1.130
R ₁ [I>2σ(I)]	0.0270	0.0238	0.0187	0.0448
wR ₂ [I>2σ(I)]	0.0835	0.0657	0.0451	0.1037
R ₁ [all data]	0.0271	0.0243	0.0190	0.0542
wR ₂ [all data]	0.0835	0.0661	0.0452	0.1072
Δ(□) (e Å ³)	0.223, -0.157	0.211, -0.168	0.395, -0.256	0.226, -0.260

All analogs of this series are monoclinic crystal systems. Three of the four compounds are of the non-centrosymmetric Cm space group, with **Cl-mPD-SMe** belonging to the similar Cc space group. The quality of the crystals analyzed by XRD was quite high, as indicated by the low R-values. R₁ across all data points was well under 3.0 % for all crystals except for **Cl-mPD-SMe**, which nevertheless demonstrated a respectable value of 5.4 %. Goodness-of-fit (an indicator as to the extent of agreement between the collected data and the solved structure) was close to the optimal value of unity in each case.

Non-centrosymmetric mPDs are comprised of dipolar layers of two-dimensional, hydrogen-bonded arrays (Figure 2.8.1). The N-H---O hydrogen bonds are shown above (black dashed lines) along with Cl---MeO close contacts (green dashed lines). It can be seen that each molecule orders itself within the two dimensional plane in the (slightly) higher relative energy “closed” conformation, where it can act as both an H-bond donor and acceptor to the adjacent molecules. This conformation also allows results in a close contact between the chlorine atom

and the methoxy-group carbons of the neighboring molecule. It is unclear however, whether this halogen interaction is favorable or if the close contact is forced by the H-bonding geometries. In either case, it seems evident that the Chlorine atom serves as “space filler”, occupying the void between the tri-substituted phenyl ring and the methoxy groups created by the closed conformation. Figure 2.8.1 also lists the N-H--O and Cl--MeO close contact distances relative to the (Bondi) van der Waals radii.⁷¹

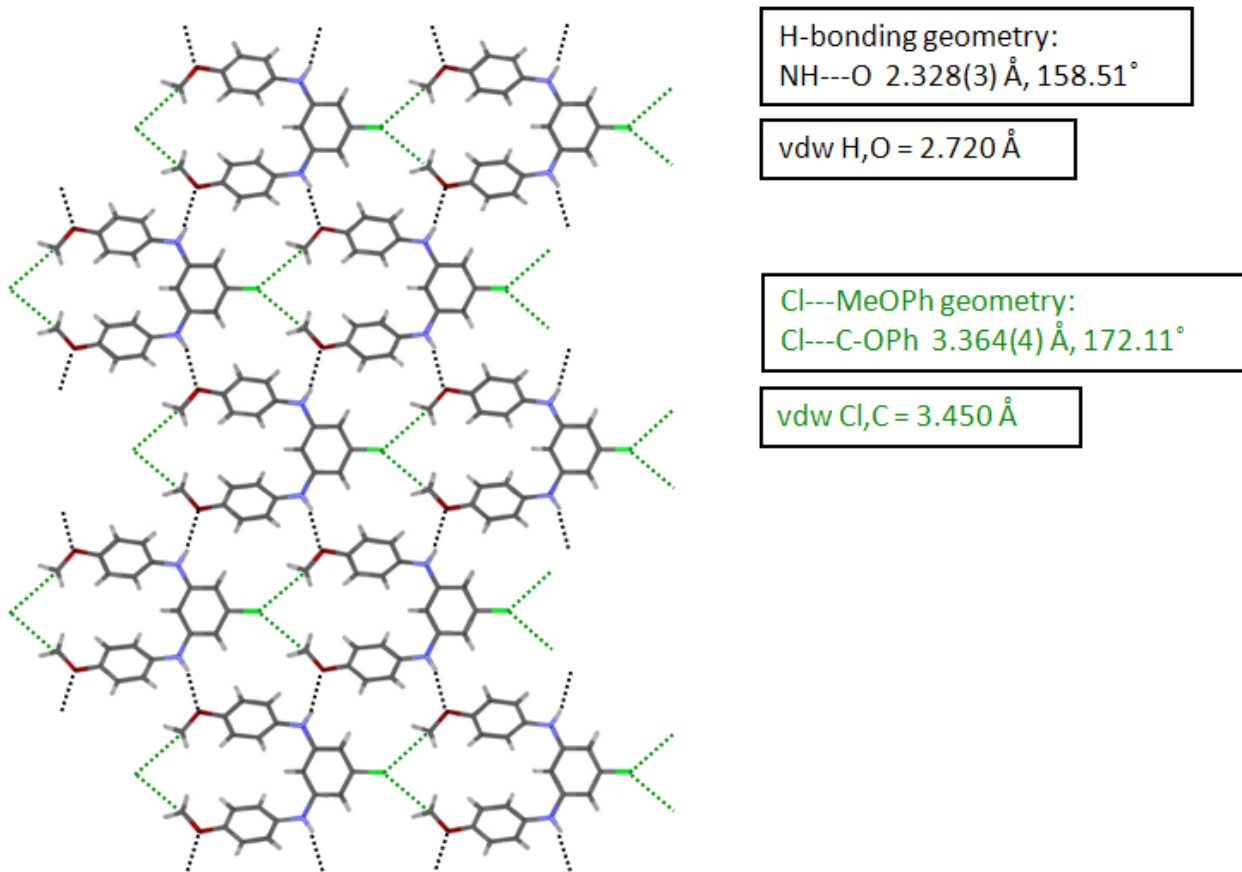


Figure 2.8.1. Two-dimensional plane of the **Cl-mPD** lattice depicting close contacts

Three-dimensional stacking consists of nested layers (Figure 2.8.2) whereby molecular dipoles are aligned and staggered. It is postulated that this stacking arrangement is preferred due to C-H--pi herringbone interactions. The herringbone interactions lend greater attractive force between molecules, and hence added stability to the crystal lattice. Though the staggered

arrangement between layers is not readily apparent in Figure 2.8.2, when a section of two layers is viewed with each layer represented by a contrasting color scheme (Figure 2.8.3), the orientation of the layers

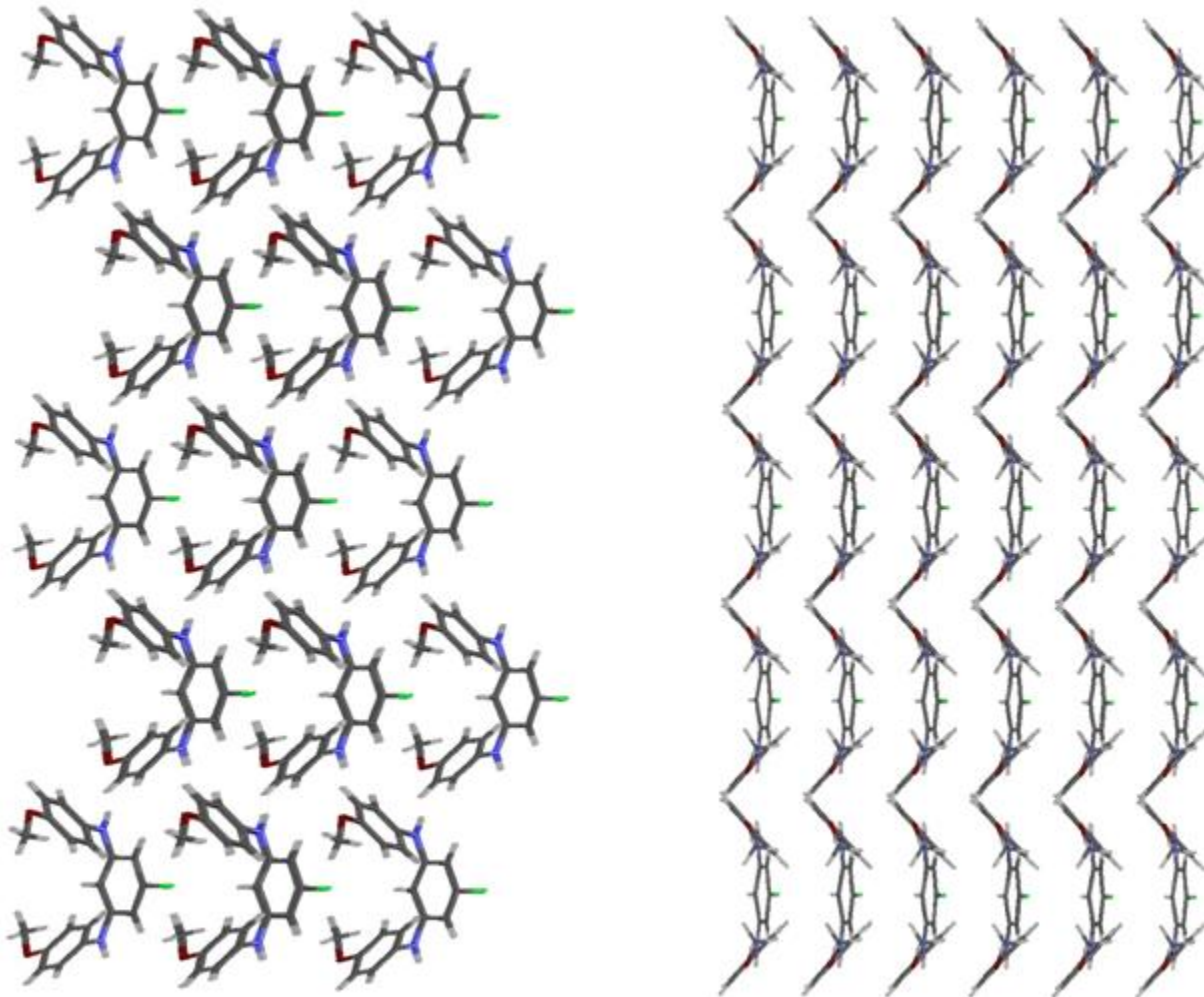


Figure 2.8.2. Two-dimensional layer and nested layers of **Cl-mPD**

Though the staggered arrangement between layers is not readily apparent when viewed through the long axis of the lattice as depicted in Figure 2.8.2, when a section of two layers is viewed, with each layer represented by a contrasting color scheme (Figure 2.8.3), the orientation of the layers can easily be seen. If the layers are superimposed atop one another in a manner in

which the dipoles cancel, it can be envisioned that this favorable interaction is lost. Therefore, ordering in which layers stack anti-parallel are not observed.

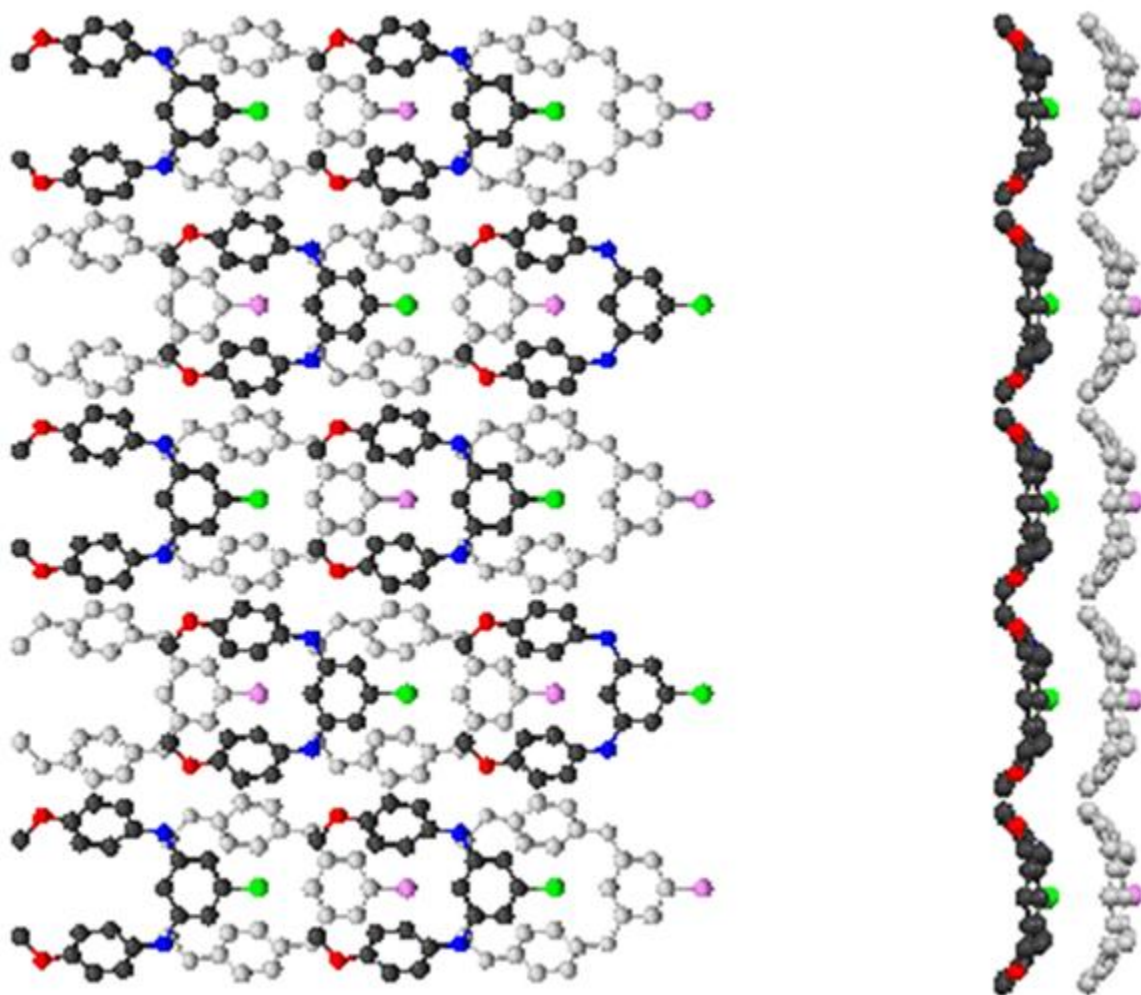


Figure 2.8.3. Color-contrasted representation of layer stacking in **Cl-*m*PD**

It is possible to explain the alignment of dipoles, which is generally an unfavorable arrangement, by comparing the spacing of dipoles across two layers of the crystal lattice (Figure 2.8.4). Between two layers, there are two dipole interactions and spacings to consider. The first is a favorable head-to-tail spacing which runs along the dipolar axis of the crystal. Second, there is a lateral head-to-head spacing between molecules perpendicular to the dipolar axis. If the relative distances between the two interactions are compared, it is evident that the favorable interaction is

much closer in space than is the unfavorable interaction. The net result is an increase in stability which allows the molecules to orient themselves in a dipolar arrangement with a mitigated energy penalty.

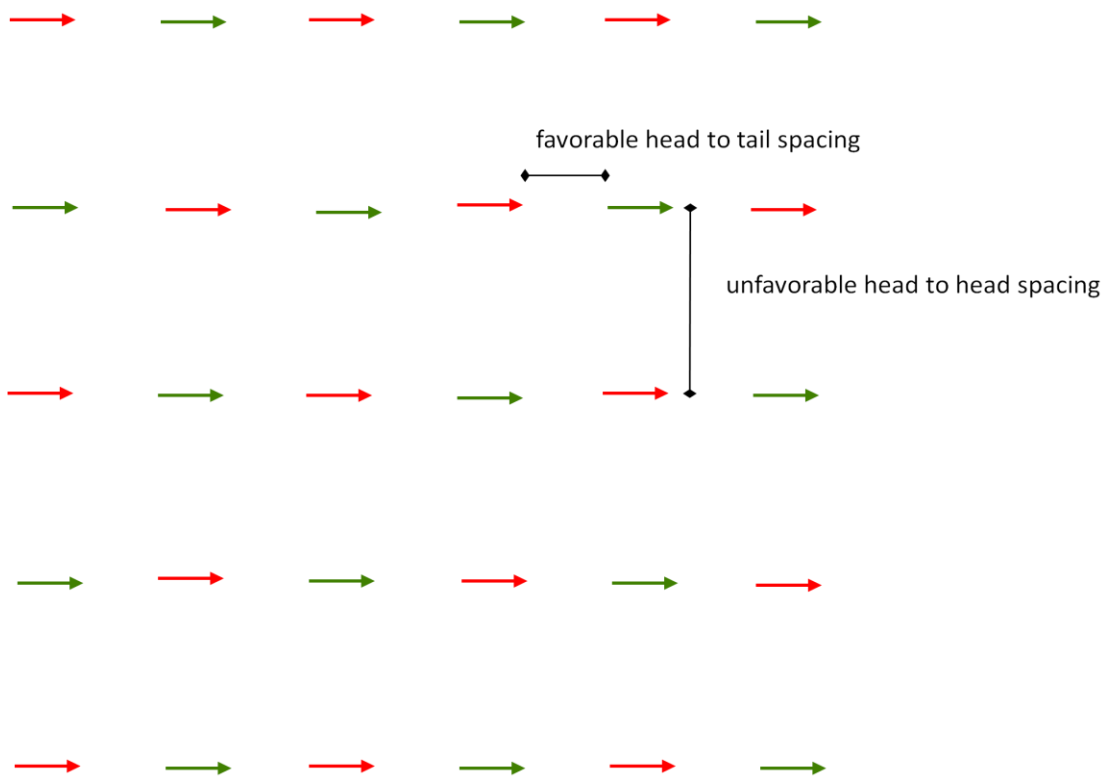


Figure 2.8.4. Interlayer molecular dipole interactions and relative distances

Packing diagrams are shown below (Figure 2.8.5-8) for all polar analogs. **F-mPD**, **Cl-mPD**, and **Br-mPD** are identical crystal systems and space groups (monoclinic, Cm). **Cl-mPD-SMe** is of the similar Cc space group.

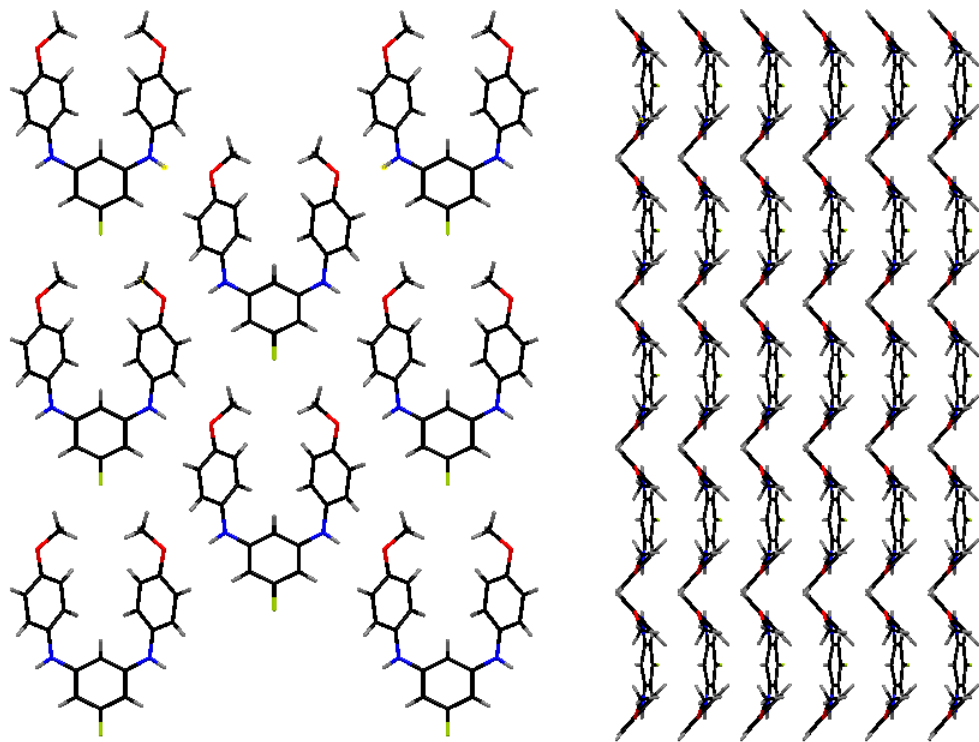


Figure 2.8.5. F-*m*PD crystal packing diagram

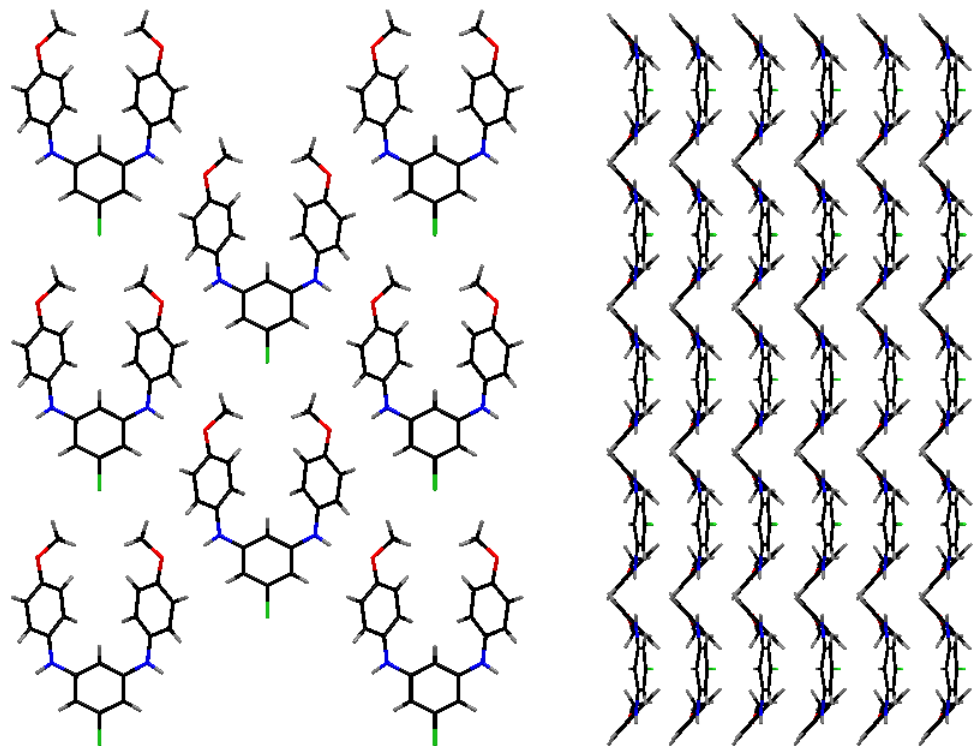


Figure 2.8.6. Cl-*m*PD crystal packing diagram

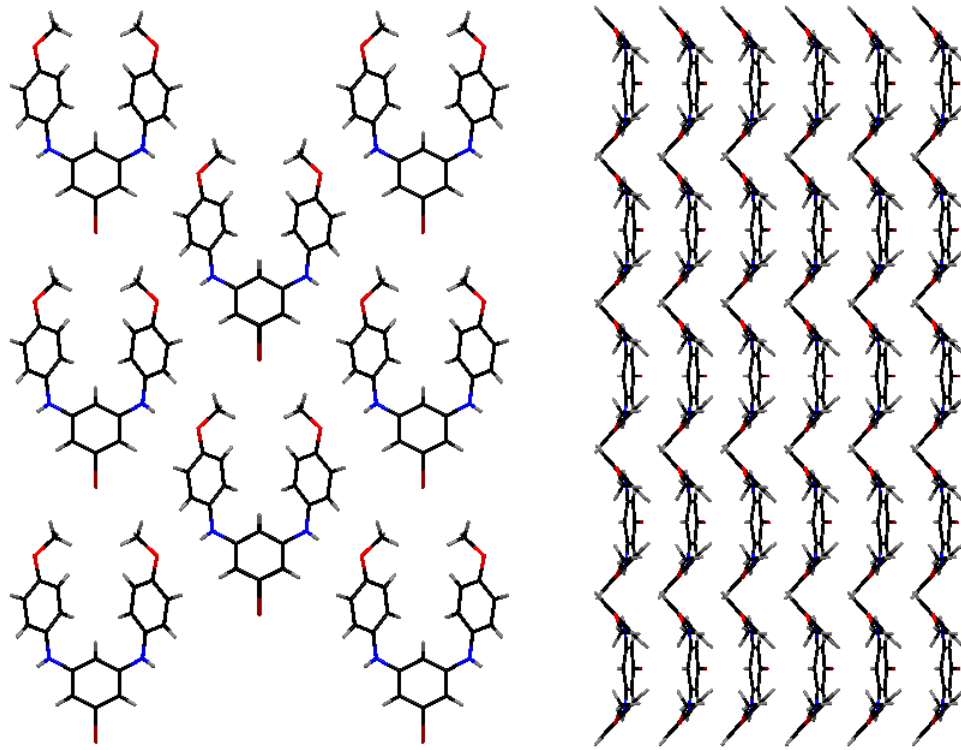


Figure 2.8.7. Br-*m*PD crystal packing diagram

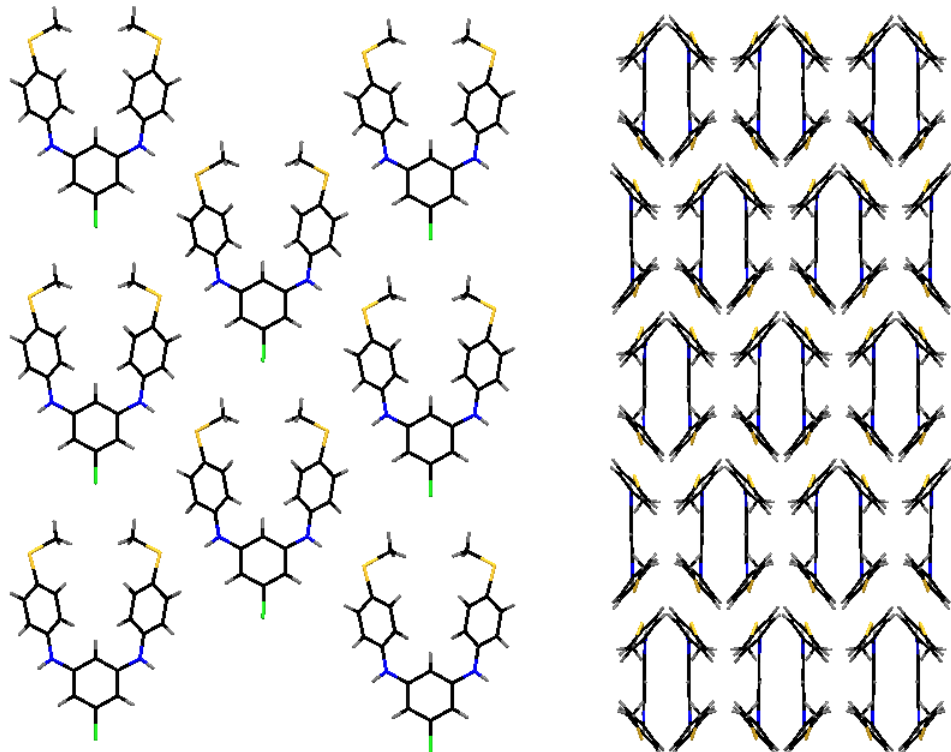


Figure 2.8.8. Cl-*m*PD-SMe crystal packing diagram

The fact that **F-mPD**, **Cl-mPD**, and **Br-mPD** maintain identical crystal structures is quite remarkable. The sensitivity toward steric and electronic perturbation of these molecules is evidently quite low, as large modifications to both are made via substitution of various halogens at the 5-position. This series of *m*PD derivatives strongly resists attempts to influence self-assembly away from the observed packing motif. Substituting oxygen with sulfur is successful to a point, though polar order is maintained, as well as the familiar two-dimensional H-bonded arrays. The difference in packing behavior, seen in Scheme 2.8.8., is confined simply to an alternation in twisting of the peripheral aryl groups.

2.9 Differential Scanning Calorimetry

All compounds were analyzed by DSC to discern the presence of multiple crystal forms in the bulk sample. Of particular interest to us was the possibility of non-polar polymorphs, as many attempts had been made through various methods of crystallization techniques in an effort to produce polymorphic species, but to no avail. This behavior is unusual, as changes in crystallization conditions, particularly solvent systems,^{72,73} are generally noted to result, at least to some extent, in alterations of the crystal system or space group. As expected,⁷⁴ solvent changes did markedly effect crystal morphology.

Table 2.9.1. DSC data for polar *m*PDs

Compound	ΔH_{fus} (kJ/mol)	ΔH_{fus} (J/g)	T_m (°C)	T_g (°C)
F-mPD	55.94	165.3	160.31	5
Cl-mPD	54.33	153.1	178.74	none observed
Br-mPD	50.07	125.4	173.22	15
Cl-mPD-SMe	59.75, 43.77 ^a	154.4, 113.1 ^a	148.73, 116.31 ^a	7

From the data presented in Table 2.9.1, a trend can be discerned in specific heat of fusion, with values decreasing as the size of the 5-halo substituent increases. A glass transition is observed for all analogs with the exception of **Cl-mPD**. This result is not surprising given the strong propensity for crystallization demonstrated by this compound. The most striking data to us however, was the behavior observed in the case of **Cl-mPD-SMe**, where two crystal forms are observed.

DSC heat-cool-heat traces are given in Figures 2.9.1-4. In all cases, the sample was equilibrated at -70 °C, heated to 200 °C, cooled to -70 °C, and then reheated to 200 °C. The rate of temperature change was maintained at 10 °C/min during the cycle. On the DSC traces, endotherms are indicated by negative values, while exotherms are positive.

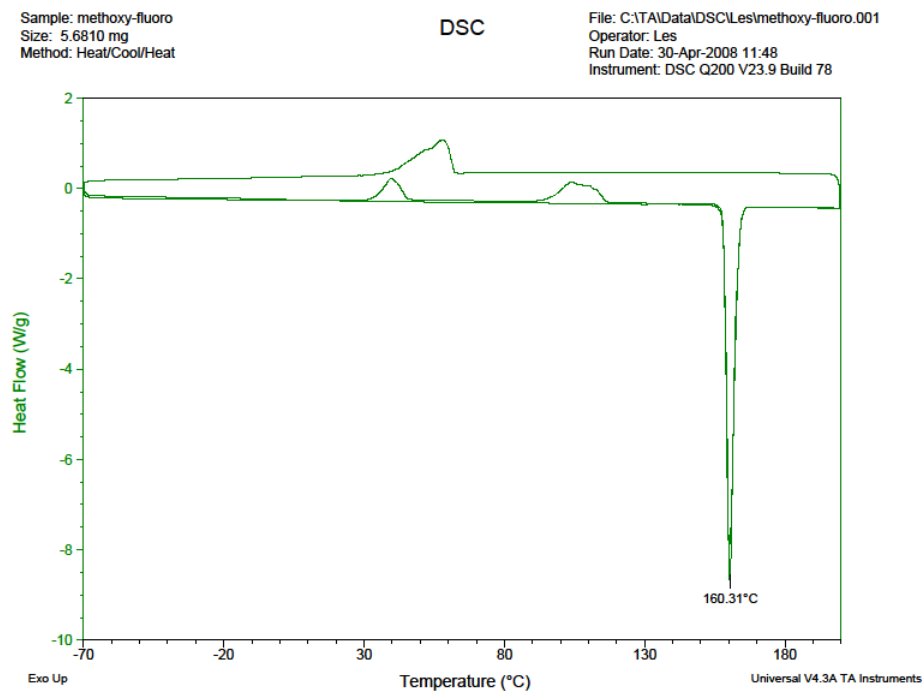


Figure 2.9.1. DSC trace of **F-mPD**

Sample: methoxy-chloro
Size: 5.8060 mg
Method: Heat/Cool/Heat

DSC

File: C:\TA\Data\DSCI\Les\methoxy-chloro.001
Operator: Les
Run Date: 30-Apr-2008 13:33
Instrument: DSC Q200 V23.9 Build 78

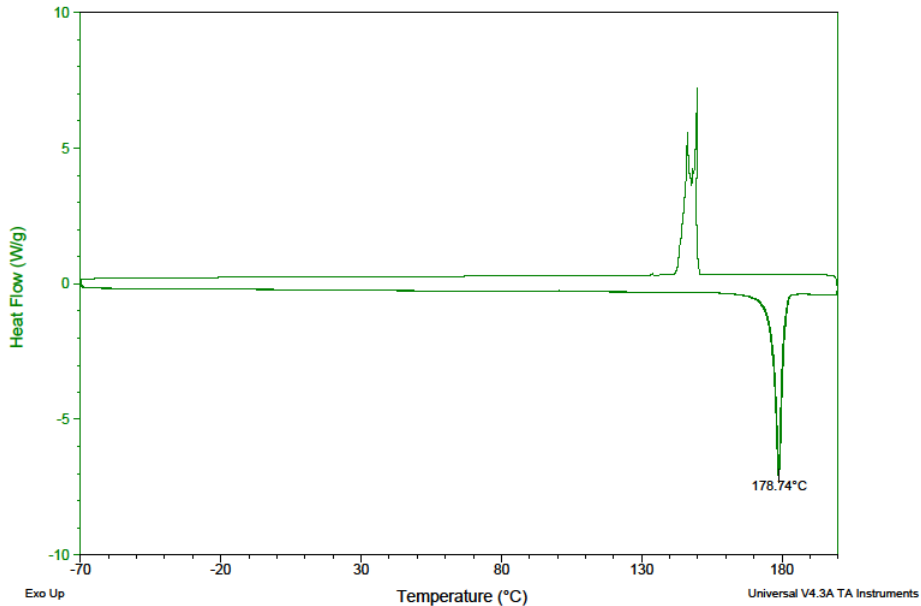


Figure 2.9.2. DSC trace of **Cl-*m*PD**

Sample: methoxy-bromo
Size: 3.7290 mg
Method: Heat/Cool/Heat

DSC

File: C:\TA\Data\DSCI\Les\methoxy-bromo.001
Operator: Les
Run Date: 30-Apr-2008 15:32
Instrument: DSC Q200 V23.9 Build 78

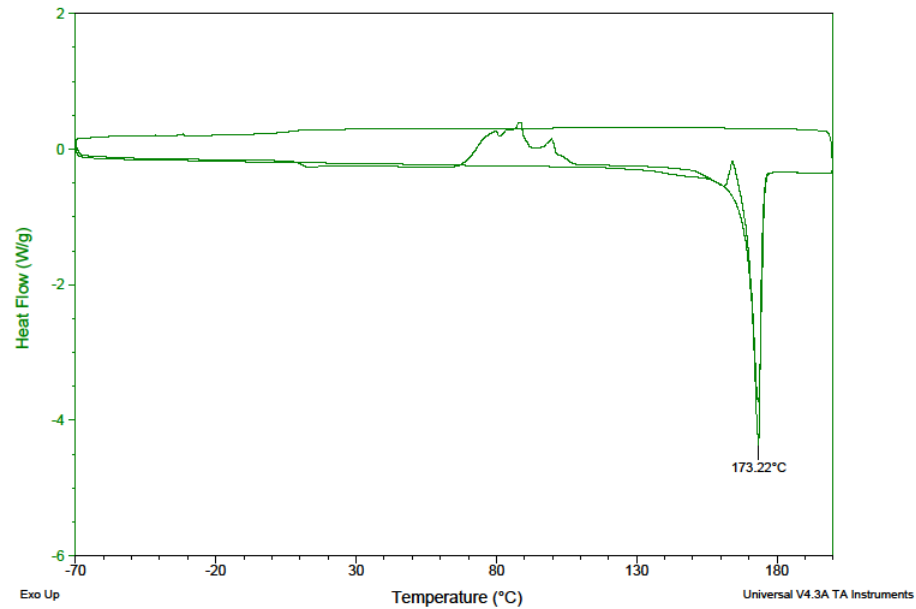


Figure 2.9.3. DSC trace of **Br-*m*PD**

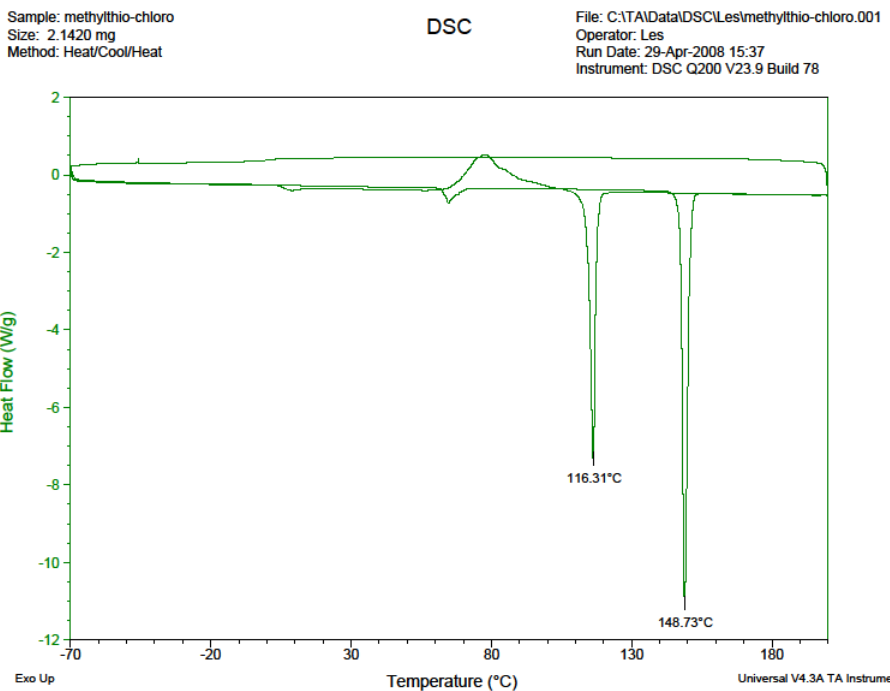


Figure 2.9.4. DSC trace of **Cl-mPD-SMe**

Cl-mPD-SMe exhibits two distinct crystal forms, though not consisting as a mixture.

During the first heating cycle, a single, sharp T_m at 148.73 °C is observed. After cooling and reheating, the T_m shifts substantially to 116.31 °C, with no other endotherm present. This indicates the complete conversion to a polymorphic crystalline species.

To rule out any possibility that the compound underwent decomposition, the sample was removed from the DSC pan and analyzed by $^1\text{H-NMR}$ (Figure 2.9.5). The $^1\text{H-NMR}$ spectrum indicates that no decomposition occurred, and the endotherm observed during the second heating cycle of the DSC experiment was indeed an alternate crystal form.

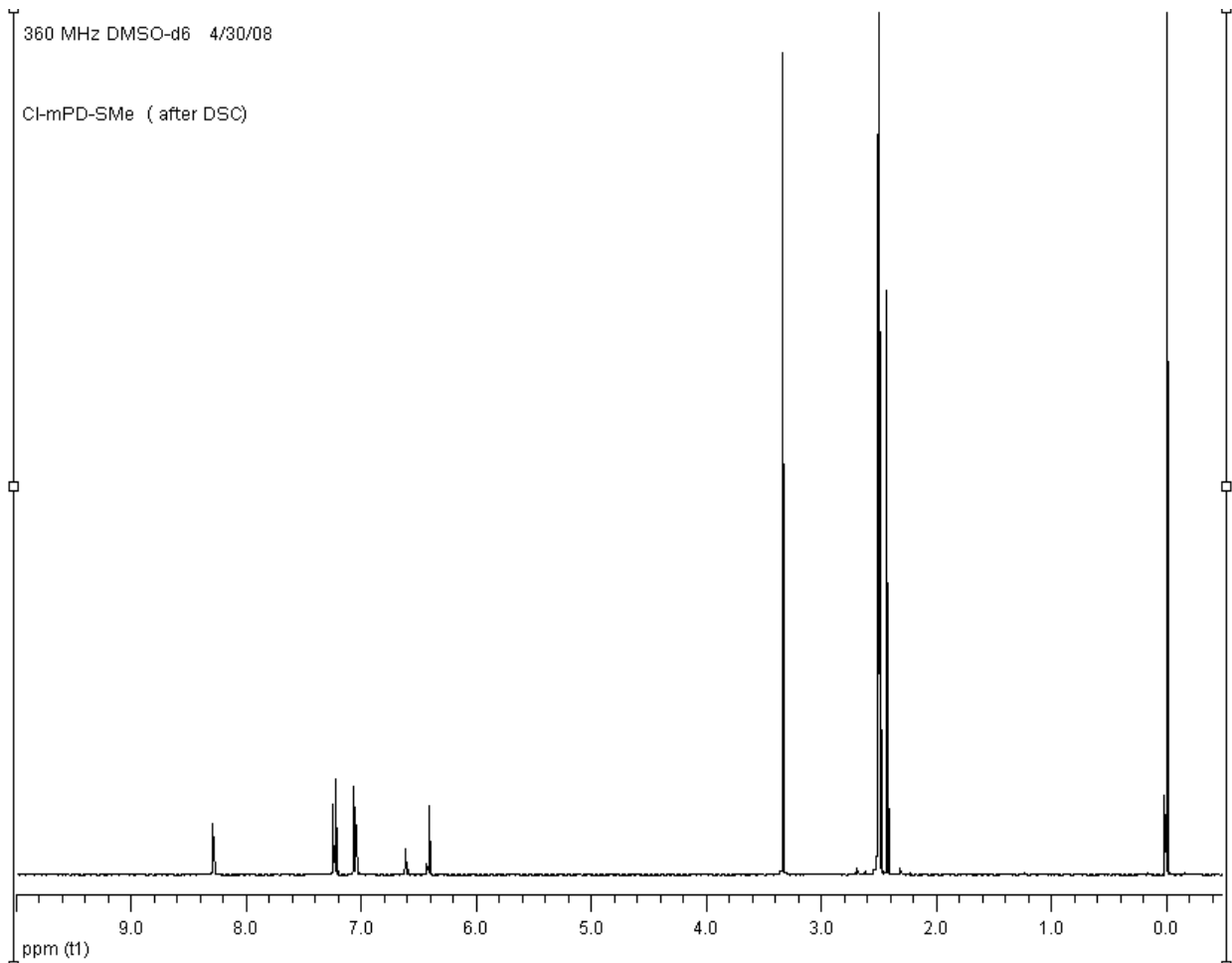
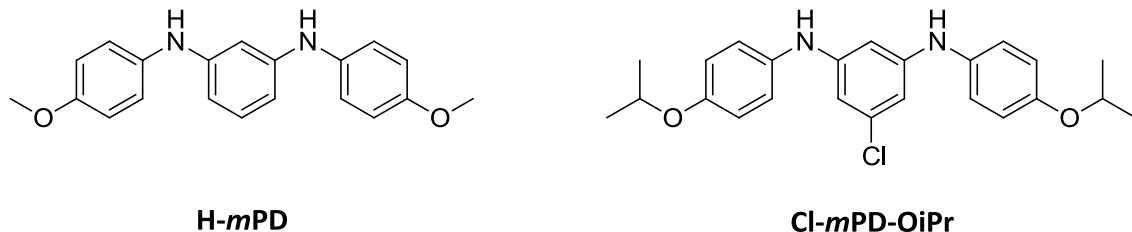


Figure 2.9.5. Post-DSC ¹H-NMR of **Cl-mPD-SMe**

Efforts were made to produce crystals of the polymorph suitable for XRD analysis, but were unsuccessful. The material present in the pan after the DSC experiment was not crystalline, but rather a melt consisted of a single, solid pellet. Various solvents and crystallization techniques were employed in attempts to isolate the polymorph, and though changes in crystal habit were observed, samples submitted for XRD proved them to be the original crystal form.

2.10 Non-polar *m*-Phenylenediamine Derivatives

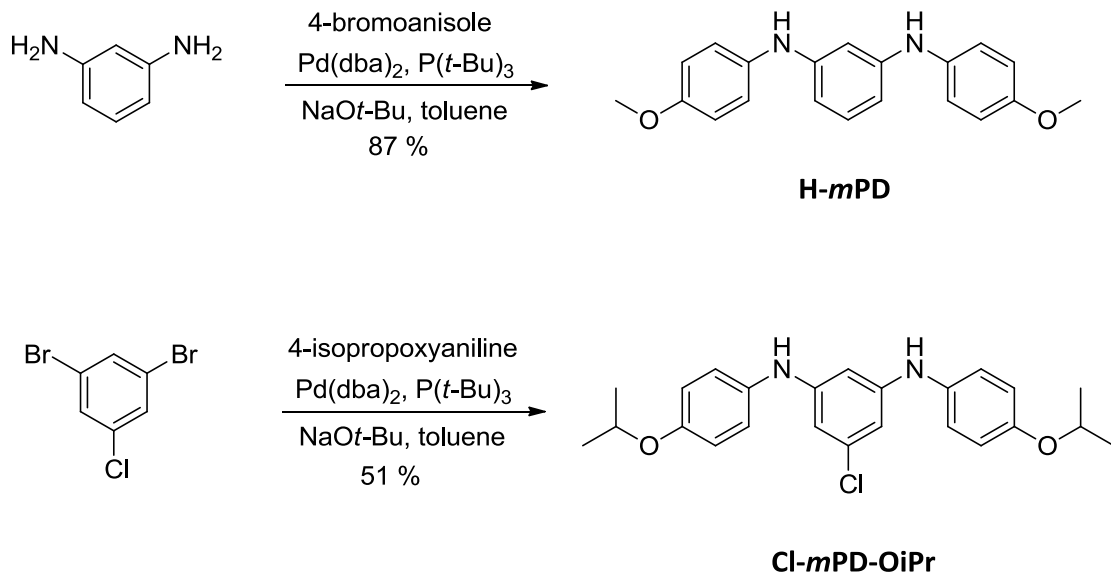
While synthesizing our series of *m*PD derivatives, we encountered two compounds which do not exhibit polar crystalline order. **H-*m*PD** and **Cl-*m*PD-O*i*Pr** were prepared and their single-crystal structures analyzed by XRD.



H-*m*PD and **Cl-*m*PD-O*i*Pr** were found to crystallize as the centrosymmetric space groups, P2(1)/n and P2/c, respectively. Moreover, this non-polar ordering in the crystalline solid was, in both cases, comprised of dipole-canceling arrangements of the molecules in the “open” conformation.

2.11 Synthesis

The synthesis of *m*PD analogs demonstrating preference for self-assembly into non-polar crystal space groups is described herein. **H-*m*PD** and **Cl-*m*PD-O*i*Pr** were prepared in analogous manner to other *m*PD derivatives, utilizing the protocol of Hartwig et al (Scheme 2.11.1).



Scheme 2.11.1. Synthesis of non-polar *m*PD derivatives

2.12 Dipole Calculations

Molecular dipole moments were calculated for **H-*m*PD** and **Cl-*m*PD-O*i*Pr** by AM1, utilizing the same benchmark references as previously described in section 2.7. Dipole moments calculated for both energy-minimized (E_{\min}) conformations and crystal geometry (XRD) conformations are presented in Figure 2.12.1.

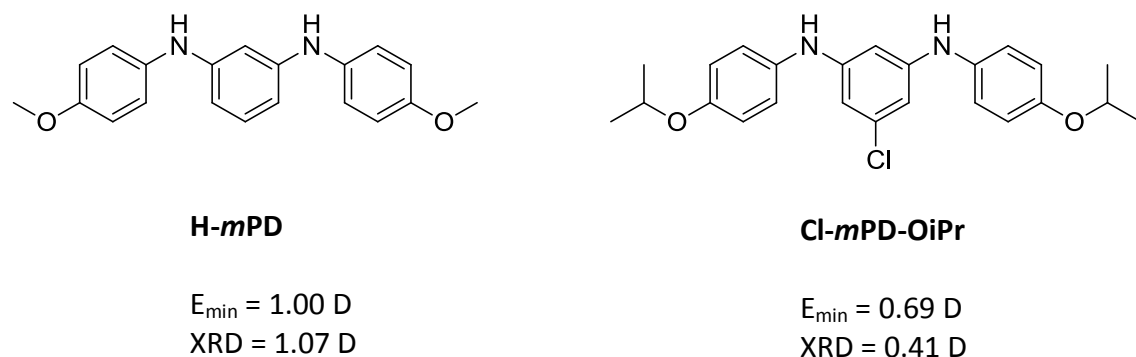


Figure 2.12.1. AM1-calculated dipole moments for non-polar *m*PD analogs

One important note regarding molecular dipoles that has yet to be mentioned is their direction. For all polar *m*PD analogs, the dipole moment is directed toward the 5-halo substituent. For **H-*m*PD**, the reverse holds true; its dipole moment is directed away from the 5-position. This is not surprising, as in this case we have substituted a halogen with the relative electropositive hydrogen atom. More interesting however, is the fact that **Cl-*m*PD-OiPr**, in its crystal conformation, also demonstrates this behavior. In fact, the net dipole moment for this compound is quite low at only 0.41 D.

2.13 X-ray Diffractometry

Single-crystal XRD was performed on **H-*m*PD** and **Cl-*m*PD-OiPr**. The pertinent data is summarized below.

Table 2.13.1. Comparative crystal parameters for non-polar *m*PDs

compound	H-<i>m</i>PD	Cl-<i>m</i>PD-OiPr
formula	C ₂₀ H ₂₀ N ₂ O ₂	C ₂₄ H ₂₇ N ₂ O ₂ Cl
FW (g/mol)	320.38	410.93
crystallization conditions	slow evaporation from benzene	slow evaporation from hexanes
crystal dimensions (mm)	0.70x0.50x0.25	0.50x0.20x0.10
crystal system	monoclinic	monoclinic
space group	P2(1)/n	P2/c
<i>a</i> (Å)	9.589(4)	12.1426(17)
<i>b</i> (Å)	6.357(3)	10.8470(15)

<i>c</i> (Å)	26.517(11)	8.6118(12)
α (deg)	90	90
β (deg)	94.446(7)	102.931(2)
γ (deg)	90	90
volume (Å ³)	1611.7(11)	1105.5(3)
Z	4	2
D _{calc} (g/cm ³)	1.320	1.234
F _{0,0,0}	680	436
λ (MoK λ) (mm ⁻¹)	0.086	0.194
diffractometer	Siemens	Siemens
	SMART	SMART
wavelength (Å)	0.71073	0.71073
temp (K)	173	298
θ range (deg)	3.02-28.33	3.07-25.00
limiting indices	-12≤ <i>h</i> ≤11 -8≤ <i>k</i> ≤8 -35≤ <i>l</i> ≤29	-14≤ <i>h</i> ≤14 -12≤ <i>k</i> ≤11 -10≤ <i>l</i> ≤10
reflections total	8358	5833
reflections unique	3561	1954
	(R _{int} =0.0714)	(R _{int} =0.0228)
decay correction	none	none
absorption correction	none	none
data/restraints/parameters	3561/0/298	1954/0/188

secondary extinction coef	0.008(2)	0.047(9)
GOF on F ²	1.224	0.817
R ₁ [I>2σ(I)]	0.1470	0.0381
wR ₂ [I>2σ(I)]	0.2859	0.1465
R ₁ [all data]	0.2147	0.0425
wR ₂ [all data]	0.3168	0.1570
Δ(□) (e Å ³)	0.481, -0.390	0.194, -0.308

As is the case for polar *mPD* analogs, both **H-*mPD*** and **Cl-*mPD-OiPr*** are monoclinic crystal systems. However, **H-*mPD*** and **Cl-*mPD-OiPr*** belong to the centrosymmetric P2(1)/n and P2/c space groups, respectively. The XRD data for **Cl-*mPD-OiPr*** was refined to give an R-value of 4.3 %, H-*mPD* gave an R-value of 21 %. This is quite high, and many attempts were made to grow crystals of higher quality. We came to find however, that non-polar *mPD* analogs were extraordinarily reluctant to produce suitable crystals for XRD. Whereas the polar *mPD* analogs generally crystallize readily under a multitude of conditions, non-polar *mPD* analogs required much experimentation to arrive at a very specific set of parameters in order to obtain even low-quality crystals. There was also observed a trend in crystal habit distinct for the two subsets of *mPD* derivatives. All of the polar *mPDs* tended to crystallize as prisms, with all dimensions more or less equivalent. The two *mPDs* which were confirmed to crystallize in centrosymmetric space groups, on the other hand, presented as thin plates or fine needles, neither of which is conducive to optimal XRD data collection.

Crystal packing diagrams (Figures 2.13.1-2.) demonstrate the “open” conformation of the molecules within the lattice, as well as inter-layer dipole cancelling.

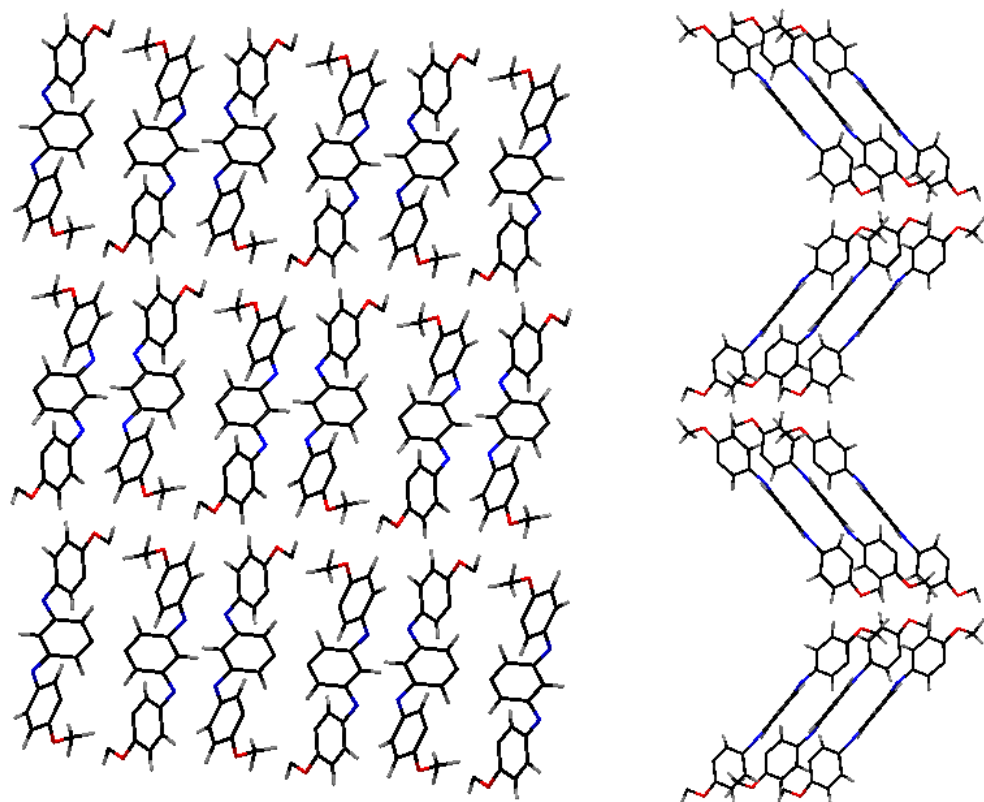


Figure 2.13.1. H-mPD crystal packing diagram

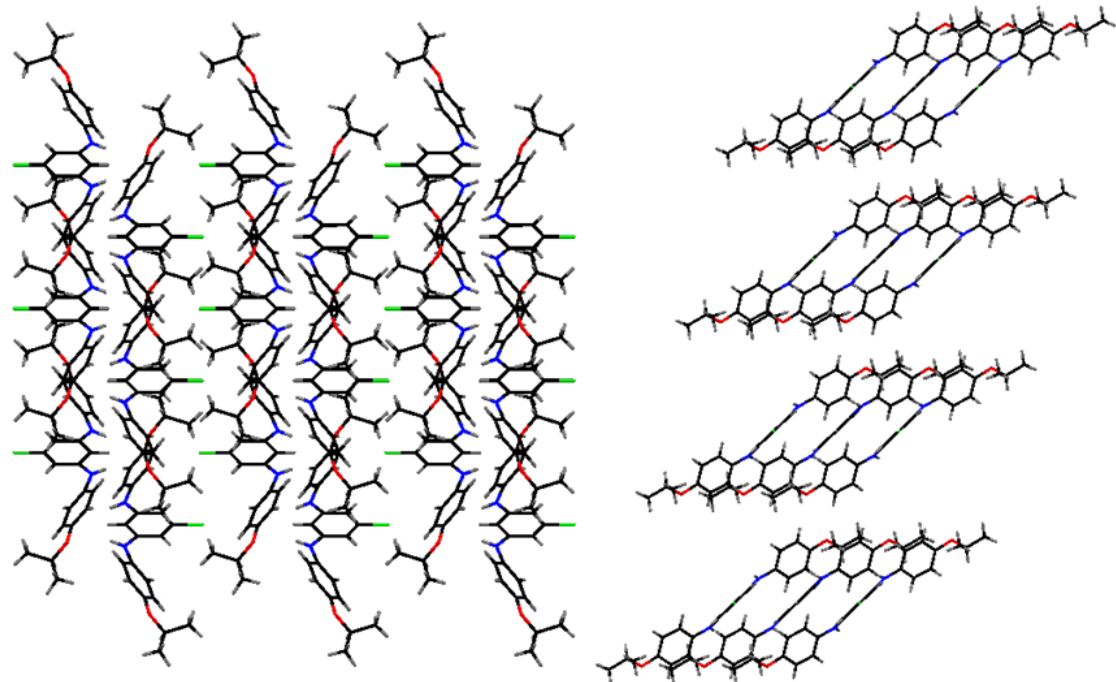


Figure 2.13.2. Cl-mPD-OiPr crystal packing diagram

2.14 Polar Order by Rational Design: H-*m*PD-OMac

By observing the conformational trends of polar and non-polar *m*PD derivatives in the crystal lattice, we were able to gain some insight as to the requirements for polar order. It seemed apparent that the “closed” conformation facilitates polar self-assembly, while the “open” conformation acts as a hindrance. It was thus envisioned that if an otherwise non-polar *m*PD were forced into the “closed” conformation by geometric constraint, the possibility of altering its preference for polar order would be feasible (Figure 2.14.1). We hypothesized that if the methoxy groups of **H-*m*PD** were bound together by a methylene bridge, the structure of the resulting macrocycle would be very close to the conformation adopted in the crystal lattice by polar *m*PD derivatives.

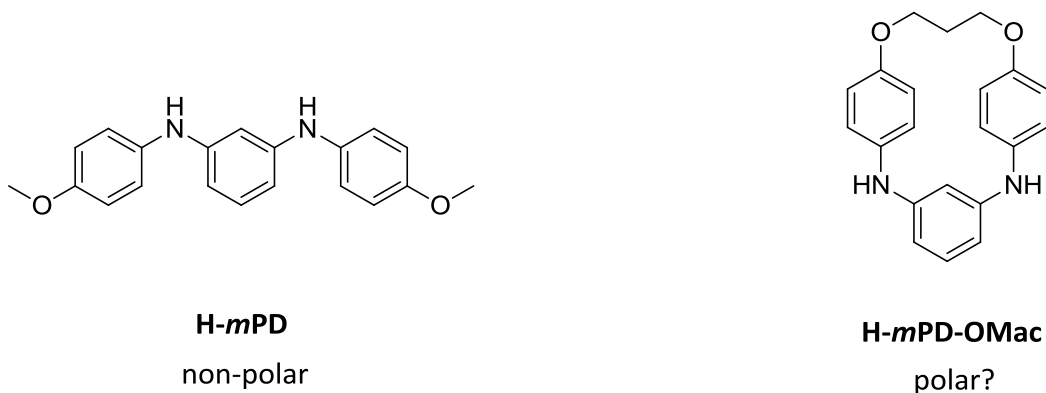
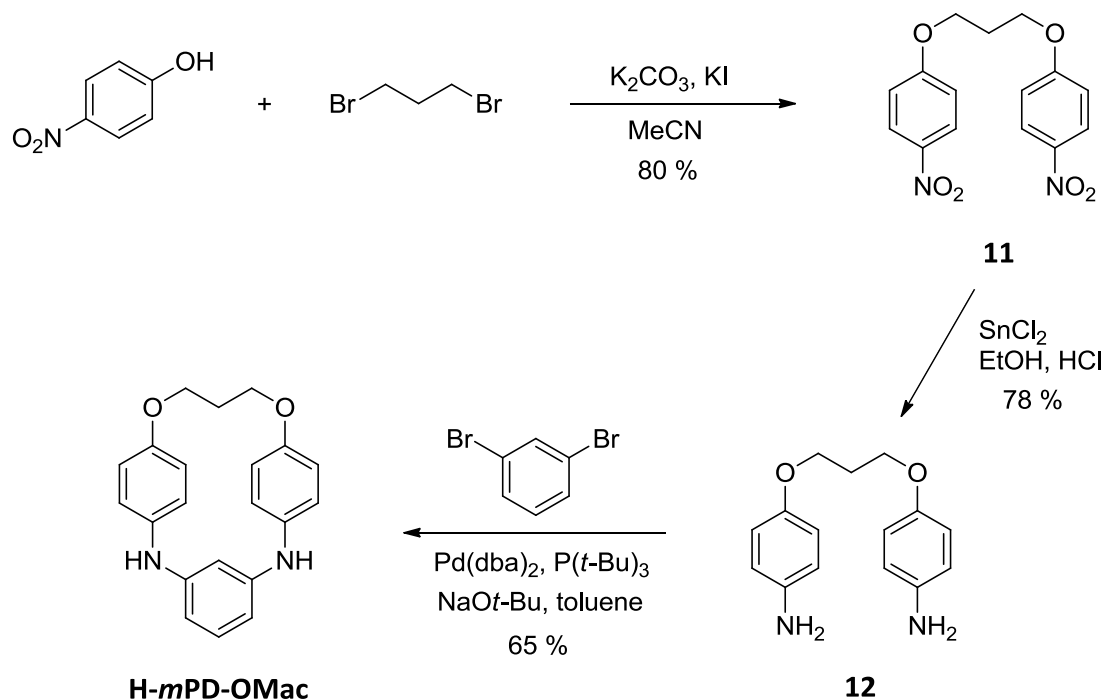


Figure 2.14.1. Rationale for putative polar ordering of **H-*m*PD-OMac**

2.15 Synthesis

The synthesis of **H-*m*PD-OMac** involves the preparation of the symmetrical “linking” unit (Scheme 2.15.1). A double S_N2 reaction of p-nitrophenol with 1,3-dibromopropane in acetonitrile under basic conditions in the presence of a nucleophilic catalyst affords the intermediate **11**.⁷⁵ Reduction of **11** with tin (II) chloride in acidic ethanol provides the diamine

12. Palladium-catalyzed N-arylation of **12** with 1,3-dibromobenzene following the protocol of Hartwig et al completes the synthesis. It is important to note that this coupling must be performed under very dilute conditions in order to avoid the formation of oligomers/polymers.



Scheme 2.15.1. Synthesis of **H-*m*PD-OMac**

2.16 X-ray Diffractometry

As hypothesized, **H-*m*PD-OMac** crystallizes as a polar space group (monoclinic, Cm). Moreover, the molecule adopts the same layered, nested lattice configuration (Figure 2.16.1) observed in all other polar *m*PDs (with the exception of **Cl-*m*PD-SMe**).

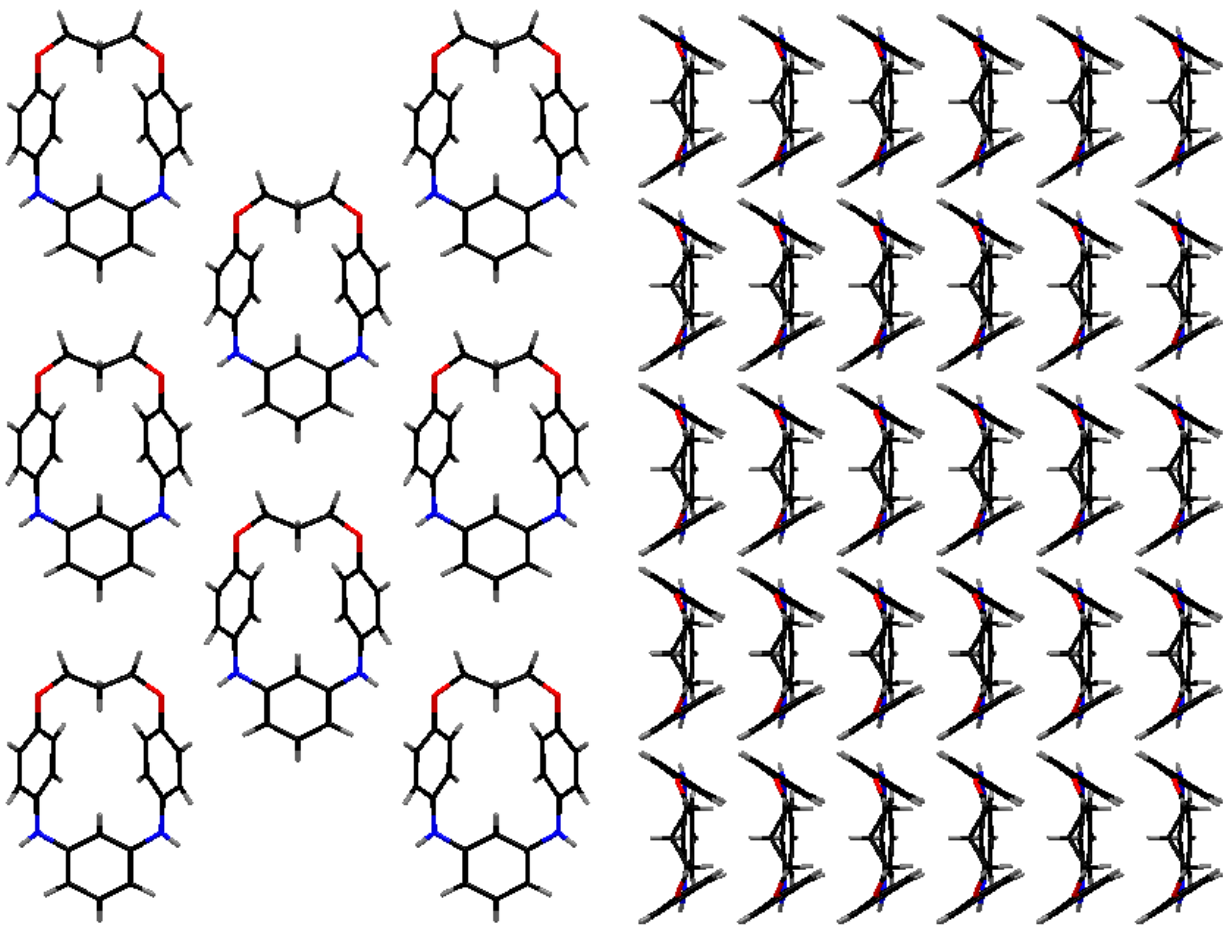


Figure 2.16.1. H-*m*PD-OMac crystal packing diagram

2.17 Conclusions

A series of *m*PD derivatives was synthesized and their crystal structures elucidated by XRD. It was discovered that a high propensity for polar ordering was observed across the series with the exception of two cases. By observing the conformation of analogs which crystallized as polar space groups and contrasting that with the conformation of the non-polar derivatives, some understanding was garnered as to the requirements for polar ordering of *m*PDs in the solid state.

The “closed” conformation invariably resulted in the formation of polar crystalline solids, while the “open” conformation yielded non-polar crystals. We were thus able to correctly predict

that an otherwise non-polar *m*PD derivative, when modified to introduce geometric constraint and lock it into the “closed” conformation, preferentially self-assembled as a polar crystal.

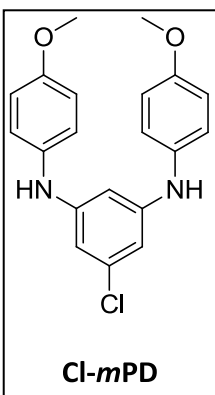
Aside from the putative practical applications of organic polar crystals, the ability to rationally engineer solids demonstrating a preference for polar order is substantial. The process of developing an understanding of the forces responsible for polar ordering in mPD derivatives also introduces the feasibility of designing polar organic crystalline materials which span a much broader scope.

2.18 Experimental

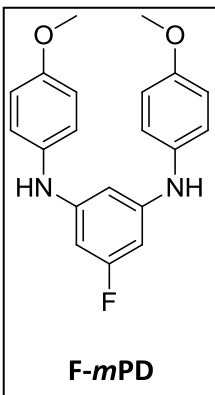
General Methods and Materials.

Pd(db_a)₂ was purchased from *Acros Organics*. 1,3-dibromo-5-chlorobenzene was prepared according to literature precedent.⁷⁶ All other reagents were purchased from *Aldrich Chemical Company*. *p*-Anisidine and *m*-phenylenediamine were purified by sublimation. Anhydrous Toluene and tetrahydrofuran were purchased from *Aldrich Chemical Company* and used without further purification. ¹H-NMR and ¹³C-NMR spectra were recorded on Bruker AM-500 or AM-360 instruments with chemical shifts reported relative to the deuterated solvent or TMS. HRMS spectra were collected on a VG Autospec high resolution mass spectrometer. Crystal diffraction data was gathered on a Siemens CCD SMART diffractometer. DSC measurements were made using a TA Instruments Q200 differential scanning calorimeter.

Synthesis

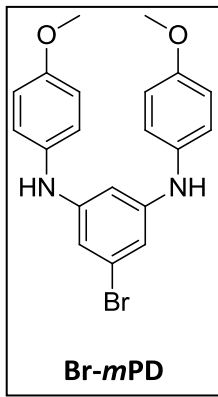


Dibromide 1,3-dibromo-5-chlorobenzene (2.000 g, 7.400 mmol) and *p*-anisidine (1.822 g, 14.80 mmol) were placed in a flame-dried, 250 mL round-bottom flask with magnetic stir bar. Pd(dba)₂ (0.256 g, 0.445 mmol), P(*t*-Bu)₃ (0.074 g, 0.37 mmol), NaOt-Bu (1.760 g, 18.30 mmol) and anhyd toluene (100 mL) were weighed and added in a dry box under a nitrogen atmosphere. The reaction mixture was removed from the box and stirred at room temperature under an argon atmosphere for 1.75 h. The crude reaction mixture was dissolved in ~400 mL tetrahydrofuran and then filtered through a 60 x 20 mm layer of basic alumina (activity III). The filtrate was concentrated *in vacuo* to a volume of 50 mL to which was added 800 mL hexanes to initiate precipitation of the product which was then dried *in vacuo* to yield **Cl-mPD** as a light tan solid (2.476 g, 94%): mp 179 °C. ¹H-NMR (500 MHz, DMSO-d₆) δ 7.89 (s, 2H), 7.02 (d, *J* = 8.94 Hz, 4H), 6.88 (d, *J* = 8.94 Hz, 4H), 6.38 (t, *J* = 1.93 Hz, 1H), 6.20 (d, *J* = 1.92 Hz, 2H), 3.71 (s, 6H). ¹³C-NMR (90 MHz, d⁶-DMSO) δ 55.1, 97.9, 103.9, 114.4, 121.8, 134.0, 135.0, 147.5, 154.3. HRMS: m/z: calc for M⁺ C₂₀H₁₉ClN₂O₂ = 354.1135, found 354.1150. Crystals for XRD analysis were grown by slow evaporation from acetonitrile.

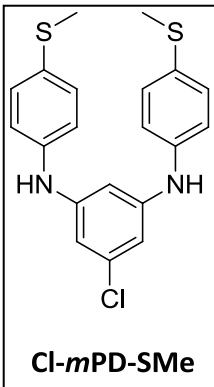


Dibromide 1,3-dibromo-5-fluorobenzene (0.518 g, 2.00 mmol) and *p*-anisidine (0.498 g, 4.00 mmol) were placed in a flame-dried, 50 mL round-bottom flask with magnetic stir bar. Pd(dba)₂ (0.023 g, 0.0040 mmol), P(*t*-Bu)₃ (0.007 g, 0.003 mmol), NaOt-Bu (0.991 g, 10.0 mmol) and anhyd toluene (10 mL) were weighed and added in a dry box. The reaction mixture was stirred at 45 °C under argon atmosphere for 18 h. The mixture was taken

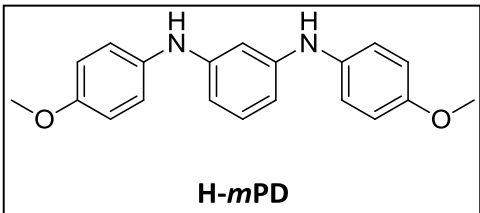
up in ethyl acetate, and then filtered through a 60 x 10 mm layer of basic alumina (activity III). The filtrate was concentrated under reduced pressure to give a black, sticky solid. The solid was recrystallized from ethanol to yield **F-mPD** as purple crystals (0.503 g, 74%): mp = 158 °C. ¹H-NMR (500 MHz, DMSO-d₆) δ 7.90 (s, 2H), 7.03 (d, *J* = 8.96 Hz, 4H), 6.87 (d, *J* = 8.98 Hz, 4H), 6.27 (t, *J* = 1.88 Hz, 1H), 5.97 (dd, *J*₁ = 1.89 Hz, *J*₂ = 11.54 Hz, 2H), 3.71 (s, 6H). Crystals for XRD were grown by sublimation, followed by recrystallization from nitromethane.



Tribromide 1,3,5-tribromobenzene (0.321 g, 1.00 mmol) and *p*-anisidine (0.249 g, 2.00 mmol) were placed in a flame-dried, 50 mL round-bottom flask with magnetic stir bar. Pd(dba)₂ (0.029 g, 0.0050 mmol), dppf (0.028 g, 0.0050 mmol), NaOt-Bu (0.384 g, 4.00 mmol) and anhyd toluene (10 mL) were weighed and added in a drybox. The reaction mixture was stirred at 80 °C under argon atmosphere for 6 h. The mixture was taken up in tetrahydrofuran and washed with 0.02 M aqueous sodium cyanide. The organic phase was filtered through a 40 x 20 mm layer of celite on top of a 40 x 20 mm layer of basic alumina (activity III). The filtrate was concentrated to an oily residue. The residue was recrystallized from ethanol/H₂O (10:1) to yield **Br-mPD** as a tan solid (0.258 g, 65%): mp = 174 °C. ¹H-NMR (500 MHz, DMSO-d₆) δ 7.88 (s, 2H), 7.02 (d, *J* = 8.93 Hz, 4H). 6.88 (d, *J* = 8.98, 4H), 6.41 (t, *J* = 1.93 Hz), 6.33 (d, *J* = 1.93 Hz), 3.71 (s, 6H). Cyrstals for XRD analysis were grown by slow evaporation from acetonitrile.



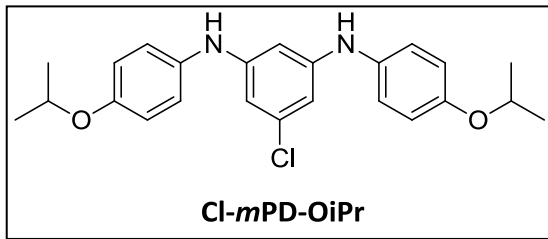
Dibromide 1,3-dibromo-5-chlorobenzene (1.081 g, 4.00 mmol) and 4-(methylthio)aniline (1.114 g, 8.00 mmol) were placed in a flame-dried, 50 mL round-bottom flask with magnetic stir bar. Pd(dba)₂ (0.023 g, 0.0040 mmol), P(t-Bu)₃ (0.008 g, 0.004 mmol), NaOt-Bu (1.538 g, 16.0 mmol) and anhyd toluene (16 mL) were weighed and added in a dry box. The reaction mixture was stirred at room temperature under nitrogen atmosphere for 20 h, then stirred at reflux for a further 20 h. The mixture was taken up in tetrahydrofuran, and then filtered through a 30 x 20 mm layer of basic alumina (activity III). The filtrate was concentrated *in vacuo* to give a brown, sticky solid. Slow evaporation from ethyl acetate afforded **Cl-mPD-SMe** as light purple crystals (0.831 g, 54%): mp = 147-149 °C. ¹H-NMR (500 MHz, DMSO-d₆) δ 8.27 (s, 2H), 7.23 (d, *J* = 8.65 Hz, 4H). 7.05 (d, *J* = 8.65, 4H), 6.61 (t, *J* = 1.92 Hz), 6.41 (d, *J* = 1.93 Hz), 2.43 (s, 6H). Crystals for XRD analysis were grown by slow evaporation in benzene.



m-Phenylenediamine (0.324 g, 3.00 mmol) and 4-bromoanisole (1.122 g, 6.00 mmol) were placed in a flame-dried, 50 mL round-bottom flask with magnetic stir bar. Pd(dba)₂ (0.086 g, 0.150 mmol), P(t-Bu)₃ (0.027 g, 0.120 mmol), NaOt-Bu (0.594 g, 6.00 mmol), anhyd toluene (10 mL), and anhyd tetrahydrofuran (10 mL) were added in a dry box. The reaction mixture was stirred at room temperature under argon atmosphere for 1.5 hr. The mixture was taken up in tetrahydrofuran, washed with 0.02 M aqueous sodium cyanide, and then filtered through celite and basic alumina (activity III). The filtrate was concentrated *in vacuo* to yield a brown solid. The solid was dissolved in hot nitromethane, allowed to cool, and then placed in a freezer overnight. Vacuum filtration afforded **H-mPD** as pale yellow crystals (0.838 g, 87%):

¹H-NMR (360 MHz, DMSO-d₆) δ 7.69 (s, 2H), 7.01 (d, *J* = 9.0, 4H), 6.94 (t, *J* = 8.0, 1H), 6.84 (d, *J* = 9.0, 4H), 6.54 (t, *J* = 2.1, 1H), 6.30 (dd, *J*₁ = 2.1 Hz, *J*₂ = 8.0 Hz, 2H), 3.70 (s, 6H).

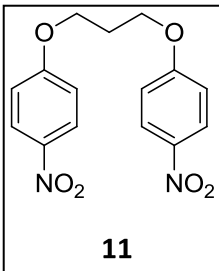
Crystals for XRD analysis were grown by slow evaporation in benzene.



Dibromide 1,3-dibromo-5-chlorobenzene (0.541 g, 2.00 mmol) and 4-(isopropoxy)aniline (0.617 g, 4.00 mmol) were placed in a flame-dried, 50 mL round-bottomed flask with magnetic stir bar. Pd(dba)₂

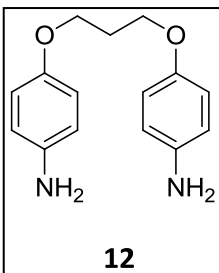
(0.058 g, 0.10 mmol), P(t-Bu)₃ (0.018 g, 0.08 mmol), NaOt-Bu (0.769 g, 8.00 mmol) and anhyd toluene (20 mL) were added in a dry box. The reaction mixture was stirred at rt under argon atmosphere for 23 h. The mixture was taken up in tetrahydrofuran, and then filtered through a 60 x 20 mm layer of basic alumina (activity III). The filtrate was concentrated *in vacuo* to yield a brown oil. The oil was dissolved in hot hexanes, allowed to cool, and then placed in a freezer overnight. Vacuum filtration afforded **Cl-mPD-OiPr** as a light tan solid (0.419 g, 51%): mp = 129 °C. ¹H-NMR (500 MHz, DMSO-d₆) δ 7.88 (s, 2H), 7.00 (d, *J* = 8.91 Hz, 4H), 6.85 (d, *J* = 8.91 Hz, 4H), 6.39 (t, *J* = 1.95 Hz), 6.21 (d, *J* = 1.91 Hz, 2H), 4.50 (sp, *J* = 6.04 Hz), 1.24 (d, *J* = 6.01 Hz, 12H); ¹³C-NMR (125 MHz, acetone-d₆) δ 23.4, 71.7, 100.7, 106.9, 118.5, 124.4, 136.8, 137.1, 149.9, 155.4. HRMS m/z: calc for M⁺ C₂₄H₂₇ClN₂O₂ = 410.1761, found 410.1776.

Crystals for XRD analysis were grown by slow evaporation in hexanes.



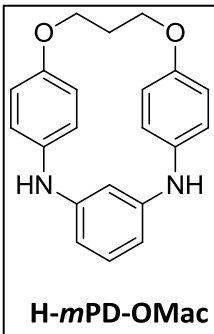
Commercially available 4-nitrophenol (23.65 g, 0.1700 mol), 1,3-dibromopropane (12.11 g, 0.06000 mol), potassium iodide (0.60 g, 0.0036 mol), and potassium carbonate (23.50 g, 0.1700 mol) were dissolved in acetonitrile (240 mL) in a 500 mL round-bottom flask with magnetic stir bar.

The reaction mixture was heated to reflux and stirred under N₂ for 22 h. The reaction mixture was removed from heat and allowed to cool rt, then poured into 600 mL stirring ice water. Dilute (5%) sodium hydroxide solution was added until alkaline. Vacuum filtration afforded a pale yellow solid which was washed with water (2 x 120 mL) poured over the filter cake. This procedure decolorized the solid. The crude solid (~18.5 g) was dissolved in a minimal amount of hot chloroform:hexanes (1:1) (~1000 mL). The solution was placed in a freezer overnight. Vacuum filtration yielded **11** as off-white needles (15.19 g, 80 %)



A mixture of **11** (15.08 g, 0.04738 mol), anhyd tin(II) chloride (89.83 g, 0.04738 mol), conc hydrochloric acid (25 mL), and ethanol (350 mL) in a 1000 mL round-bottom flask was magnetically stirred at reflux under N₂ for 24 h. The reaction mixture was removed from heat and allowed to cool to rt.

The solvent was removed in vacuo to leave a yellow viscous liquid which was carefully poured into 1000 mL stirring ice water. The mixture was basified to pH 12 with 15% sodium hydroxide solution. The aqueous phase was extracted with ethyl acetate (3 x 400 mL) and the pooled organics were dried over anhyd sodium sulfate, and then evaporated in vacuo to give 11.80 g of light pink solid. Recrystallization from ethanol:water 1:1 gave **12** as beige crystals (9.59 g, 78%)



Diamine **12** (0.302 g, 1.20 mmol) and dibromobenzene (0.280 g, 1.20 mmol) were combined in a flame-dried 500 mL three-neck, round-bottom flask with magnetic stir bar. The flask was placed in a drybox and anhyd toluene (200 mL) was added to completely dissolve the starting materials. $\text{Pd}(\text{dba})_2$ (0.135 g, 0.235 mmol), $\text{P}(t\text{-Bu})_3$ (0.047 g, 0.23 mmol), and NaOt-Bu (0.450 g, 4.68 mmol) were added, and the reaction mixture was transferred from the dry box to a reflux condenser fitted with an oil bubbler. The reaction mixture was stirred at reflux under N_2 for 6 days. The reaction mixture was then removed from heat, allowed to cool to rt, and then filtered through a plug of basic alumina (activity III). The filtrate was concentrated *in vacuo* to give **H-mPD-OMac** as a pale yellow solid (0.240 g, 65 %). Crystals for XRD analysis were grown by slow evaporation from toluene at rt.

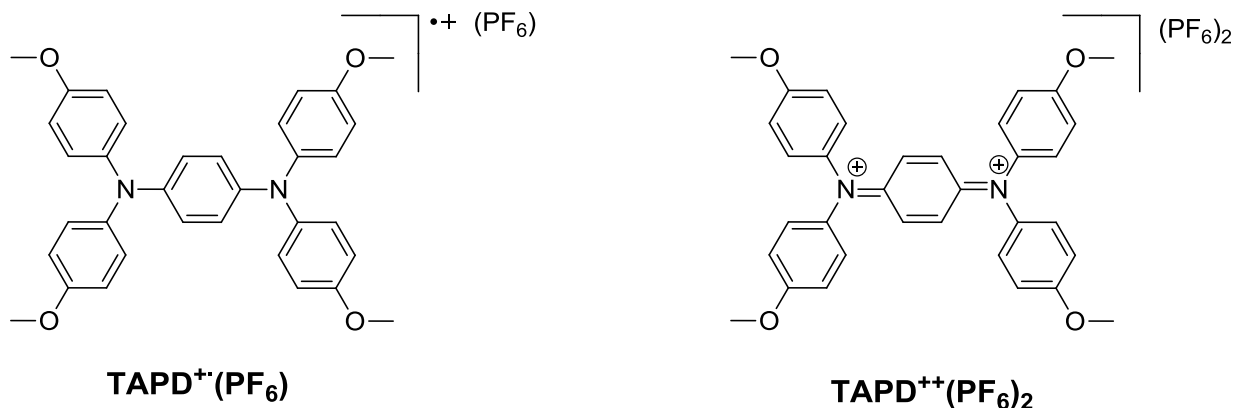
Chapter 3

Semiconductive Tetra(*p*-anisyl)-*p*-phenylenediamine Radical Cation and Dication Salts

3.1 Introduction

Organic semiconductors have attracted much attention in recent years due to the growing interest in organic electronics for applications including field-effect transistors, solar cells, and light-emitting diodes.⁷⁷⁻⁸⁰ Such devices constructed from organic substrates are appealing due to their light weight, flexibility, and low processing costs compared to traditional inorganic semiconductors.⁸¹

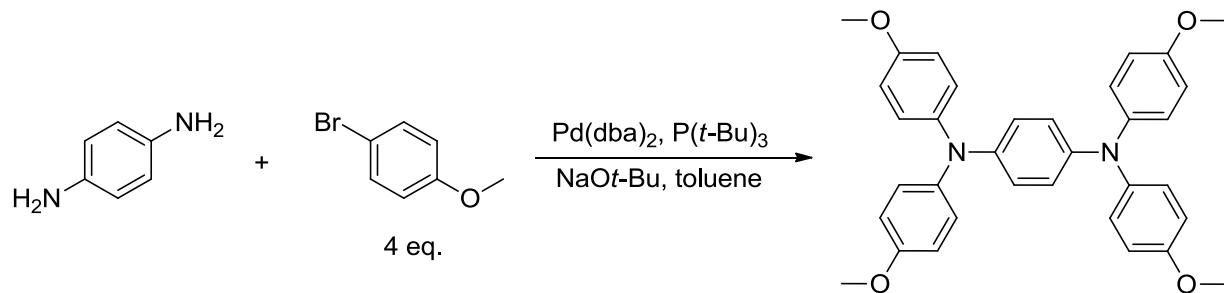
We have synthesized two novel tetra(*p*-anisyl)-*p*-phenylenediamine (**TAPD**) salts, **TAPD⁺(PF₆)** and **TAPD^{++(PF₆)₂}**, which exhibit semiconductive properties.



Although much of the data presented is preliminary, we believe these compounds demonstrate promise for use as organic semiconductors. The synthesis, electrochemistry, single-crystal X-ray diffractometry, and conductivity of **TAPD**, **TAPD⁺(PF₆)**, **TAPD^{++(PF₆)₂}** and **TAPD³⁺(PF₆)₃** is described herein.

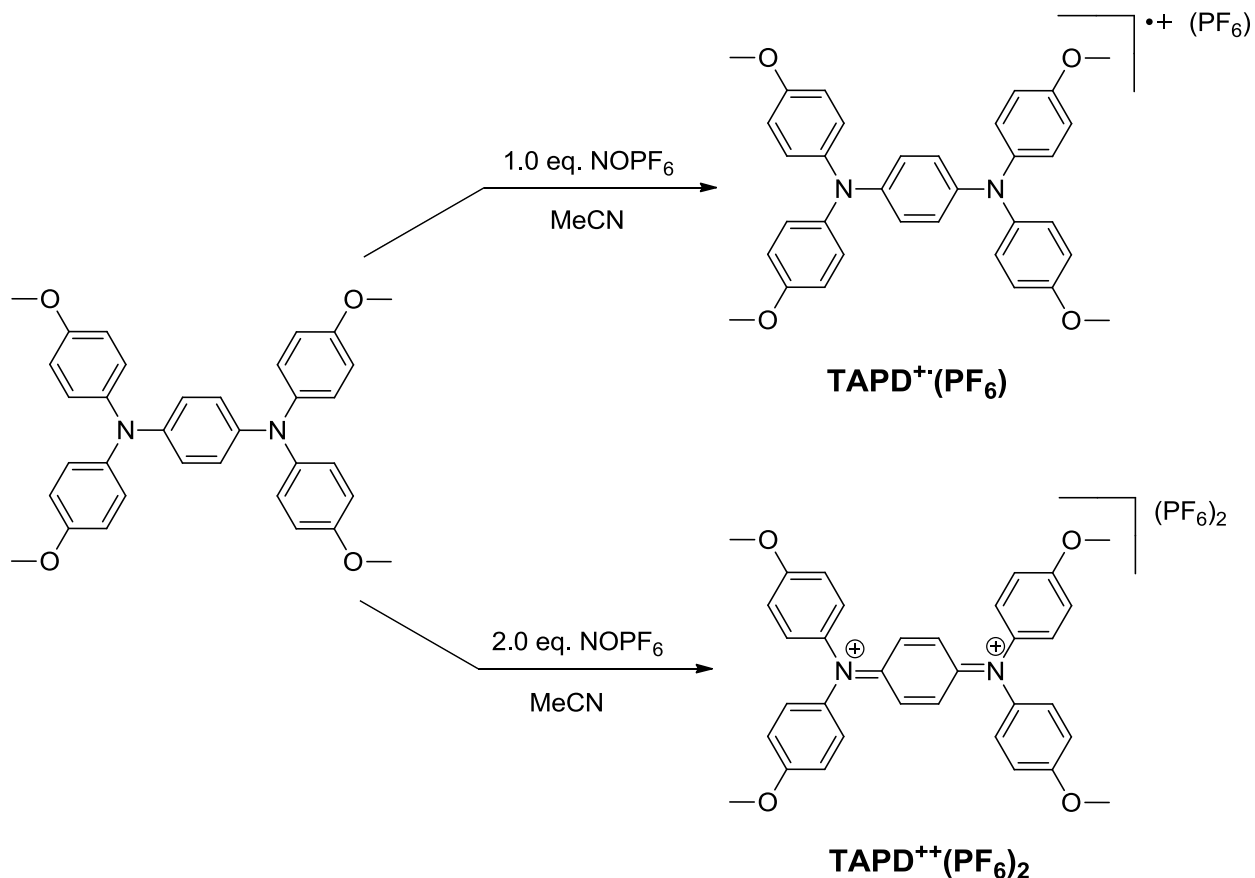
3.2 Synthesis of TAPD and TAPD Salts

The preparation of **TAPD** is straightforward, involving the palladium-catalyzed cross-coupling of *p*-phenylenediamine with four equivalents of 4-bromoanisole, following the procedure of Hartwig et al. (Scheme 3.2.1).



Scheme 3.2.1. Synthesis of **TAPD**

The **TAPD** radical cation and dication were prepared by combining TAPD with the appropriate equivalent of nitrosonium hexafluorophosphate (NOPF₆) in acetonitrile solution at rt while continuously purging with N₂ (Scheme 3.2.2).



Scheme 3.2.2. Synthesis of **TAPD**⁺(PF₆) and **TAPD**⁺⁺(PF₆)₂

3.3 Cyclic Voltammetry

TAPD was analyzed by CV to determine its electrochemical behavior (Figure 3.3.1). The cyclic voltammogram of **TAPD** shows, as expected, two redox couples, which demonstrate that the compound can exist in either the radical cation or dication state.

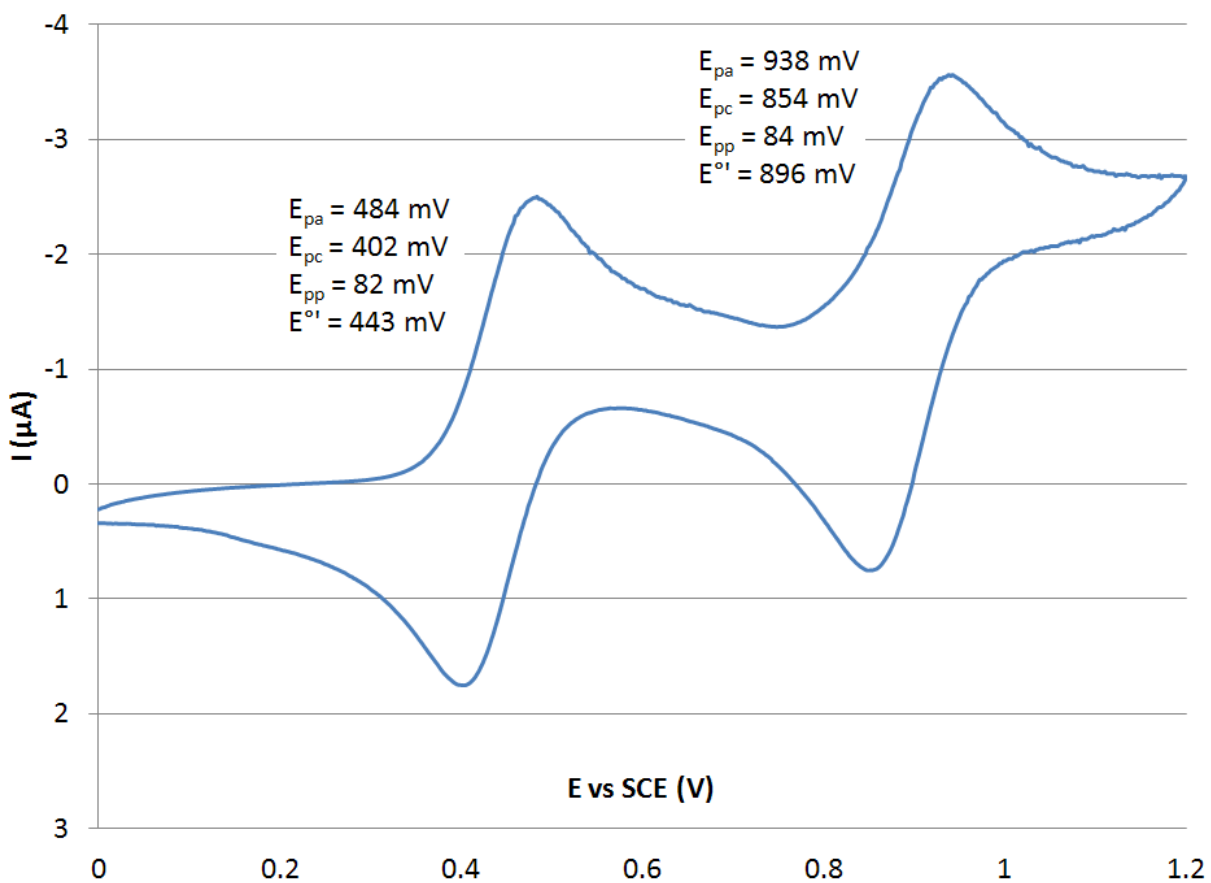


Figure 3.3.1. Cyclic voltammogram of **TAPD** - 1.0 mM in dichloromethane (0.1 M TBABF₄) at 20 mV/s scan rate

3.4 Redox Titrations of TAPD

In order to establish a baseline for testing the purity of our isolated **TAPD** salts, redox titration of a known concentration of **TAPD** was carried out and monitored by UV-vis. Our first efforts involved using Orange CRET as the oxidant (Figures 3.4.1 and 3.4.2), however it became apparent that less than one equivalent of oxidant was required to effect conversion of **TAPD** to its radical cation species.

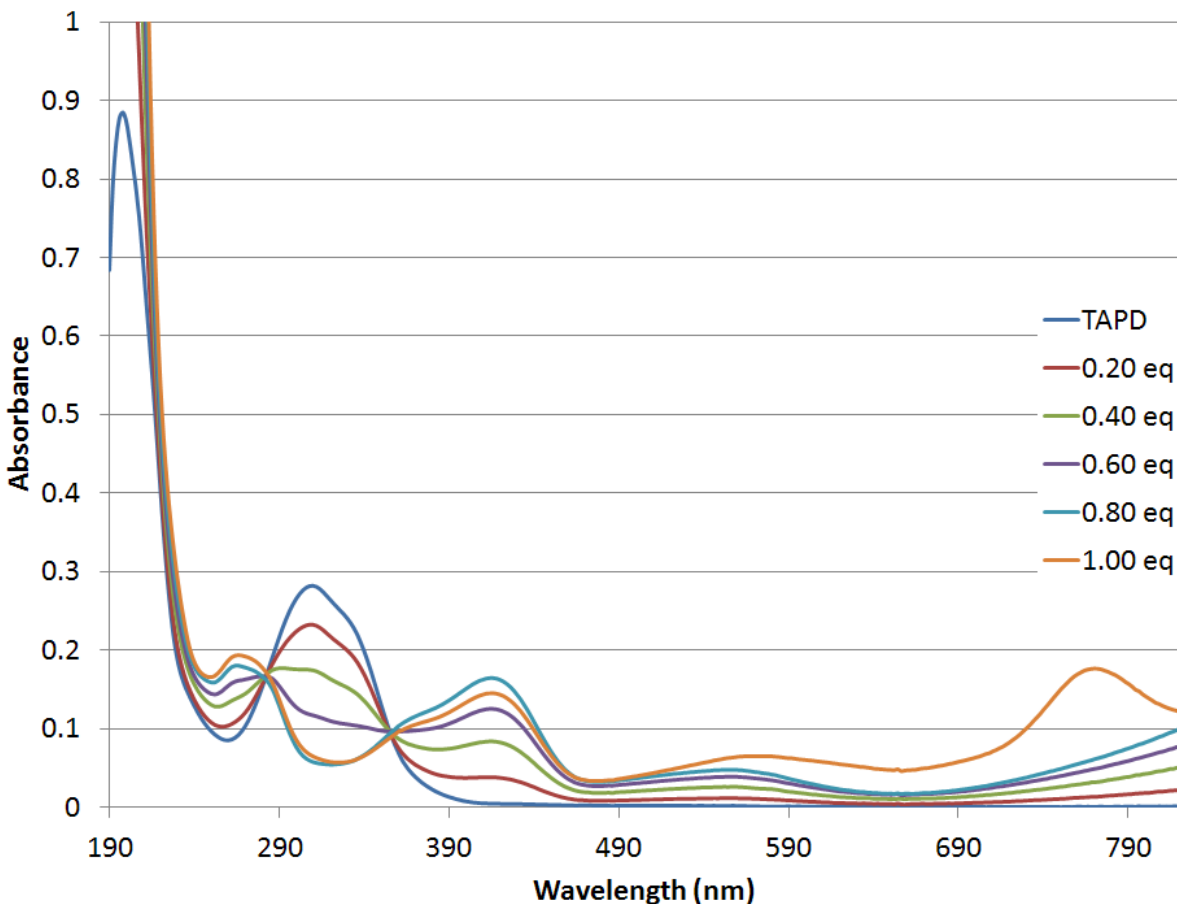


Figure 3.4.1. Redox titration of **TAPD** (8.56×10^{-6} M in acetonitrile) with Orange CRET to 1.0 equivalent

It is clearly discernible from Figure 3.3.1 that a new species (presumably TAPD dication) is present from the appearance of a new peak ($\lambda_{\text{max}} = 766$ nm). This would of course imply that we have over-oxidized TAPD at this point, and upon addition of 1.00 equivalents Orange CRET, the solution consists as a mixture of both radical cation and dication.

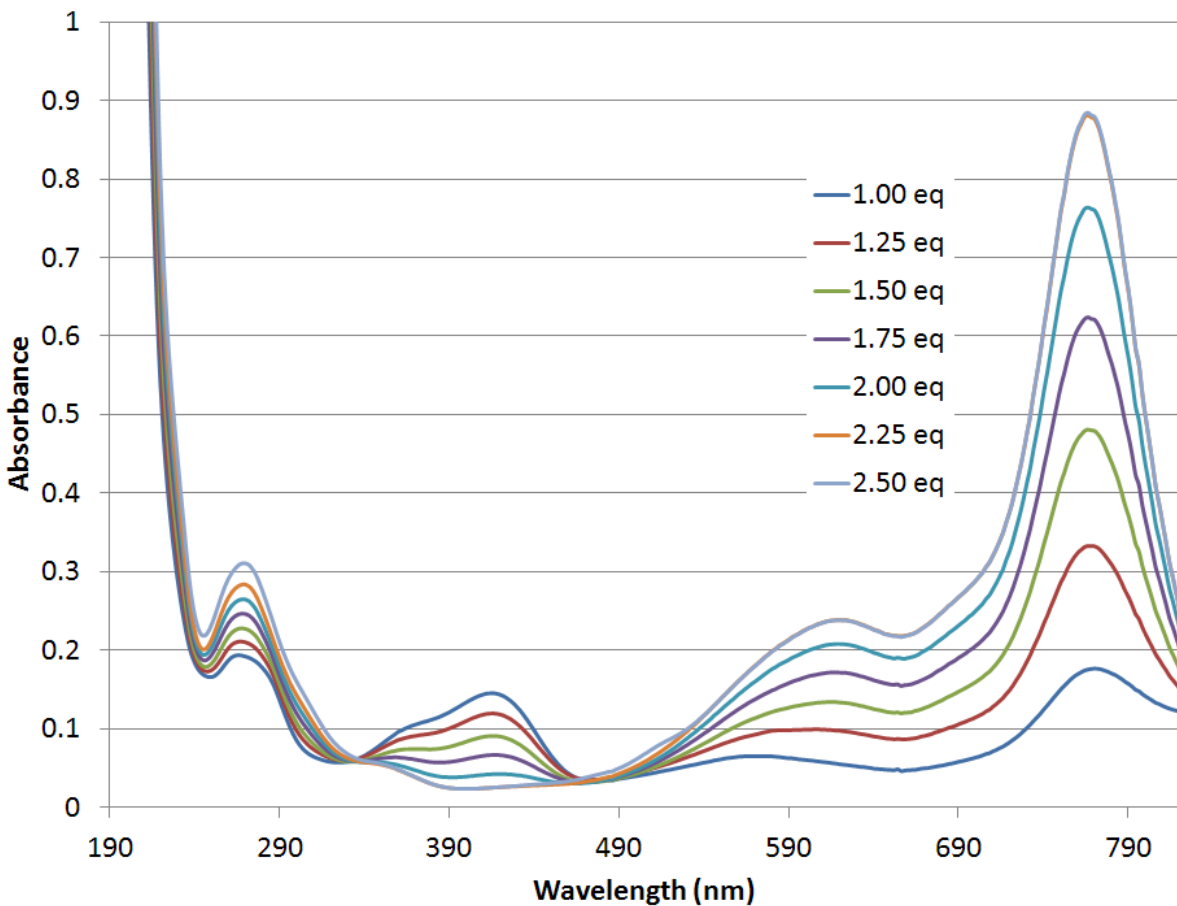


Figure 3.4.2. Redox titration of **TAPD** (8.56×10^{-6} M in acetonitrile) with Orange CRET from 1.0 to 2.25 equivalents

In Figure 3.4.2, it is seen that the peak at 766 nm does not stop increasing until over 2.25 equivalents of Orange CRET have been added. This data was difficult to interpret, as we obtained over-oxidation from zero to 1.00 equivalents, but under-oxidation from 1.00 to 2.50 equivalents Orange CRET.

Our explanation for this behavior is that the Orange CRET counter-ion, hexachloroantimonate, possesses some intrinsic oxidizing power of its own, which is additive to that of the Orange CRET radical cation. However, the hexachloroantimonate anion must only be a strong enough oxidant to effect the first oxidation, but too weak to effect the second. Further, it

must also be the case that our Orange CRET is impure, thus explaining the need for more than 2.00 equivalents to fully oxidize **TAPD** to the dication species.

We thus sought an alternative one-electron oxidant which would possess an electrochemically inactive counter-ion for subsequent redox titration experiments.

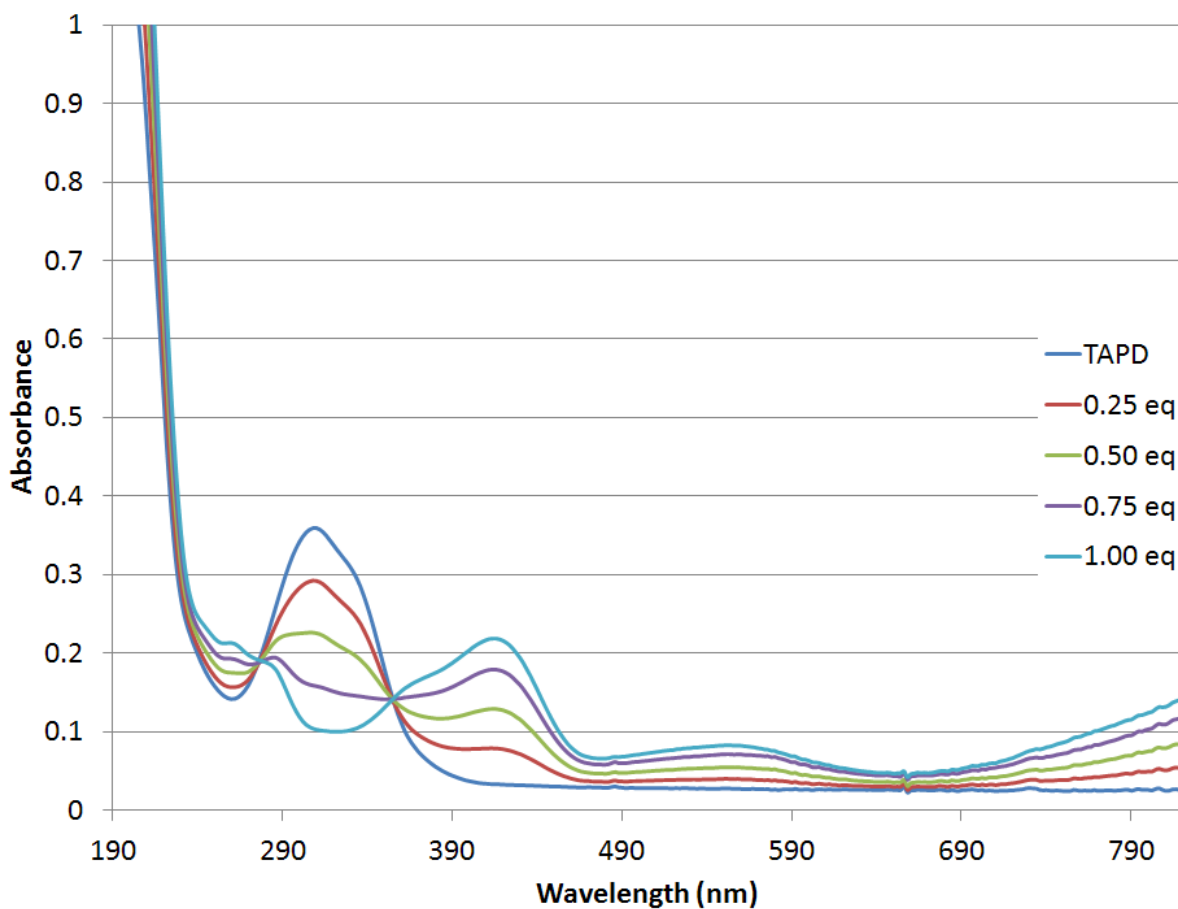


Figure 3.4.3. Redox titration of **TAPD** (1.03×10^{-5} M in acetonitrile) with CAN to 1.0 equivalent

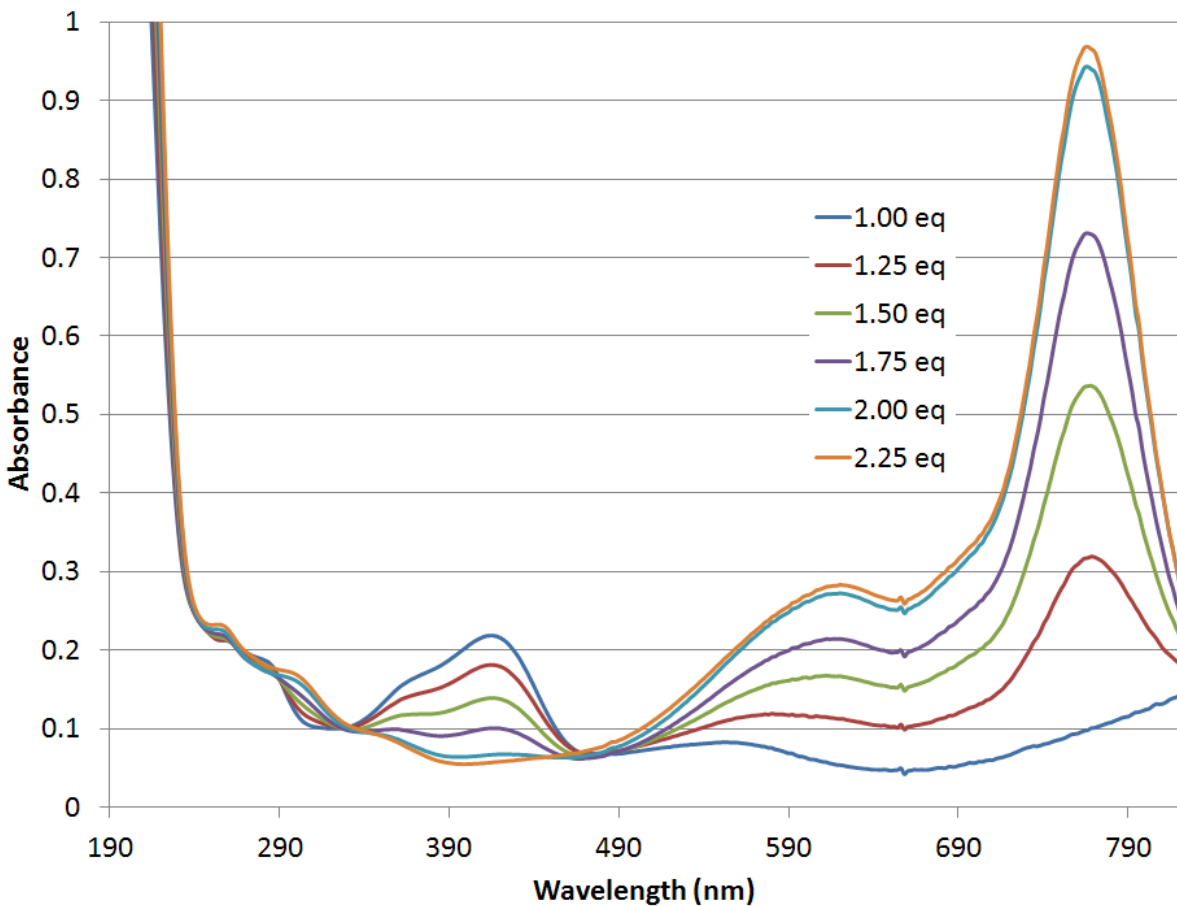


Figure 3.4.4. Redox titration of **TAPD** (1.03×10^{-5} M in acetonitrile) with CAN from 1.0 to 2.25 equivalents

3.5 Solvent Stability Testing of TAPD Salts

Although solid TAPD salts are stable indefinitely at low temperature (-20 °C), in solution, they tend to be unstable. Since we desired to grow high-quality crystals for XRD analysis, it was of great importance to us to find solvent conditions which would allow the **TAPD** salts to remain sufficiently stable for recrystallization.

Acetonitrile was chosen as our first candidate for stability testing, as our initial recrystallization attempts found it promising. **TAPD⁺(PF₆)** was found to have sufficient stability in HPLC-grade acetonitrile, as Figure 3.5.1 demonstrates.

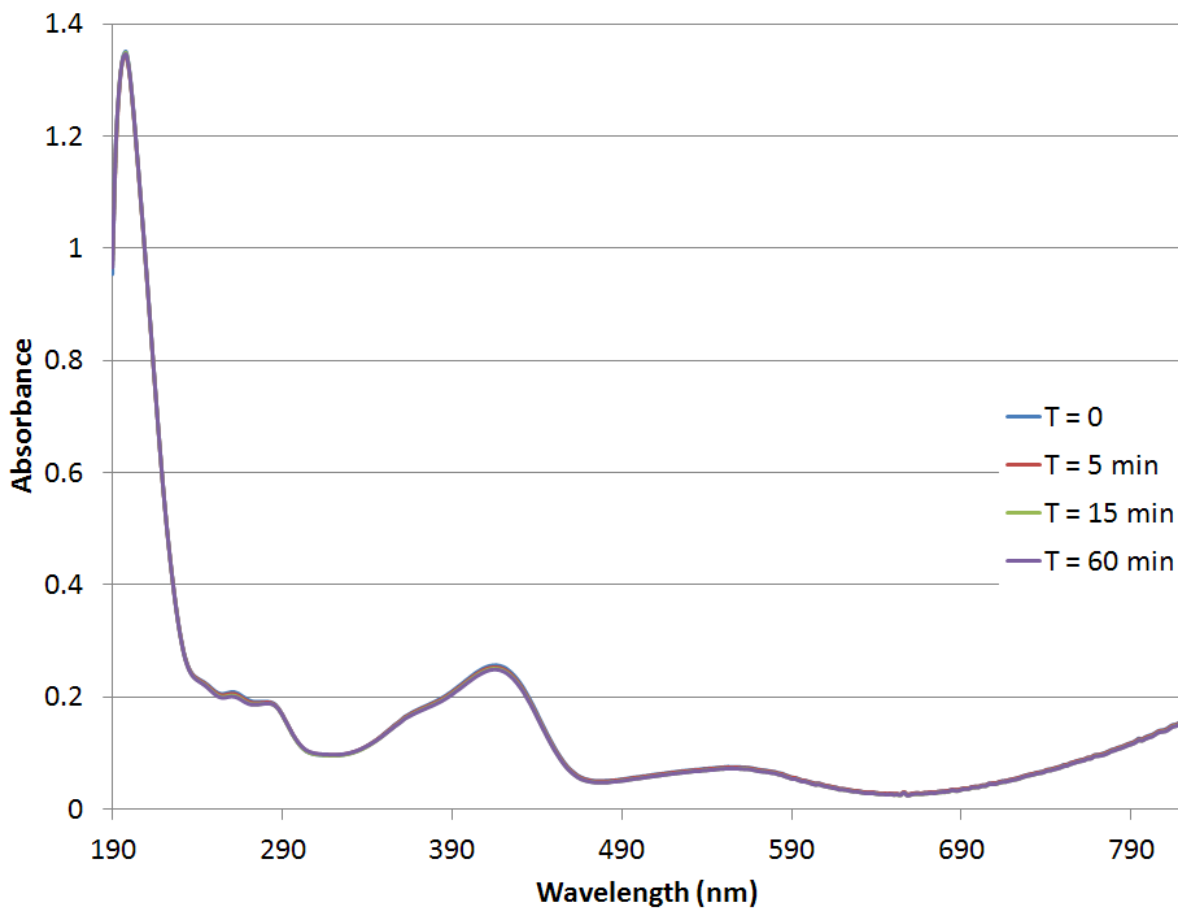


Figure 3.5.1. Stability of **TAPD⁺(PF₆)** (1.29×10^{-5} M in HPLC-grade acetonitrile) monitored by UV-vis

The monocation shows only a minimal amount of decay under these conditions. Unfortunately, such was not the case with dication. **TAPD^{++(PF₆)₂}** showed a much higher degree of inherent instability in solution. Figure 3.5.2 depicts the clear decay of **TAPD^{++(PF₆)₂}** in HPLC-grade acetonitrile.

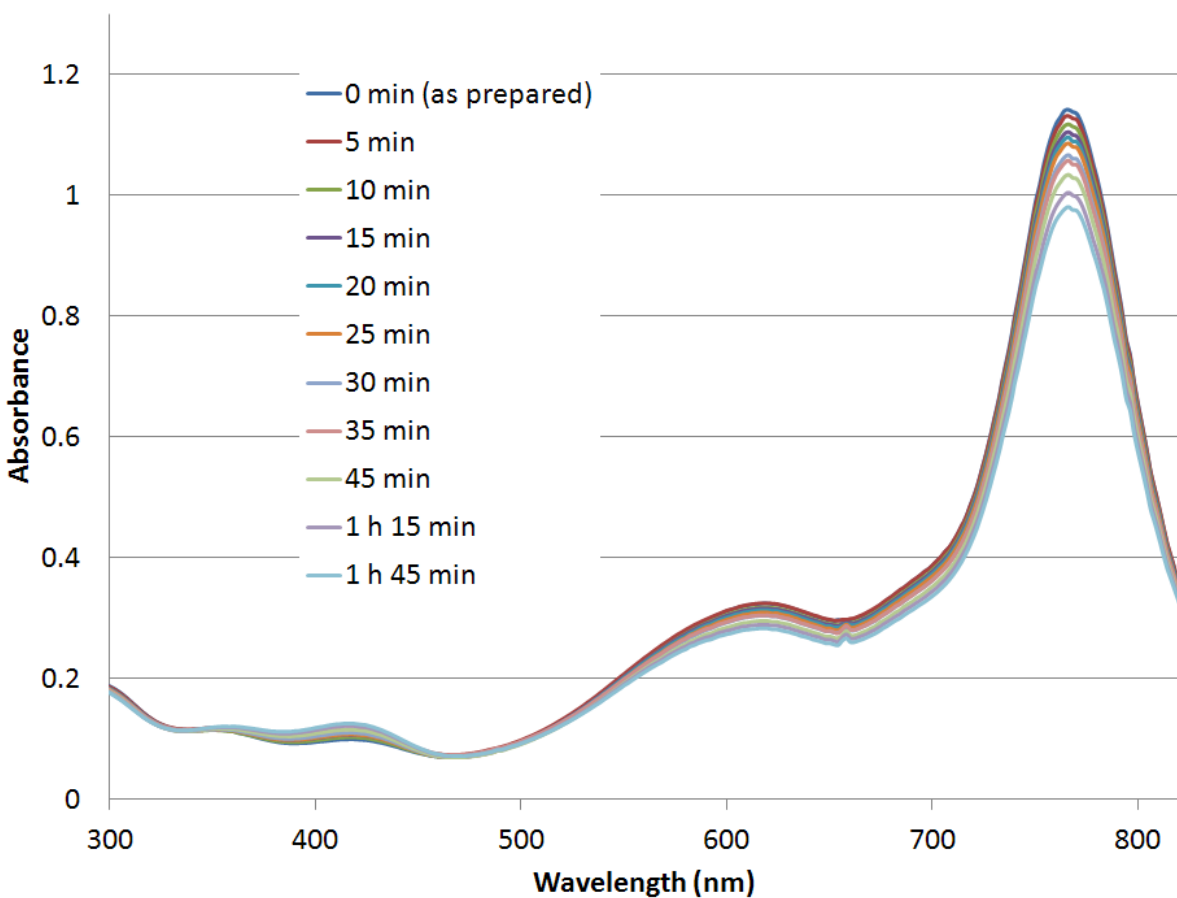


Figure 3.5.2. Stability of $\text{TAPD}^{++}(\text{PF}_6)_2$ (1.07×10^{-5} M in HPLC-grade acetonitrile) monitored by UV-vis

The data shows a relatively short lifetime for $\text{TAPD}^{++}(\text{PF}_6)_2$ in acetonitrile. The dication is being reduced to the radical cation by acetonitrile at a rate far too fast to be feasible for use as a recrystallization solvent. Any crystals formed would likely be a mixture of the two species.

The cause of this reduction was unclear. We thought perhaps that trace water present in the solvent may be at least partially responsible for this instability. Thus, we added 2.5 v/v% trifluoroacetic anhydride to the acetonitrile and again monitored the stability of $\text{TAPD}^{++}(\text{PF}_6)_2$ by UV-vis (Figure 3.5.3).

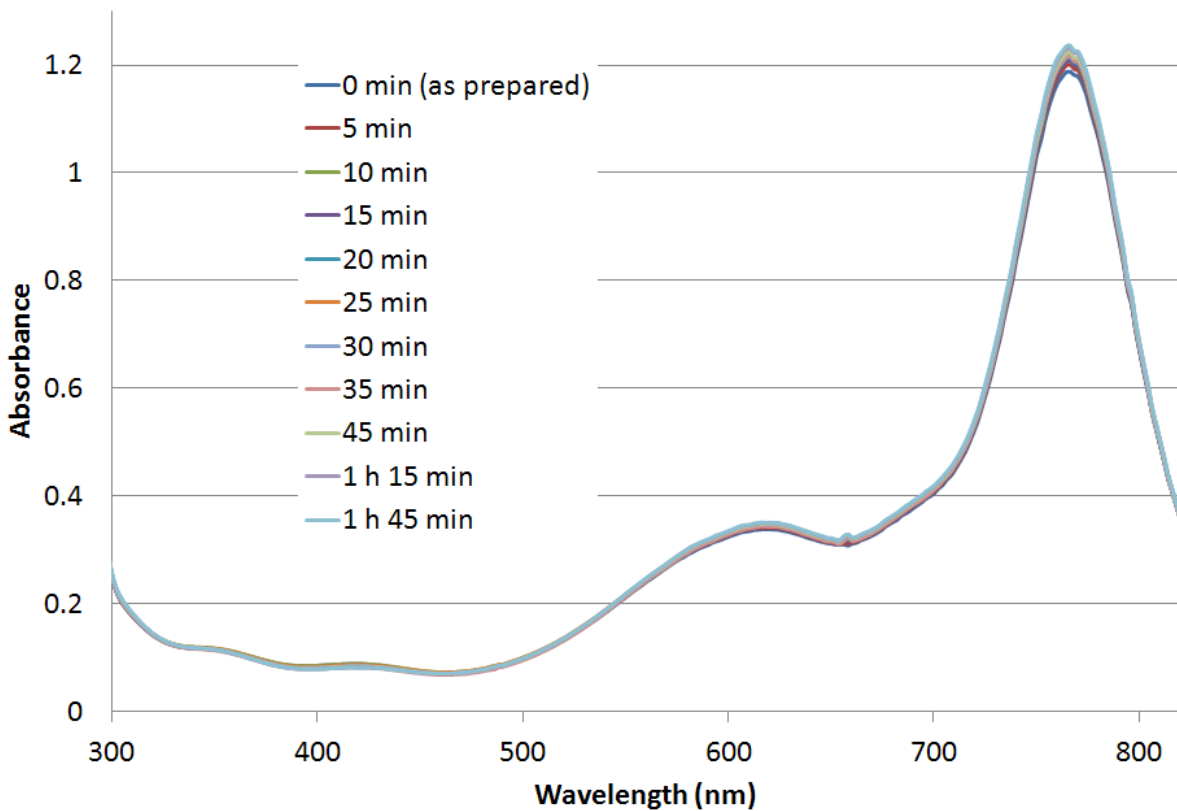


Figure 3.5.3. Stability of $\text{TAPD}^{++}(\text{PF}_6)_2$ (1.07×10^{-5} M in HPLC-grade acetonitrile) with 2.5 v/v% TFAA monitored by UV-vis

To our surprise, not only did the addition of TFAA halt the reduction of $\text{TAPD}^{++}(\text{PF}_6)_2$ to radical cation, it actually *increased* the concentration of dication from baseline over time, eventually reaching an end point between 75 and 105 minutes. By a mechanism unknown to us, TFAA (or TFA) acts as a strong enough oxidant to generate the dication species. Acetonitrile with TFAA (2.5 v/v%) was used for the recrystallization of $\text{TAPD}^{++}(\text{PF}_6)_2$.

3.6 Conductance Measurements

The conductive properties of $\text{TAPD}^+(\text{PF}_6)$ and $\text{TAPD}^{++}(\text{PF}_6)_2$ in the solid state were measured. The single-scan, powder pellet, I-V curve of $\text{TAPD}^+(\text{PF}_6)$ is shown in Figure 3.6.1. At 1.0 volt applied potential, the current reaches a maximum of 2.25×10^{-7} A. This number is borderline for being considered semiconductive. The step-potentials, both positive and negative, show the same behavior (Figures 3.6.2 and 3.6.3).

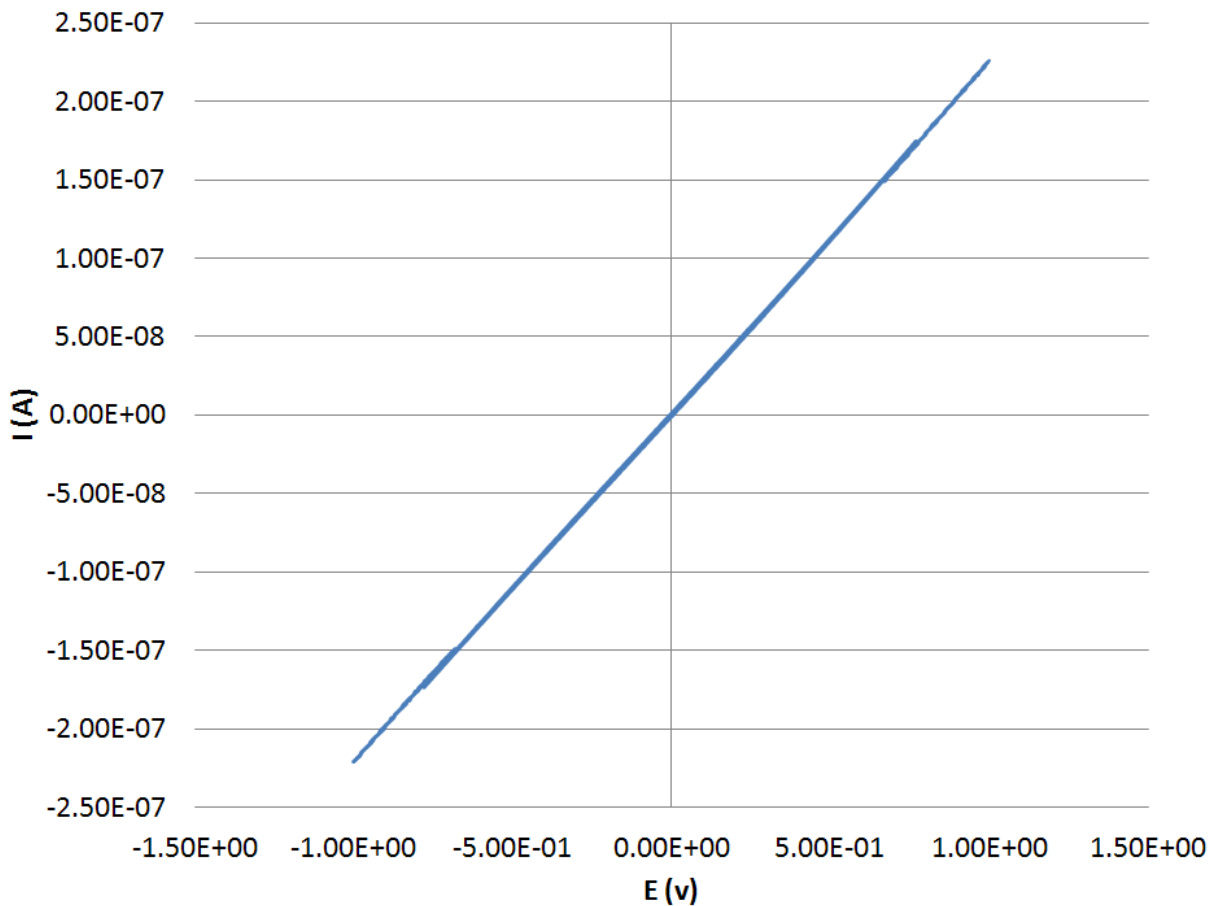


Figure 3.6.1. Powder pellet I-V curve of $\text{TAPD}^+(\text{PF}_6)$ – 12.0 mg, 20 mV/s

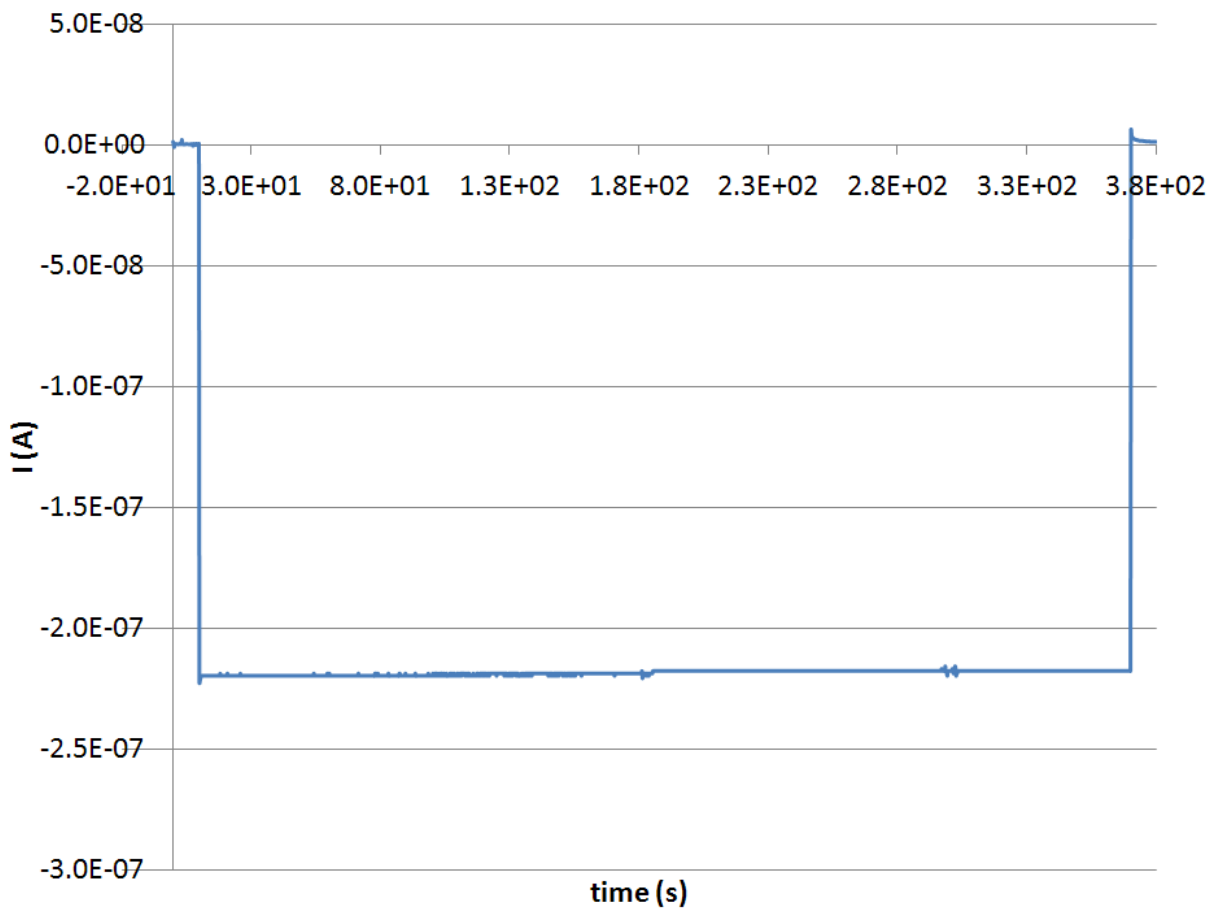


Figure 3.6.2. Powder pellet step-potential of $\text{TAPD}^+(\text{PF}_6^-)$ – 12.0 mg, -1.0 V, 360 s

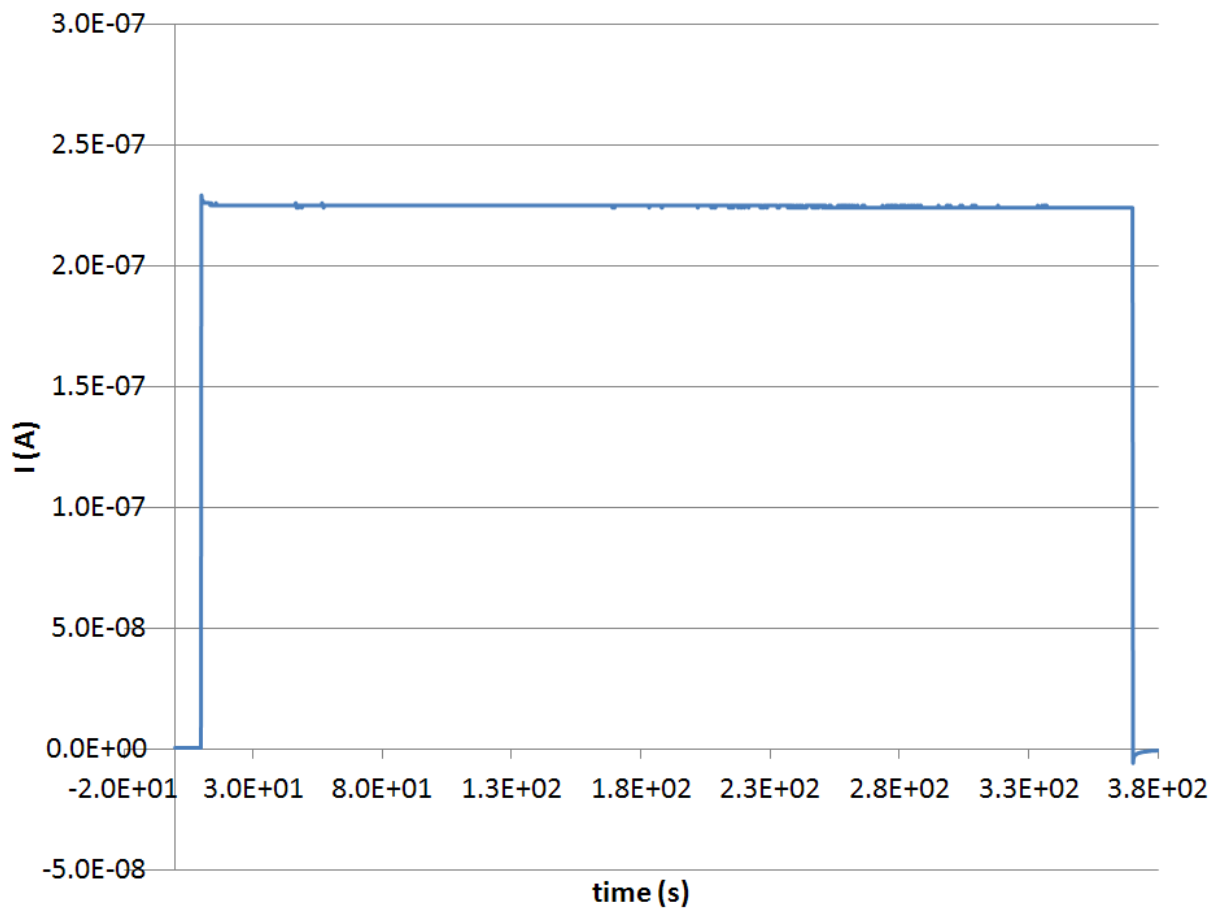


Figure 3.6.3. Powder pellet step-potential of $\text{TAPD}^+(\text{PF}_6^-)$ – 12.0 mg, +1.0 V, 360 s

The single-scan, powder pellet I-V curve of **TAPD⁺⁺(PF₆)₂** is shown in Figure 3.6.4. As opposed to **TAPD⁺(PF₆)**, which showed a linear I-V curve, **TAPD⁺⁺(PF₆)₂** demonstrates a substantial degree of hysteresis. It is unclear to us at this time what this behavior implies. It may be that there is some mobility of ions during the timescale of the experiment, which would indicate that **TAPD⁺⁺(PF₆)₂** is a non-ohmic material. This non-linear behavior is likewise observed in the step-potential experiments (Figures 3.6.5 and 3.6.6).

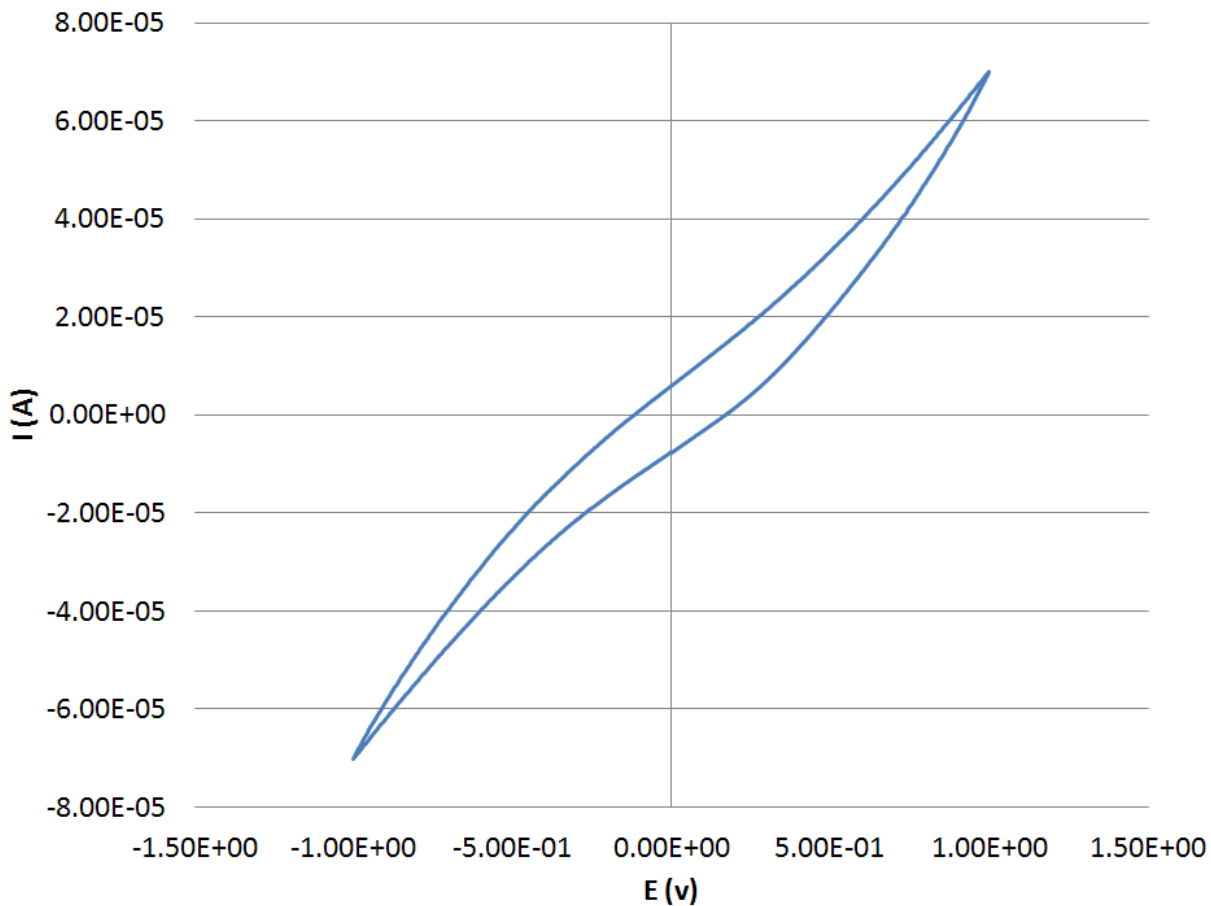


Figure 3.6.4. Powder pellet I-V curve of **TAPD⁺⁺(PF₆)₂** – 17.3 mg, 20 mV/s

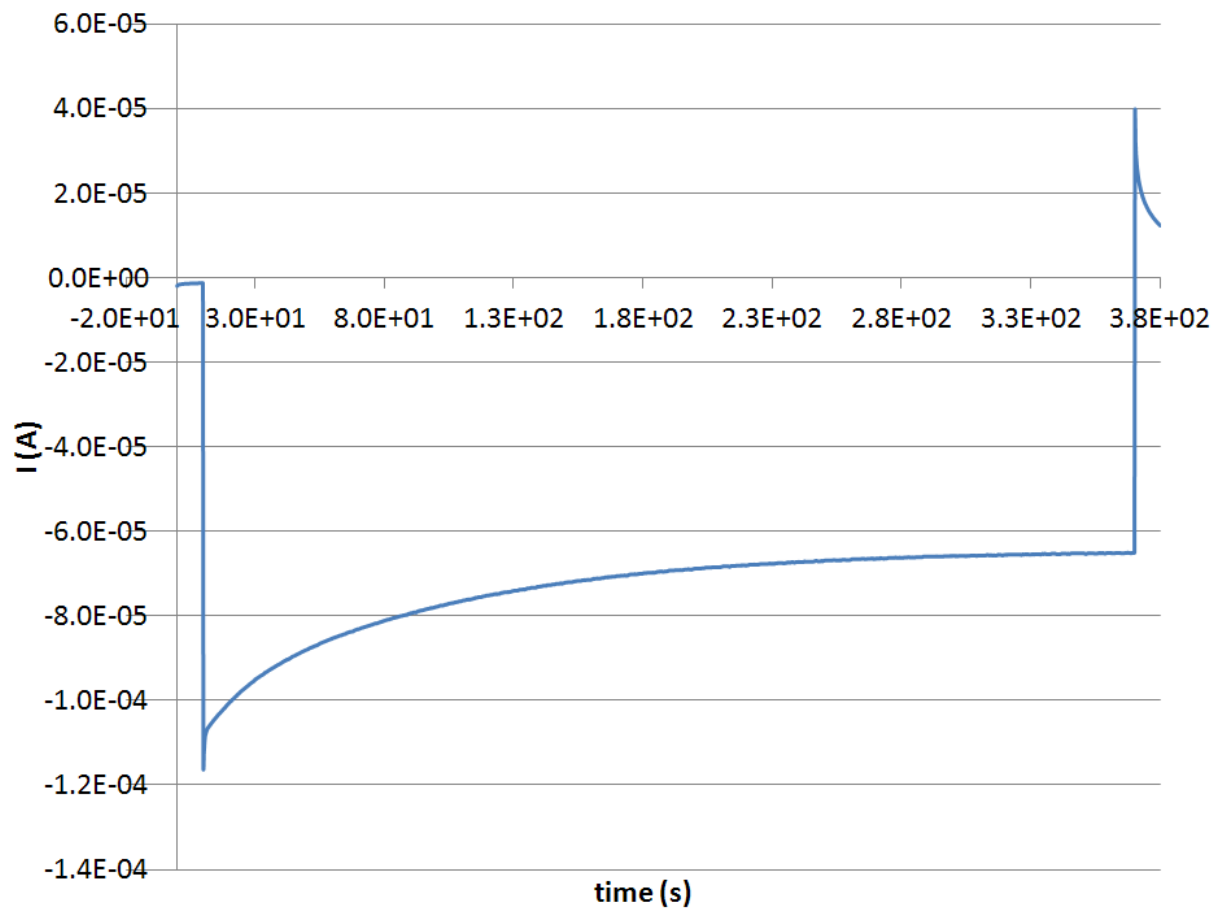


Figure 3.6.5. Powder pellet step-potential of $\text{TAPD}^{++}(\text{PF}_6)_2$ – 17.3 mg, -1.0 V, 360 s

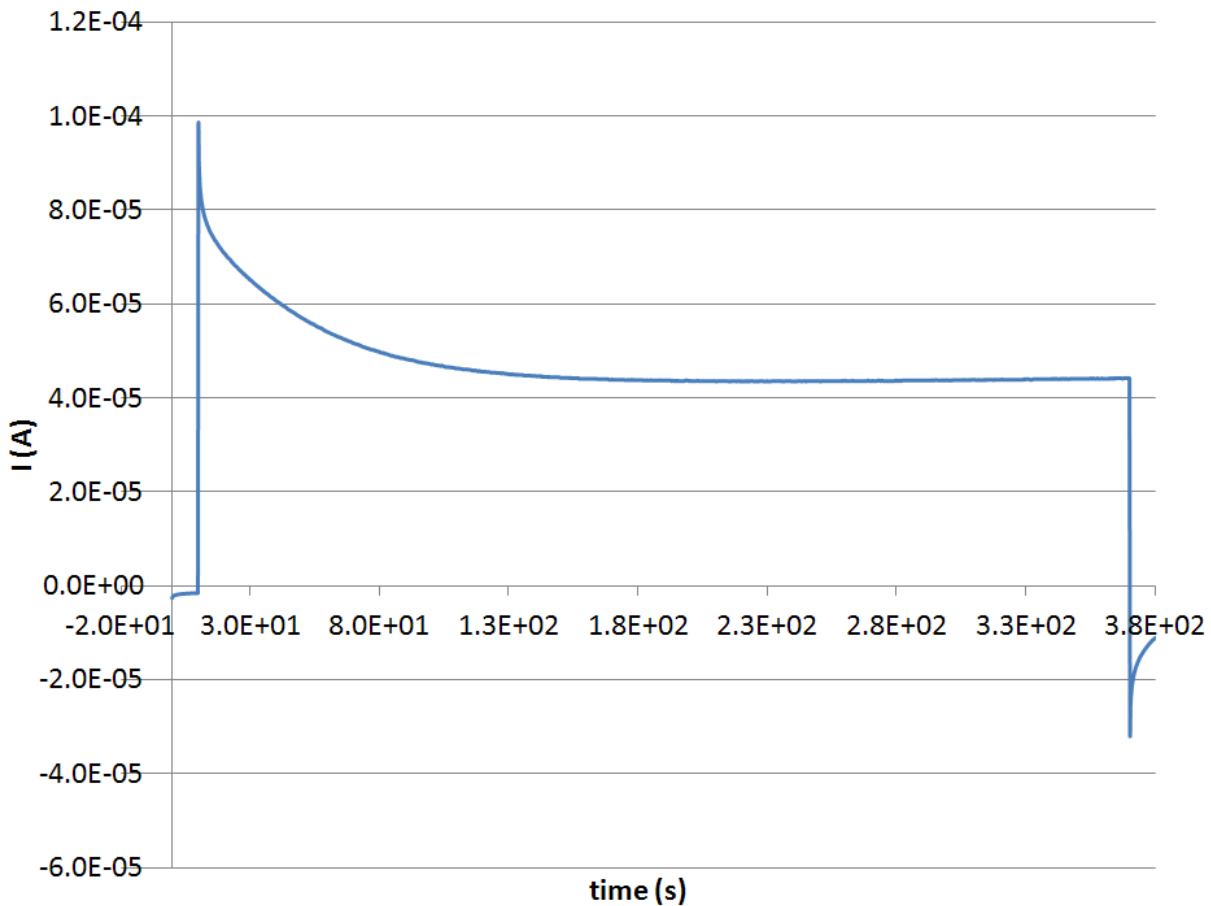


Figure 3.6.6. Powder pellet step-potential of $\text{TAPD}^{++}(\text{PF}_6)_2$ – 17.3 mg, +1.0 V, 360 s

To test this further, we subjected the $\text{TAPD}^{++}(\text{PF}_6)_2$ sample to a high number of I-V scans to look for an increase in current and/or hysteresis over an extended period of cycled potential. The multi-scan I-V curve of $\text{TAPD}^{++}(\text{PF}_6)_2$ is shown in Figure 3.6.7. The results show that both the current and the degree of hysteresis increased substantially during the course of the experiment. Seeking to test the limits of this behavior, the number of scans was doubled to 256 (Figure 3.6.8).

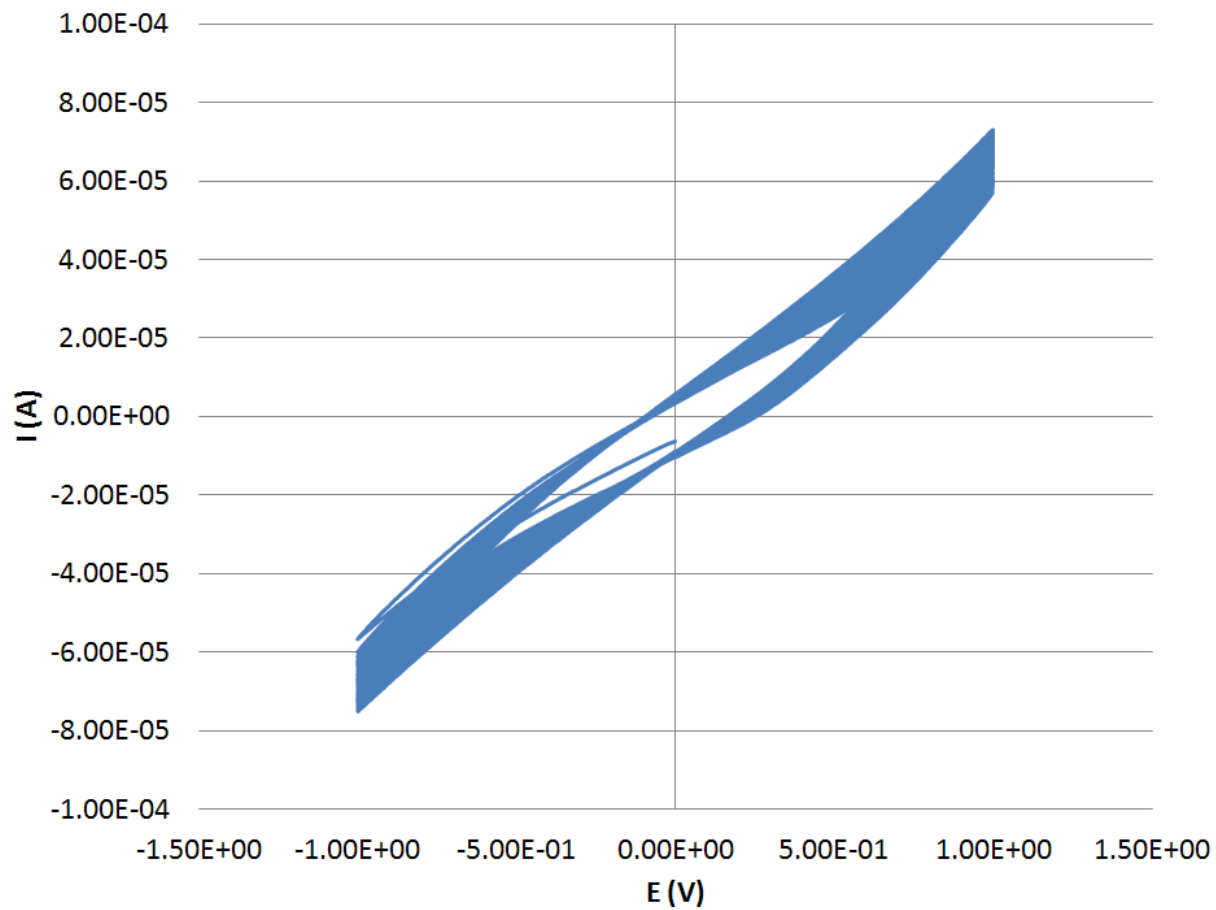


Figure 3.6.7. Powder pellet I-V curve of $\text{TAPD}^{++}(\text{PF}_6)_2$ – 17.3 mg, 200 mV/s, 128 scans

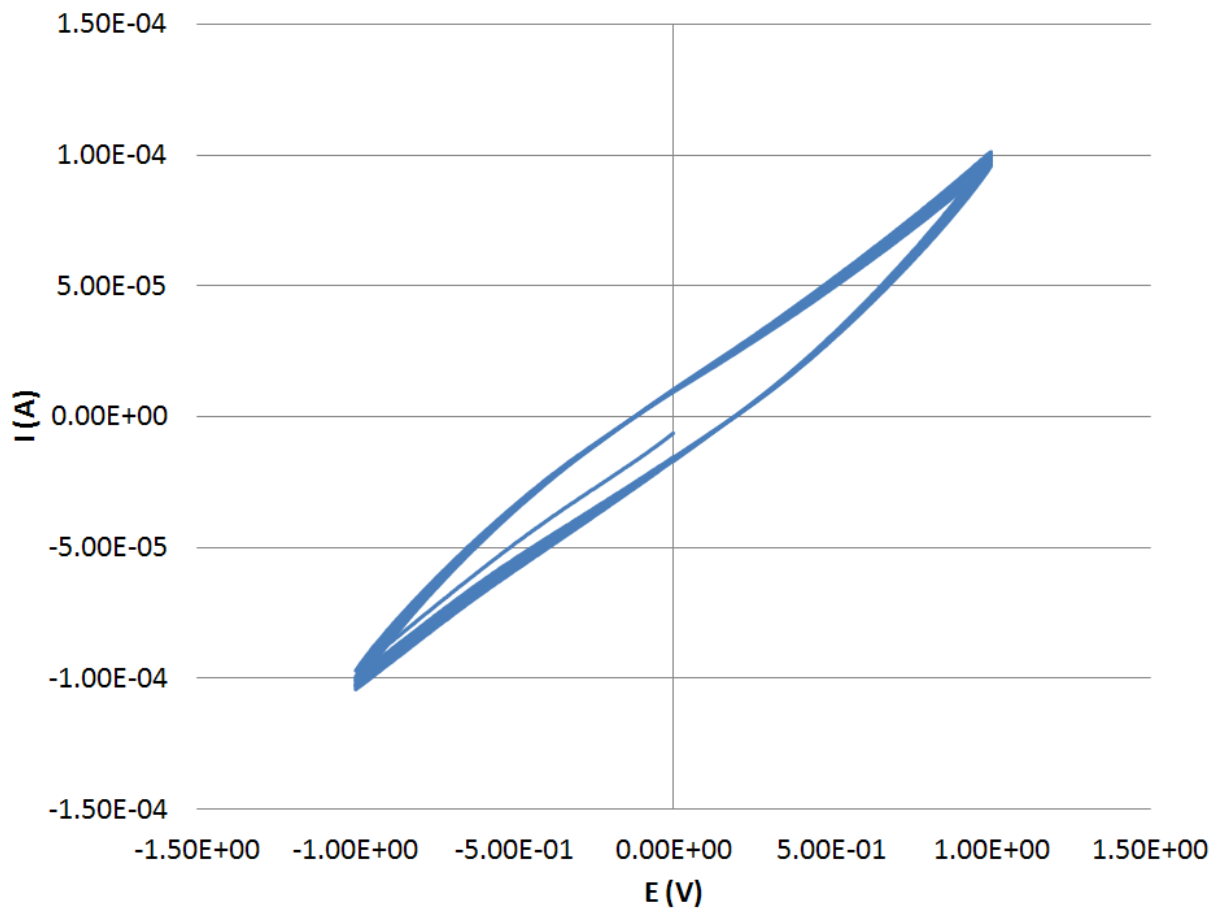


Figure 3.6.8. Powder pellet I-V curve of $\text{TAPD}^{+}(\text{PF}_6)_2$ – 17.3 mg, 200 mV/s, 256 scans

3.7 Conclusions

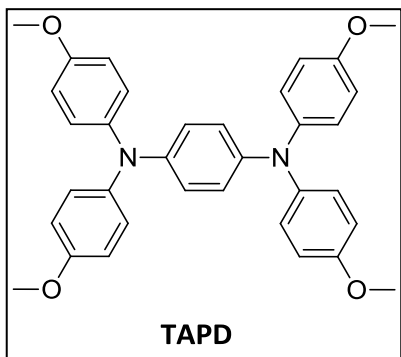
We have examined various properties of two novel organic semiconductive materials, $\text{TAPD}^+(\text{PF}_6)$ and $\text{TAPD}^{++}(\text{PF}_6)_2$. As mentioned previously, this data is preliminary, and more work is needed to determine the full capabilities of $\text{TAPD}^+(\text{PF}_6)$ and $\text{TAPD}^{++}(\text{PF}_6)_2$. For now, it can only be said that the results are intriguing, and warrant further research.

3.8 Experimental

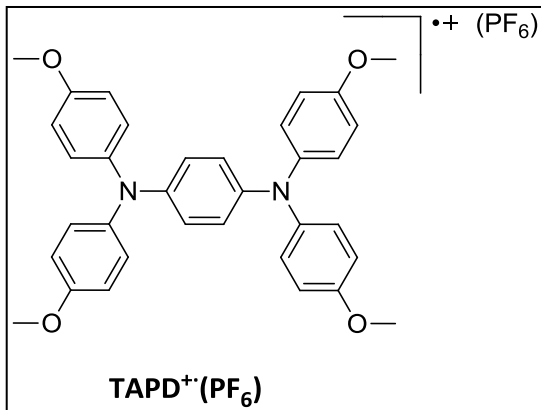
General Methods and Materials.

All reagents were purchased from *Aldrich Chemical Company*. *p*-phenylenediamine was purified by sublimation. HPLC-grade acetonitrile was purchased from *Aldrich Chemical Company* and used without further purification. ^1H -NMR spectra were recorded on Bruker AM-500 or AM-360 instruments with chemical shifts reported relative to the deuterated solvent or TMS. Solution CV was performed on a PAR 273 electrochemical potentiostat (EG&G Instruments). Tetrabutylammonium tetrafluoroborate (TBABF_4), a supporting electrolyte, was purchased from *TCI America* and was purified according to standard literature procedures,⁴¹ or recrystallized from 30 % ethanol three times, then dried in a vacuum oven (100 °C, 0.1 Torr). UV-vis spectra were collected on a Hewlett Packard 8452A diode array spectrophotometer. Methylene chloride, a CV solvent (Fisher) was pre-dried by stirring over H_2SO_4 , washed & neutralized, and finally distilled from CaH_2 under nitrogen atmosphere according to standard literature procedures.⁴¹ Solid-state CV and step-potentials were performed on a custom apparatus of Dr. Thomas Vaid's design, powered by a 263A electrochemical potentiostat/galvanostat (EG&G Instruments). Crystal diffraction data was gathered on a Siemens CCD SMART diffractometer.

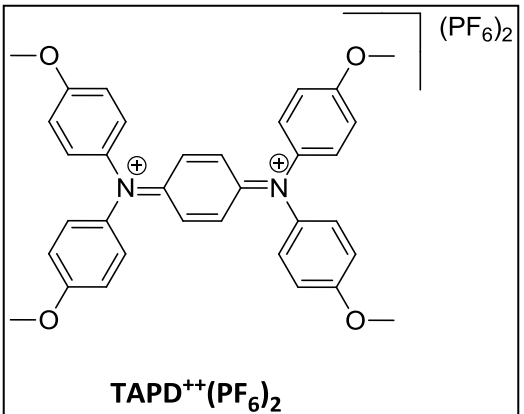
Synthesis



p-Phenylenediamine (3.00 g, 27.8 mmol) and 4-bromoanisole (20.80 g, 111.2 mmol) were placed in a flame-dried 500 mL round-bottom flask with magnetic stir bar inside a dry box. The reagents were dissolved in anhyd toluene (200 mL), and Pd(dba)₂ (0.128 g, 0.222 mmol), P(*t*-Bu)₃ (0.045 g, 0.22 mmol), and NaOt-Bu (16.03 g, 1668 mmol) were added. The reaction mixture was removed from the drybox and stirred under N₂ on a 60 °C oil bath for 20 h. The reaction mixture was taken up in ethyl acetate (~200 mL) and filtered through a 60 x 20 mm plug of basic alumina (activity III) under a 60 x 10 mm plug of celite. The filtrate was concentrated in vacuo to give a brown sticky solid. Recrystallization from ether gave pale yellow crystals (11.84 g, 80 %): mp = 155-158 °C, lit³² = 160 °C. ¹H-NMR (500 MHz, CDCl₃) δ 7.30-6.55 (br m, 20 H), 3.79 (s, 12H).



TAPD (0.532 g, 1.00 mmol) was stirred in HPLC-grade acetonitrile (100 mL) with N₂ purge. NOPF₆ (0.175 g, 1.00 mmol) was added in small portions over a period of 10 min. The reaction flask was transferred directly to a rotary evaporator and the solvent was removed in vacuo. Collected a dark blue-black crystalline solid (0.623 g, 92 %): λ_{max} (acetonitrile) = 414 nm (ε = 10100).



TAPD (0.532 g, 1.00 mmol) was stirred in HPLC-grade acetonitrile (100 mL) with N₂ purge. NOPF₆ (0.350 g, 2.00 mmol) was added in small portions over a period of 10 min. The reaction flask was transferred directly to a rotary evaporator and the solvent was removed in vacuo. Collected a copper-colored crystalline solid (0.750 g, 85 %): λ_{max} (acetonitrile) = 766 nm (ϵ = 72500).

REFERENCES

- (1) Nagano, T.; Jia, Z.; Li, X.; Yan, M.; Lu, G.; Chan, A. S. C.; Hayashi, T. Redox Catalysis of Halide Ion for Formal Cross-dehydrogenative Coupling: Bromide Ion-catalyzed Direct Oxidative α -Acetoxylation of Ketones. *Chem. Lett.* **2010**, 39, 929-931.
- (2) Uranga, J. G.; Santiago, A. N. Reactions of Halonorbornane and Oxo-substituted Derivatives with Different Anions by the Electron Transfer Mechanism; Redox Catalysis in Stabilized Radicals. *New J. Chem.* **2010**, 34, 2006-2012.
- (3) Hernandez-Munoz, L. S.; Fragoso-Soriano, R. J.; Vazquez-Lopez, C.; Klimova, E.; Ortiz-Frade, L. A.; Astudillo, P. D.; Gonzalez, F. J. Modification of Carbon Surfaces with Methyl Groups by using Ferrocene Derivatives as Redox Catalysts of the Oxidation of Acetate Ions. *J. Electroanal. Chem.* **2010**, 650, 62-67.
- (4) Scialdone, O.; Galia, A.; Silvestri, G.; Amatore, C.; Thouin, L.; Verpeaux, J-N. Electrocaryoxylation of Benzyl Halides through Redox Catalysis on the Preparative Scale. *Chem. Eur. J.* **2006**, 12, 7433-7447.
- (5) Lin, S.; Ischay, M. A.; Fry, C. G.; Yoon, T. P. Radical Cation Diels-Alder Cycloadditions by Visible Light Photocatalysis. *J. Am. Chem. Soc.* **2011**, 133, 19350-19353.
- (6) Cristol, S. J.; Snell, R. L. Bridged Polycyclic Compounds. VI. The Photoisomerization of Bicyclo[2.2.1]hepta-2,5-diene-2,3-dicarboxylic Acid to Quardricyclo[2.2.1.0^{2,6}.0^{3,5}]heptane-2,3-dicarboxylic Acid. *J. Am. Chem. Soc.* **1958**, 80, 1950-1952.
- (7) Dauben, W. G.; Cargill, R. L. Photochemical Transformations – VIII The Isomerization of $\Delta^{2,5}$ -Bicyclo[2.2.1]heptadiene to Quadricyclo[2.2.1.0^{2,6}.0^{3,5}]heptane (Quadricyclene). *Tetrahedron* **1961**, 15, 197-201.
- (8) Kabakoff, D. S.; Bünzli, J-C. G.; Oth, J. F. M.; Hammond, W. B.; Berson, J. A. Enthalpy and Kinetics of Isomerization of Quadricyclane to Norbornadiene. Strain Energy of Quadricyclane. *J. Am. Chem. Soc.* **1975**, 97, 1510-1512.

- (9) For a review see: Dubosonov, A. D.; Bren, V. A.; Chernoivanov, V. A. Norbornadiene-Quadricyclane as an Abiotic System for the Storage of Solar Energy. *Russ. Chem. Rev.* **2002**, *71*, 917-927.
- (10) Gassman, P. G.; Yamaguchi, R. Electron Transfer from Highly Strained Polycyclic Molecules. *Tetrahedron* **1982**, *38*, 1113-1122.
- (11) Gassman, P. G.; Hershberger, J. W. An Electrochemical "Switch" for Starting and Stopping the Energy-Releasing Conversion of Quadricyclanes to Norbornadienes. *J. Org. Chem.* **1987**, *52*, 1337-1339.
- (12) Arai, T.; Oguchi, T.; Wakabayashi, T.; Tsuchiya, M.; Nishimura, Y; Oishi, S.; Sakuragi, H.; Tokumaru, K. Mechanistic Approach to the Sensitization Process of Aromatic Ketone in the Isomerization between Norbornadiene and Quadricyclane. *Bull. Chem. Soc. Jpn.* **1987**, *60*, 2937-2943.
- (13) Cupoletti, A.; Dinnocenzo, J. P.; Goodman, J. L.; Gould, I. R. Bond-Coupled Electron Transfer Reactions: Photoisomerization of Norbornadiene to Quadricyclane. *J. Phys. Chem. A* **1999**, *103*, 11253-11256.
- (14) Hammond, G. S.; Turro, N. J.; Fischer, A. Photosensitized Cycloaddition Reactions. *J. Am. Chem. Soc.* **1961**, *83*, 4674-4675.
- (15) Murov, S. L.; Cole, R. S.; Hammond, G. S. Mechanisms of Photochemical Reactions in Solution, LIV. A New Mechanism for Photosensitization. *J. Am. Chem. Soc.* **1968**, *90*, 2957-2958.
- (16) Gorman, A. A.; Hamblett, I.; McNeeney, S. P. Sensitization of the Norbornadiene to Quadricyclene Conversion by Substituted Benzophenones: Evidence against Biradical Intermediacy. *Photchem. Photobiol.* **1990**, *51*, 145-149
- (17) Kalsi, P. S. *Organic Reactions and Their Mechanisms*, 2nd ed.; New Age International Publishers: New Dehli, 2000.
- (18) Rosi, M.; Sgamellotti, A. Use of Norbornadiene in Solar Energy Storage: Theoretical Study of a Copper(I) Photosensitizer for the Norbornadiene-Quadricyclane Transformation. *Inorg. Chem.* **1999**, *38*, 1520-1522.
- (19) Diffey, B. L. Solar Ultraviolet Radiation Effects on Biological Systems. *Phys. Med. Biol.* **1991**, *36*, 299-328.
- (20) Kaupp, G.; Prinzbach, H. Photochemical Conversions. XXX. Kinetics of the Norbornadiene-Quadricyclane Photocycloaddition. *Helv. Chim. Acta* **1969**, *52*, 956-966.

- (21) Ikezawa, H.; Katal, C.; Yasufuku, K.; Yamazaki, H. Direct and Sensitized Valence Photoisomerization of a Substituted Norbornadiene. Examination of the Disparity between Singlet- and Triplet-State Reactivities. *J. Am. Chem. Soc.* **1986**, *108*, 1589-1594.
- (22) Minkin, V. I.; Bren, V. A.; Chernoivanov, V. A.; Dubonosov, A. D.; Galichev, S. V. Photochromic Behavior of 2,3-Substituted Norbornadienes. *Mol. Cryst. Liq. Cryst. Sci. Technol., Sect. A* **1994**, *246*, 151-154.
- (23) Fraysse, S.; Coudret, C.; Launay, J-P. Synthesis and Properties of Dinuclear Complexes with a Photochromic Bridge: An Intervalence Electron Transfer Switching “On and “Off”. *Eur. J. Inorg. Chem.* **2000**, *7*, 1581-1590.
- (24) Nagai, T.; Fujii, K.; Takahashi, I.; Shimada, M. Trifluoromethyl-Substituted Donor-Acceptor Norbornadiene, Useful Solar Energy Material. *Bull. Chem. Soc. Jpn.* **2001**, *74*, 1673-1678.
- (25) De Luchi, O.; Licini, G.; Pasquato, L.; Senta, M. Reactivity of Phenyl(toluenesulfonyl)acetylene Towards Dienes and Homo-dienes: Cycloadditions Versus Fragmentation-Addition Reactions. *Tetrahedron Lett.* **1988**, *29*, 831-834.
- (26) Das, B.; Srinivas, Y.; Sudhakar, C.; Damodar, K.; Narender, R. Efficient Bromination of Alkenes and Alkynes Using Potassium Bromide and Diacetoxy Iodobenzene. *Syn. Commun.* **2009**, *39*, 220-227.
- (27) Das, B.; Srinivas, Y.; Sudhakar, C.; Ravikanth, B. Bromination of Alkenes and Alkynes with (Bromodimethyl)sulfonium Bromide. *J. Chem. Res.* **2008**, (4), 188-190.
- (28) Modified from: Dakka, J.; Sasson, Y. Bromination of α -Substituted Alkylbenzenes: Synthesis of (*p*-Bromophenyl)acetylene. *J. Org. Chem.* **1989**, *54*, 3224-3226.
- (29) Adapted from: Nair, V.; Augustine, A.; Suja, T. D. CAN Mediated Reaction of Aryl Sulfinate with Alkenes and Alkynes: Synthesis of Vinyl Sulfones, β -Iodovinyl Sulfones and Acetylenic Sulfones. *Synthesis* **2002**, *15*, 2259.
- (30) For a related example see: Davis, A. P.; Whitham, G. H. Ethynyl p-Tolyl Sulfone as an Acetylene Equivalent in Diels-Alder Reactions. *J. Chem. Soc., Chem Commun.* **1980**, *13*, 639-640.
- (31) Adapted from: Alcazar-Roman, L. M.; Hartwig, J. F.; Hauck, S. I.; Kawatsura, M.; Shaughnessy, K. H. Transition-metal catalyzed process for preparing N-aryl amine compounds. U.S. Patent 6,100,398, August 8, 2000.

- (32) Selby, T. D. Polyarylamino Redox Arrays for Control of Spin Alignment and Charge Transport. Ph.D Dissertation, University of Alabama, Tuscaloosa, AL, May 2001.
- (33) Montalti, M.; Credi, A.; Prodi, L.; Gandolfi, M. T. *Handbook of Photochemistry*, 3rd ed.; CRC Press: Boca Raton, 2006.
- (34) Hatchard, C. G.; Parker, C. A. A New Sensitive Chemical Actinometer. II. Potassium Ferrioxalate as a Standard Chemical Actinometer. *Proc. Roy. Soc. A* **1956**, 235, 518-536.
- (35) Kuhn, H. J.; Braslavsky, S. E.; Schmidt, R. Chemical Actinometry (IUPAC Technical Report). *Pure Appl. Chem.* **2004**, 76, 2105-2146.
- (36) Lee, J.; Kim, J.; Choi, W. Ferrioxalate-Polyoxometalate System as a New Chemical Actinometer. *Environ. Sci. Technol.* **2007**, 41, 5433-5438.
- (37) Maafi, M.; Aaron, J-J.; Lion, C. Direct Valence Isomerization of Newly Synthesized Norbornadiene Aromatic Derivatives. A Kinetic and Photophysical Study. *Chem. Lett.* **1994**, 10, 1865-1868.
- (38) Maafi, M.; Lion, C.; Aaron, J-J. Synthesis, Photophysical Properties, and Valence Photoisomerization of New Fluorescent Aromatic Norbornadienes. *New J. Chem.* **1996**, 20, 559-570.
- (39) Bren, V. A.; Minkin, V. I.; Dubonosov, A.D.; Chernovivanov, V. A.; Rybalkin, V. P., Borodkin, G. S. Biphotochromic Norbornadiene Systems. *Mol. Cryst. Liq. Cryst. Sci. Technol., Sect. A* **1997**, 297, 247-253.
- (40) Rathore, R.; Kochi, J. K. Isolation of Novel Radical Cations from Hydroquinone Ethers. Conformational Transition of the Methoxy Group upon Electron Transfer. *J. Org. Chem.* **1995**, 60, 4399-4411.
- (41) Perrin, D. D. and Armarego, W. L. F., *Purification of Laboratory Chemicals*, Pergamon Press: Oxford, 1988.
- (42) Das, B.; Srinivas, Y.; Sudhakar, C.; Damodar, K.; Narendar, R. PMA/SiO₂, an Efficient and Reusable Heterogenous Catalyst for the Synthesis of β-Acetamidocarbonyl Compounds by Multicomponent Reaction. *Synth. Commun.* **2009**, 39, 220-227.
- (43) Sasson, Y.; Dakka, J. Bromination of α-Substituted Alkylbenzenes: Synthesis of (p-Bromophenyl)acetylene. *J. Org. Chem.* **1989**, 54, 3224-3226.

- (44) Chudomel, J. M.; Yang, B.; Barnes, M. D.; Achermann, M.; Mague, J. T.; Lahti, P. M. Highly Twisted Triarylamines for Photoinduced Intramolecular Charge Transfer. *J. Phys. Chem. A* 2011, **115**, 8361-8368.
- (45) Kim, K. Y. Polyarylamino Redox Arrays for Control of Charge Transport and Charge Storage. Ph.D. Dissertation, University of Alabama, Tuscaloosa, AL, May 2003.
- (46) Braga, D.; Grepioni, F.; Orpen, A. G. *Crystal Engineering: From Molecules and Crystals to Materials*, Kluwer Academic Publishers: Dordrecht, 1999.
- (47) Braga, D.; Grepioni, F. *Making Crystals by Design: Methods, Techniques and Applications*, WILEY-VCH Verlag GmbH & Co. KGaA: Weinheim, 2007.
- (48) Tiekenk, E. R. T.; Vittal, J. J. *Frontiers in Crystal Engineering*, John Wiley & Sons Ltd: West Sussex, 2006.
- (49) Desiraju, G. R. Crystal Enginering: A Brief Overview. *J. Chem. Sci.* **2010**, *122*, 667-675.
- (50) Aakeroy, C. B.; Champness, N. R.; Janiak, C. Recent Advances in Crystal Engineering. *CrystEngComm* **2010**, *12*, 22-43.
- (51) Steed, J. W.; Atwood, J. L. *Supramolecular Chemistry*, John Wiley & Sons Ltd: West Sussex, 2000.
- (52) Steed, J. W.; Turner, D. R.; Wallace, K. J. *Core Concepts in Supramolecular Chemistry and Nanochemistry*, John Wiley & Sons Ltd: West Sussex, 2007.
- (53) Lehn, J-M. Toward Complex Matter: Supramolecular Chemistry and Self-organization. *PNAS* **2002**, *99*, 4763-4768.
- (54) Fyfe, M. C. T.; Stoddart, F. F. Synthetic Supramolecular Chemistry. *Acc. Chem. Res.* **1997**, *30*, 393-401.
- (55) Shan, N.; Zaworotko, M. J. The Role of Cocrystals in Pharmaceutical Science. *Drug Discov. Today* **2008**, *13*, 440-446.
- (56) Desiraju, G. R. Crystal Engineering: From Molecules to Materials. *J. Mol. Struct.* **2003**, *656*, 5-15.
- (57) Mutheraman, M.; Masse, R.; Nicoud, J-F.; Desiraju, G. R. Molecular Complexation as a Design Tool in the Crystal Engineering of Noncentrosymmetric Structures. Ideal Orientation of Chromophores Linked by O-H---O and C-H---O Hydrogen Bonds for Nonlinear Optics. *Chem. Mater.* **2001**, *13*, 1473-1479.

- (58) Renuka, N.; Vijayan, N.; Rathi, B.; Babu, R. R.; Nagarajan, K.; Haranath, D.; Bhagavannarayana, G. Synthesis, Growth, and Optical Properties of Semi Organic Non Linear Optical Single Crystal: L-Arginine Acetate. *Optik*, **2012**, *123*, 189-192.
- (59) Glaser, R. Polar Order by Rational Design: Crystal Engineering with Parallel Beloamphiphile Monolayers. *Acc. Chem. Res.* **2007**, *40*, 9-17.
- (60) Bailey, R. T.; Cruickshank, F. R.; Dines, T. J.; Sherwood, N.; Tedford, M. C. A Single-crystal Raman and Infrared Study of the Nonlinear Optical Crystal MBANP. *J. Raman Spectrosc.* **2011**, *42*, 1174-1184.
- (61) Park, J. W.; Hong, H-K.; Lee K-S.; Yoon, C. S. Effect of Dimer Formation on the Growth Cessation of Polar Organic Crystals. *Cryst. Growth Des.* **2006**, *6*, 2011-2020.
- (62) Pralle, M. U.; Urayama, K.; Tew, G. N.; Neher, D.; Wegner, G.; Stupp, S. I. Piezoelectricity in Polar Supramolecular Materials. *Angew. Chem. Int. Ed.* **2000**, *39*, 1486-1489.
- (63) Weissflog, W.; Pelzl, G.; Kresse, H.; Baumeister, U.; Brand, K.; Schroder, M. W.; Tamba, M. G.; Findeisen-Tandel, S.; Kornek, U.; Stern, S.; Eremin, A.; Stannarius, R.; Svoboda, J. In Search of a New Design Strategy for Solid Single-component Organic Ferroelectrics: Polar Crystalline Phases Formed by Bent-core Molecules. *J. Mater. Chem.* **2010**, *20*, 6057-6079.
- (64) Ladd, M; Palmer, R. *Structure Determination by X-ray Crystallography*, 4th ed.; Kluwer Academic/Plenum Publishers: New York, 2003.
- (65) Stout, G. H.; Jensen, L. H. *X-ray Structure Determination: A Practical Guide*, 2nd Ed.; John Wiley & Sons: New York, 1989.
- (66) For a concise practical guide describing modern XRD techniques refer to: Massa, W. *Crystal Structure Determination.*; Springer-Verlag: Berlin Heidelberg, 2000.
- (67) Sheldrick, G. M. A Short History of SHELX. *Acta Cryst.* **2008**, *64*, 112-122.
- (68) Hohne, G. W. H.; Hemminger, W. F.; Flammersheim, H-J. *Differential Scanning Calorimetry*, 2nd Ed.; Springer-Verlag: Berlin Heidelberg, 2003.
- (69) Glaser, R.; Knotts, N.; Yu, P.; Li, L.; Chandrasekhar, M.; Martin, C.; Barnes, C. L. Perfect Polar Stacking of Parallel Beloamphiphile Layers. Synthesis, Structure and Solid-state Optical Properties of the Unsymmetrical Acetophenone Azine DCA. *Dalton Trans.* **2006**, 2891-2899.

- (70) Duncan, J. R. Changing the Redox-Gradient in Geometrically Equivalent Aryl Amines. Ph.D Dissertation, University of Alabama, Tuscaloosa, AL, May 2007.
- (71) Bondi, A. van der Waals Volumes and Radii. *J. Phys. Chem.* **1964**, *68*, 441-451.
- (72) Lahav, M.; Leiserowitz, L. A Stereochemical Approach that Demonstrates the Effect of Solvent on the Growth of Polar Crystals: A Perspective. *Cryst. Growth Des.* **2006**, *6*, 619-624.
- (73) Braga, D.; Grepioni, F.; Maini, L. The Growing World of Crystal Forms. *Chem. Commun.* **2010**, *46*, 6232-6242.
- (74) Hod, I.; Mastai, Y.; Medina, D. D. Effect of Solvents on the growth morphology of DL-Alanine Crystals. *CrystEngComm* **2011**, *13*, 502-509.
- (75) Rajakumar, P.; Rasheed, A. M. A. Synthesis, Characterization and Ion Transportation Studies of some Novel Cyclophane Amides. *Tetrahedron*, **2005**, *61*, 5351-5362.
- (76) Patoux, C.; Coudret, C.; Launay, J-P.; Joachim, C.; Gourdon, A. Topological Effects on Intramolecular Electron Transfer via Quantum Interference. *Inorg. Chem.* **1997**, *36*, 5037-5049.
- (77) Dong, H.; Wang, C.; Hu, W. High Performance Organic Semiconductors for Field-effect Transistors. *Chem. Commun.* **2010**, *46*, 5211-5222.
- (78) Operamolla, A; Farinola, G. M. Molecular and Supramolecular Architectures of Organic Semicunductors for Field-Effect Transistor Devices and Sensors: A Synthetic Chemical Perspective. *Eur. J. Org. Chem.* **2011**, 423-450.
- (79) Tang, M. L.; Bao, Z. Halogenated Materials as Organic Semiconductors. *Chem. Mater.* **2011**, *23*, 446-455.
- (80) Mishra, A.; Bauerle, P. Small Molecule Organic Semiconductors on the Move: Promises for Future Solar Energy Technology. *Angew. Chem. Int. Ed.* **2012**, *51*, 2020-2067.
- (81) Ruiz, C.; Garcia-Frutos, E. M.; Hennrich, G.; Gomez-Lor, B. Organic Semiconductors toward Electronic Devices: High Mobility and Easy Processability. *J. Phys. Chem. Lett.* **2012**, *3*, 1428-1436.

Appendix A

NMR Spectra

LIST OF NMR SPECTRA FOR SELECTED COMPOUNDS

Figure A1.	^1H -NMR Spectrum (360 MHz) of 1 in CDCl_3	158
Figure A2.	^1H -NMR Spectrum (360 MHz) of 3 in CDCl_3	159
Figure A3.	^{13}C -NMR Spectrum (125 MHz) of 3 in acetone- <i>d</i> 6	160
Figure A4.	^1H -NMR Spectrum (360 MHz) of 4 in CDCl_3	161
Figure A5.	^{13}C -NMR Spectrum (125 MHz) of 4 in acetone- <i>d</i> 6	162
Figure A6.	^1H -NMR Spectrum (360 MHz) of 4-BrPh-N-Ts in CDCl_3	163
Figure A7.	^{13}C -NMR Spectrum (125 MHz) of 4-BrPh-N-Ts in acetone- <i>d</i> 6	164
Figure A8.	^1H -NMR Spectrum (500 MHz) of 5 in $\text{DMSO-}d_6$	165
Figure A9.	^1H -NMR Spectrum (360 MHz) of 6 in CDCl_3	166
Figure A10.	^1H -NMR Spectrum (500 MHz) of 7 in CD_3CN	167
Figure A11.	^1H -NMR Spectrum (360 MHz) of AA-N-Ts in C_6D_6	168
Figure A12.	^{13}C -NMR Spectrum (125 MHz) of AA-N-Ts in acetone- <i>d</i> 6	169
Figure A13.	^1H -NMR Spectrum (360 MHz) of PD-N-Ts in CDCl_3	170
Figure A14.	^1H -NMR Spectrum (360 MHz) of Ph-N-Ac in CDCl_3	171
Figure A15.	^1H -NMR Spectrum (500 MHz) of Ph-Q-Ac in C_6D_6	172
Figure A16.	^1H -NMR Spectrum (500 MHz) of Cl-mPD in $\text{DMSO-}d_6$	173
Figure A17.	^1H -NMR Spectrum (500 MHz) of F-mPD in $\text{DMSO-}d_6$	174

Figure A18.	^{13}C -NMR Spectrum (125 MHz) of F-mPD in acetone- <i>d</i> 6	175
Figure A19.	^1H -NMR Spectrum (500 MHz) of Br-mPD in DMSO- <i>d</i> 6	176
Figure A20.	^{13}C -NMR Spectrum (125 MHz) of Br-mPD in acetone- <i>d</i> 6	177
Figure A21.	^1H -NMR Spectrum (500 MHz) of Cl-mPD-SMe in DMSO- <i>d</i> 6	178
Figure A22.	^{13}C -NMR Spectrum (125 MHz) of Cl-mPD-SMe in acetone- <i>d</i> 6	179
Figure A23.	^1H -NMR Spectrum (360 MHz) of H-mPD in DMSO- <i>d</i> 6	180
Figure A24.	^1H -NMR Spectrum (500 MHz) of Cl-mPD-OiPr in DMSO- <i>d</i> 6	181
Figure A25.	^{13}C -NMR Spectrum (125 MHz) of Cl-mPD-OiPr in acetone- <i>d</i> 6	182
Figure A26.	^1H -NMR Spectrum (500 MHz) of 10 in CDCl_3	183
Figure A27.	^1H -NMR Spectrum (500 MHz) of 11 in CDCl_3	184
Figure A28.	^1H -NMR Spectrum (500 MHz) of H-mPD-OMac in CDCl_3	185

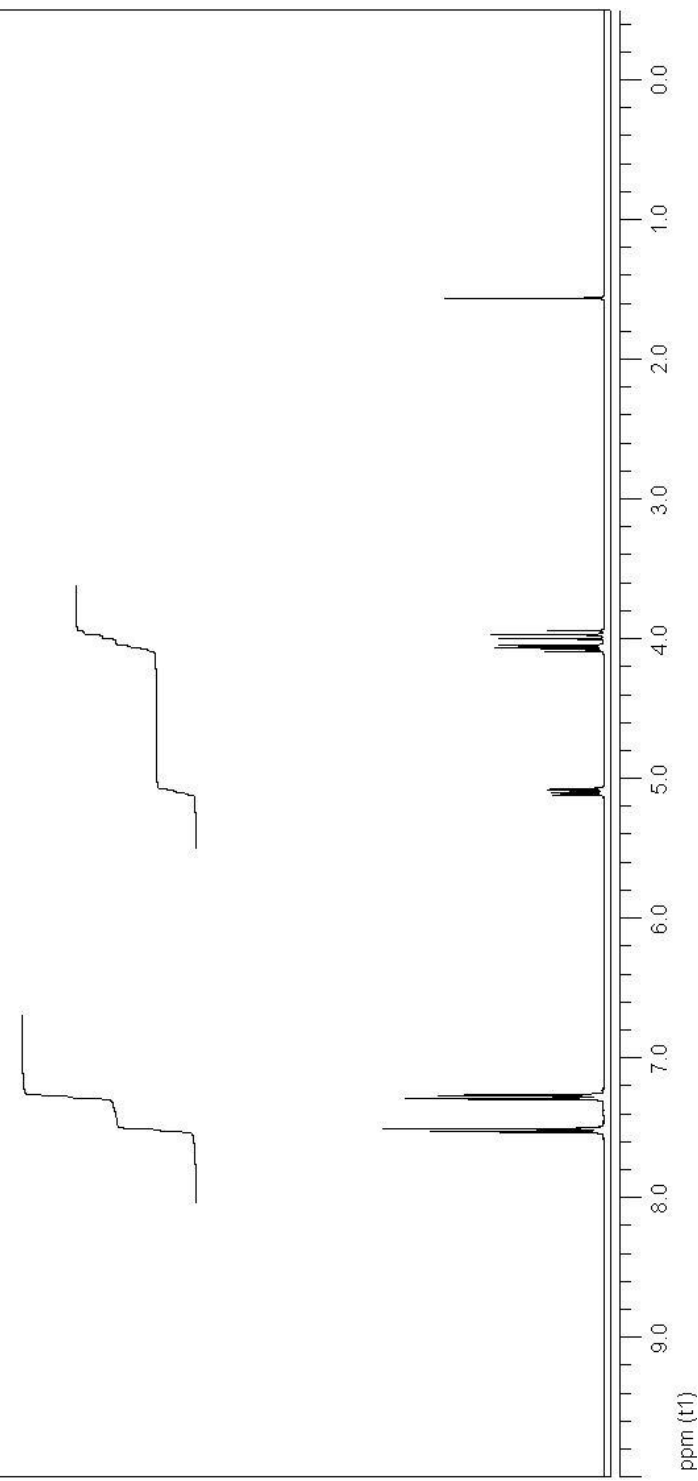
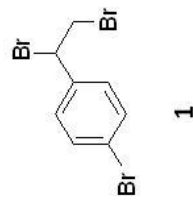


Figure A1. ¹H-NMR Spectrum (360 MHz) of **1** in CDCl_3 .

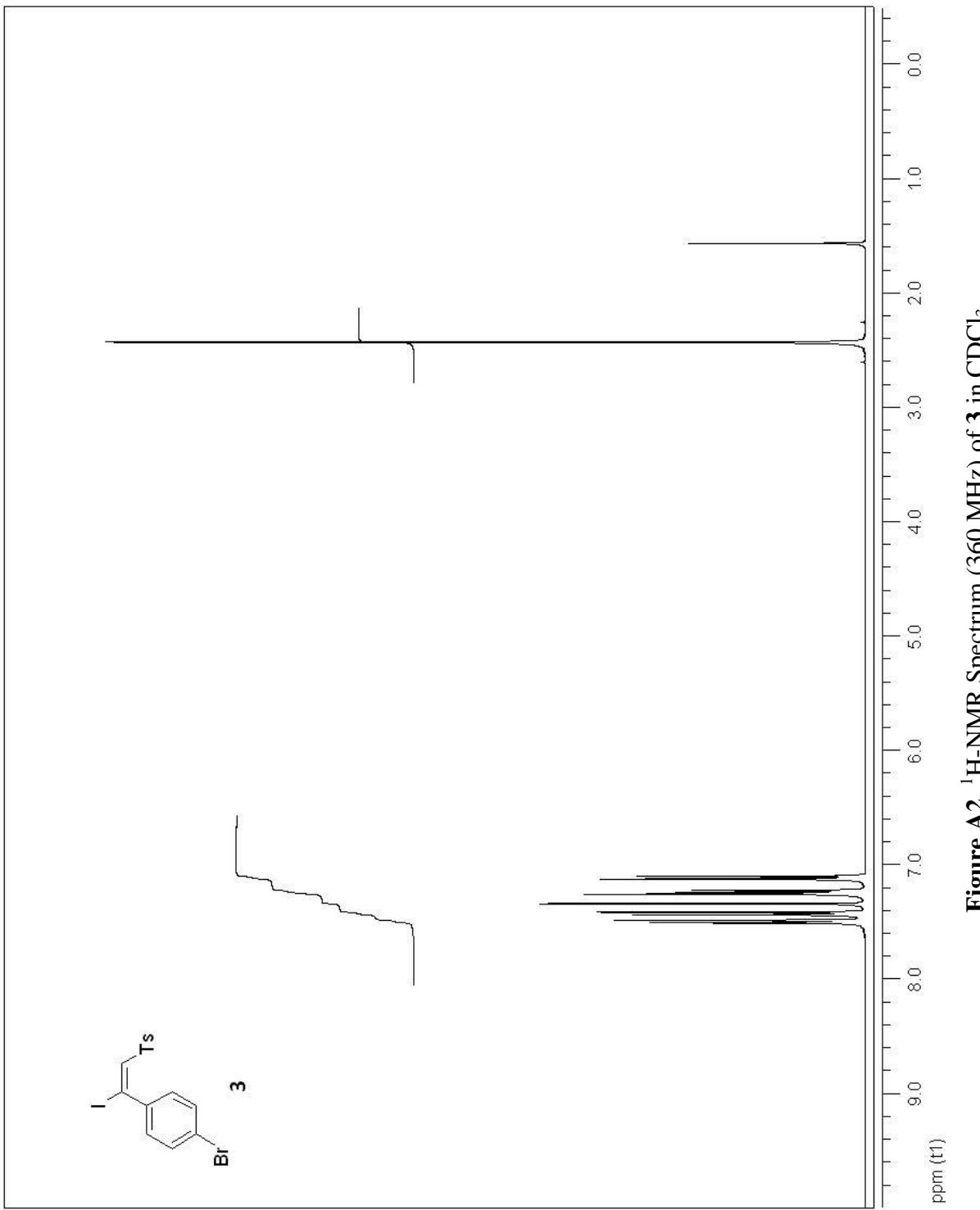


Figure A2. ^1H -NMR Spectrum (360 MHz) of **3** in CDCl_3 .

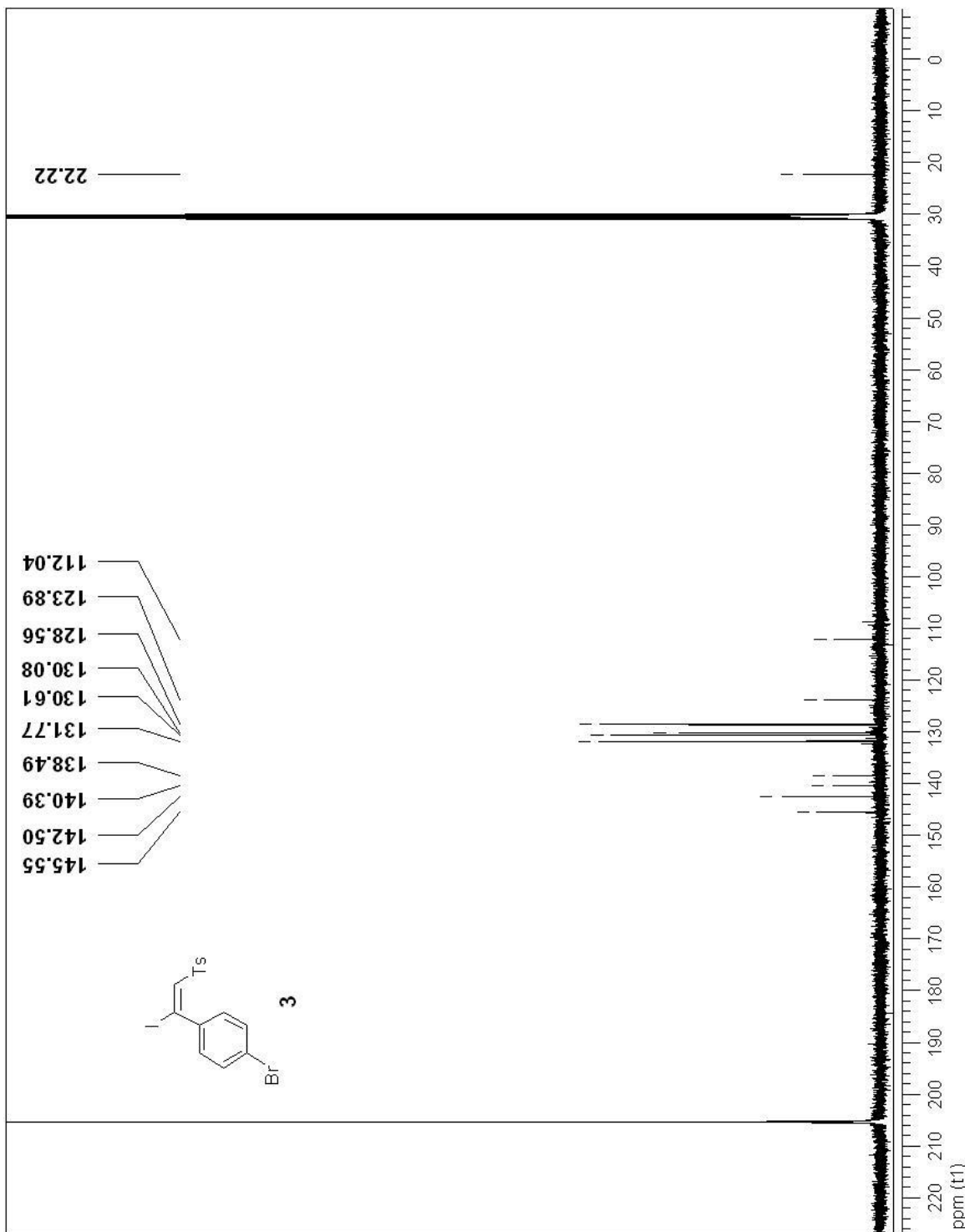


Figure A3. ^{13}C -NMR Spectrum (125 MHz) of **3** in acetone-*d*6.

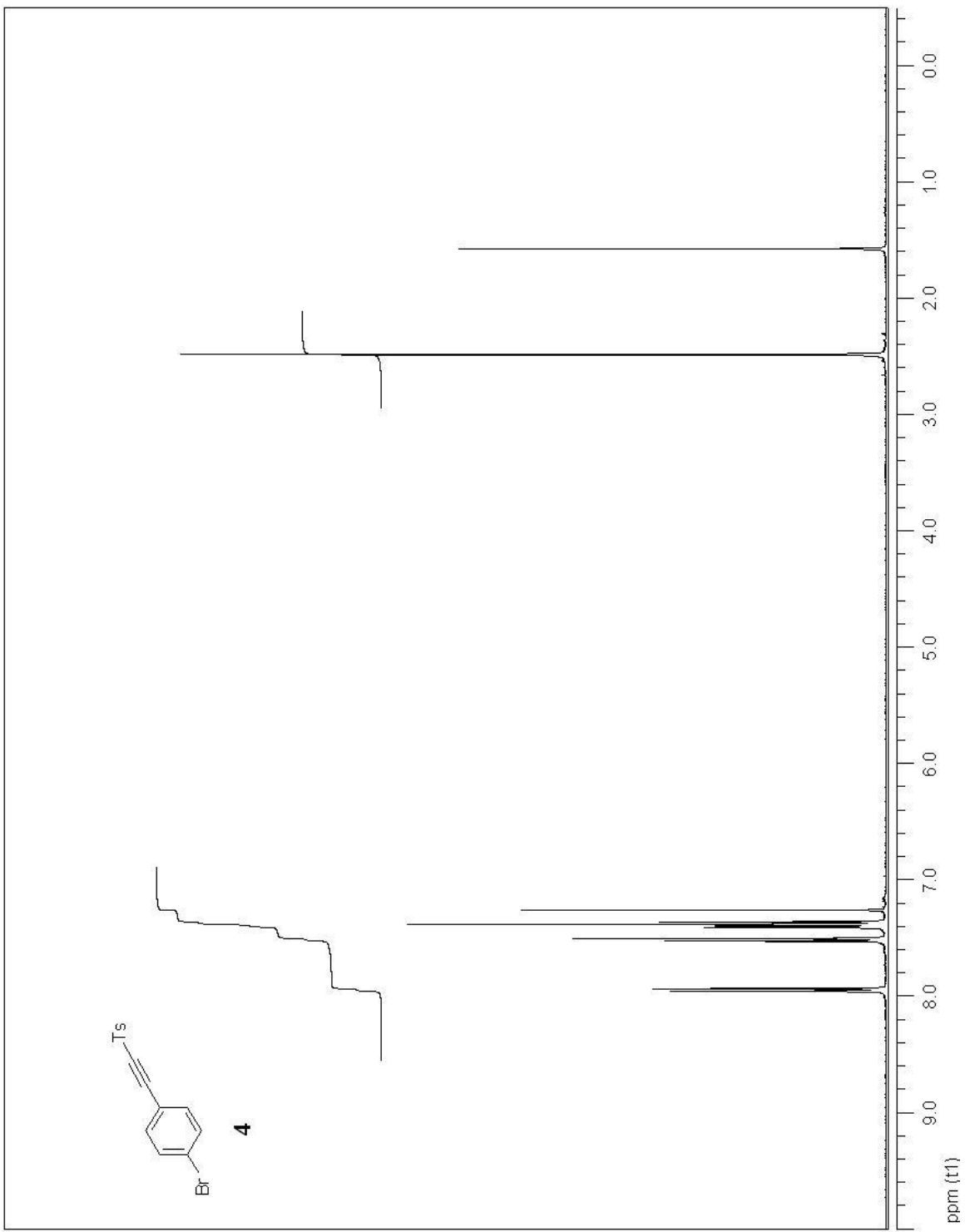


Figure A4. ^1H -NMR Spectrum (360 MHz) of **4** in CDCl_3 .

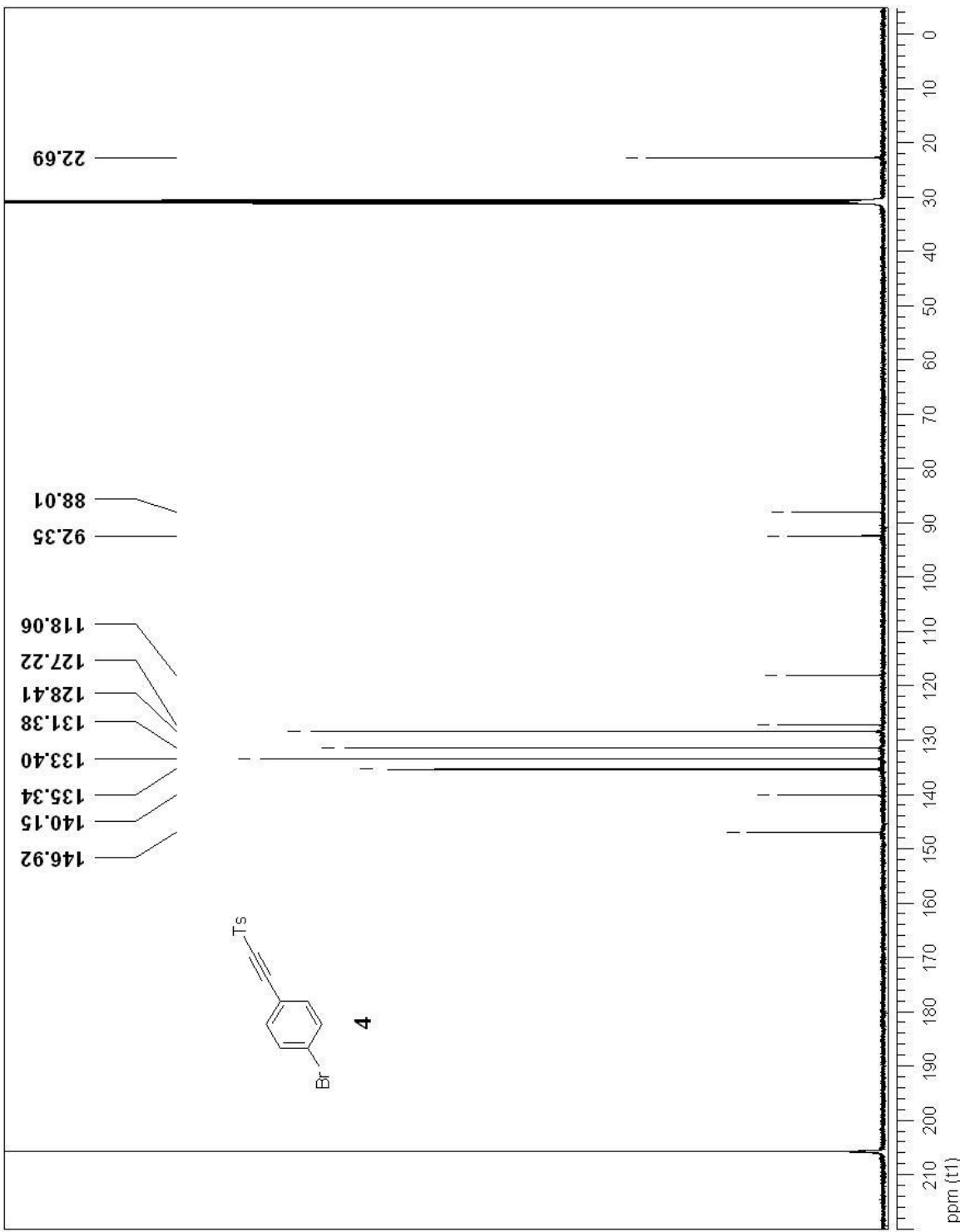


Figure A5. ^{13}C -NMR Spectrum (125 MHz) of **4** in acetone- d_6 .

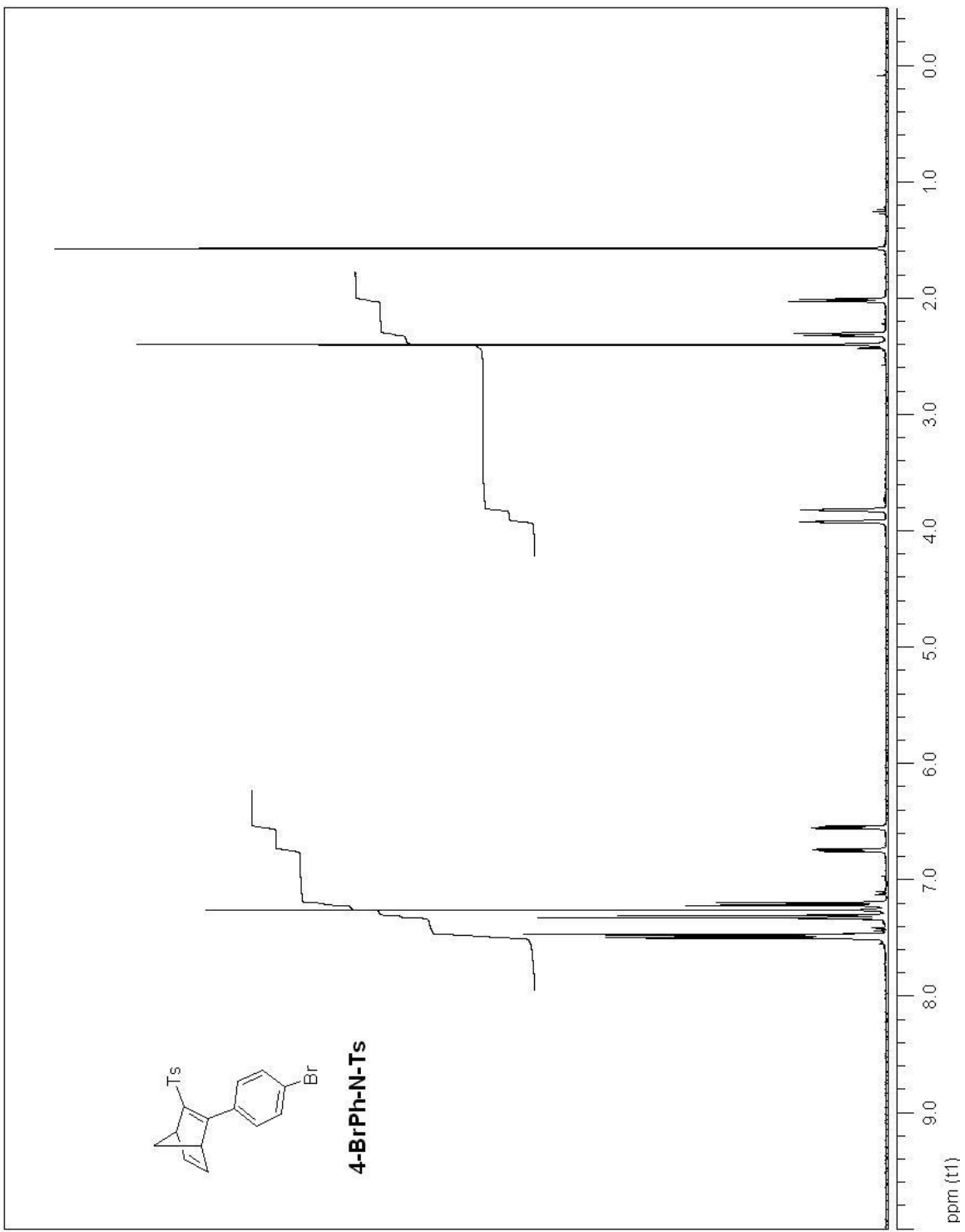


Figure A6. ¹H-NMR Spectrum (360 MHz) of 4-BrPh-N-Ts in CDCl₃.

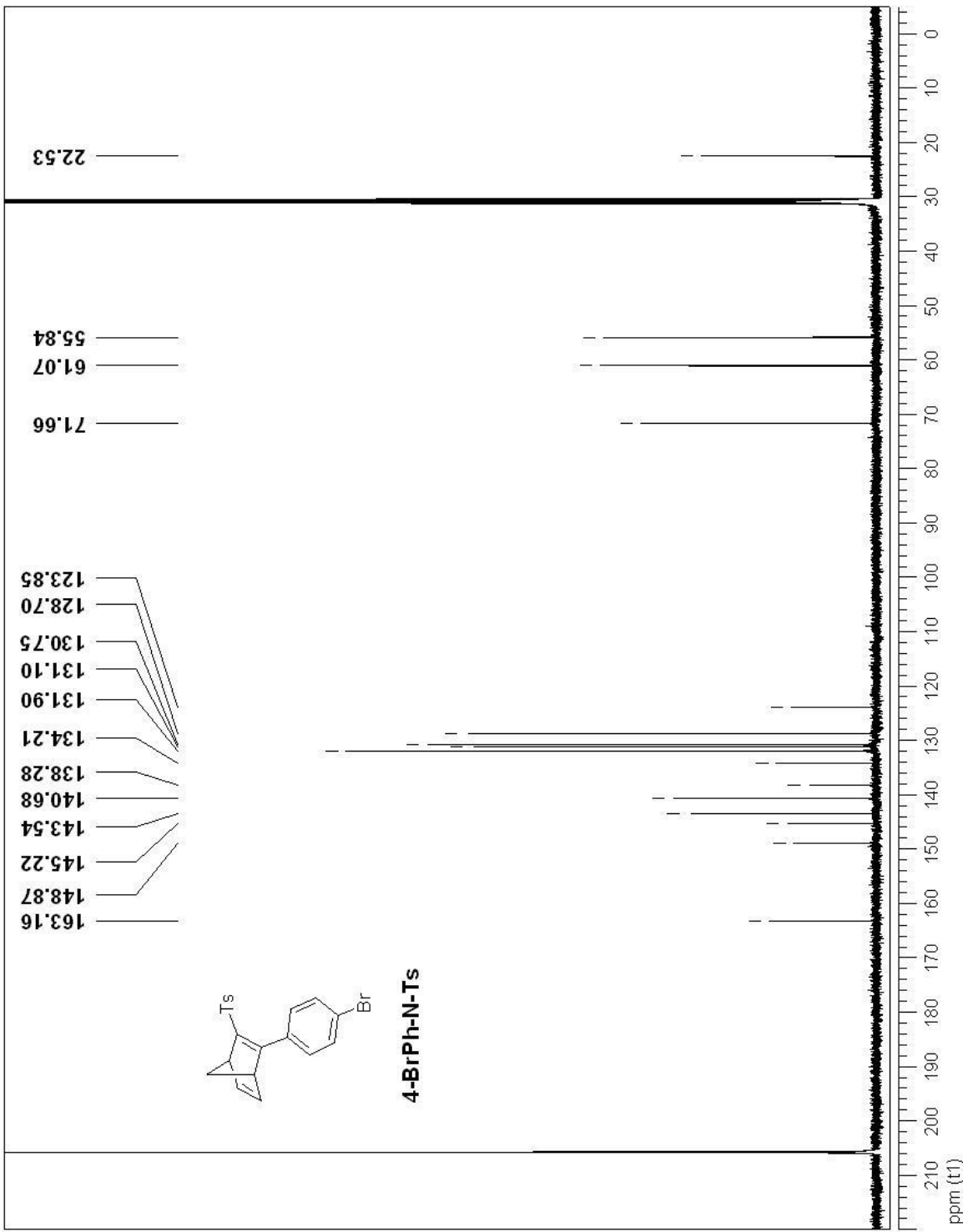
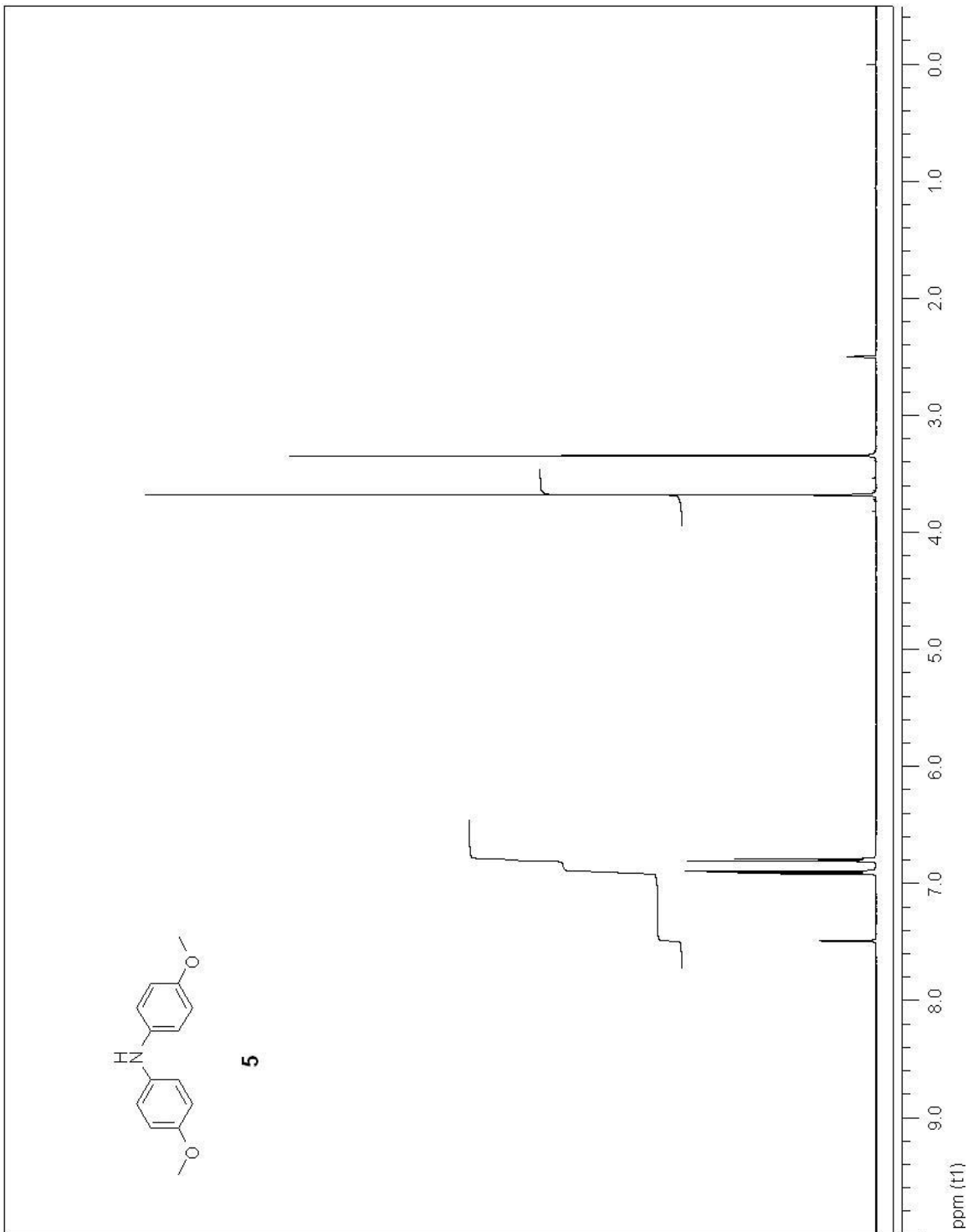


Figure A7. ^{13}C -NMR Spectrum (125 MHz) of 4-BrPh-N-Ts in acetone- d_6 .



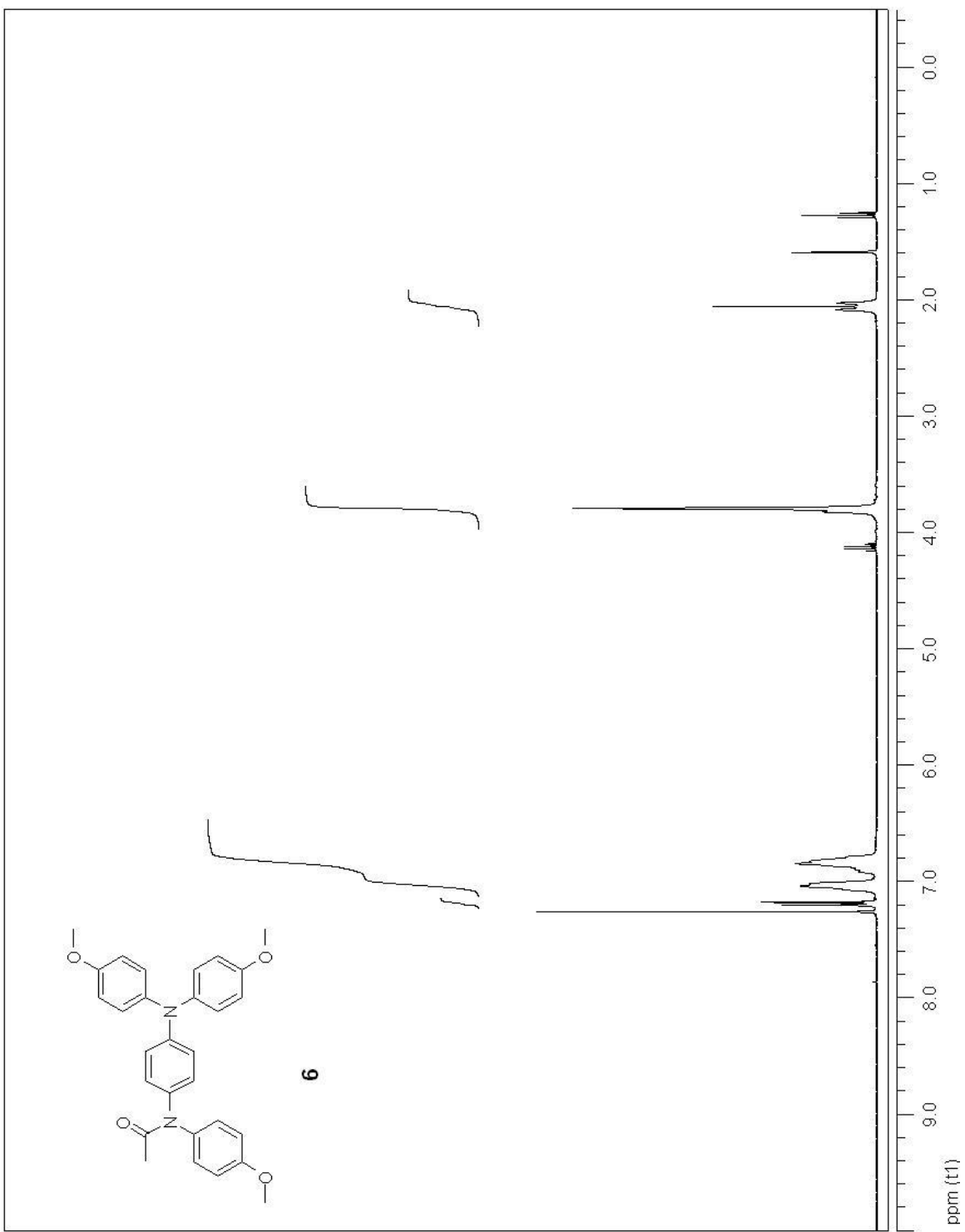


Figure A9. ^1H -NMR Spectrum (360 MHz) of **6** in CDCl_3 .

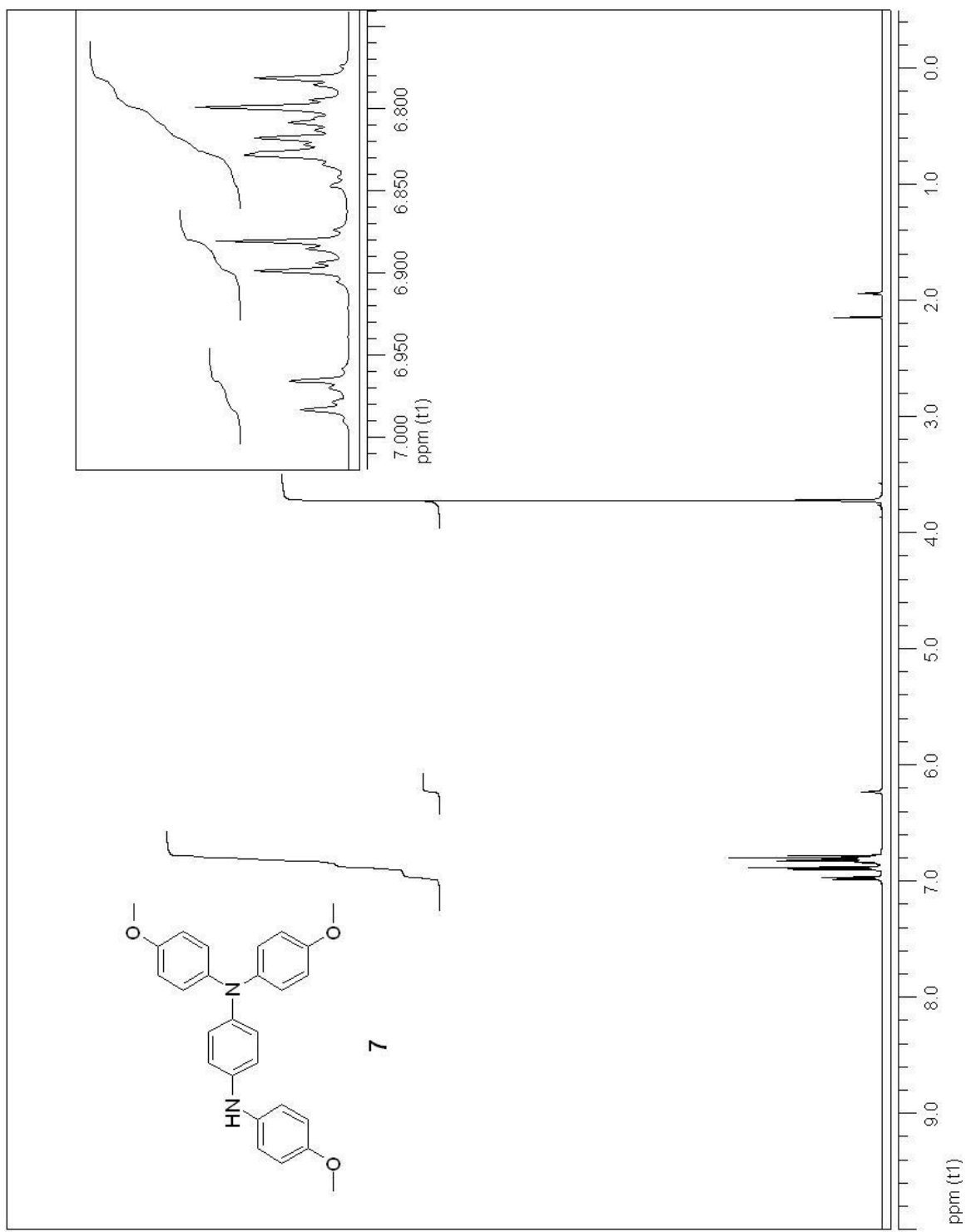


Figure A10. ^1H -NMR Spectrum (500 MHz) of 7 in CD_3CN .

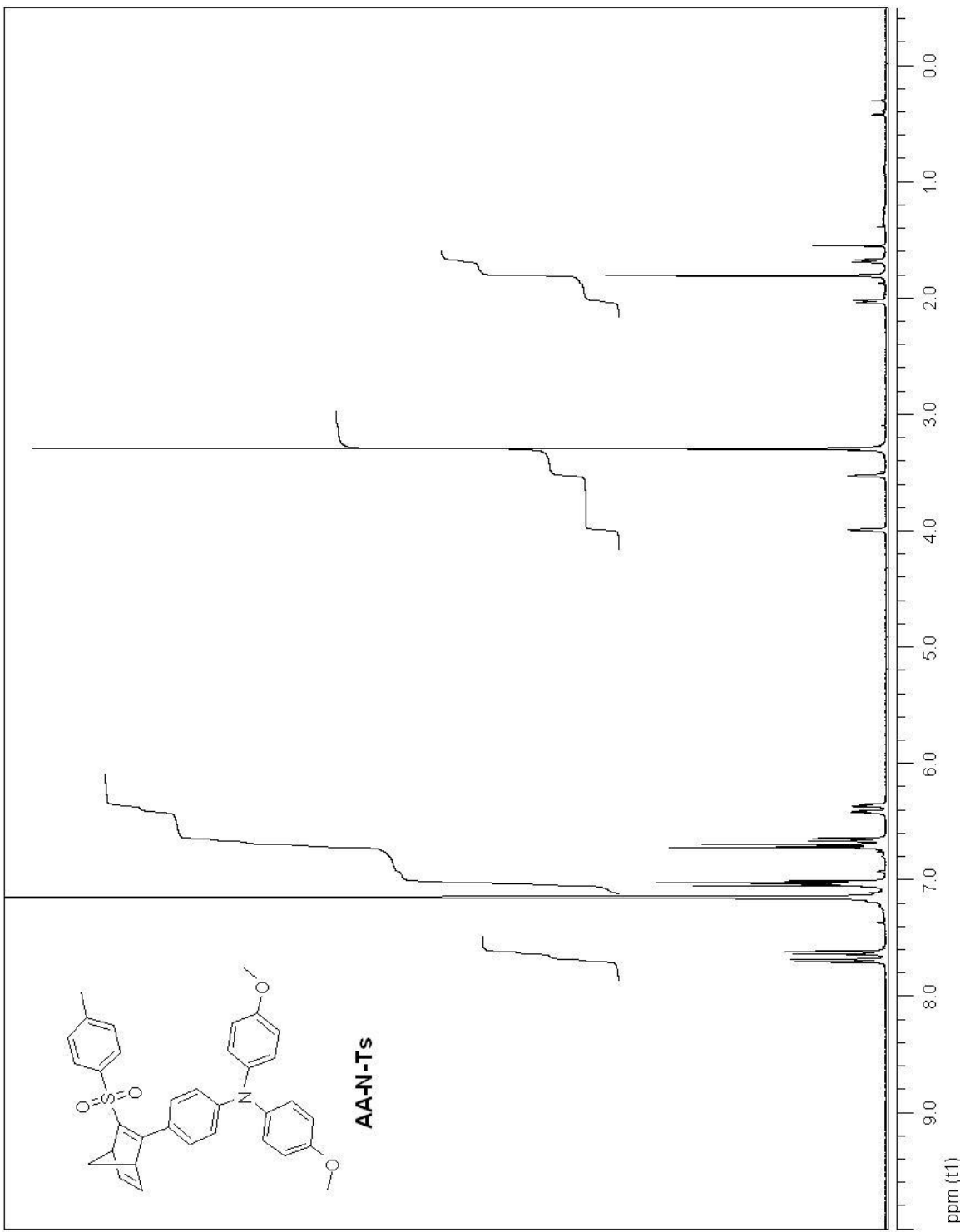


Figure A11. ^1H -NMR Spectrum (360 MHz) of AA-N-Ts in C_6D_6 .

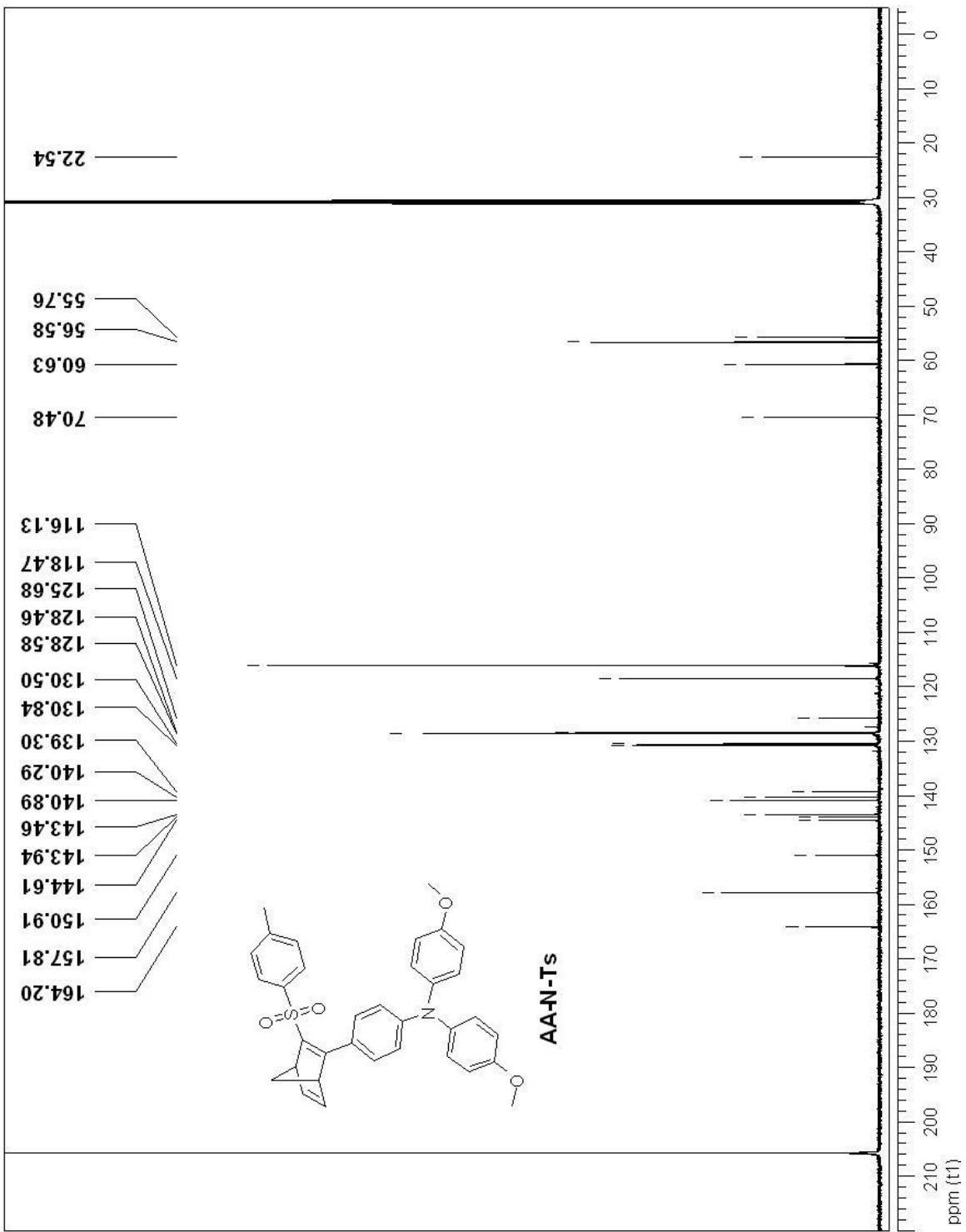


Figure A12. ^{13}C -NMR Spectrum (125 MHz) of AA-N-Ts in acetone- d_6 .

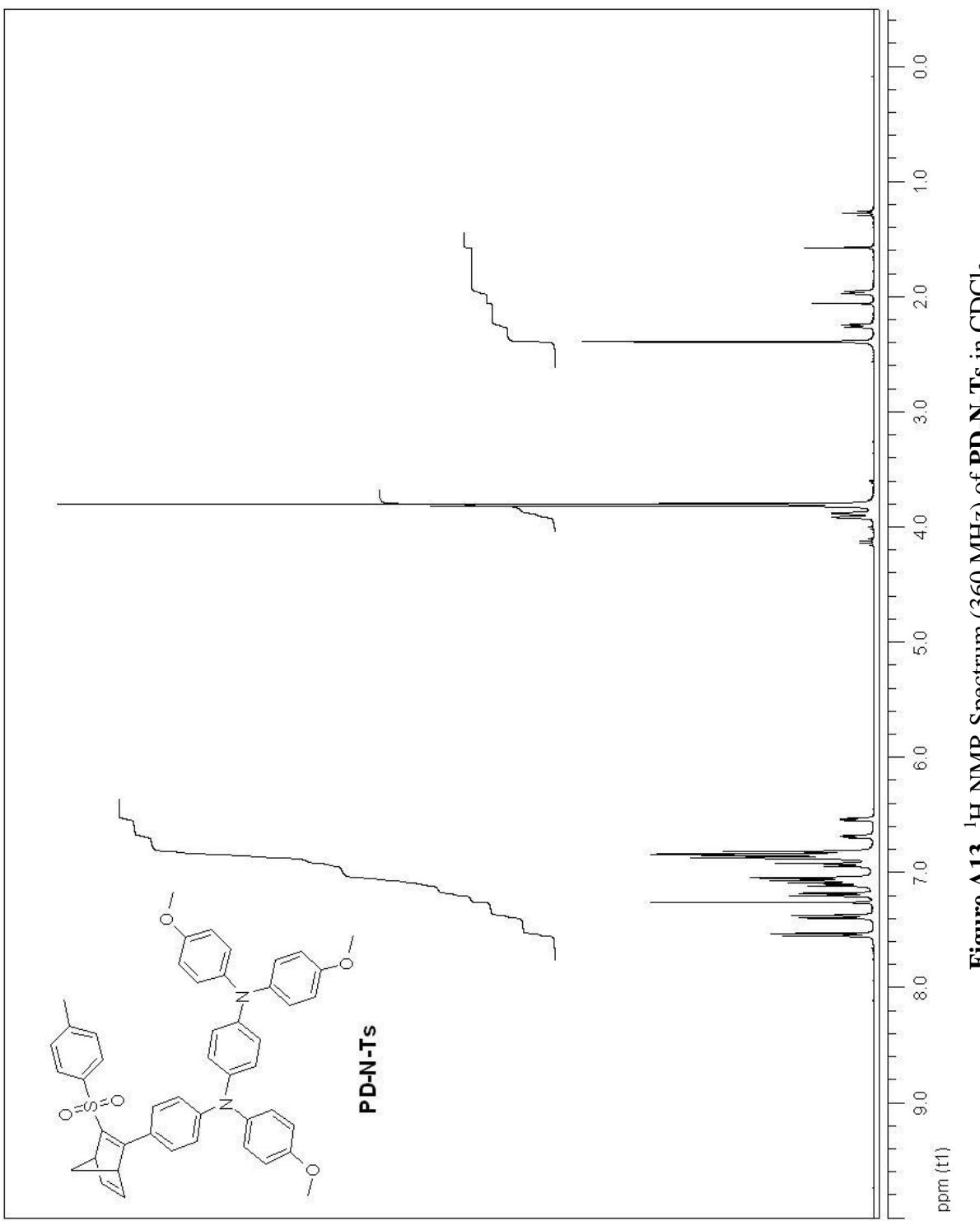


Figure A13. ^1H -NMR Spectrum (360 MHz) of PD-N-Ts in CDCl_3 .

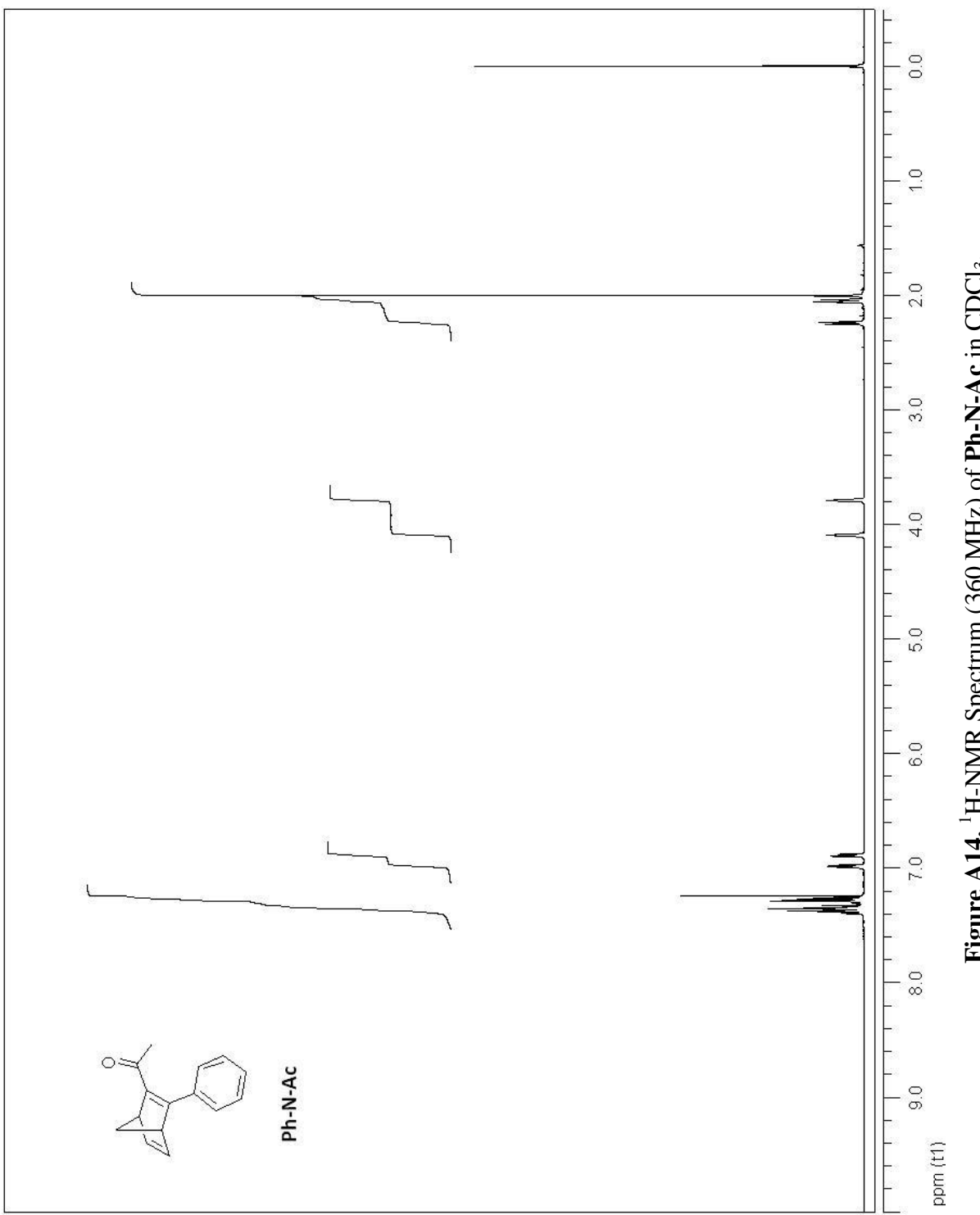


Figure A14. ${}^1\text{H}$ -NMR Spectrum (360 MHz) of Ph-N-Ac in CDCl_3 .

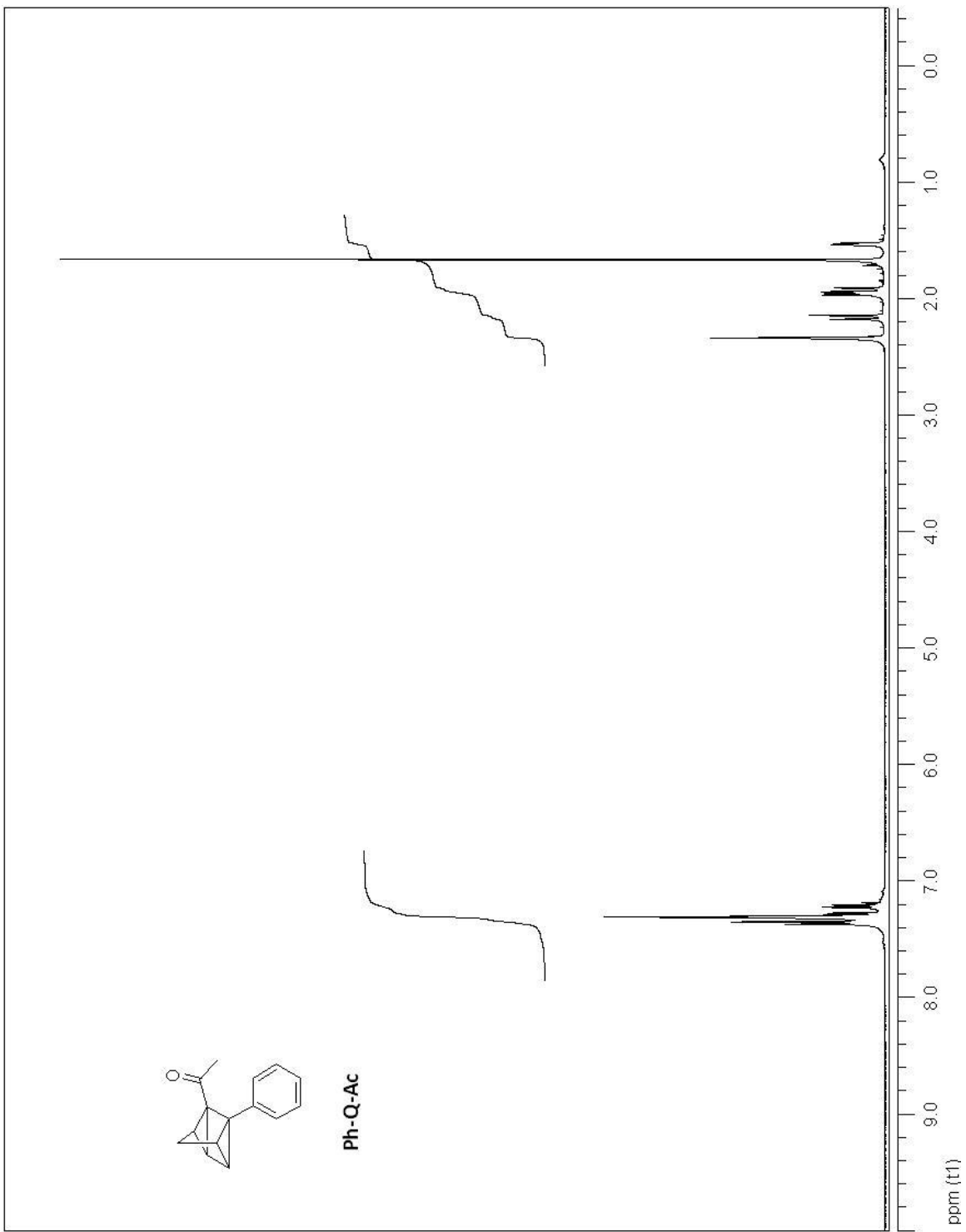


Figure A15. ¹H-NMR Spectrum (500 MHz) of Ph-Q-Ac in C_6D_6 .

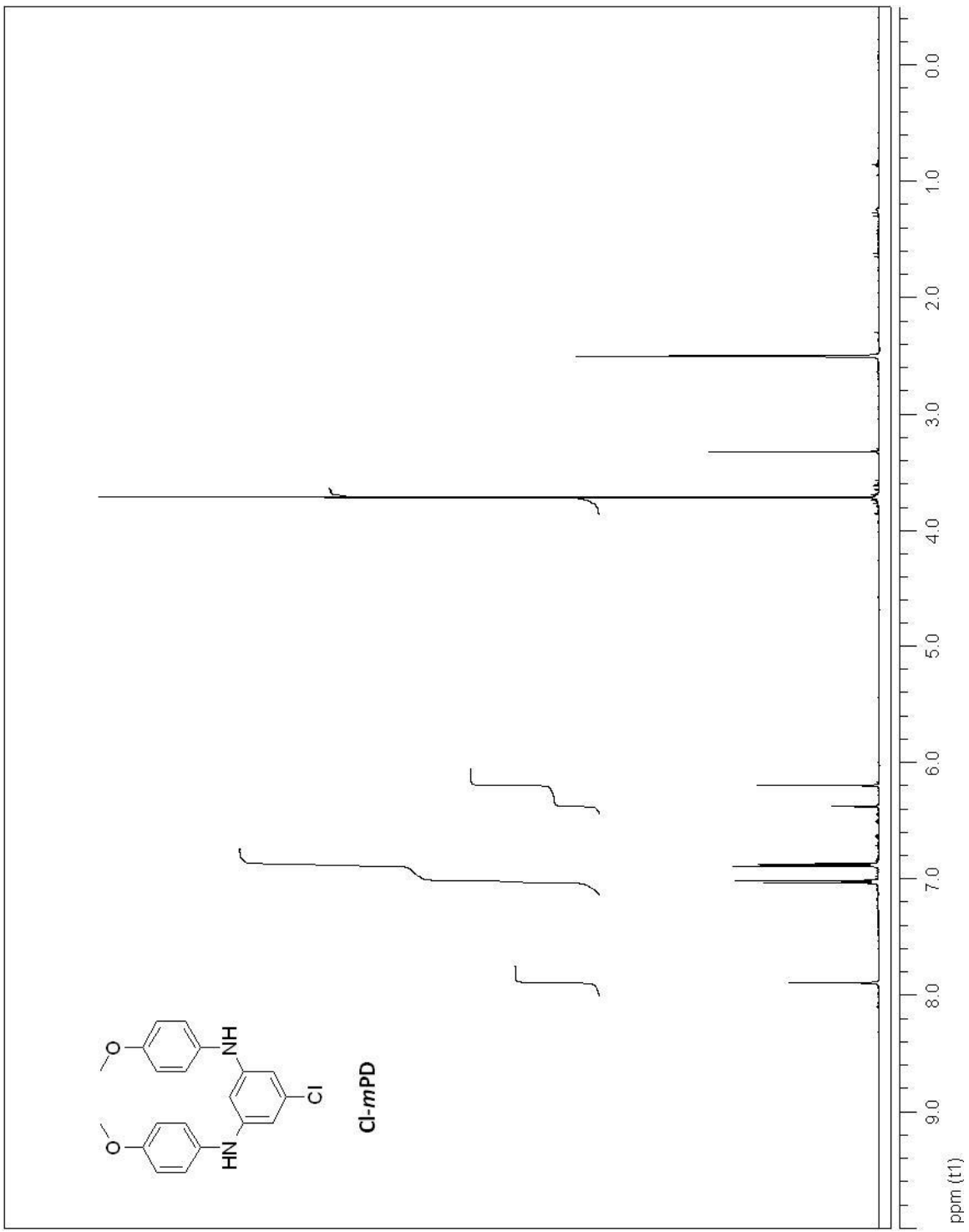


Figure A16. ^1H -NMR Spectrum (500 MHz) of Cl-*m*PD in DMSO-*d*6.

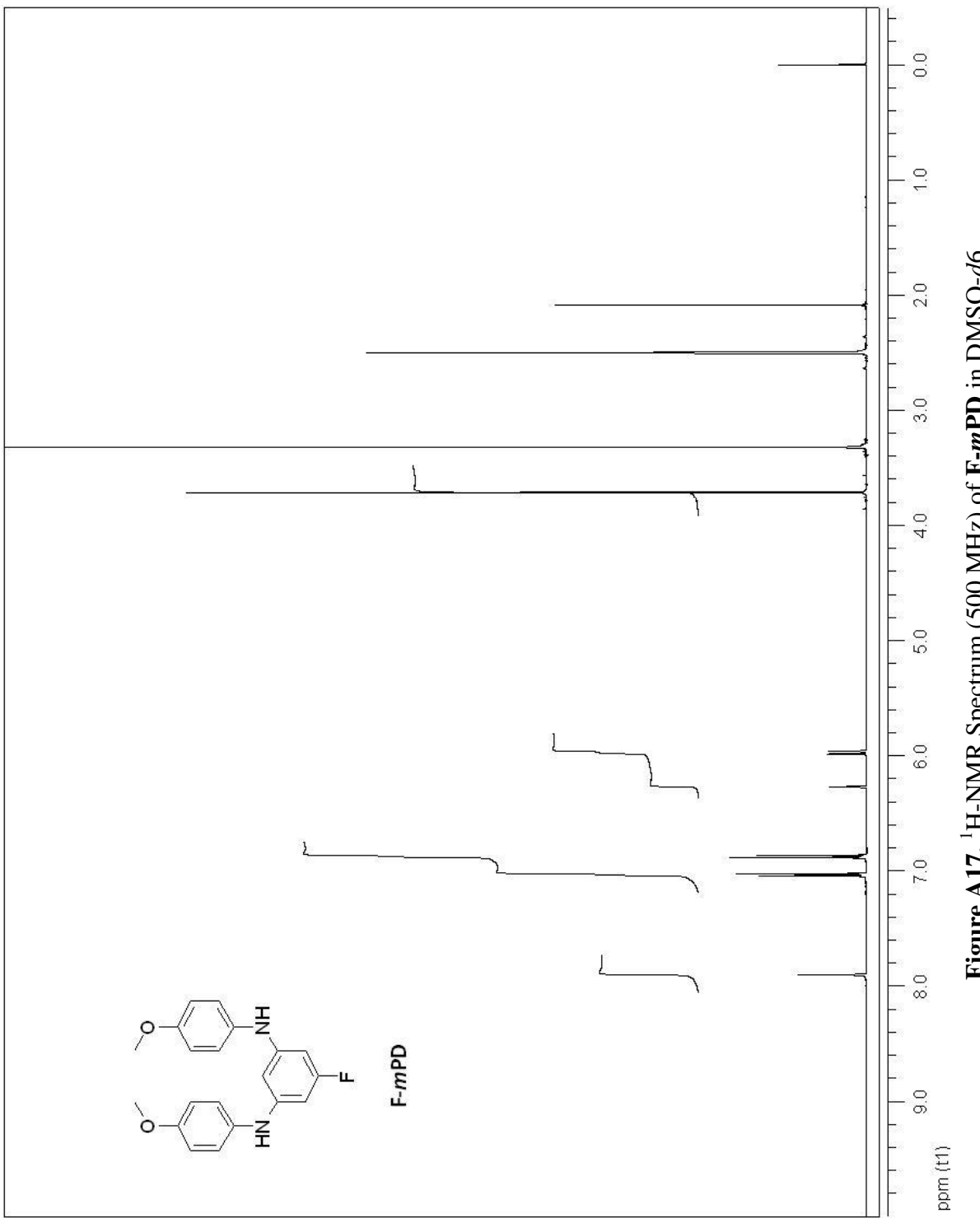


Figure A17. ^1H -NMR Spectrum (500 MHz) of F-*m*PD in $\text{DMSO}-d_6$.

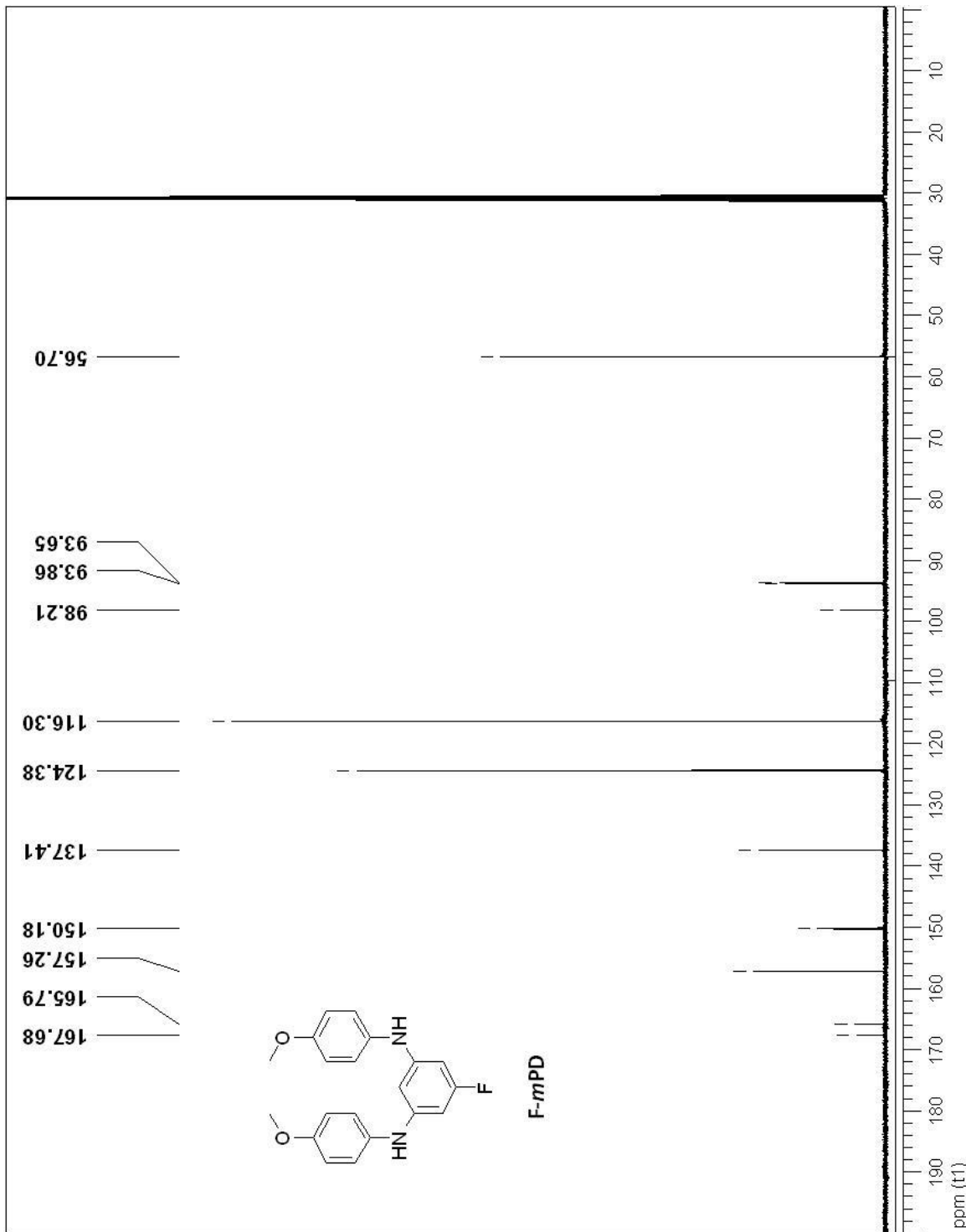


Figure A18. ^{13}C -NMR Spectrum (125 MHz) of F-*m*PD in acetone-*d*₆.

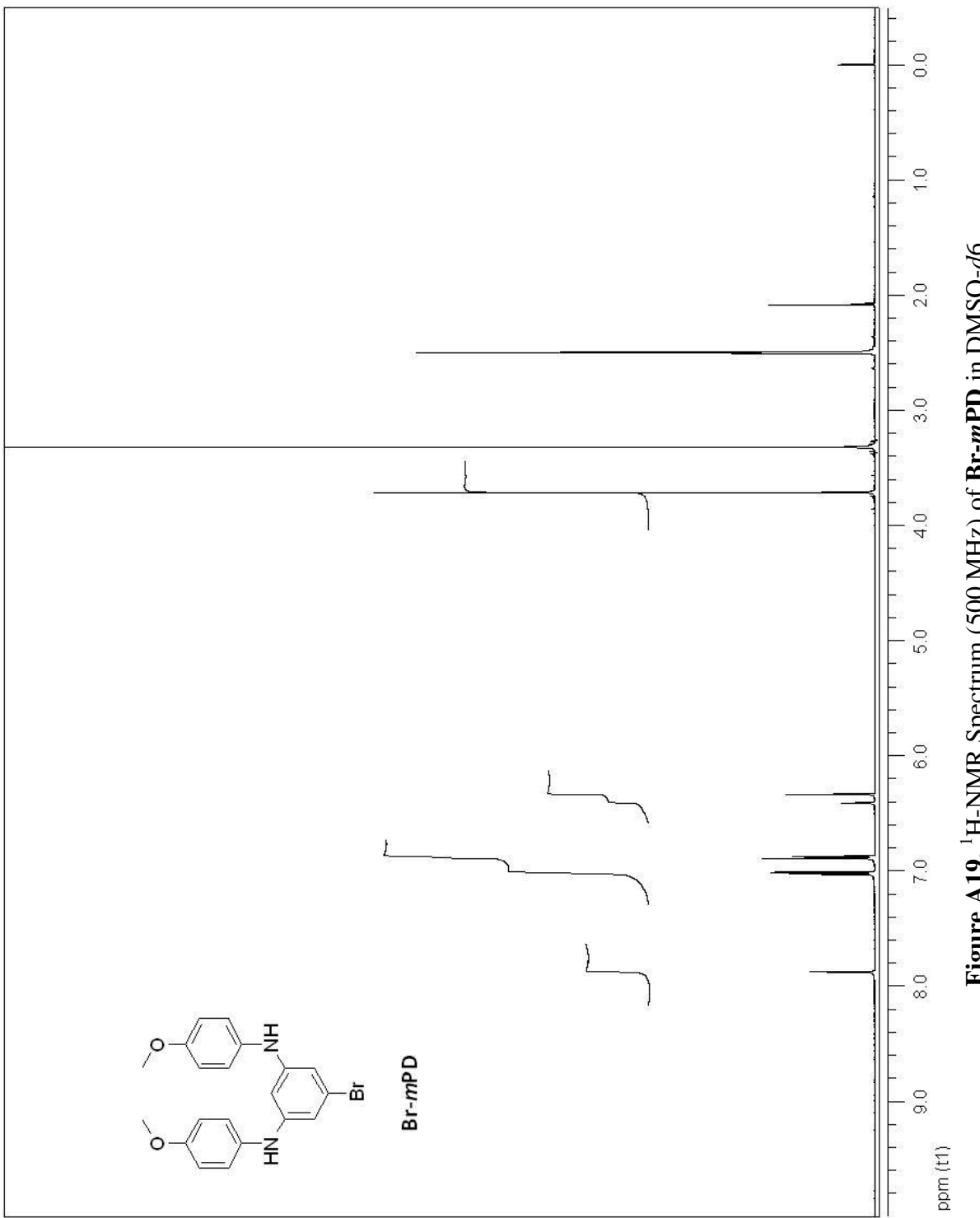


Figure A19. ^1H -NMR Spectrum (500 MHz) of Br-*m*PD in DMSO-*d*6.

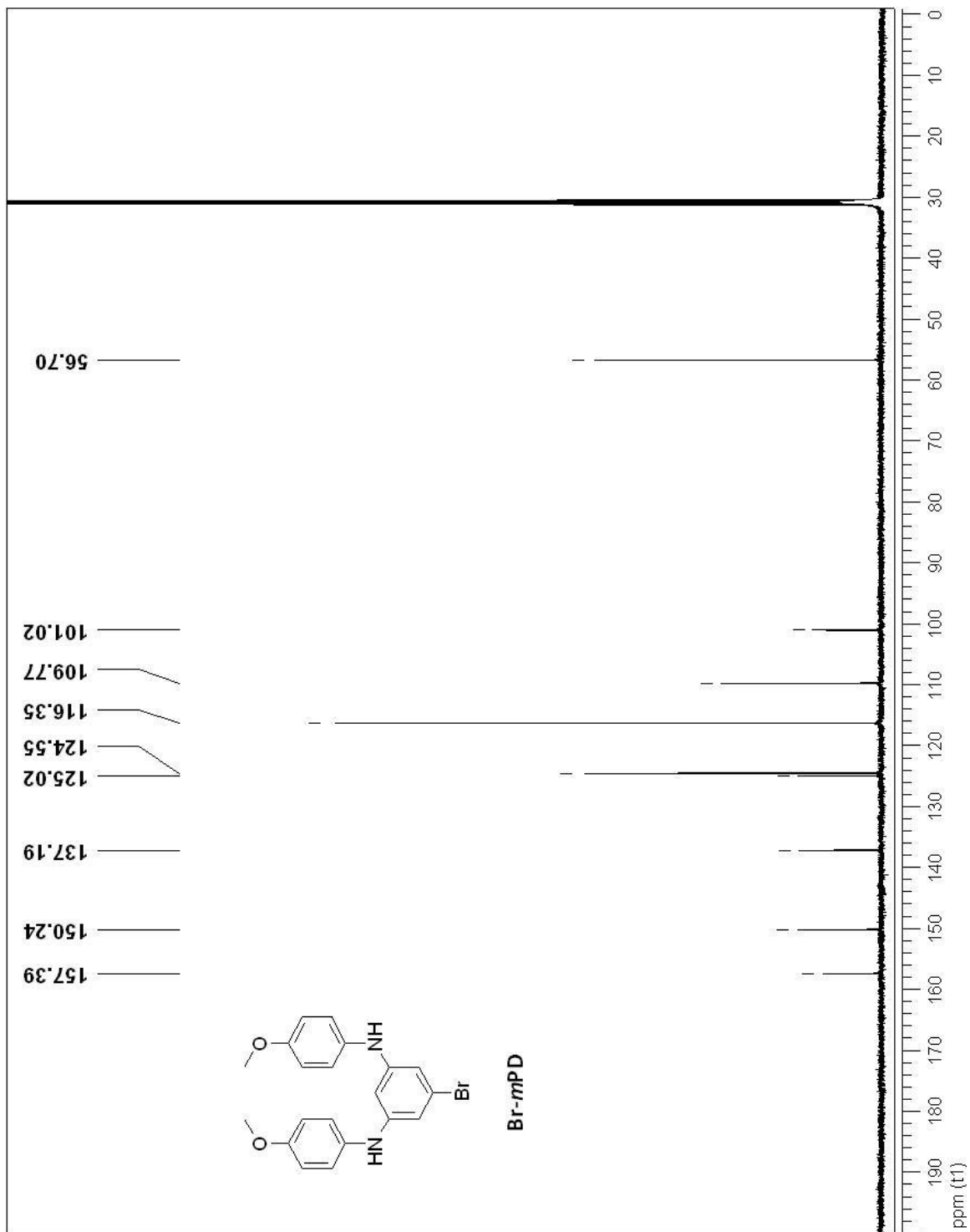


Figure A20. ^{13}C -NMR Spectrum (125 MHz) of Br-*m*PD in acetone-*d*6.

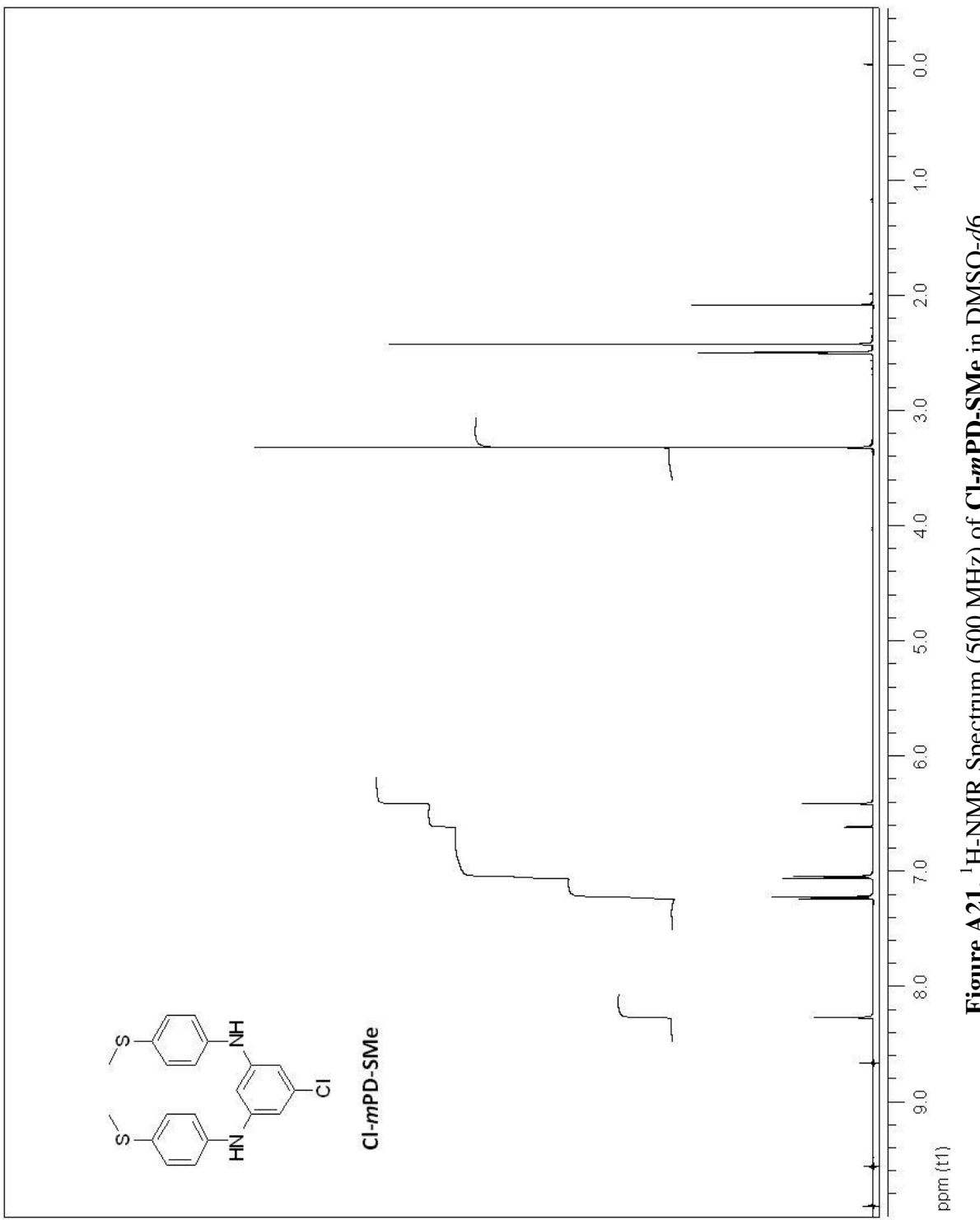


Figure A21. ¹H-NMR Spectrum (500 MHz) of Cl-*m*PD-SMe in DMSO-*d*6.

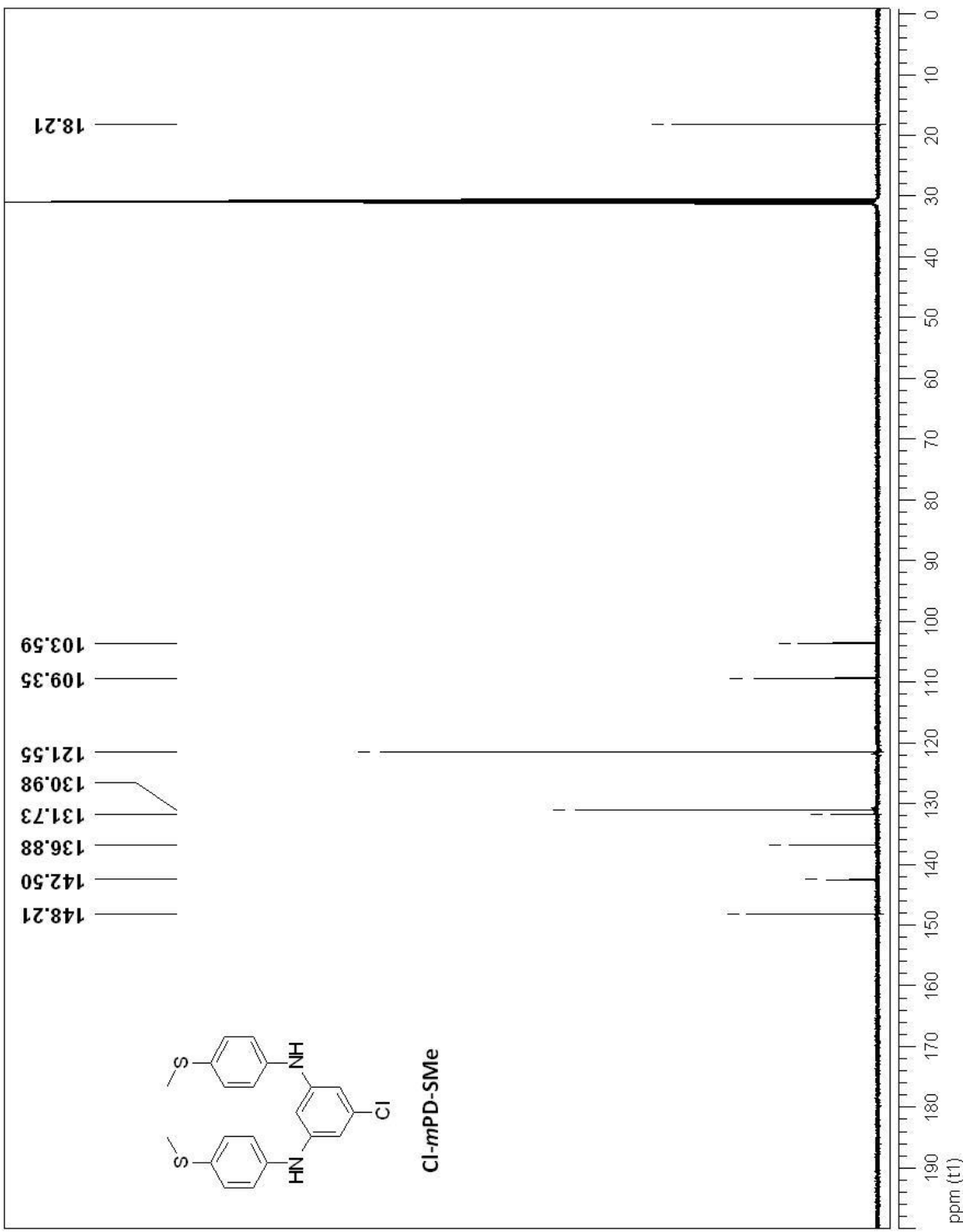


Figure A22. ^{13}C -NMR Spectrum (125 MHz) of **Cl-*m*PD-SMe** in acetone-*d*6.

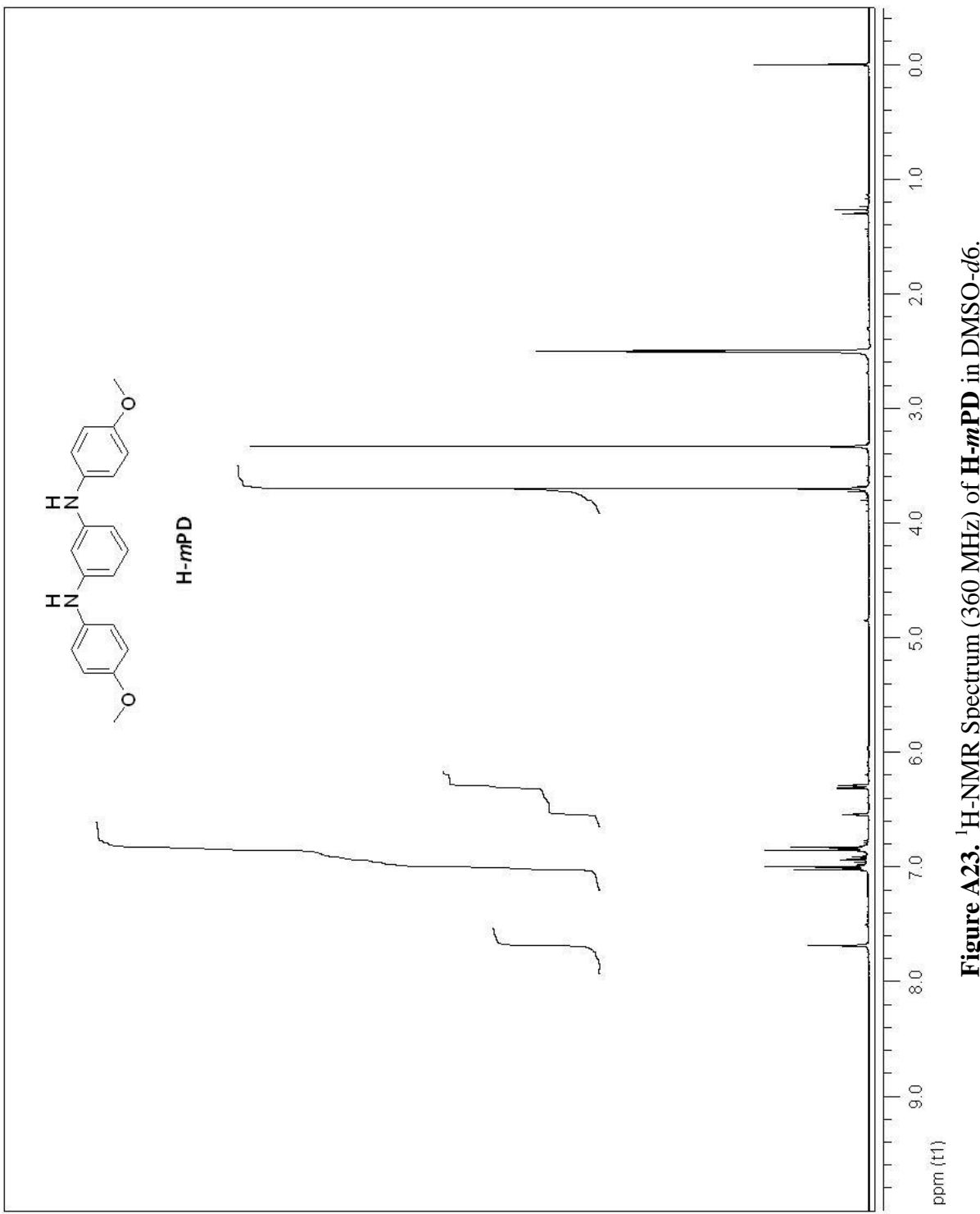


Figure A23. ^1H -NMR Spectrum (360 MHz) of **H-mPD** in $\text{DMSO}-d_6$.

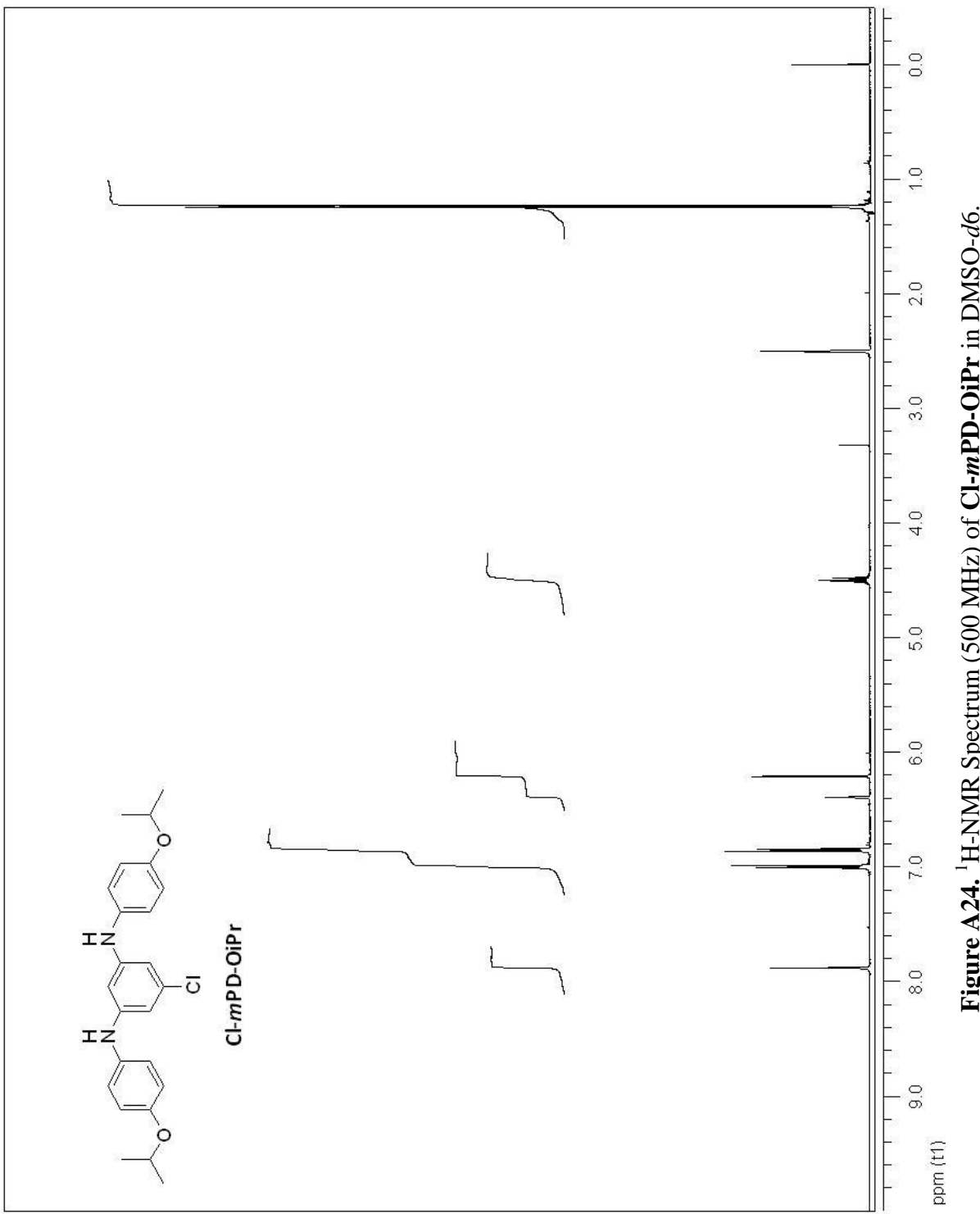


Figure A24. ^1H -NMR Spectrum (500 MHz) of Cl-*m*PD-O*i*Pr in $\text{DMSO}-d_6$.

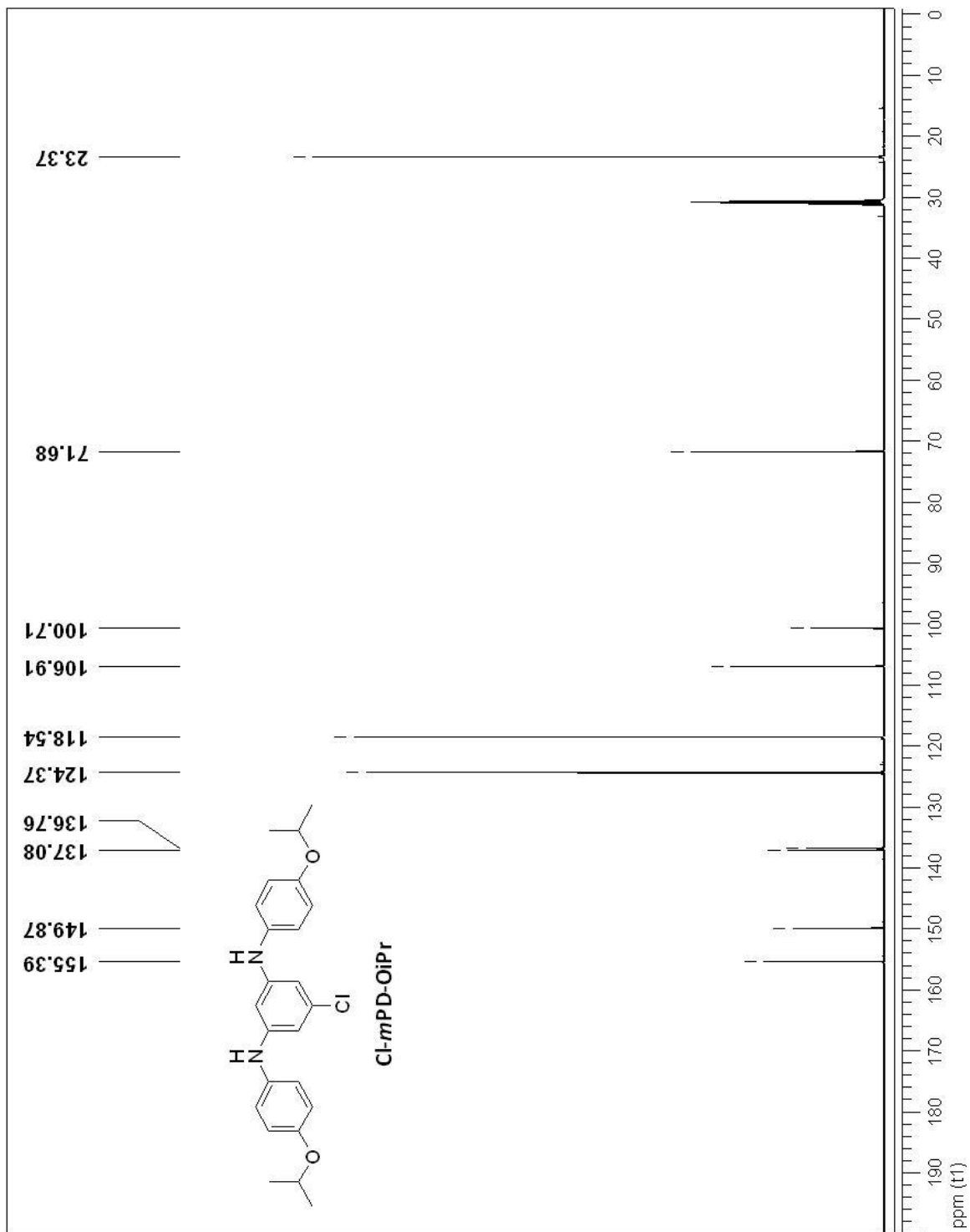
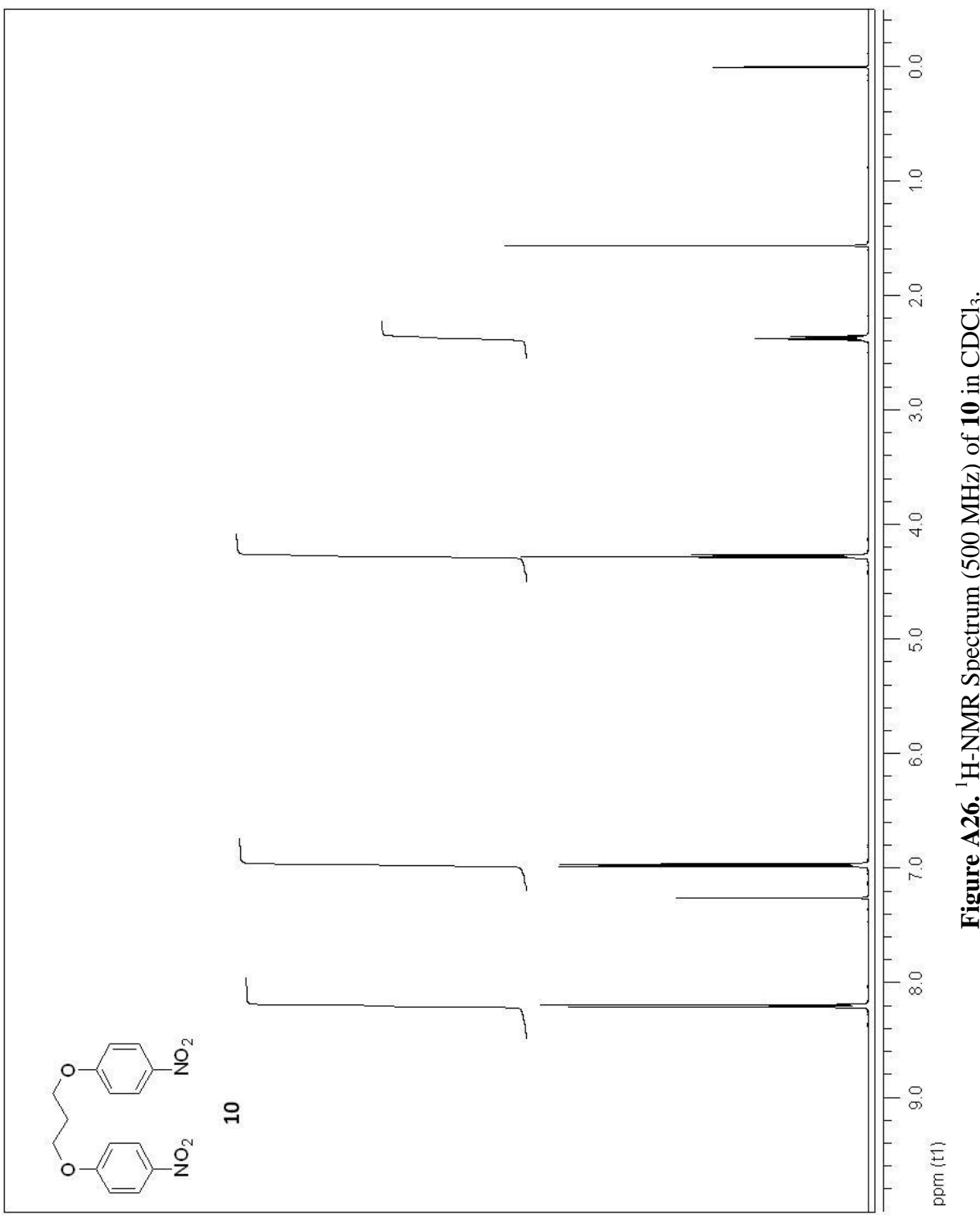


Figure A25. ^{13}C -NMR Spectrum (125 MHz) of $\text{Cl-}m\text{PD-OiPr}$ in acetone- d_6 .



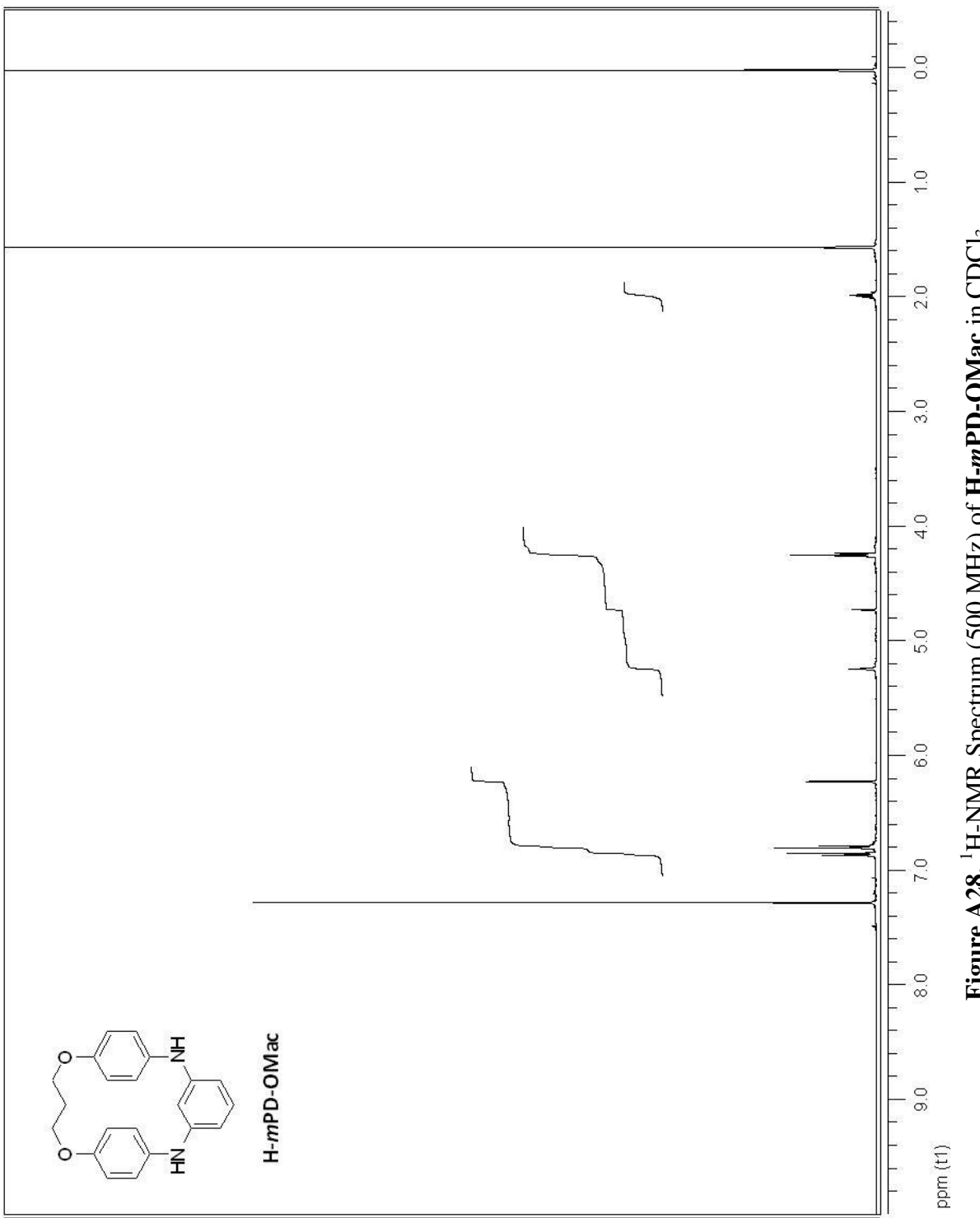


Figure A28. ¹H-NMR Spectrum (500 MHz) of H-*m*PD-OMac in CDCl₃.

Appendix B

Crystallographic Data

LIST OF X-RAY CRYSTAL STRUCTURES

Figure B1.	Single crystal X-Ray data for PD-N-Ts	187
Figure B2.	Single crystal X-Ray data for Cl-<i>m</i>PD	197
Figure B3.	Single crystal X-Ray data for F-<i>m</i>PD	203
Figure B4.	Single crystal X-Ray data for Br-<i>m</i>PD	208
Figure B5.	Single crystal X-Ray data for Cl-<i>m</i>PD-SMe	214
Figure B6.	Single crystal X-Ray data for H-<i>m</i>PD	221
Figure B7.	Single crystal X-Ray data for Cl-<i>m</i>PD-OiPr	227
Figure B8.	Single crystal X-Ray data for Cl-<i>m</i>PD-OMac	233

Single-crystal X-Ray data for **PD-N-Ts**

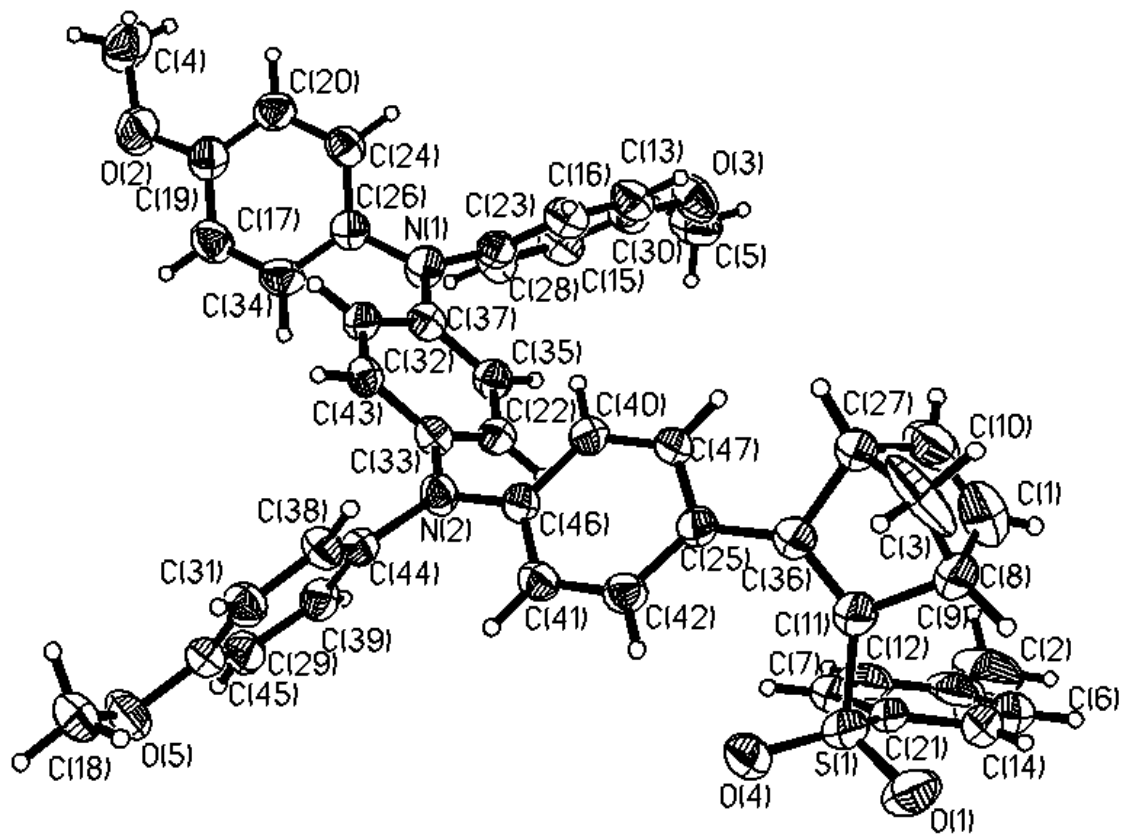


Figure B1. ORTEP (50 % ellipsoids) diagram of **PD-N-Ts** generated with SHELXTL software.

Table 1. Crystal data and structure refinement for **PD-N-Ts**.

Identification code	PD-N-Ts
Empirical formula	C47 H42 N2 O5 S
Formula weight	746.89
Temperature	173(2) K
Wavelength	0.71073 Å
Crystal system, space group	Triclinic, P-1
Unit cell dimensions	a = 10.9170(12) Å alpha = 71.565(2) deg. b = 13.9925(15) Å beta = 72.039(2) deg. c = 14.1241(16) Å gamma = 72.829(2) deg.
Volume	1899.8(4) Å ³
Z, Calculated density	2, 1.306 Mg/m ³
Absorption coefficient	0.137 mm ⁻¹
F(000)	788
Crystal size	0.18 x 0.09 x 0.05 mm
Theta range for data collection	1.92 to 23.29 deg.
Limiting indices	-9<=h<=12, -15<=k<=15, -15<=l<=15
Reflections collected / unique	8821 / 5432 [R(int) = 0.0171]
Completeness to theta = 23.29	98.9 %
Refinement method	Full-matrix least-squares on F ²
Data / restraints / parameters	5432 / 0 / 497
Goodness-of-fit on F ²	1.017
Final R indices [I>2sigma(I)]	R1 = 0.0507, wR2 = 0.1342

R indices (all data)	R1 = 0.0593, wR2 = 0.1415
Extinction coefficient	0.0020(10)
Largest diff. peak and hole	0.800 and -0.497 e.A^-3

Table 2. Atomic coordinates ($x \times 10^4$) and equivalent isotropic displacement parameters ($A^2 \times 10^3$) for **PD-N-Ts**.
U(eq) is defined as one third of the trace of the orthogonalized Uij tensor.

	x	y	z	U(eq)
S(1)	3800(1)	2748(1)	343(1)	53(1)
N(2)	2266(2)	4768(2)	-4458(2)	37(1)
N(1)	-1171(2)	8569(2)	-5723(2)	45(1)
O(5)	6480(2)	3079(2)	-7325(2)	55(1)
O(4)	4552(2)	2811(2)	-694(2)	62(1)
C(47)	675(2)	4020(2)	-1691(2)	36(1)
O(3)	-3798(2)	11103(2)	-3021(2)	65(1)
C(46)	2056(2)	4255(2)	-3415(2)	33(1)
O(2)	-2094(2)	9869(2)	-9654(2)	69(1)
C(45)	5420(2)	3447(2)	-6612(2)	40(1)
C(44)	3318(2)	4323(2)	-5201(2)	33(1)
C(43)	884(2)	5925(2)	-5616(2)	35(1)
C(42)	2859(2)	2995(2)	-1991(2)	38(1)
C(41)	3042(2)	3469(2)	-3026(2)	36(1)
O(1)	4345(2)	1984(2)	1152(2)	68(1)
C(40)	849(2)	4501(2)	-2720(2)	36(1)
C(39)	4246(3)	4881(2)	-5864(2)	39(1)
C(38)	3454(2)	3334(2)	-5267(2)	39(1)
C(37)	-284(2)	7638(2)	-5428(2)	37(1)
C(36)	1467(3)	2845(2)	-180(2)	40(1)
C(35)	291(2)	7464(2)	-4617(2)	39(1)
C(34)	-408(3)	8966(2)	-7605(2)	49(1)
C(33)	1445(2)	5748(2)	-4802(2)	35(1)
C(32)	50(2)	6851(2)	-5934(2)	36(1)
C(31)	4503(2)	2886(2)	-5953(2)	40(1)
C(30)	-3143(3)	10526(2)	-3732(2)	47(1)
C(29)	5278(3)	4447(2)	-6566(2)	42(1)

C(28)	-1831(3)	9230(2)	-5043(2)	40(1)
C(27)	86(3)	2703(2)	495(2)	45(1)
C(26)	-1430(3)	8903(2)	-6725(2)	39(1)
C(25)	1685(2)	3279(2)	-1286(2)	35(1)
C(24)	-2715(3)	9179(2)	-6838(2)	44(1)
C(23)	-1759(3)	10250(2)	-5344(2)	49(1)
C(22)	1157(2)	6539(2)	-4319(2)	38(1)
C(21)	3478(2)	3962(2)	601(2)	48(1)
C(20)	-2979(3)	9513(2)	-7802(2)	47(1)
C(19)	-1953(3)	9560(2)	-8666(2)	48(1)
C(18)	6582(3)	2084(2)	-7444(2)	55(1)
C(17)	-664(3)	9283(2)	-8563(2)	54(1)
C(16)	-2590(3)	8869(2)	-4075(2)	45(1)
C(15)	-2419(3)	10905(2)	-4698(2)	52(1)
C(14)	3250(3)	4018(3)	1602(2)	59(1)
C(13)	-3243(3)	9513(2)	-3429(2)	49(1)
C(12)	3442(3)	4857(3)	-188(2)	53(1)
C(11)	2235(3)	2565(2)	490(2)	52(1)
C(10)	-317(3)	3440(3)	1155(3)	69(1)
C(9)	2876(3)	5869(3)	1052(3)	68(1)
C(8)	1365(3)	2271(3)	1578(2)	62(1)
C(7)	3145(3)	5802(3)	36(3)	62(1)
C(6)	2955(3)	4951(4)	1814(3)	68(1)
C(5)	-3521(3)	12081(3)	-3234(3)	72(1)
C(4)	-3384(4)	10055(3)	-9810(3)	78(1)
C(3)	500(4)	1668(2)	1313(3)	88(1)
C(2)	2483(4)	6915(4)	1276(4)	99(2)
C(1)	404(4)	3190(3)	1736(3)	83(1)

Table 3. Bond lengths [Å] and angles [deg] for **PD-N-Ts**.

S(1)-O(4)	1.431(2)
S(1)-O(1)	1.440(2)
S(1)-C(11)	1.742(3)
S(1)-C(21)	1.762(3)
N(2)-C(46)	1.400(3)
N(2)-C(33)	1.429(3)
N(2)-C(44)	1.434(3)
N(1)-C(37)	1.403(3)
N(1)-C(26)	1.433(3)
N(1)-C(28)	1.428(3)

O(5)-C(45)	1.371(3)
O(5)-C(18)	1.422(3)
C(47)-C(40)	1.374(3)
C(47)-C(25)	1.398(4)
O(3)-C(30)	1.379(3)
O(3)-C(5)	1.408(4)
C(46)-C(41)	1.398(3)
C(46)-C(40)	1.402(3)
O(2)-C(19)	1.366(3)
O(2)-C(4)	1.427(4)
C(45)-C(29)	1.381(4)
C(45)-C(31)	1.382(4)
C(44)-C(38)	1.377(4)
C(44)-C(39)	1.391(4)
C(43)-C(32)	1.377(3)
C(43)-C(33)	1.387(4)
C(42)-C(41)	1.380(4)
C(42)-C(25)	1.398(4)
C(39)-C(29)	1.381(4)
C(38)-C(31)	1.386(3)
C(37)-C(35)	1.394(4)
C(37)-C(32)	1.400(3)
C(36)-C(11)	1.346(4)
C(36)-C(25)	1.457(4)
C(36)-C(27)	1.547(4)
C(35)-C(22)	1.388(4)
C(34)-C(17)	1.374(4)
C(34)-C(26)	1.389(4)
C(33)-C(22)	1.389(3)
C(30)-C(13)	1.373(4)
C(30)-C(15)	1.376(4)
C(28)-C(23)	1.373(4)
C(28)-C(16)	1.387(4)
C(27)-C(10)	1.488(4)
C(27)-C(3)	1.585(5)
C(26)-C(24)	1.385(4)
C(24)-C(20)	1.384(4)
C(23)-C(15)	1.386(4)
C(21)-C(14)	1.381(4)
C(21)-C(12)	1.388(4)
C(20)-C(19)	1.378(4)
C(19)-C(17)	1.386(4)
C(16)-C(13)	1.375(4)
C(14)-C(6)	1.354(5)
C(12)-C(7)	1.381(5)
C(11)-C(8)	1.537(4)

C(10)-C(1)	1.213(5)
C(9)-C(6)	1.390(5)
C(9)-C(7)	1.400(5)
C(9)-C(2)	1.506(5)
C(8)-C(1)	1.430(5)
C(8)-C(3)	1.623(5)
O(4)-S(1)-O(1)	118.25(14)
O(4)-S(1)-C(11)	110.88(13)
O(1)-S(1)-C(11)	107.13(14)
O(4)-S(1)-C(21)	108.41(14)
O(1)-S(1)-C(21)	107.57(14)
C(11)-S(1)-C(21)	103.58(14)
C(46)-N(2)-C(33)	120.67(19)
C(46)-N(2)-C(44)	120.59(19)
C(33)-N(2)-C(44)	118.74(19)
C(37)-N(1)-C(26)	121.3(2)
C(37)-N(1)-C(28)	121.3(2)
C(26)-N(1)-C(28)	117.4(2)
C(45)-O(5)-C(18)	117.5(2)
C(40)-C(47)-C(25)	122.1(2)
C(30)-O(3)-C(5)	117.2(2)
C(41)-C(46)-N(2)	121.1(2)
C(41)-C(46)-C(40)	117.3(2)
N(2)-C(46)-C(40)	121.6(2)
C(19)-O(2)-C(4)	118.0(3)
O(5)-C(45)-C(29)	116.7(2)
O(5)-C(45)-C(31)	124.2(2)
C(29)-C(45)-C(31)	119.1(2)
C(38)-C(44)-C(39)	118.4(2)
C(38)-C(44)-N(2)	121.4(2)
C(39)-C(44)-N(2)	120.2(2)
C(32)-C(43)-C(33)	121.4(2)
C(41)-C(42)-C(25)	121.6(2)
C(42)-C(41)-C(46)	121.2(2)
C(47)-C(40)-C(46)	120.9(2)
C(29)-C(39)-C(44)	120.4(2)
C(44)-C(38)-C(31)	121.5(2)
C(35)-C(37)-N(1)	121.1(2)
C(35)-C(37)-C(32)	117.6(2)
N(1)-C(37)-C(32)	121.3(2)
C(11)-C(36)-C(25)	133.7(2)
C(11)-C(36)-C(27)	104.7(2)
C(25)-C(36)-C(27)	121.5(2)
C(37)-C(35)-C(22)	121.1(2)
C(17)-C(34)-C(26)	120.7(3)

C(43)-C(33)-C(22)	118.1(2)
C(43)-C(33)-N(2)	120.5(2)
C(22)-C(33)-N(2)	121.4(2)
C(43)-C(32)-C(37)	120.9(2)
C(45)-C(31)-C(38)	119.8(2)
C(13)-C(30)-C(15)	119.7(3)
C(13)-C(30)-O(3)	116.1(3)
C(15)-C(30)-O(3)	124.2(3)
C(39)-C(29)-C(45)	120.8(2)
C(23)-C(28)-C(16)	118.2(2)
C(23)-C(28)-N(1)	120.7(2)
C(16)-C(28)-N(1)	121.1(2)
C(10)-C(27)-C(36)	105.2(2)
C(10)-C(27)-C(3)	99.0(3)
C(36)-C(27)-C(3)	99.7(2)
C(24)-C(26)-C(34)	118.5(3)
C(24)-C(26)-N(1)	120.4(2)
C(34)-C(26)-N(1)	121.1(2)
C(42)-C(25)-C(47)	116.7(2)
C(42)-C(25)-C(36)	123.9(2)
C(47)-C(25)-C(36)	119.5(2)
C(20)-C(24)-C(26)	121.0(3)
C(28)-C(23)-C(15)	121.2(3)
C(33)-C(22)-C(35)	120.8(2)
C(14)-C(21)-C(12)	120.1(3)
C(14)-C(21)-S(1)	119.3(3)
C(12)-C(21)-S(1)	120.6(2)
C(19)-C(20)-C(24)	119.9(3)
O(2)-C(19)-C(17)	115.4(3)
O(2)-C(19)-C(20)	125.0(3)
C(17)-C(19)-C(20)	119.6(3)
C(19)-C(17)-C(34)	120.3(3)
C(13)-C(16)-C(28)	120.9(3)
C(30)-C(15)-C(23)	119.7(3)
C(6)-C(14)-C(21)	119.8(3)
C(30)-C(13)-C(16)	120.3(3)
C(7)-C(12)-C(21)	119.6(3)
C(36)-C(11)-C(8)	107.8(2)
C(36)-C(11)-S(1)	131.3(2)
C(8)-C(11)-S(1)	119.2(2)
C(1)-C(10)-C(27)	110.2(4)
C(6)-C(9)-C(7)	117.6(3)
C(6)-C(9)-C(2)	123.0(4)
C(7)-C(9)-C(2)	119.4(4)
C(1)-C(8)-C(11)	106.1(3)
C(1)-C(8)-C(3)	100.7(3)

C(11)-C(8)-C(3)	97.4(2)
C(12)-C(7)-C(9)	120.7(3)
C(14)-C(6)-C(9)	122.2(3)
C(27)-C(3)-C(8)	87.1(2)
C(10)-C(1)-C(8)	109.8(4)

Symmetry transformations used to generate equivalent atoms:

Table 4. Anisotropic displacement parameters ($\text{Å}^2 \times 10^3$) for **PD-N-Ts**.

The anisotropic displacement factor exponent takes the form:
 $-2 \pi^2 [h^2 a^* a^* U_{11} + \dots + 2 h k a^* b^* U_{12}]$

	U11	U22	U33	U23	U13	U12
S(1)	35(1)	79(1)	43(1)	-10(1)	-13(1)	-13(1)
N(2)	38(1)	36(1)	31(1)	-9(1)	-6(1)	1(1)
N(1)	51(1)	36(1)	43(1)	-12(1)	-17(1)	5(1)
O(5)	39(1)	69(1)	55(1)	-32(1)	7(1)	-12(1)
O(4)	38(1)	103(2)	51(1)	-30(1)	0(1)	-24(1)
C(47)	29(1)	48(2)	35(1)	-14(1)	-5(1)	-10(1)
O(3)	58(1)	61(1)	73(2)	-34(1)	5(1)	-9(1)
C(46)	34(1)	34(1)	32(1)	-11(1)	-8(1)	-8(1)
O(2)	64(1)	86(2)	48(1)	-14(1)	-23(1)	3(1)
C(45)	31(1)	52(2)	38(1)	-17(1)	-6(1)	-6(1)
C(44)	32(1)	36(1)	31(1)	-10(1)	-9(1)	-4(1)
C(43)	38(1)	33(1)	33(1)	-11(1)	-5(1)	-9(1)
C(42)	35(1)	37(1)	40(2)	-8(1)	-11(1)	-5(1)
C(41)	31(1)	38(1)	38(2)	-12(1)	-5(1)	-4(1)
O(1)	53(1)	82(2)	65(1)	-3(1)	-31(1)	-9(1)
C(40)	33(1)	40(1)	36(1)	-12(1)	-11(1)	-4(1)
C(39)	43(2)	40(1)	37(1)	-12(1)	-11(1)	-11(1)
C(38)	34(1)	41(2)	39(2)	-11(1)	-1(1)	-11(1)
C(37)	37(1)	34(1)	39(1)	-7(1)	-7(1)	-8(1)
C(36)	36(1)	49(2)	37(2)	-8(1)	-8(1)	-12(1)
C(35)	40(1)	36(1)	43(2)	-16(1)	-7(1)	-6(1)
C(34)	38(2)	50(2)	50(2)	-1(1)	-12(1)	-8(1)
C(33)	33(1)	34(1)	34(1)	-8(1)	-3(1)	-7(1)
C(32)	37(1)	38(1)	33(1)	-8(1)	-8(1)	-9(1)
C(31)	38(2)	39(1)	43(2)	-15(1)	-7(1)	-6(1)

C(30)	36(2)	48(2)	56(2)	-22(1)	-7(1)	-1(1)
C(29)	39(2)	53(2)	37(2)	-12(1)	-2(1)	-20(1)
C(28)	38(1)	36(1)	43(2)	-11(1)	-13(1)	-1(1)
C(27)	36(1)	64(2)	36(2)	-10(1)	-6(1)	-19(1)
C(26)	42(2)	32(1)	41(2)	-8(1)	-11(1)	-3(1)
C(25)	35(1)	40(1)	35(1)	-10(1)	-8(1)	-12(1)
C(24)	40(2)	43(2)	46(2)	-14(1)	-6(1)	-4(1)
C(23)	48(2)	42(2)	49(2)	-11(1)	-3(1)	-10(1)
C(22)	35(1)	41(2)	37(1)	-13(1)	-9(1)	-5(1)
C(21)	26(1)	84(2)	32(2)	-8(1)	-8(1)	-13(1)
C(20)	41(2)	46(2)	55(2)	-18(1)	-17(1)	0(1)
C(19)	53(2)	42(2)	44(2)	-9(1)	-16(1)	-1(1)
C(18)	43(2)	62(2)	54(2)	-28(2)	-4(1)	3(1)
C(17)	46(2)	60(2)	42(2)	-3(1)	-6(1)	-6(1)
C(16)	43(2)	37(2)	51(2)	-8(1)	-10(1)	-6(1)
C(15)	49(2)	37(2)	64(2)	-16(1)	-3(2)	-12(1)
C(14)	39(2)	99(3)	40(2)	-19(2)	-9(1)	-15(2)
C(13)	41(2)	46(2)	50(2)	-10(1)	-4(1)	-5(1)
C(12)	32(2)	86(2)	39(2)	-11(2)	-7(1)	-14(2)
C(11)	40(2)	77(2)	37(2)	-5(1)	-10(1)	-17(1)
C(10)	41(2)	97(3)	74(2)	-46(2)	6(2)	-15(2)
C(9)	24(2)	105(3)	92(3)	-53(2)	-7(2)	-13(2)
C(8)	46(2)	100(3)	34(2)	0(2)	-14(1)	-20(2)
C(7)	31(2)	77(2)	73(2)	-16(2)	-10(2)	-12(2)
C(6)	37(2)	123(3)	52(2)	-37(2)	-8(2)	-16(2)
C(5)	48(2)	73(2)	107(3)	-57(2)	-5(2)	-9(2)
C(4)	79(3)	84(3)	71(2)	-21(2)	-45(2)	11(2)
C(3)	75(2)	49(2)	91(3)	-18(2)	57(2)	-23(2)
C(2)	48(2)	129(4)	147(4)	-82(3)	-9(2)	-21(2)
C(1)	74(3)	110(3)	57(2)	-36(2)	7(2)	-17(2)

Table 5. Hydrogen coordinates ($\times 10^4$) and isotropic displacement parameters ($\text{Å}^2 \times 10^3$) for **PD-N-Ts**.

	x	y	z	U(eq)
H(47A)	-157	4197	-1240	43
H(43A)	1079	5396	-5961	41
H(42A)	3548	2462	-1751	46

H(41A)	3853	3258	-3483	44
H(40A)	141	5006	-2963	43
H(39A)	4171	5566	-5835	46
H(38A)	2814	2950	-4831	46
H(35A)	87	7987	-4263	47
H(34A)	479	8788	-7542	58
H(32A)	-303	6956	-6505	44
H(31A)	4592	2195	-5971	48
H(29A)	5897	4840	-7022	51
H(27A)	-574	2711	133	53
H(24A)	-3425	9138	-6244	53
H(23A)	-1249	10512	-6006	58
H(22A)	1557	6445	-3777	45
H(20A)	-3865	9709	-7867	56
H(18A)	7381	1909	-7969	82
H(18B)	5806	2086	-7655	82
H(18C)	6630	1571	-6789	82
H(17A)	46	9313	-9157	65
H(16A)	-2660	8168	-3855	54
H(15A)	-2371	11611	-4922	62
H(14A)	3299	3405	2140	71
H(13A)	-3766	9255	-2770	59
H(12A)	3620	4818	-879	64
H(10A)	-1035	4023	1124	83
H(8A)	1834	1878	2138	74
H(7A)	3123	6415	-504	74
H(6A)	2798	4978	2506	82
H(5A)	-4052	12417	-2680	107
H(5B)	-3737	12506	-3886	107
H(5C)	-2582	12001	-3285	107
H(4B)	-3343	10273	-10548	116
H(4C)	-3975	10599	-9482	116
H(4D)	-3718	9420	-9508	116
H(3A)	1032	1082	1010	105
H(3B)	-241	1464	1887	105
H(2A)	2325	6832	2017	149
H(2B)	1675	7308	1048	149
H(2C)	3193	7288	910	149
H(1B)	339	3550	2224	99

Single-crystal X-Ray data for **Cl-mPD**

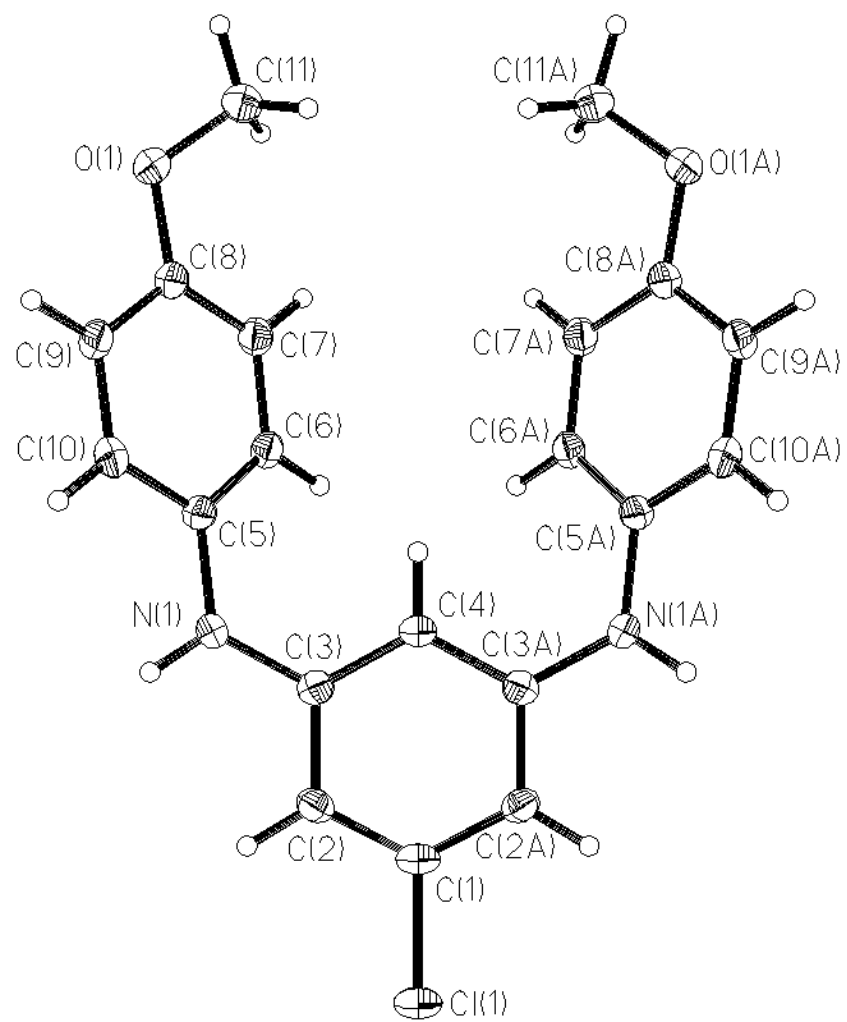


Figure B2. ORTEP (50 % ellipsoids) diagram of **Cl-mPD** generated with SHELXTL software.

Table 1. Crystal data and structure refinement for **Cl-mPD**.

Identification code	Cl-mPD
Empirical formula	C20 H19 Cl N2 O2
Formula weight	354.82
Temperature	173(2) K
Wavelength	0.71073 Å
Crystal system, space group	Monoclinic, Cm
Unit cell dimensions	a = 7.4663(8) Å alpha = 90 deg. b = 17.0964(18) Å beta = 112.206(2) deg. c = 7.0281(7) Å gamma = 90 deg.
Volume	830.58(15) Å ³
Z, Calculated density	2, 1.419 Mg/m ³
Absorption coefficient	0.247 mm ⁻¹
F(000)	372
Crystal size	0.60 x 0.60 x 0.42 mm
Theta range for data collection	3.13 to 28.31 deg.
Limiting indices	-9<=h<=8, -19<=k<=22, -8<=l<=9
Reflections collected / unique	3316 / 1659 [R(int) = 0.0124]
Completeness to theta = 25.30	99.6 %
Absorption correction	None
Refinement method	Full-matrix least-squares on F ²
Data / restraints / parameters	1659 / 2 / 158
Goodness-of-fit on F ²	1.064
Final R indices [I>2sigma(I)]	R1 = 0.0231, wR2 = 0.0632

R indices (all data)	R1 = 0.0236, wR2 = 0.0636
Absolute structure parameter	0.03(4)
Extinction coefficient	0.009(2)
Largest diff. peak and hole	0.212 and -0.169 e. \AA^{-3}

Table 2. Atomic coordinates ($\times 10^4$) and equivalent isotropic displacement parameters ($\text{\AA}^2 \times 10^3$) for **Cl-*m*PD**.

U(eq) is defined as one third of the trace of the orthogonalized Uij tensor.

	x	y	z	U(eq)
Cl	8404(1)	5000	17036(1)	32(1)
O(1)	-825(2)	6858(1)	2381(1)	28(1)
N(1)	3947(2)	6425(1)	10631(2)	24(1)
C(1)	6636(3)	5000	14551(3)	21(1)
C(2)	6008(2)	5715(1)	13620(2)	20(1)
C(3)	4589(2)	5710(1)	11609(2)	19(1)
C(4)	3848(3)	5000	10665(2)	20(1)
C(5)	2785(2)	6517(1)	8525(2)	20(1)
C(6)	3083(2)	6077(1)	6998(2)	20(1)
C(7)	1877(2)	6161(1)	4940(2)	22(1)
C(8)	421(2)	6719(1)	4377(2)	21(1)
C(9)	170(2)	7190(1)	5878(2)	23(1)
C(10)	1325(2)	7081(1)	7930(2)	22(1)
C(11)	-1004(2)	6245(1)	936(2)	27(1)

Table 3. Bond lengths [Å] and angles [deg] for **Cl-*m*PD**.

Cl-C(1)	1.7464(18)
O(1)-C(8)	1.3799(14)
O(1)-C(11)	1.4296(17)

N(1)-C(3)	1.3947(16)
N(1)-C(5)	1.4129(14)
N(1)-H(1N)	0.852(18)
C(1)-C(2)#1	1.3814(15)
C(1)-C(2)	1.3815(15)
C(2)-C(3)	1.4098(16)
C(2)-H(2)	0.951(16)
C(3)-C(4)	1.3943(15)
C(4)-C(3)#1	1.3943(15)
C(4)-H(4)	0.99(3)
C(5)-C(6)	1.3953(18)
C(5)-C(10)	1.3963(18)
C(6)-C(7)	1.3927(17)
C(6)-H(6)	0.950(18)
C(7)-C(8)	1.3864(19)
C(7)-H(7)	0.924(18)
C(8)-C(9)	1.3942(18)
C(9)-C(10)	1.3849(17)
C(9)-H(9)	0.970(18)
C(10)-H(10)	0.968(19)
C(11)-H(11C)	0.949(18)
C(11)-H(11B)	0.983(19)
C(11)-H(11A)	0.93(2)
C(8)-O(1)-C(11)	116.27(10)
C(3)-N(1)-C(5)	125.08(11)
C(3)-N(1)-H(1N)	117.7(12)
C(5)-N(1)-H(1N)	116.6(12)
C(2)#1-C(1)-C(2)	124.32(16)
C(2)#1-C(1)-Cl	117.82(8)
C(2)-C(1)-Cl	117.82(8)
C(1)-C(2)-C(3)	117.53(12)
C(1)-C(2)-H(2)	124.0(9)
C(3)-C(2)-H(2)	118.4(9)
C(4)-C(3)-N(1)	121.81(11)
C(4)-C(3)-C(2)	119.63(11)
N(1)-C(3)-C(2)	118.55(11)
C(3)-C(4)-C(3)#1	121.14(15)
C(3)-C(4)-H(4)	119.42(8)
C(3)#1-C(4)-H(4)	119.42(8)
C(6)-C(5)-C(10)	118.36(11)
C(6)-C(5)-N(1)	122.15(11)
C(10)-C(5)-N(1)	119.46(11)
C(7)-C(6)-C(5)	120.98(11)
C(7)-C(6)-H(6)	118.7(10)
C(5)-C(6)-H(6)	120.3(10)

C(8)-C(7)-C(6)	119.79(11)
C(8)-C(7)-H(7)	121.4(11)
C(6)-C(7)-H(7)	118.8(11)
O(1)-C(8)-C(7)	124.25(11)
O(1)-C(8)-C(9)	115.98(11)
C(7)-C(8)-C(9)	119.76(11)
C(10)-C(9)-C(8)	120.09(11)
C(10)-C(9)-H(9)	120.7(10)
C(8)-C(9)-H(9)	119.2(10)
C(9)-C(10)-C(5)	120.87(12)
C(9)-C(10)-H(10)	120.6(11)
C(5)-C(10)-H(10)	118.4(11)
O(1)-C(11)-H(11C)	111.9(10)
O(1)-C(11)-H(11B)	107.7(10)
H(11C)-C(11)-H(11B)	113.5(15)
O(1)-C(11)-H(11A)	106.5(13)
H(11C)-C(11)-H(11A)	109.0(15)
H(11B)-C(11)-H(11A)	107.9(16)

Symmetry transformations used to generate equivalent atoms:

#1 x,-y+1,z

Table 4. Anisotropic displacement parameters ($\text{Å}^2 \times 10^3$) for **Cl-mPD**.

The anisotropic displacement factor exponent takes the form:

$$-2 \pi^2 [h^2 a^*{}^2 U_{11} + \dots + 2 h k a^* b^* U_{12}]$$

	U11	U22	U33	U23	U13	U12
Cl	33(1)	35(1)	17(1)	0	-3(1)	0
O(1)	33(1)	21(1)	21(1)	1(1)	2(1)	3(1)
N(1)	32(1)	15(1)	19(1)	-3(1)	2(1)	1(1)
C(1)	18(1)	29(1)	14(1)	0	4(1)	0
C(2)	21(1)	21(1)	18(1)	-3(1)	6(1)	-3(1)
C(3)	19(1)	19(1)	18(1)	1(1)	7(1)	1(1)
C(4)	20(1)	21(1)	16(1)	0	3(1)	0
C(5)	22(1)	16(1)	18(1)	1(1)	4(1)	-2(1)
C(6)	21(1)	16(1)	23(1)	2(1)	7(1)	2(1)
C(7)	27(1)	18(1)	22(1)	0(1)	10(1)	0(1)

C(8)	24(1)	17(1)	21(1)	2(1)	6(1)	-1(1)
C(9)	22(1)	18(1)	25(1)	1(1)	5(1)	3(1)
C(10)	26(1)	17(1)	24(1)	-3(1)	9(1)	0(1)
C(11)	32(1)	26(1)	21(1)	-1(1)	7(1)	1(1)

Table 5. Hydrogen coordinates ($\times 10^4$) and isotropic displacement parameters ($\text{Å}^2 \times 10^3$) for **Cl-mPD**.

	x	y	z	U(eq)
H(1N)	4130(30)	6831(11)	11380(20)	23(4)
H(2)	6430(20)	6205(9)	14270(20)	21(4)
H(4)	2750(40)	5000	9310(40)	29(6)
H(6)	4120(30)	5712(10)	7350(20)	24(4)
H(7)	2100(30)	5854(10)	3970(30)	23(4)
H(9)	-810(30)	7597(10)	5460(20)	23(4)
H(10)	1080(30)	7372(10)	8990(30)	31(4)
H(11C)	150(30)	6178(9)	680(20)	23(4)
H(11B)	-1420(30)	5770(12)	1450(20)	31(5)
H(11A)	-2000(30)	6391(12)	-280(30)	39(5)

Single-crystal X-Ray data for **F-mPD**

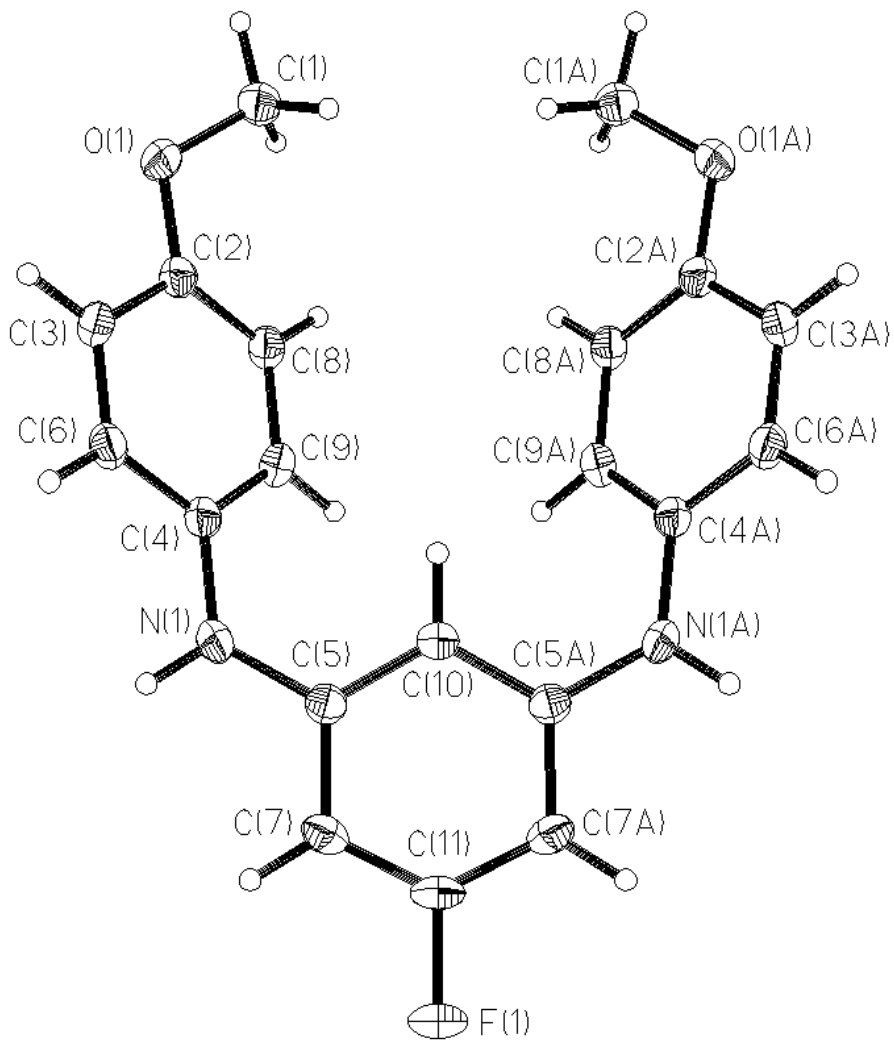


Figure B3. ORTEP (50 % ellipsoids) diagram of **F-mPD** generated with SHELXTL software.

Table 1. Crystal data and structure refinement for **F-mPD**.

Identification code	F-mPD
Empirical formula	C20 H19 F N2 O2
Formula weight	338.37
Temperature	173(2) K
Wavelength	0.71073 Å
Crystal system, space group	Monoclinic, Cm
Unit cell dimensions	a = 7.5150(10) Å alpha = 90 deg. b = 17.187(2) Å beta = 113.736(2) deg. c = 6.7768(9) Å gamma = 90 deg.
Volume	801.27(19) Å ³
Z, Calculated density	2, 1.402 Mg/m ³
Absorption coefficient	0.099 mm ⁻¹
F(000)	356
Crystal size	0.64 x 0.26 x 0.18 mm
Theta range for data collection	3.19 to 28.18 deg.
Limiting indices	-9<=h<=7, -22<=k<=22, -7<=l<=8
Reflections collected / unique	2747 / 976 [R(int) = 0.0130]
Completeness to theta = 28.18	95.7 %
Refinement method	Full-matrix least-squares on F ²
Data / restraints / parameters	976 / 2 / 120
Goodness-of-fit on F ²	1.086
Final R indices [I>2sigma(I)]	R1 = 0.0270, wR2 = 0.0835
R indices (all data)	R1 = 0.0271, wR2 = 0.0835

Absolute structure parameter	0(10)
Extinction coefficient	0.039(5)
Largest diff. peak and hole	0.223 and -0.157 e. Å^{-3}

Table 2. Atomic coordinates ($\times 10^4$) and equivalent isotropic displacement parameters ($\text{\AA}^2 \times 10^3$) for **F-mPD**.
U(eq) is defined as one third of the trace of the orthogonalized Uij tensor.

	x	y	z	U(eq)
F(1)	4354(2)	5000	8112(2)	39(1)
C(11)	2921(3)	5000	6070(3)	25(1)
N(1)	106(2)	3587(1)	1994(2)	28(1)
O(1)	-4817(2)	3173(1)	-6686(2)	30(1)
C(10)	18(3)	5000	2039(3)	22(1)
C(9)	-827(2)	3938(1)	-1810(2)	23(1)
C(8)	-2062(2)	3858(1)	-3977(2)	23(1)
C(7)	2282(3)	4288(1)	5120(2)	24(1)
C(6)	-2537(2)	2925(1)	-862(3)	24(1)
C(5)	799(2)	4291(1)	3022(2)	21(1)
C(4)	-1077(2)	3493(1)	-217(2)	22(1)
C(3)	-3735(2)	2825(1)	-3025(3)	25(1)
C(2)	-3527(2)	3301(1)	-4583(2)	23(1)
C(1)	-5073(3)	3800(1)	-8171(3)	29(1)

Table 3. Bond lengths [Å] and angles [deg] for **F-mPD**.

F(1)-C(11)	1.369(2)
C(11)-C(7)	1.3756(19)
C(11)-C(7)#1	1.3756(19)
N(1)-C(5)	1.390(2)
N(1)-C(4)	1.4101(18)

O(1)-C(2)	1.3810(17)
O(1)-C(1)	1.433(2)
C(10)-C(5)	1.3993(18)
C(10)-C(5)#1	1.3993(18)
C(9)-C(8)	1.393(2)
C(9)-C(4)	1.396(2)
C(8)-C(2)	1.391(2)
C(7)-C(5)	1.4098(19)
C(6)-C(3)	1.388(2)
C(6)-C(4)	1.401(2)
C(3)-C(2)	1.393(2)

Table 4. Anisotropic displacement parameters ($\text{Å}^2 \times 10^3$) for **F-mPD**.

The anisotropic displacement factor exponent takes the form:

$$-2 \pi^2 [h^2 a^* a^* U_{11} + \dots + 2 h k a^* b^* U_{12}]$$

	U11	U22	U33	U23	U13	U12
F(1)	41(1)	43(1)	19(1)	0	-5(1)	0
C(11)	22(1)	37(1)	14(1)	0	4(1)	0
N(1)	38(1)	17(1)	22(1)	4(1)	6(1)	1(1)
O(1)	37(1)	22(1)	23(1)	-2(1)	3(1)	-4(1)
C(10)	22(1)	21(1)	19(1)	0	6(1)	0
C(9)	26(1)	17(1)	26(1)	-2(1)	11(1)	-3(1)
C(8)	29(1)	18(1)	23(1)	-1(1)	12(1)	-1(1)
C(7)	26(1)	27(1)	19(1)	4(1)	8(1)	4(1)
C(6)	28(1)	18(1)	26(1)	4(1)	11(1)	0(1)
C(5)	23(1)	22(1)	19(1)	0(1)	9(1)	0(1)
C(4)	26(1)	17(1)	21(1)	0(1)	7(1)	1(1)
C(3)	25(1)	17(1)	29(1)	-1(1)	8(1)	-3(1)
C(2)	26(1)	18(1)	23(1)	-1(1)	8(1)	3(1)
C(1)	35(1)	26(1)	23(1)	1(1)	8(1)	0(1)

Table 5. Hydrogen coordinates ($\times 10^4$) and isotropic displacement parameters ($\text{Å}^2 \times 10^3$) for **F-mPD**.

	x	y	z	U(eq)
H(1)	434	3163	2789	33
H(10)	-1060	5000	681	26
H(9)	209	4303	-1407	27
H(8)	-1906	4182	-5032	27
H(7)	2817	3816	5844	29
H(6)	-2708	2605	191	29
H(3)	-4701	2430	-3446	30
H(1A)	-5418	4275	-7604	44
H(1B)	-6116	3669	-9564	44
H(1C)	-3861	3885	-8359	44

Single-crystal X-Ray data for **Br-*m*PD**

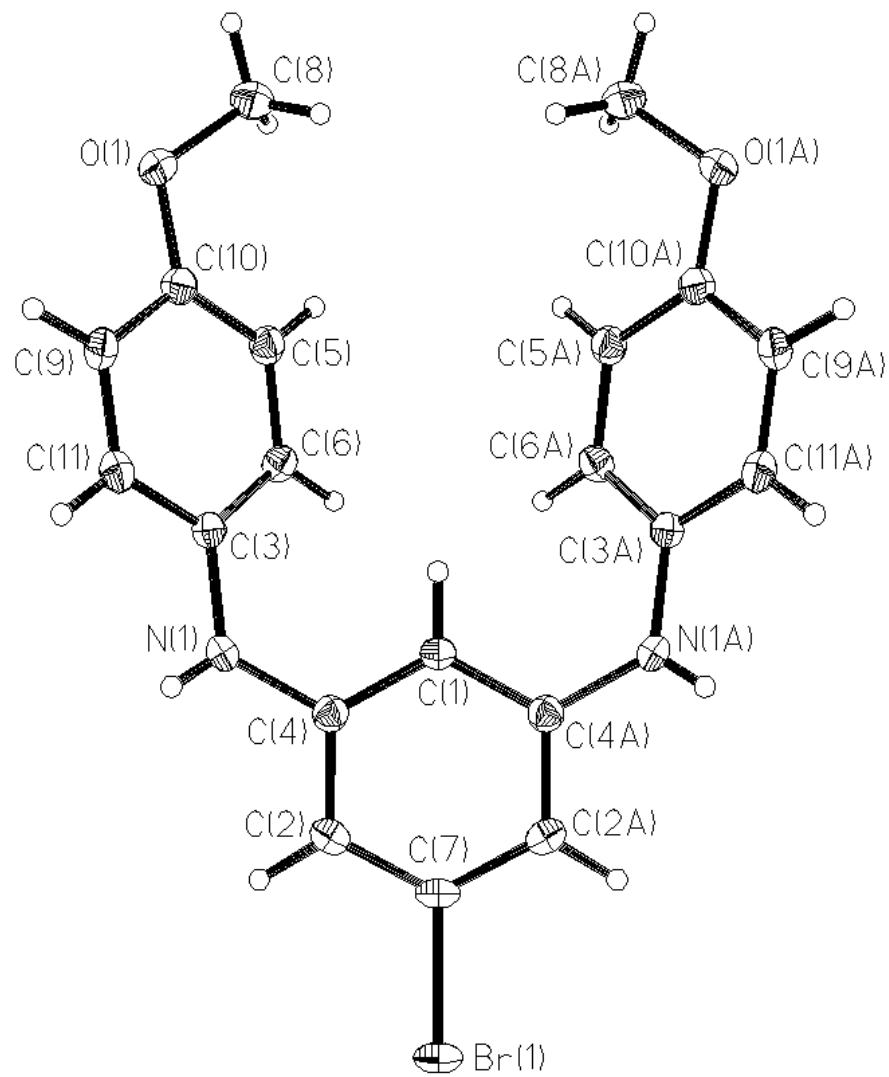


Figure B4. ORTEP (50 % ellipsoids) diagram of **Br-*m*PD** generated with SHELXTL software.

Table 1. Crystal data and structure refinement for **Br-*m*PD**.

Identification code	Br-<i>m</i>PD
Empirical formula	C20 H19 Br N2 O2
Formula weight	399.28
Temperature	173(2) K
Wavelength	0.71073 Å
Crystal system, space group	Monoclinic, Cm
Unit cell dimensions	a = 7.4852(6) Å alpha = 90 deg. b = 17.0650(13) Å beta = 111.4910(10) deg. c = 7.1322(6) Å gamma = 90 deg.
Volume	847.69(12) Å ³
Z, Calculated density	2, 1.564 Mg/m ³
Absorption coefficient	2.441 mm ⁻¹
F(000)	408
Crystal size	0.20 x 0.11 x 0.10 mm
Theta range for data collection	2.39 to 28.23 deg.
Limiting indices	-9<=h<=7, -22<=k<=22, -8<=l<=9
Reflections collected / unique	2878 / 1394 [R(int) = 0.0183]
Completeness to theta = 25.30	99.5 %
Absorption correction	Semi-empirical from equivalents
Max. and min. transmission	0.783 and 0.592588494
Refinement method	Full-matrix least-squares on F ²
Data / restraints / parameters	1394 / 2 / 148
Goodness-of-fit on F ²	1.071

Final R indices [I>2sigma(I)]	R1 = 0.0187, wR2 = 0.0451
R indices (all data)	R1 = 0.0190, wR2 = 0.0452
Absolute structure parameter	0.015(7)
Largest diff. peak and hole	0.395 and -0.256 e.A^-3

Table 2. Atomic coordinates ($\times 10^4$) and equivalent isotropic displacement parameters ($\text{Å}^2 \times 10^3$) for **Br-mPD**.

U(eq) is defined as one third of the trace of the orthogonalized Uij tensor.

	x	y	z	U(eq)
Br(1)	2942(1)	5000	1923(1)	29(1)
C(7)	1070(4)	5000	-738(4)	19(1)
C(6)	-2377(3)	3918(1)	-8166(5)	19(1)
N(1)	-1529(3)	3571(1)	-4603(2)	23(1)
C(5)	-3551(3)	3831(1)	-10177(3)	20(1)
C(4)	-902(3)	4286(1)	-3624(3)	18(1)
C(3)	-2673(3)	3478(1)	-6651(3)	19(1)
C(2)	465(3)	4282(1)	-1655(3)	20(1)
C(1)	-1622(4)	5000	-4569(4)	18(1)
O(1)	-6231(2)	3128(1)	-12664(2)	27(1)
C(11)	-4134(3)	2916(1)	-7227(3)	21(1)
C(10)	-5013(3)	3273(1)	-10715(3)	20(1)
C(9)	-5273(3)	2808(1)	-9229(3)	22(1)
C(8)	-6396(3)	3739(1)	-14105(3)	27(1)

Table 3. Bond lengths [Å] and angles [deg] for **Br-*m*PD**.

Br(1)-C(7)	1.902(2)
C(7)-C(2)	1.384(2)
C(7)-C(2)#1	1.384(2)
C(6)-C(5)	1.388(4)
C(6)-C(3)	1.399(3)
N(1)-C(4)	1.398(2)
N(1)-C(3)	1.405(2)
C(5)-C(10)	1.394(3)
C(4)-C(1)	1.401(2)
C(4)-C(2)	1.402(3)
C(3)-C(11)	1.399(3)
C(1)-C(4)#1	1.401(2)
O(1)-C(10)	1.377(2)
O(1)-C(8)	1.437(2)
C(11)-C(9)	1.381(3)
C(10)-C(9)	1.394(3)
C(2)-C(7)-C(2)#1	124.5(2)
C(2)-C(7)-Br(1)	117.74(12)
C(2)#1-C(7)-Br(1)	117.74(12)
C(5)-C(6)-C(3)	121.41(17)
C(4)-N(1)-C(3)	125.66(16)
C(6)-C(5)-C(10)	119.55(17)
N(1)-C(4)-C(1)	121.25(17)
N(1)-C(4)-C(2)	118.96(16)
C(1)-C(4)-C(2)	119.78(17)
C(11)-C(3)-C(6)	118.00(18)
C(11)-C(3)-N(1)	119.75(17)
C(6)-C(3)-N(1)	122.22(18)
C(7)-C(2)-C(4)	117.48(17)
C(4)-C(1)-C(4)#1	120.8(2)
C(10)-O(1)-C(8)	116.32(15)
C(9)-C(11)-C(3)	121.03(17)
O(1)-C(10)-C(9)	116.10(17)
O(1)-C(10)-C(5)	124.26(17)
C(9)-C(10)-C(5)	119.62(17)
C(11)-C(9)-C(10)	120.29(17)

Symmetry transformations used to generate equivalent atoms:

#1 x,-y+1,z

Table 4. Anisotropic displacement parameters ($\text{Å}^2 \times 10^3$) for **Br-mPD**.

The anisotropic displacement factor exponent takes the form:

$$-2 \pi^2 [h^2 a^*{}^2 U_{11} + \dots + 2 h k a^* b^* U_{12}]$$

	U11	U22	U33	U23	U13	U12
Br(1)	30(1)	34(1)	14(1)	0	-3(1)	0
C(7)	17(1)	27(1)	12(1)	0	3(1)	0
C(6)	20(1)	18(1)	20(1)	-2(1)	7(1)	-3(1)
N(1)	31(1)	15(1)	18(1)	3(1)	3(1)	-1(1)
C(5)	24(1)	18(1)	19(1)	0(1)	9(1)	0(1)
C(4)	20(1)	17(1)	18(1)	-1(1)	8(1)	0(1)
C(3)	21(1)	15(1)	18(1)	-1(1)	5(1)	2(1)
C(2)	19(1)	21(1)	18(1)	3(1)	6(1)	2(1)
C(1)	17(1)	17(1)	17(1)	0	2(1)	0
O(1)	34(1)	21(1)	19(1)	-1(1)	2(1)	-4(1)
C(11)	25(1)	16(1)	23(1)	3(1)	9(1)	-1(1)
C(10)	23(1)	18(1)	19(1)	-1(1)	6(1)	2(1)
C(9)	24(1)	16(1)	25(1)	0(1)	7(1)	-3(1)
C(8)	32(1)	28(1)	18(1)	2(1)	5(1)	-1(1)

Table 5. Hydrogen coordinates ($\times 10^4$) and isotropic displacement parameters ($\text{Å}^2 \times 10^3$) for **Br-mPD**.

	x	y	z	U(eq)
H(1N)	-1400(40)	3241(18)	-4000(40)	27
H(5)	-3330(40)	4139(16)	-11150(40)	24
H(2)	970(40)	3807(17)	-970(40)	24
H(1)	-2620(50)	5000	-5830(50)	22

H(11)	-4320(40)	2596(16)	-6300(40)	26
H(9)	-6250(40)	2408(17)	-9560(40)	27
H(8C)	-6780(50)	4212(18)	-13540(40)	41
H(8B)	-5170(50)	3810(20)	-14350(50)	41
H(8A)	-7350(50)	3605(19)	-15280(50)	41
H(6)	-1320(40)	4276(16)	-7820(50)	33(7)

Single-crystal X-Ray data for **Cl-mPD-SMe**

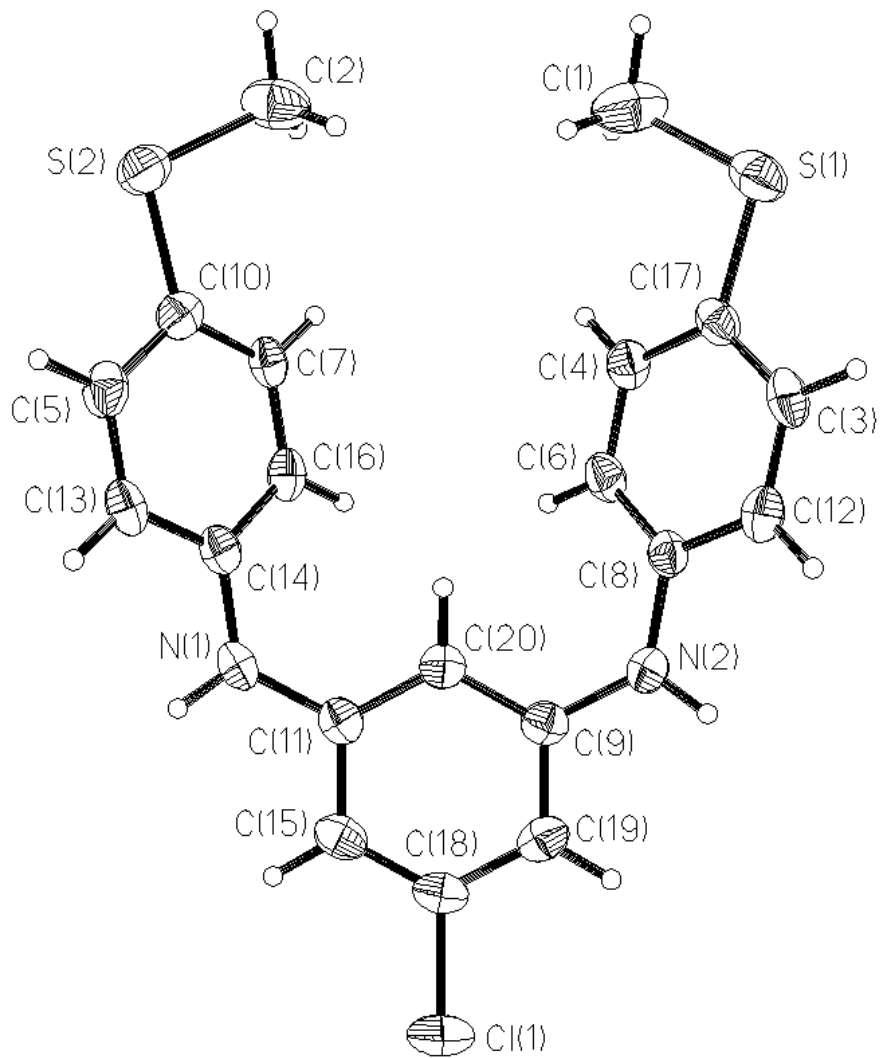


Figure B5. ORTEP (50 % ellipsoids) diagram of **Cl-mPD-SMe** generated with SHELXTL software.

Table 1. Crystal data and structure refinement for **Cl-*m*PD-SMe**.

Identification code	Cl-<i>m</i>PD-SMe
Empirical formula	C20 H19 Cl N2 S2
Formula weight	386.94
Temperature	173(2) K
Wavelength	0.71073 Å
Crystal system, space group	Monoclinic, Cc
Unit cell dimensions	a = 18.532(3) Å alpha = 90 deg. b = 7.1762(11) Å beta = 92.166(3) deg. c = 14.215(2) Å gamma = 90 deg.
Volume	1889.1(5) Å ³
Z, Calculated density	4, 1.361 Mg/m ³
Absorption coefficient	0.428 mm ⁻¹
F(000)	808
Crystal size	0.34 x 0.28 x 0.10 mm
Theta range for data collection	2.20 to 28.35 deg.
Limiting indices	-24<=h<=23, -9<=k<=9, -18<=l<=15
Reflections collected / unique	6167 / 3707 [R(int) = 0.0222]
Completeness to theta = 28.35	94.6 %
Absorption correction	None
Refinement method	Full-matrix least-squares on F ²
Data / restraints / parameters	3707 / 2 / 229
Goodness-of-fit on F ²	1.130
Final R indices [I>2sigma(I)]	R1 = 0.0448, wR2 = 0.1037

R indices (all data)	R1 = 0.0542, wR2 = 0.1072
Absolute structure parameter	0.09(8)
Extinction coefficient	0.0002(3)
Largest diff. peak and hole	0.266 and -0.260 e. \AA^{-3}

Table 2. Atomic coordinates ($\times 10^4$) and equivalent isotropic displacement parameters ($\text{\AA}^2 \times 10^3$) for **Cl-mPD-SMe**.

U(eq) is defined as one third of the trace of the orthogonalized Uij tensor.

	x	y	z	U(eq)
S(2)	9941(1)	7810(2)	2218(1)	43(1)
Cl(1)	11858(1)	8083(1)	9585(1)	50(1)
S(1)	13849(1)	7835(2)	2439(1)	45(1)
C(20)	11859(2)	8090(4)	6432(3)	29(1)
C(19)	12515(2)	8060(5)	7926(3)	35(1)
C(18)	11853(2)	8065(5)	8358(3)	33(1)
C(17)	13604(2)	7846(5)	3631(3)	31(1)
C(16)	10826(2)	6742(4)	4829(3)	33(1)
C(15)	11205(2)	8013(5)	7859(3)	34(1)
C(14)	10426(2)	7896(5)	5397(3)	33(1)
N(2)	13175(2)	8100(4)	6516(2)	36(1)
C(13)	9867(2)	8924(5)	4974(3)	36(1)
C(12)	13861(2)	9057(5)	5193(3)	37(1)
C(11)	11205(2)	8021(4)	6869(2)	28(1)
C(10)	10166(2)	7794(5)	3432(3)	32(1)
C(9)	12518(2)	8066(5)	6940(2)	29(1)
N(1)	10538(2)	7983(4)	6377(2)	37(1)
C(8)	13301(2)	7987(4)	5549(2)	29(1)
C(7)	10705(2)	6705(4)	3864(2)	30(1)
C(6)	12921(2)	6803(5)	4939(3)	33(1)
C(5)	9740(2)	8883(5)	4007(3)	37(1)
C(4)	13063(2)	6734(5)	3982(3)	33(1)
C(3)	14009(2)	8974(5)	4253(3)	37(1)
C(2)	10765(3)	7075(6)	1696(3)	52(1)

C(1)	13046(3)	7016(6)	1819(3)	61(1)
------	----------	---------	---------	-------

Table 3. Bond lengths [Å] and angles [deg] for **Cl-*m*PD-SMe**.

S(2)-C(10)	1.760(4)
S(2)-C(2)	1.802(4)
Cl(1)-C(18)	1.744(4)
S(1)-C(17)	1.771(4)
S(1)-C(1)	1.799(5)
C(20)-C(11)	1.383(5)
C(20)-C(9)	1.396(5)
C(19)-C(18)	1.393(6)
C(19)-C(9)	1.402(5)
C(18)-C(15)	1.372(5)
C(17)-C(4)	1.388(5)
C(17)-C(3)	1.397(5)
C(16)-C(7)	1.382(5)
C(16)-C(14)	1.391(5)
C(15)-C(11)	1.408(5)
C(14)-C(13)	1.390(5)
C(14)-N(1)	1.403(5)
N(2)-C(9)	1.379(4)
N(2)-C(8)	1.405(4)
C(13)-C(5)	1.387(5)
C(12)-C(3)	1.376(5)
C(12)-C(8)	1.402(5)
C(11)-N(1)	1.396(4)
C(10)-C(7)	1.392(5)
C(10)-C(5)	1.397(5)
C(8)-C(6)	1.386(5)
C(6)-C(4)	1.396(5)
C(10)-S(2)-C(2)	103.22(19)
C(17)-S(1)-C(1)	103.5(2)
C(11)-C(20)-C(9)	122.1(3)
C(18)-C(19)-C(9)	118.5(3)
C(15)-C(18)-C(19)	122.7(4)
C(15)-C(18)-Cl(1)	119.3(3)
C(19)-C(18)-Cl(1)	118.0(3)
C(4)-C(17)-C(3)	118.9(3)
C(4)-C(17)-S(1)	123.8(3)

C(3)-C(17)-S(1)	117.2(3)
C(7)-C(16)-C(14)	121.2(3)
C(18)-C(15)-C(11)	118.9(3)
C(13)-C(14)-C(16)	118.1(3)
C(13)-C(14)-N(1)	119.1(3)
C(16)-C(14)-N(1)	122.7(3)
C(9)-N(2)-C(8)	127.4(3)
C(5)-C(13)-C(14)	120.9(3)
C(3)-C(12)-C(8)	120.3(3)
C(20)-C(11)-N(1)	123.3(3)
C(20)-C(11)-C(15)	118.8(3)
N(1)-C(11)-C(15)	117.8(3)
C(7)-C(10)-C(5)	117.9(3)
C(7)-C(10)-S(2)	125.1(3)
C(5)-C(10)-S(2)	116.8(3)
N(2)-C(9)-C(20)	122.9(3)
N(2)-C(9)-C(19)	118.3(3)
C(20)-C(9)-C(19)	118.7(3)
C(11)-N(1)-C(14)	126.4(3)
C(6)-C(8)-C(12)	118.4(3)
C(6)-C(8)-N(2)	123.3(3)
C(12)-C(8)-N(2)	118.3(3)
C(16)-C(7)-C(10)	120.9(3)
C(8)-C(6)-C(4)	121.4(3)
C(13)-C(5)-C(10)	120.9(3)
C(17)-C(4)-C(6)	119.7(3)
C(12)-C(3)-C(17)	121.2(3)

Symmetry transformations used to generate equivalent atoms:

Table 4. Anisotropic displacement parameters ($\text{Å}^2 \times 10^3$) for **Cl-*m*PD-SMe**.

The anisotropic displacement factor exponent takes the form:

$$-2 \pi^2 [h^2 a^{*2} U_{11} + \dots + 2 h k a^{*} b^{*} U_{12}]$$

	U11	U22	U33	U23	U13	U12
S(2)	41(1)	52(1)	36(1)	7(1)	-4(1)	-9(1)
Cl(1)	71(1)	54(1)	25(1)	-3(1)	4(1)	-1(1)
S(1)	47(1)	50(1)	39(1)	11(1)	12(1)	11(1)

C(20)	32(2)	25(2)	29(2)	2(1)	2(1)	-1(1)
C(19)	40(2)	32(2)	32(2)	-4(2)	-7(2)	3(2)
C(18)	47(2)	26(2)	26(2)	0(1)	6(2)	0(2)
C(17)	28(2)	30(2)	34(2)	7(1)	7(1)	7(1)
C(16)	24(2)	30(2)	44(2)	1(1)	1(2)	4(1)
C(15)	42(2)	28(2)	33(2)	-2(2)	9(2)	3(2)
C(14)	26(2)	37(2)	37(2)	1(2)	6(1)	-3(1)
N(2)	27(1)	49(2)	33(2)	-7(1)	-1(1)	-8(1)
C(13)	27(2)	33(2)	48(2)	-3(2)	10(2)	6(1)
C(12)	28(2)	35(2)	46(2)	-1(2)	-2(2)	-6(1)
C(11)	30(2)	21(2)	33(2)	-1(1)	4(1)	2(1)
C(10)	32(2)	29(2)	34(2)	3(1)	-1(2)	-6(1)
C(9)	34(2)	24(2)	30(2)	-3(1)	2(1)	-3(1)
N(1)	26(1)	51(2)	36(2)	-4(1)	9(1)	3(1)
C(8)	24(2)	31(2)	32(2)	1(1)	2(1)	2(1)
C(7)	22(2)	27(2)	41(2)	-2(1)	5(1)	-2(1)
C(6)	27(2)	33(2)	40(2)	-2(2)	8(1)	-7(1)
C(5)	31(2)	34(2)	45(2)	9(2)	0(2)	5(1)
C(4)	30(2)	31(2)	39(2)	-6(2)	3(2)	-1(1)
C(3)	27(2)	33(2)	51(2)	6(2)	9(2)	-6(1)
C(2)	74(3)	43(2)	39(2)	-4(2)	10(2)	12(2)
C(1)	90(4)	54(3)	38(2)	-1(2)	-6(2)	-15(2)

Table 5. Hydrogen coordinates (x 10^4) and isotropic displacement parameters (A^2 x 10^3) for **Cl-mPD-SMe**.

	x	y	z	U(eq)
H(20A)	11859	8155	5764	34
H(19A)	12955	8054	8292	42
H(16A)	11190	5966	5109	39
H(15A)	10763	7973	8177	41
H(2A)	13560	8204	6895	44
H(13A)	9567	9665	5353	43
H(12A)	14140	9844	5603	44
H(1A)	10151	8016	6716	45
H(7A)	10993	5926	3489	36
H(6A)	12557	6021	5177	40
H(5A)	9358	9606	3731	44

H(4A)	12791	5930	3573	40
H(3A)	14394	9697	4023	44
H(2B)	10708	7150	1008	78
H(2C)	10874	5787	1881	78
H(2D)	11162	7889	1913	78
H(1B)	13106	7130	1139	92
H(1C)	12632	7764	2001	92
H(1D)	12964	5706	1979	92

Single-crystal X-Ray data for **H-mPD**

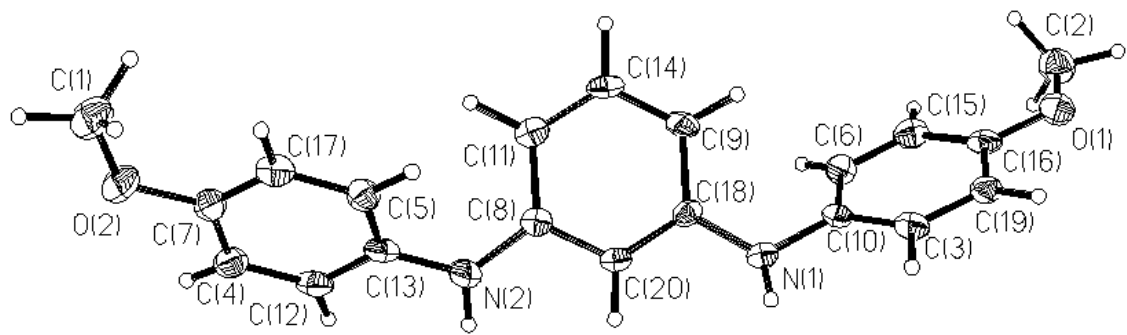


Figure B6. ORTEP (50 % ellipsoids) diagram of **H-mPD** generated with SHELXTL software.

Table 1. Crystal data and structure refinement for **H-mPD**.

Identification code	H-mPD
Empirical formula	C20 H20 N2 O2
Formula weight	320.38
Temperature	173(2) K
Wavelength	0.71073 Å
Crystal system, space group	Monoclinic, P2(1)/n
Unit cell dimensions	a = 9.589(4) Å alpha = 90 deg. b = 6.357(3) Å beta = 94.446(7) deg. c = 26.517(11) Å gamma = 90 deg.
Volume	1611.7(11) Å ³
Z, Calculated density	4, 1.320 Mg/m ³
Absorption coefficient	0.086 mm ⁻¹
F(000)	680
Crystal size	0.70 x 0.50 x 0.25 mm
Theta range for data collection	3.02 to 28.33 deg.
Limiting indices	-12<=h<=11, -8<=k<=8, -35<=l<=29
Reflections collected / unique	8358 / 3561 [R(int) = 0.0714]
Completeness to theta = 28.33	88.4 %
Absorption correction	None
Refinement method	Full-matrix least-squares on F ²
Data / restraints / parameters	3561 / 0 / 298
Goodness-of-fit on F ²	1.224
Final R indices [I>2sigma(I)]	R1 = 0.1470, wR2 = 0.2859

R indices (all data)	R1 = 0.2147, wR2 = 0.3168
Extinction coefficient	0.008(2)
Largest diff. peak and hole	0.481 and -0.390 e.A^-3

Table 2. Atomic coordinates ($\times 10^4$) and equivalent isotropic displacement parameters ($\text{\AA}^2 \times 10^3$) for **H-mPD**.
U(eq) is defined as one third of the trace of the orthogonalized Uij tensor.

	x	y	z	U(eq)
N(2)	4166(6)	9359(10)	622(2)	31(1)
O(2)	3016(5)	15668(9)	1984(2)	38(1)
O(1)	782(5)	-644(8)	-2199(2)	35(1)
N(1)	3578(5)	4687(10)	-792(2)	29(1)
C(20)	3790(6)	7082(11)	-99(2)	21(1)
C(19)	2244(6)	2189(12)	-2000(2)	27(2)
C(18)	2950(6)	5957(11)	-441(2)	21(1)
C(17)	2644(7)	14228(11)	1134(3)	27(2)
C(16)	1435(6)	560(11)	-1831(3)	25(2)
C(15)	1347(7)	325(12)	-1313(3)	29(2)
C(14)	940(6)	7363(11)	-70(2)	26(2)
C(13)	3852(6)	10983(11)	953(2)	26(2)
C(12)	4500(6)	11043(11)	1439(3)	28(2)
C(11)	1772(6)	8495(11)	280(3)	24(1)
C(10)	2835(6)	3358(11)	-1142(2)	24(2)
C(9)	1480(6)	6073(11)	-427(2)	24(2)
C(8)	3243(6)	8356(10)	270(2)	21(1)
C(7)	3271(6)	14202(11)	1617(3)	26(2)
C(6)	2053(7)	1689(12)	-979(2)	25(2)
C(5)	2955(7)	12615(12)	801(2)	27(2)
C(4)	4217(7)	12621(12)	1769(3)	29(2)
C(3)	2921(6)	3600(11)	-1662(3)	27(2)
C(2)	-17(8)	-2400(14)	-2041(3)	39(2)
C(1)	2011(9)	17275(14)	1854(4)	42(2)

Table 3. Bond lengths [Å] and angles [deg] for **H-mPD**.

N(2)-C(8)	1.392(8)
N(2)-C(13)	1.402(9)
O(2)-C(7)	1.383(8)
O(2)-C(1)	1.428(9)
O(1)-C(16)	1.353(8)
O(1)-C(2)	1.435(9)
N(1)-C(18)	1.403(8)
N(1)-C(10)	1.408(8)
C(20)-C(18)	1.368(9)
C(20)-C(8)	1.401(9)
C(19)-C(16)	1.388(9)
C(19)-C(3)	1.391(10)
C(18)-C(9)	1.415(8)
C(17)-C(7)	1.373(9)
C(17)-C(5)	1.399(10)
C(16)-C(15)	1.390(9)
C(15)-C(6)	1.380(10)
C(14)-C(11)	1.380(9)
C(14)-C(9)	1.382(9)
C(13)-C(12)	1.387(9)
C(13)-C(5)	1.388(9)
C(12)-C(4)	1.372(10)
C(11)-C(8)	1.415(8)
C(10)-C(6)	1.387(9)
C(10)-C(3)	1.397(9)
C(7)-C(4)	1.393(9)
C(8)-N(2)-C(13)	127.0(5)
C(7)-O(2)-C(1)	117.7(6)
C(16)-O(1)-C(2)	117.3(6)
C(18)-N(1)-C(10)	124.2(5)
C(18)-C(20)-C(8)	122.1(6)
C(16)-C(19)-C(3)	121.2(6)
C(20)-C(18)-N(1)	118.7(5)
C(20)-C(18)-C(9)	119.4(6)
N(1)-C(18)-C(9)	121.9(6)
C(7)-C(17)-C(5)	118.7(6)
O(1)-C(16)-C(19)	115.4(6)
O(1)-C(16)-C(15)	126.2(6)
C(19)-C(16)-C(15)	118.4(6)
C(6)-C(15)-C(16)	120.2(7)
C(11)-C(14)-C(9)	122.8(6)
C(12)-C(13)-C(5)	118.2(6)

C(12)-C(13)-N(2)	120.0(6)
C(5)-C(13)-N(2)	121.8(6)
C(4)-C(12)-C(13)	121.1(6)
C(14)-C(11)-C(8)	118.7(6)
C(6)-C(10)-C(3)	117.9(6)
C(6)-C(10)-N(1)	120.7(6)
C(3)-C(10)-N(1)	121.3(6)
C(14)-C(9)-C(18)	118.5(6)
N(2)-C(8)-C(20)	118.7(5)
N(2)-C(8)-C(11)	122.7(6)
C(20)-C(8)-C(11)	118.5(6)
C(17)-C(7)-O(2)	124.1(6)
C(17)-C(7)-C(4)	120.5(6)
O(2)-C(7)-C(4)	115.4(6)
C(15)-C(6)-C(10)	122.0(6)
C(13)-C(5)-C(17)	121.5(6)
C(12)-C(4)-C(7)	119.9(6)
C(19)-C(3)-C(10)	120.2(6)

Symmetry transformations used to generate equivalent atoms:

Table 4. Anisotropic displacement parameters ($\text{Å}^2 \times 10^3$) for **H-mPD**.

The anisotropic displacement factor exponent takes the form:

$$-2 \pi^2 [h^2 a^*{}^2 U_{11} + \dots + 2 h k a^* b^* U_{12}]$$

	U11	U22	U33	U23	U13	U12
N(2)	20(3)	36(4)	37(3)	-9(3)	-3(2)	3(3)
O(2)	35(3)	33(3)	45(3)	-6(3)	4(2)	13(2)
O(1)	28(2)	39(3)	38(3)	-5(3)	4(2)	-10(2)
N(1)	18(3)	40(4)	29(3)	-5(3)	6(2)	-3(3)
C(20)	15(3)	22(4)	26(3)	2(3)	2(2)	2(3)
C(19)	19(3)	39(4)	22(3)	5(3)	4(2)	-2(3)
C(18)	20(3)	25(4)	19(3)	4(3)	3(2)	5(3)
C(17)	24(3)	18(4)	37(4)	8(3)	2(3)	1(3)
C(16)	16(3)	21(4)	37(4)	0(3)	4(3)	-3(3)
C(15)	26(3)	29(4)	33(4)	6(3)	4(3)	2(3)
C(14)	14(3)	30(4)	34(4)	7(3)	3(3)	6(3)
C(13)	14(3)	32(4)	30(4)	2(3)	-1(2)	1(3)

C(12)	17(3)	23(4)	44(4)	3(3)	0(3)	1(3)
C(11)	23(3)	17(3)	31(4)	4(3)	6(3)	1(3)
C(10)	15(3)	33(4)	25(3)	-1(3)	-3(2)	4(3)
C(9)	18(3)	24(4)	28(4)	4(3)	-6(3)	6(3)
C(8)	21(3)	17(3)	24(3)	4(3)	1(2)	1(3)
C(7)	25(3)	19(4)	34(4)	-2(3)	5(3)	-3(3)
C(6)	26(3)	33(4)	17(3)	8(3)	4(3)	-4(3)
C(5)	26(3)	32(4)	24(3)	1(3)	-2(3)	2(3)
C(4)	24(3)	39(4)	24(3)	1(3)	2(3)	2(3)
C(3)	20(3)	26(4)	34(4)	1(3)	1(3)	-3(3)
C(2)	36(4)	35(5)	45(5)	-5(4)	0(4)	-2(4)
C(1)	42(4)	33(5)	50(5)	-1(4)	6(4)	11(4)

Table 5. Hydrogen coordinates (x 10⁴) and isotropic displacement parameters (Å² x 10³) for **H-mPD**.

	x	y	z	U(eq)
H(4)	4580(50)	12630(90)	2110(20)	0(12)
H(19)	2300(60)	2430(100)	-2360(20)	18(16)
H(9)	920(50)	5300(90)	-700(19)	0(13)
H(5)	2530(50)	12740(90)	440(20)	3(13)
H(3)	3570(70)	4960(120)	-1800(30)	40(20)
H(2C)	660(80)	-3210(130)	-1800(30)	40(20)
H(1C)	2060(80)	18230(140)	2180(30)	60(30)
H(2B)	-330(70)	-3000(120)	-2390(30)	31(19)
H(1B)	1060(100)	16620(150)	1710(30)	60(30)
H(1A)	2160(80)	17970(140)	1540(30)	50(20)
H(2A)	-800(90)	-1650(140)	-1830(30)	60(30)
H(17)	2040(80)	15400(140)	1010(30)	50(20)
H(12)	5110(60)	9900(110)	1550(20)	18(17)
H(6)	1990(50)	1300(90)	-660(20)	1(13)
H(11)	1350(80)	9460(130)	560(30)	50(20)
H(1N)	4270(100)	5360(170)	-930(40)	80(30)
H(2N)	5020(110)	8780(170)	690(40)	80(30)
H(15)	870(80)	-990(140)	-1190(30)	50(20)
H(20)	4780(80)	7010(130)	-80(30)	50(20)
H(14)	-110(90)	7280(140)	-60(30)	50(20)

Single-crystal X-Ray data for **Cl-*m*PD-OiPr**

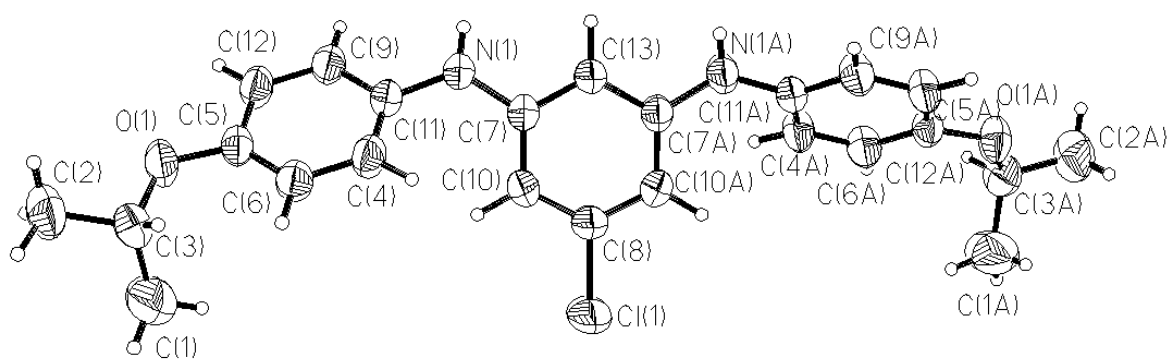


Figure B7. ORTEP (50 % ellipsoids) diagram of **Cl-*m*PD-OiPr** generated with SHELXTL software.

Table 1. Crystal data and structure refinement for **Cl-mPD-OiPr**.

Identification code	Cl-mPD-OiPr
Empirical formula	C24 H27 Cl N2 O2
Formula weight	410.93
Temperature	298(2) K
Wavelength	0.71073 Å
Crystal system, space group	Monoclinic, P2/c
Unit cell dimensions	a = 12.1426(17) Å alpha = 90 deg. b = 10.8470(15) Å beta = 102.931(2) deg. c = 8.6118(12) Å gamma = 90 deg.
Volume	1105.5(3) Å^3
Z, Calculated density	2, 1.234 Mg/m^3
Absorption coefficient	0.194 mm^-1
F(000)	436
Crystal size	0.50 x 0.20 x 0.10 mm
Theta range for data collection	3.07 to 25.00 deg.
Limiting indices	-14<=h<=14, -12<=k<=11, -10<=l<=10
Reflections collected / unique	5833 / 1954 [R(int) = 0.0228]
Completeness to theta = 25.00	99.4 %
Absorption correction	None
Refinement method	Full-matrix least-squares on F^2
Data / restraints / parameters	1954 / 0 / 188
Goodness-of-fit on F^2	0.817
Final R indices [I>2sigma(I)]	R1 = 0.0381, wR2 = 0.1465

R indices (all data)	R1 = 0.0425, wR2 = 0.1570
Extinction coefficient	0.047(9)
Largest diff. peak and hole	0.194 and -0.308 e.A^-3

Table 2. Atomic coordinates ($\times 10^4$) and equivalent isotropic displacement parameters ($\text{\AA}^2 \times 10^3$) for **Cl-*m*PD-OiPr**.
U(eq) is defined as one third of the trace of the orthogonalized Uij tensor.

	x	y	z	U(eq)
Cl(1)	0	-54(1)	2500	113(1)
C(13)	0	4059(2)	2500	46(1)
O(1)	3668(1)	2786(1)	-3731(1)	61(1)
N(1)	1427(1)	4120(1)	990(2)	60(1)
C(12)	3574(1)	3839(2)	-1410(2)	54(1)
C(11)	1977(1)	3719(1)	-191(2)	47(1)
C(10)	704(1)	2148(1)	1694(2)	51(1)
C(9)	3043(1)	4175(2)	-223(2)	54(1)
C(8)	0	1557(2)	2500	55(1)
C(7)	706(1)	3434(1)	1698(2)	45(1)
C(6)	2003(1)	2579(2)	-2587(2)	55(1)
C(5)	3068(1)	3030(1)	-2608(2)	46(1)
C(4)	1476(1)	2923(2)	-1388(2)	55(1)
C(3)	3227(2)	1958(2)	-5016(2)	63(1)
C(2)	3853(2)	2248(3)	-6290(3)	83(1)
C(1)	3340(5)	637(3)	-4493(6)	121(1)

Table 3. Bond lengths [Å] and angles [deg] for **Cl-*m*PD-OiPr**.

Cl(1)-C(8)	1.747(2)
C(13)-C(7)#1	1.3915(16)

C(13)-C(7)	1.3915(16)
O(1)-C(5)	1.3605(17)
O(1)-C(3)	1.432(2)
N(1)-C(7)	1.3893(18)
N(1)-C(11)	1.4051(18)
C(12)-C(9)	1.374(2)
C(12)-C(5)	1.388(2)
C(11)-C(4)	1.377(2)
C(11)-C(9)	1.392(2)
C(10)-C(8)	1.3749(17)
C(10)-C(7)	1.395(2)
C(8)-C(10)#1	1.3749(17)
C(6)-C(5)	1.386(2)
C(6)-C(4)	1.382(2)
C(3)-C(1)	1.499(3)
C(3)-C(2)	1.502(3)
C(7)#1-C(13)-C(7)	121.69(19)
C(5)-O(1)-C(3)	120.29(13)
C(7)-N(1)-C(11)	126.90(14)
C(9)-C(12)-C(5)	121.16(13)
C(4)-C(11)-C(9)	117.73(13)
C(4)-C(11)-N(1)	122.24(13)
C(9)-C(11)-N(1)	119.95(14)
C(8)-C(10)-C(7)	117.77(13)
C(12)-C(9)-C(11)	120.87(15)
C(10)-C(8)-C(10)#1	124.4(2)
C(10)-C(8)-Cl(1)	117.80(10)
C(10)#1-C(8)-Cl(1)	117.81(10)
N(1)-C(7)-C(13)	118.41(14)
N(1)-C(7)-C(10)	122.33(12)
C(13)-C(7)-C(10)	119.19(13)
C(5)-C(6)-C(4)	120.24(15)
O(1)-C(5)-C(6)	126.15(14)
O(1)-C(5)-C(12)	115.65(13)
C(6)-C(5)-C(12)	118.18(13)
C(11)-C(4)-C(6)	121.82(14)
O(1)-C(3)-C(1)	112.0(2)
O(1)-C(3)-C(2)	105.70(16)
C(1)-C(3)-C(2)	113.1(2)

Symmetry transformations used to generate equivalent atoms:

#1-x,y,-z+1/2

Table 4. Anisotropic displacement parameters ($\text{A}^2 \times 10^3$) for **Cl-mPD-OiPr**.
The anisotropic displacement factor exponent takes the form:
 $-2 \pi^2 [h^2 a^{*2} U_{11} + \dots + 2 h k a^* b^* U_{12}]$

	U11	U22	U33	U23	U13	U12
Cl(1)	181(1)	37(1)	156(1)	0	114(1)	0
C(13)	54(1)	40(1)	51(1)	0	24(1)	0
O(1)	58(1)	80(1)	54(1)	-12(1)	28(1)	-6(1)
N(1)	71(1)	49(1)	72(1)	-12(1)	45(1)	-13(1)
C(12)	47(1)	66(1)	55(1)	-3(1)	22(1)	-11(1)
C(11)	49(1)	46(1)	51(1)	2(1)	24(1)	-1(1)
C(10)	56(1)	47(1)	58(1)	-2(1)	28(1)	5(1)
C(9)	56(1)	59(1)	52(1)	-8(1)	23(1)	-13(1)
C(8)	68(1)	39(1)	65(1)	0	29(1)	0
C(7)	46(1)	47(1)	46(1)	-2(1)	19(1)	-2(1)
C(6)	53(1)	62(1)	52(1)	-9(1)	18(1)	-11(1)
C(5)	47(1)	53(1)	43(1)	4(1)	19(1)	4(1)
C(4)	44(1)	67(1)	58(1)	-5(1)	21(1)	-10(1)
C(3)	75(1)	67(1)	50(1)	-9(1)	24(1)	-1(1)
C(2)	100(2)	101(2)	60(1)	-12(1)	39(1)	-7(1)
C(1)	196(5)	68(2)	125(3)	-1(2)	91(3)	8(2)

Table 5. Hydrogen coordinates ($\times 10^4$) and isotropic displacement parameters ($\text{A}^2 \times 10^3$) for **Cl-mPD-OiPr**.

	x	y	z	U(eq)
H(12)		4332(18)	4130(20)	-1380(30)
H(10)		1177(17)	1700(20)	1120(30)
H(9)		3404(16)	4710(20)	600(20)
H(6)		1637(18)	2040(20)	-3430(30)
H(3)		2420(20)	2140(20)	-5420(30)
H(4)		710(20)	2640(20)	-1370(30)
H(13)		0	4980(30)	2500
H(1)		1565(17)	4830(20)	1340(30)

H(2)	4620(30)	2070(30)	-5890(40)	104(9)
H(2)	3820(30)	3080(40)	-6560(40)	127(11)
H(2)	3580(20)	1740(30)	-7280(30)	104(8)
H(1)	3070(30)	420(40)	-3600(50)	143(12)
H(1)	3090(40)	0(40)	-5260(50)	161(15)
H(1)	4150(40)	620(40)	-3990(50)	153(18)

Single-crystal X-Ray data for **Cl-*m*PD-OMac**

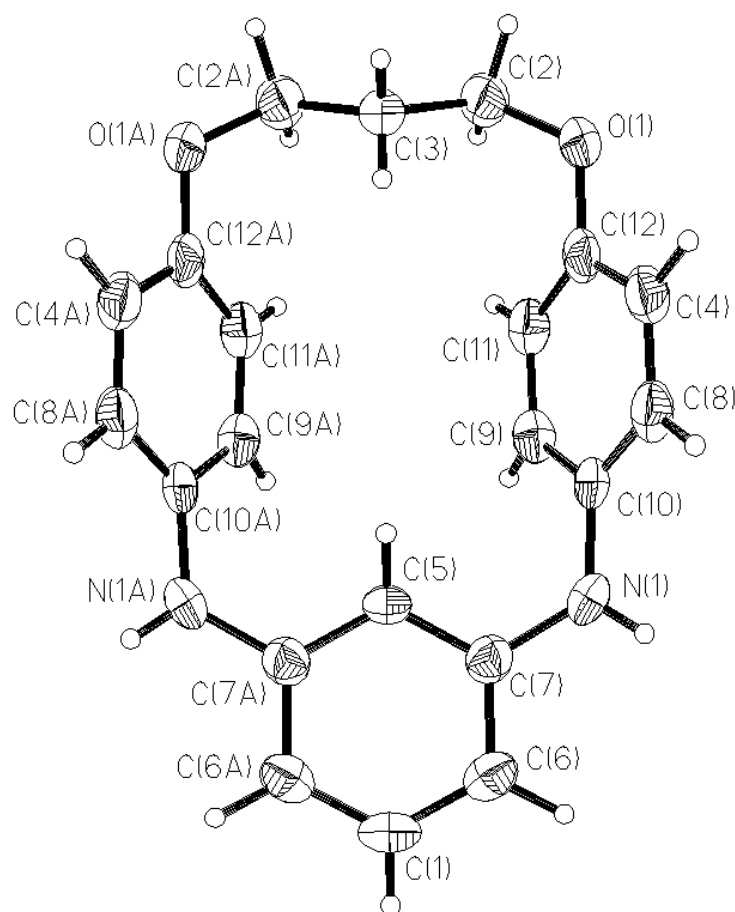


Figure B8. ORTEP (50 % ellipsoids) diagram of **H-*m*PD-OMac** generated with SHELXTL software.

Table 1. Crystal data and structure refinement for **H-mPD-OMac**.

Identification code	H-mPD-OMac
Empirical formula	C21 H20 N2 O2
Formula weight	332.39
Temperature	298(2) K
Wavelength	0.71073 Å
Crystal system, space group	Monoclinic, Cm
Unit cell dimensions	a = 8.589(2) Å alpha = 90 deg. b = 15.531(4) Å beta = 115.452(5) deg. c = 6.9256(19) Å gamma = 90 deg.
Volume	834.2(4) Å^3
Z, Calculated density	2, 1.323 Mg/m^3
Absorption coefficient	0.086 mm^-1
F(000)	352
Crystal size	0.20 x 0.07 x 0.07 mm
Theta range for data collection	2.62 to 28.22 deg.
Limiting indices	-7<=h<=11, -20<=k<=20, -9<=l<=7
Reflections collected / unique	2715 / 1425 [R(int) = 0.0176]
Completeness to theta = 28.22	95.4 %
Refinement method	Full-matrix least-squares on F^2
Data / restraints / parameters	1425 / 2 / 162
Goodness-of-fit on F^2	1.270
Final R indices [I>2sigma(I)]	R1 = 0.0544, wR2 = 0.1557
R indices (all data)	R1 = 0.0604, wR2 = 0.1600

Absolute structure parameter	3(2)
Largest diff. peak and hole	0.209 and -0.309 e. Å^{-3}

Table 2. Atomic coordinates ($\times 10^4$) and equivalent isotropic displacement parameters ($\text{\AA}^2 \times 10^3$) for **H-mPD-OMac**.

$U(\text{eq})$ is defined as one third of the trace of the orthogonalized U_{ij} tensor.

	x	y	z	$U(\text{eq})$
O(1)	2611(3)	1554(1)	6656(4)	54(1)
N(1)	7282(4)	1556(2)	15261(5)	52(1)
C(12)	3843(4)	1555(2)	8758(5)	40(1)
C(11)	5435(4)	1162(2)	9442(5)	39(1)
C(10)	6154(4)	1598(2)	13082(5)	36(1)
C(9)	6586(4)	1188(2)	11582(5)	37(1)
C(8)	4579(5)	2024(2)	12343(6)	43(1)
C(7)	7902(4)	783(2)	16343(4)	36(1)
C(6)	9207(4)	784(2)	18433(5)	42(1)
C(5)	7239(6)	0	15369(7)	31(1)
C(4)	3432(4)	2005(2)	10193(6)	45(1)
C(3)	2108(7)	0	6192(7)	38(1)
C(2)	2580(6)	821(2)	5367(5)	50(1)
C(1)	9796(7)	0	19425(7)	45(1)

Table 3. Bond lengths [Å] and angles [deg] for **H-mPD-OMac**.

O(1)-C(12)	1.384(3)
O(1)-C(2)	1.440(4)
N(1)-C(7)	1.394(4)
N(1)-C(10)	1.401(4)
C(12)-C(4)	1.380(5)
C(12)-C(11)	1.382(5)
C(11)-C(9)	1.384(4)

C(10)-C(8)	1.391(5)
C(10)-C(9)	1.398(5)
C(8)-C(4)	1.388(5)
C(7)-C(5)	1.388(3)
C(7)-C(6)	1.399(4)
C(6)-C(1)	1.383(4)
C(5)-C(7)#1	1.388(3)
C(3)-C(2)	1.522(4)
C(3)-C(2)#1	1.522(4)
C(1)-C(6)#1	1.383(4)
C(12)-O(1)-C(2)	117.0(3)
C(7)-N(1)-C(10)	123.1(2)
O(1)-C(12)-C(4)	116.2(3)
O(1)-C(12)-C(11)	123.8(3)
C(4)-C(12)-C(11)	119.9(3)
C(9)-C(11)-C(12)	120.0(3)
C(8)-C(10)-C(9)	118.1(3)
C(8)-C(10)-N(1)	122.1(3)
C(9)-C(10)-N(1)	119.9(3)
C(11)-C(9)-C(10)	120.9(3)
C(4)-C(8)-C(10)	121.0(3)
N(1)-C(7)-C(5)	120.7(2)
N(1)-C(7)-C(6)	120.4(3)
C(5)-C(7)-C(6)	118.9(3)
C(7)-C(6)-C(1)	118.1(3)
C(7)-C(5)-C(7)#1	122.3(3)
C(12)-C(4)-C(8)	120.0(3)
C(2)-C(3)-C(2)#1	113.8(4)
O(1)-C(2)-C(3)	111.5(3)
C(6)#1-C(1)-C(6)	123.5(4)

Symmetry transformations used to generate equivalent atoms:

#1 x,-y,z

Table 4. Anisotropic displacement parameters ($\text{Å}^2 \times 10^3$) for **H-mPD-OMac**.

The anisotropic displacement factor exponent takes the form:

$$-2 \pi^2 [h^2 a^{*2} U_{11} + \dots + 2 h k a^* b^* U_{12}]$$

	U11	U22	U33	U23	U13	U12
O(1)	71(2)	27(1)	42(1)	4(1)	5(1)	2(1)
N(1)	71(2)	29(1)	41(2)	-13(1)	10(1)	0(1)
C(12)	57(2)	20(1)	42(2)	5(1)	22(2)	-3(1)
C(11)	52(2)	29(1)	45(2)	0(1)	30(2)	1(1)
C(10)	46(2)	18(1)	42(2)	0(1)	16(2)	-5(1)
C(9)	37(2)	30(1)	49(2)	2(1)	21(2)	0(1)
C(8)	60(2)	27(1)	49(2)	-3(1)	30(2)	3(1)
C(7)	42(2)	34(2)	33(2)	-3(1)	17(1)	-1(1)
C(6)	46(2)	45(2)	35(2)	-9(1)	16(2)	-5(1)
C(5)	24(2)	36(2)	28(2)	0	5(2)	0
C(4)	46(2)	30(2)	56(2)	1(1)	20(2)	7(1)
C(3)	38(3)	34(2)	37(2)	0	10(2)	0
C(2)	74(3)	38(2)	34(2)	4(1)	19(2)	-4(2)
C(1)	42(3)	60(3)	25(2)	0	6(2)	0

Table 5. Hydrogen coordinates (x 10^4) and isotropic displacement parameters (A^2 x 10^3) for **H-mPD-OMac**.

	x	y	z	U(eq)
H(3B)	2670(60)	0	7560(80)	28(11)
H(5)	6330(50)	0	14160(70)	21(10)
H(11)	5750(50)	900(20)	8530(60)	33(8)
H(4)	2310(50)	2278(19)	9710(50)	37(8)
H(3)	950(80)	0	5830(80)	38(13)
H(8)	4290(50)	2290(20)	13390(50)	42(9)